THE VALUE OF STRUCTURAL HEALTH MONITORING OF A CORRODED REINFORCED CONCRETE BEAM

A Thesis Submitted to the

College of Graduate and Postdoctoral Studies

In Partial Fulfillment of the Requirements

For the Degree of Master of Science

In the Department of Civil, Geological Engineering and Environmental Engineering

University of Saskatchewan

Saskatoon

By

Xiaoyi Mao

PERMISSION TO USE

In presenting this thesis/dissertation in partial fulfillment of the requirements for a Postgraduate degree from the University of Saskatchewan, I agree that the Libraries of this University may make it freely available for inspection. I further agree that permission for copying of this thesis/dissertation in any manner, in whole or in part, for scholarly purposes may be granted by the professor or professors who supervised my thesis/dissertation work or, in their absence, by the Head of the Department or the Dean of the College in which my thesis work was done. It is understood that any copying or publication or use of this thesis/dissertation or parts thereof for financial gain shall not be allowed without my written permission. It is also understood that due recognition shall be given to me and to the University of Saskatchewan in any scholarly use which may be made of any material in my thesis/dissertation.

Requests for permission to copy or to make other uses of materials in this thesis/dissertation in whole or part should be addressed to:

Head of the Department of Civil, Geological and Environmental Engineering
57 Campus Drive
University of Saskatchewan
Saskatoon, Saskatchewan S7N 5A9 Canada

OR

Dean
College of Graduate and Postdoctoral Studies
University of Saskatchewan
116 Thorvaldson Building, 110 Science Place
Saskatoon, Saskatchewan S7N 5C9 Canada

ABSTRACT

With the increasing number of aging structures worldwide, structural health monitoring (SHM) has gained considerable research interest. Structural health monitoring (SHM) can provide real-time information about a structure's actual condition, thereby mitigating the risk of failure if the structural condition is worse than presumed, or extending the service life and saving the replacement costs if it has an adequate level of safety. Many SHM techniques have been developed in the past 40 years; however, few of them have been successfully implemented on real structures. The limited practical application of SHM has been attributed to the lack of mature and sophisticated SHM techniques and the lack of economic studies to clearly demonstrate the financial benefits to the structural owners.

Christensen et. al described the theoretical principle of a surface strain-based SHM technique for reinforced concrete beams in the book "Monitoring Technologies for Bridge Management" in 2011. This SHM technique is designed to estimate the remaining effective cross-sectional area of the reinforcing bars after corrosion, which can then be used to predict the remaining structural capacity and service life, as well as the degree of certainty associated with these predictions. As part of the current research project, laboratory experiments were conducted to evaluate the effectiveness of the surface strain-based SHM technique on nine small-scale reinforced concrete beams. The experimental and data processing procedures were first calibrated to obtain more reliable results. The effectiveness of the proposed SHM technique was then determined and quantified using the errors between the predicted beam capacities using the identified optimal procedures and the actual failure loads. It was found that the proposed technique did not achieve accurate estimates of the remaining cross-sectional area of the reinforcing bars or failure load when applied to the small and slender beams. However, it is believed to have potential to provide better result on large-scale beams.

The experimental results were also used to demonstrate the value of SHM systems through reliability and economic analyses. Two monitoring systems with different levels of uncertainty were created. The standard monitoring system was composed of strain measuring equipment only, while the enhanced monitoring system included the strain measuring equipment and a cover meter, used to reduce the uncertainty of the reinforcing bar locations. It was demonstrated that, although the enhanced SHM system was associated with a higher cost, it consistently

provided a higher reliability index – leading to an extension of service life – and lower annual worth of life cycle costs (AWLCC) when replacement decisions were based on the respective SHM data.

ACKNOWLEDGEMENTS

First and foremost, I am grateful to have Dr. Leon Wegner as my supervisor. I could not have finished my master program without his continuous support and guidance over the years. I also want to express my gratitude to Dr. Moh Boulfiza and Dr. Bruce Sparling for being my committee members. In addition, I would like to thank Dr. Richard Evitts for helping me with corrosion related questions and welcoming me to his group meetings.

I received much technical guidance in experimental design from Brennan Pokoyoway, Helen Yin, and Gang Li. Their expertise and generous help are deeply appreciated. Many thanks to the tutors at the writing help center for their prompt and informative feedbacks. I would like to extend my gratitude to all my peers. I would miss the time we spent together in structural or computer labs.

At last, the people I could not thank enough are my parents. I have not spent much time with them since I studied abroad at the age of 18. However, they unconditionally support all my decisions and always have faiths in me. I would not have finished my degree and lived a happy and healthy life without them.

At last, special thanks to Dr. Peng Qi: watching you fight with cancer and finish your PhD degree have been my biggest inspirations. Thank you for the company in the last four years, especially during the pandemic.

DEDICATION

This thesis is dedicated to my parents, Yifeng Wang and Weijun Mao,
for their unconditional and endless love and support.

TABLE OF CONTENTS

LIST OF TABLES

LIST OF FIGURES

LIST OF SYMBOLS

A_{allow}	The minimum allowable reinforcing bar area due to corrosion (mm^2)
A_s	Actual rebar cross-sectional area (mm^2)
A_t	Transformed rebar area (mm^2)
Al	Aluminum
b	Width of the beam (mm)
b_{DIC}	Estimated neutral axis location considering data from the DIC side (mm)
b_{ESG}	Estimated neutral axis location considering data from the ESG side (mm)
b_{ESGDIC}	Estimated neutral axis location considering using data from two faces combined (mm)
c	The distance from the top of the beam to the neutral axis (mm)
cc	Concrete cover thickness (mm)
d	Distance from the top surface to the rebar location (mm)
d_1	The distance from the top of the beam to the first strain gauge (mm)
d_b	Rebar diameter (mm)
E_c	Concrete Young's modulus (GPa)
E_s	Steel Young's modulus (GPa)
f_c'	Compressive strength of concrete (MPa)
f_s	Ultimate strength of steel (MPa)
f_y	Yielding stress of steel (MPa)

F	Faraday's constant, which equals 96487 A·s/mol
Fe	Iron
h	Beam height (mm)
i	Discount rate (%)
I_{app}	Applied current density (A)
l	Length of the corroded section (mm)
M	Mass loss per unit surface area (g)
M_u	Bending moment capacity (kN·m)
n	Number of equivalents exchanged
n	Ratio of the Young's modulus of steel and concrete
P	Present value of the total life cycle cost (US Dollars)
R^2	Coefficient of determination
T	Total time that the current has been applied (s)
y	Compounding Period (yr)
$\bar{y}$	The distance from the top of the beam to the centroid (mm)
Zn	Zinc
α_1	Whitney stress block parameter
β	Reliability index
$\beta_{critical}$	Minimum acceptable value of reliability index
ε	Strain

ε_1	Strain reading provided by the gauge at depths of d_1
μ_R	Mean value of resistance (kN·m)
μ_L	Mean value of load effect (kN·m)
μ_{Rallow}	The minimum allowable mean resistance of the structure (kN·m)
$\mu\varepsilon$	Microstrain
ρ	Density of the steel (kg/m^3)
σ_{A_t}	Standard deviation of transformed area (mm^2)
σ_b	Standard deviation of beam width (mm)
σ_c	Standard deviation of neutral axis location (mm)
σ_d	Standard deviation of depth of reinforcing bar (mm)
σ_L	Standard deviation of load effect (kN·m)
σ_R	Standard deviation of resistance (kN·m)

LIST OF ABBREVIATIONS

1D	One Dimensional
2D	Two Dimensional
3D	Three Dimensional
AE	Acoustic Emission
ASCE	American Society of Civil Engineers
ASTM	American Society for Testing Materials
AWLCC	Annual Worth of Life-cycle Cost
CC BY	Creative Common Attribution
CSA	Canadian Standards Association
DAQ	Data Acquisition
DC	Direct Current
DIC	Digital Image Correlation
EC	Eddy Current
EMI	Electromagnetic Impedance
ESG	Electrical Strain Gauge
FBG	Fiber Bragg Grating
FHWA	Federal Highway Administration
FOS	Fiber Optic Sensors
IASC	International Association for Structural Control
ISIS	Intelligent Sensing for Innovative Structures (Network of Centres of Excellence)

LCC	Life-cycle Cost
MDPI	Multidisciplinary Digital Publishing Institute
NaCl	Sodium Chloride
N.A.	Neutral Axis
NACE	National Association of Corrosion Engineers (NACE and the Society for Protective Coatings have merged to become the Association for Materials Protection and Performance.)
NDT	Non-destructive Testing
OSP	Optimal Sensor Placement
PZT	Piezoelectric
pH	A figure expresses the acidity or alkalinity of a solution
SHI	Structural Health Information
SHM	Structural Health Monitoring
STDV	Standard Deviation
UTM	Universal Test Machine
VBDD	Vibration-based Damage Detection
VOI	Value of Information
WSN	Wireless Sensor Network

CHAPTER 1 INTRODUCTION

1.1. Background

The capacity of a structural element is continuously decreasing due to aging, fatigue, corrosion, or damage caused by accidents (Yan et al. 2017b). The phenomenon of aging structures is a global issue. For example, the average age of bridges in the U.S. is 47 years (ASCE 2017). In many developed countries such as Italy or Japan, most of the transportation infrastructure was constructed after World War II and before 1975 (Tonelli et al. 2020). In developing countries like China, new structures are being built at a rapid rate, and there are also many historical structures that require protection (Gopal et al. 2017). Corrosion is the main reason for the degradation of reinforced concrete structures, especially in cold regions like Canada due to the use of de-icing salts, since the chloride ions in these salts can accelerate the corrosion of reinforcing bars (Palumbo 1991, Fu et al. 2018). It has been estimated that the direct annual cost of corrosion is approximately $41 billion in Canada (Shipilov 2016) and $2.5 trillion globally (Koch et al. 2016). Under the current circumstances, the traditional inspection method, which involves visual inspection performed at certain time intervals, is considered inadequate (FHWA 2001, Dubey et al. 2008).

The life-safety issues and huge economic burden associated with the deterioration of structures have greatly stimulated the research interest in structural health monitoring (SHM). SHM provides continual evaluation of a structure's integrity using the data obtained from on-board sensors (SAE 2013). The implementation of an SHM system can convert the time-based inspection and maintenance approach to a condition-based approach (Farrar and Worden 2007). Rytter (1993) classified various SHM systems into four levels of sophistication:

Level 1 detects whether damage exists;

Level 2 locates the damage;

Level 3 quantifies the magnitude of the damage, as well as specifies its location; and

Level 4 provides a prognostication of the remaining service life, in addition to the information provided by Levels 1 through 3.

Although many promising SHM techniques have been developed in recent years, their transition from research to real-life applications has been slow and difficult. One of the main reasons for this problem is the lack of technological maturity (Amafabia et al. 2017, Kralovec and Schagerl 2020). A literature review regarding the state-of-the-art developments of the main SHM techniques is presented in Chapter 2. It was found that most of the techniques can only provide Level 2 monitoring. Moreover, many of them only work for a certain type of structure or damage. For example, the eddy current method only works for metal structures (Ghoni et al. 2014), and the acoustic emission method can only detect crack propagations (Calabrese and Proverbio 2020). There has not been an SHM method that can perform Level 4 monitoring on reinforced concrete structures.

In the book "Monitoring Technologies for Bridge Management", Christensen et al. (2011) described the theoretical principles of a new surface strain-based SHM method which can perform Level 4 monitoring on corroded reinforced concrete beams. This method only required a couple of strain gauges attached to the side of the beam and could estimate the effective reinforcing bar area left after corrosion from the measured flexural strain distribution. The effective area was then used to predict the remaining load-bearing capacity of the beam. This method was demonstrated on a hypothetical beam, but has never been validated experimentally. If proven to be effective, this would be a user-friendly and cost-effective Level 4 SHM method for reinforced concrete structures.

Besides the inadequate technical feasibility of SHM systems, another main reason for the slow adoption of the SHM technologies is that their value has not been clearly demonstrated to structural owners (Farrar and Worden 2007, Cawley 2018). The value of SHM mainly comes from two aspects: the life-safety and economic benefits (Farrar and Worden 2007, Yan et al. 2017b).

To assess the safety of a structure, the reliability index, β, is commonly used and is associated with the risk of failure (Frangopol and Messervey 2011). The reliability index is defined as the

difference of the mean resistance and load effect divided by the standard deviation of the difference. A high reliability index indicates a high level of safety and a low probability of failure. A reliability index of 2 (corresponding to a probability of failure of 0.02275) to 4 (probability of failure of 0.0000316) is commonly used in structural assessment (Frangopol and Messervey 2011). If the reliability index drops below a certain threshold for a structure, it can be increased by repair or replacement of the structural element (increasing the mean resistance) or by implementing an SHM system (reducing the uncertainty in structural condition and thereby the standard deviation of the difference between mean resistance and load effect). If the second option is selected, the monitored structure may be allowed to remain in service while ensuring the safe operation of the structure through ongoing monitoring. Therefore, economic benefits can be generated through the optimized maintenance schedule, reduced down-time, and prolonged lifespan.

Christensen et al. (2011) also presented a framework for quantifying the economic benefits of SHM using the value of information (VOI) approach. VOI is a commonly used concept in decision analysis and, in the context of SHM, it is defined as the difference between the expected life-cycle costs of the structure with and without the SHM information (Zonta et al. 2014). The framework considered two SHM systems with different levels of uncertainty implemented on the hypothetical beam mentioned above, and then VOI was quantified considering the data provided by the two SHM systems. It was shown that a standard SHM system was able to generate savings in the beam's annualized life-cycle cost, and an enhanced SHM system with higher precision measurements could generate more savings. However, this framework also has not been demonstrated using experimental data.

The implementation of an SHM system is an extra cost to the structure's owner and does not change the physical condition of the structure. However, the information provided by an SHM system can aid in the structural management decision making and provide life-safety and economic benefits regardless of the actual condition of the structure. If the health diagnostics provided by the SHM system show that the actual structural condition is worse than presumed, a timely replacement or repair may avoid a catastrophic failure of the structure, and thus avoid the huge economic loss associated with the failure. If the structural condition is better than presumed, the structure's reliability index will be increased through increased capacity and reduced

uncertainty. Even if the structure's condition is the same as presumed, its reliability index can still be improved through the reduced uncertainty alone. The structure can remain in service for a longer period of time, and the future inspection and maintenance schedule can be optimized, given that its condition is being continuously monitored.

1.2. Objectives

The primary objective of this research study was to demonstrate the ability of structural health monitoring to extend the service life of a corroding reinforced concrete beam by estimating its remaining bending moment capacity and increasing the reliability index, and thereby to develop a framework to make the economic case for implementing SHM systems in practice. Specific sub-objectives include the following:

- To experimentally evaluate the effectiveness of the strain-based technique described in Christensen et al. (2011) as a Level 4 SHM method for a corroding reinforced concrete beam;
- To demonstrate the improvement in structural reliability that can be achieved using data obtained from an enhanced SHM system with a higher level of precision; and
- To perform life-cycle cost benefit analyses associated with implementing two SHM systems (a 'standard' and an 'enhanced' SHM system) in order to demonstrate the economic value of SHM systems.

1.3. Scope of Research

This research project involved conducting laboratory experiments to test the effectiveness of the surface strain-based SHM technique described in Christensen et al. (2011). The data collected through the experiments were used in reliability and economic analyses to demonstrate the value of SHM systems.

For the laboratory experiment, three batches of small-scale reinforced concrete beams were cast and subjected to different levels of accelerated corrosion by the impressed current method. Strain data were obtained using two different types of instrumentation: electrical strain gauges and a digital image correlation (DIC) system. The two sets of data were compared to each other first, and then were combined to achieve the optimum SHM diagnostics to estimate the effective

reinforcement area and remaining bending moment capacity. The optimum estimates were compared to the real beam conditions to evaluate the effectiveness of the proposed SHM technique. The real beam conditions were determined using the experimental failure loads and the actual remaining reinforcing bar area due to corrosion obtained through gravimetric analyses after the extraction of the bar.

A cover meter was also used in the lab experiment to reduce the uncertainty associated with the location of the reinforcing bars. Thus, two SHM systems with different levels of uncertainty were formed. The standard SHM system considered only the strain data provided by the electrical strain gauges and the DIC system, while the enhanced SHM system considered both the strain data and the cover meter data. The experiment was followed by reliability and economic analyses to demonstrate and compare the benefits gained through the two SHM systems with different levels of uncertainty.

The reliability index, β, was used to demonstrate the improvement in structural reliability associated with using the SHM systems. It was calculated based on the load effect, the estimated mean beam resistance, as well as the precision of the measured data gathered from each SHM scheme. The economic benefits associated with using the SHM systems were quantified using the value of information approach described in Christensen et al. (2011). The allowable life spans of the beams estimated by each monitoring scheme were identified. The economic value of SHM systems was demonstrated by the savings in the Annual Worth of Life Cycle Costs (AWLCC), which were calculated using a total life-cycle cost, an inflation rate, and a life span.

The effect of loss of bond due to corrosion was not within the scope of this research. The prediction of the beam resistance was mainly based on the remaining cross-sectional area of the reinforcing bar. The impact caused by loss of bond was eliminated in the proposed lab experiment by controlling the corrosion location to be within the constant moment region produced by using a four-point loading set up.

1.4. Organization of Thesis

This thesis contains five chapters. Details of each chapter are summarized below.

Chapter 1 provides an introduction to this thesis, which consists of the background, objectives and scope of this research study.

Chapter 2 presents the results of the literature review relevant to this research. The literature review was conducted in four areas, including the technical development of various SHM techniques, the economic studies of SHM, prevalent strain measuring equipment, and the techniques used for inducing accelerated corrosion on reinforced concrete.

Chapter 3 describes the setup of the experimental program, as well as the methodologies used for the experimental, reliability and economic analyses.

Chapter 4 provides an evaluation of the practical effectiveness of the proposed surface strain-based SHM technique based on the experimental results.

Chapter 5 presents and discusses the results of the reliability and economic analyses considering the standard and enhanced SHM systems. A comparison of the estimated reliability indices and annualized life-cycle costs between the two SHM systems is provided to demonstrate the value of additional precision associated with an enhanced monitoring system.

Chapter 6 contains the conclusions from this research and recommendations for future work.

CHAPTER 2 LITERATURE REVIEW

2.1. Introduction

Although a wide variety of promising SHM technologies have been developed in the last a few decades, few have been adapted to real-world operational structures. Many research papers have discussed the reasons why the transition from research to industrial applications is difficult (Farrar and Worden 2007, Li et al. 2014, Yan et al. 2017b, Cawley 2018). One fundamental reason is that there is lack of a user-friendly yet robust and sophisticated SHM technique that is suitable for all kinds of structures (Amafabia et al. 2017, Kralovec and Schagerl 2020). Most SHM techniques use very complicated damage identification algorithms, which would typically require an expert to interpret (Tonelli et al. 2020). Moreover, different techniques are tested on various structures based on the author's choice (Das and Saha 2018). Thus, it is difficult to compare different techniques and to design regulations and standards based on the best practices. Lack of guidance from the regulatory agencies is another commonly recognized reason that hinders the implementation of SHM (Zhou et al. 2013, Li et al. 2014, Tonelli et al. 2020, Sykora et al. 2020). Lastly, a non-technical issue is that its economic benefit is usually not demonstrated to the structural owner (Farrar and Worden 2007, Cawley 2018).

To better understand the current capabilities of various SHM techniques and to identify the opportunities for the surface-strain based SHM technique being tested in this thesis, a technical review is provided in Section 2.2. Since this research study not only investigates the technical feasibility of a new SHM method, but also demonstrates its economic value, existing economic studies related to SHM have also been reviewed and discussed in Section 2.3. Strain is an important factor for the SHM method being evaluated in this research study and for many other SHM systems; thus, different strain measuring equipment is compared in Section 2.4. Lastly, as this experimental study involves laboratory experiments on corroded reinforced concrete beams, methods to induce accelerated corrosion are introduced in Section 2.5.

2.2. Review of Common SHM Technologies

2.2.1. Introduction

There are hundreds of review papers about SHM technologies that have been published in the past 10 years (569 search results in Engineering Village using the key words "SHM" and "Review"). Most of them focus on a specific SHM technique, such as reviews on guided waves (Mitra and Gopalakrishnan 2016, Elwalwal et al. 2017), vibration-based damage detection (Das and Patro 2016, Avci et al. 2021), fibre optic sensors (Hassan et al. 2012, Bado and Casas 2021), piezoelectric sensors (Annamdas and Radhika 2013, Na and Baek 2018), and acoustic emission (Khan 2018, Calabrese and Proverbio 2020). Some of them look at the SHM technologies suitable for a certain type of structure, such as for composite structures (Amafabia et al. 2017, Güemes et al. 2020) or bridges (Bakht et al. 2011, Seo et al. 2016). In fact, such reviews would still be too broad. Many of the researchers would further narrow down their scopes to a specific technique for certain types of structures. Examples include a review of acoustic emission in mines (Manthei and Plenkers 2018) and a review of acoustic emission for reinforced concrete structures (Benedetti 2012).

Although many of the review papers summarize the historical and state-of-the-art development of a particular field of SHM well and reading them all would lead to a comprehensive understanding of the industry, this approach is not accessible to students, engineers or structural owners who are new to SHM. Few attempts have been made to present an overview of SHM. This is a challenging task because SHM is multi-disciplinary in nature, and it is getting increasingly difficult as the number of techniques and applications of these techniques increase. A worthwhile attempt is the book "Structural Health Monitoring" published in 2010 (Balageas et al. 2006). This book provides an introduction to SHM followed by comprehensive reviews on extensively researched SHM areas including vibration-based damage detection (VBDD), fiber-optic sensors (FOS), piezoelectric (PZT) sensors, SHM using electrical resistance, electromagnetic techniques, and capacitive methods. Through observing the number of papers published about a certain topic, VBDD, FOS, PZT, and electromagnetic techniques remain to be the areas of focus from the publication of this book until now; however, there are not as many research studies and applications about the methods based on electrical resistance and capacitance. Additionally, a topic that has become one of the most popular research topics in the

last ten years (Cawley 2018, Güemes et al. 2020, Kralovec and Schagerl 2020) but is not included in this book is guided wave monitoring. Besides being slightly outdated, another shortcoming of this book is that it does not classify various of SHM technologies and introduce them by classification. For one, this does not help readers to understand the connections between different technologies. Another potential issue is that the methods listed are hot research areas about SHM, and they are not mutually exclusive to each other. FOS and PZT sensors focus on the sensor technologies, and they need to be combined with other SHM techniques to form a system; for instance, PZT sensors are most often used in electromagnetic impedance (EMI) based SHM methods. Thus, for the same system, one researcher might call it "an SHM system using PZT sensors" and another one might call it "an EMI SHM system".

To avoid overlapping, some review studies classify SHM technologies based on the sensor type, such as FOS, PZT sensors, eddy current sensors, and accelerometers (Taheri 2019, Warsi et al. 2019, Maraveas and Bartzanas 2021). But Güemes et al. (2020) argue that it is better to classify technologies based on their physical underlying principles, because the same type of sensors can be used for different SHM systems. However, classifying based on physical principles also has its drawbacks. Novice SHM engineers or structural owners might not be familiar with all the underlying physical principles. Moreover, much research in SHM has been devoted to sensing technologies and focusing on physical principles might overlook the advancements made in sensing technologies or other areas. Thus, the real issue is that an SHM system is generally made of three components: sensors, a data acquisition system (which can be further broken down into data processing, data transmission and data storage), and a health diagnostics algorithm (Housner et al. 1997). The names of different SHM methods are typically given by their developers based on the key innovative features. However, the key feature could be associated with any one of the three components of an SHM system.

Most classification methods and SHM technologies are only referable to one of the components, as shown in Figure 2.1. For example, FOS is a type of sensor, whereas VBDD is mostly a methodology used for health diagnostics, and wireless sensors refer to a type of data transmission technology. Therefore, the following sections, 2.2.2 to 2.2.4, discuss the classifications and technologies associated with each component in an SHM system. Note that the review can not be provided in too much detail considering the broad scope and the large

number of technologies developed lately, but it is an attempt to cover the major advancements in all the components of SHM. Lastly, the future of SHM is discussed in Section 2.2.5.

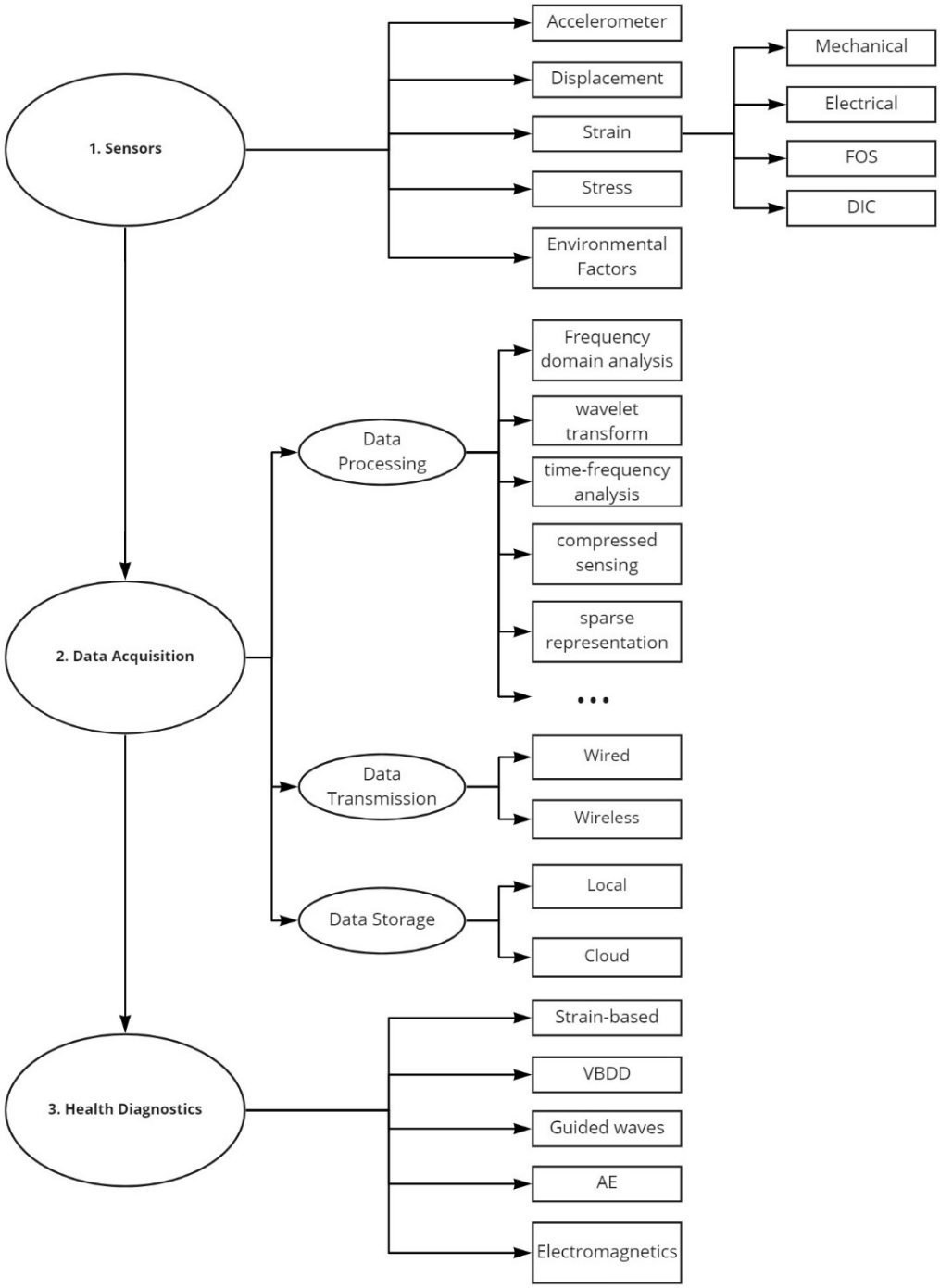

Figure 2.1. Classifications of SHM technologies based on components of an SHM system.

2.2.2 Sensing Technologies

The rapid development of SHM methods is largely driven by the advancements in sensing technologies (Bisby and Briglio 2006). Depending on the specific requirements of the structure being monitored, engineers might be interested in certain measurements indicating structural status, such as strains, displacements, accelerations, and stress, or in some environmental factors, such as temperatures, moisture levels, wind pressure and soil condition of the foundation (Bisby and Briglio 2006, Yi and Li 2012). The area that has received the most research attention is strain sensors, such as fibre optic sensors (FOS) and digital image correlation (DIC). Other popular types of sensors include piezoelectric sensors, ultra-sonic sensors, and acoustic emission devices (AE). Maraveas & Bartzanas (2021) reviewed the most prevalently used sensors for SHM of agricultural structures. The review included both traditional and novel sensors and concluded that notable improvements in sensing technologies include increased accuracy and transmission speed, reduced noise, and deployment of machine learning. Warsi et al. (2019) also conducted a review of cutting-edge sensing technologies used in SHM and concluded that micro and nano electric sensors have drawn significant interest in the past ten years due to the advantages of being compact, durable, and cost effective. They provided a thorough discussion and comparison of the present micro-electromechanical sensors including accelerometers, bolometers, resonators, and their corresponding data acquisition systems.

The developments of various sensing technologies are too extensive to be reviewed in this chapter. However, since strain is an important factor for the SHM method being evaluated in this thesis and for many other SHM methods, a detailed review of the prevalent strain measuring techniques is provided in Section 2.3.

Besides the advancements in sensor design, there are also many studies that focus on the optimal sensor placement (OSP). Since a wide distribution of sensors for a large structure can be costly, the goal of OSP is to use a minimum number of sensors to acquire adequate information for SHM analysis (Yi and Li 2012, Sun and Büyüköztürk 2015). Techniques such as neural networks (Worden and Burrows 2001), information entropy (Papadimitriou 2004), particle swarm optimization (Rao and Anandakumar 2007) and Bayesian optimization (Flynn and Todd 2010) have been applied to OSP. Yi & Li (2012) discussed the evaluation criteria for identifying the suitability of sensor locations and compared multiple influential OSP methods including

deterministic optimization method, sequential sensor placement method, genetic algorithms, simulated annealing algorithm, monkey algorithm, ant colony optimization algorithm and particle swarm optimization algorithm. Sun and Büyüköztürk (2015) conducted a review of the developments in OSP and proposed a new discrete optimization method using the artificial bee colony algorithm. This method was tested on a truss bridge and two high-rise buildings and was proven to be efficient and effective.

2.2.3 Data Acquisition

The data acquisition system can be further divided into data processing, transmission, and storage (Housner et al. 1997). While these components are usually developed by researchers in mathematical, electrical and computer engineering fields independently, the advancements made in these areas have contributed to the development of SHM.

The amount of data collected by an SHM system can be massive and may contain misleading information due the influence of environmental factors. Thus, the data need to be processed first to reduce their size and noise before being analyzed by the health diagnostics system (Bisby and Briglio 2006). Data are usually processed after they have been transferred to the base station. However, due to the bandwidth limit of emerging wireless technologies, data sometimes are processed at the sensor nodes before transmission. Yan et al. (2017) discussed the most commonly used techniques for feature extraction: frequency domain analysis, wavelet transform, time-frequency analysis, compressed sensing and sparse representation, empirical mode decomposition and stochastic resonance. However, there is no technique that is suitable for all situations. Vibration-based SHM methods generally rely heavily on data processing. Pablo & Adeli (2016) compared the advantages and disadvantages of ten data processing techniques for vibration-based SHM. They also introduced four novel mathematical algorithms that have the potential to be used but have not yet been applied to SHM. Albuquerque et al. (2019) reviewed the conventional data processing techniques used for impedance-based SHM methods and introduced a new technique based on the Hinkley criterion that can detect structural defects more effectively in a noisy environment.

Data transmission methods can mainly be classified as wired or wireless. Conventional wired monitoring systems have the advantage of anti-interference and have been successfully implemented on many operating structures, for instance, the Tsing Ma suspension bridge in Hong Kong (Shaladi et al. 2015). However, the installation and equipment costs associated with wired systems are very large, and they are vulnerable to deterioration for long-term monitoring (Abdulkarem et al. 2020). Thus, an increasing amount of research focuses on adapting wireless sensor network (WSN) technologies to SHM systems (Wang et al. 2012, Shaladi et al. 2015). A WSN system contains sensor nodes, which collect data from sensors, and then the sensor nodes transmit the data to the base station through various communication technologies (Abdulkarem et al. 2020). Currently, the most popular communication technologies are Zigbee, Bluetooth, Wi-Fi, and Tele Communication (Yan et al. 2017b). These communication technologies were developed independently and have had mature applications in other areas. However, bringing these technologies to WSN for SHM can be challenging because different SHM systems have varying degrees of requirements regarding data transfer rate, coverage range, energy efficiency, expected lifespan and working condition (Yan et al. 2017b). Abdulkarem et al. (2020) conducted a comprehensive review and chronologically summarized the academic prototypes and commercial WSN platforms tested for SHM from 2005 to 2019. Over the years, advancements have been made to the compatibility of different sensor types, optimization of sensor topology, and the functionality of the sensor node. Now most of the accelerometers, conventional strain sensors, and fibre optic sensors are compatible with WSNs. Some of the data processing is carried out at the sensor nodes instead of at the base station to significantly reduce the amount of raw data needed to be transferred, which further saves storage space, energy consumption and transmission bandwidth (Abdulkarem et al. 2020). The possible areas of focus for future research about WSN-based SHM include fault tolerance, cloud data storage and processing, SHM algorithms and distributed processing, optimal sensor node placement, and energy harvesting technologies (Abdulkarem et al. 2020).

An SHM system usually has high demand on the longevity and storage space of the data storage system. A large scale structure with hundreds of sensors implemented can generate gigabytes of data every day (Furtner et al. 2013). These data need to be available for many years. A common practice is to remove raw data and only keep processed data. However, reinterpretation would

not be possible if raw data are lost (Bisby and Briglio 2006). The development of cloud storage and computing technologies has provided an excellent solution to this issue. The cloud databases can be classified as open source, academic and commertial databases; Tsvetanov (2021) listed and compared the options available under each category. In recent years, the theoretical frameworks of several cloud-based SHM systems have been proposed (Lan and Liu 2013, Zhao et al. 2015, Searls et al. 2019). Jeong et al. (2019) successfully tested their system on bridges along the I-275 corridor in Michigan and concluded that a cloud-based cyber infrastructure platform can manage the sensor data effectively and retrieve the data efficiently.

2.2.4 Health Diagnostics

Diagnostics is arguably the most important component of an SHM system (Bisby and Briglio 2006). The principles used for diagnostics and prognostics typically determine the level of sophistication of an SHM system, also known as the Rytter levels (Rytter 1993, see p.1). At the same time, these principles play an important role in the selection of other components, i.e., the type of sensors, data processing algorithms, data transfer methods, and data storage platforms. Therefore, most of the SHM methods are named by the underlying physical principles used by the health diagnostics system. Some of the main SHM methods that have been studied extensively and applied successfully to real structures include strain-based methods, vibration-based damage detection (VBDD), guided waves, acoustic emission (AE), ultrasonic and electromagnetics (Cawley 2018).

Strain-based SHM methods have been applied to a wide range of structures including buildings, bridges, highways, tunnels, pipes and wind turbines (Bado and Casas 2021). Research about strain-based SHM techniques mainly focuses on the advancements of the strain sensors such as FOS and DIC technologies. In terms of the health diagnostics principles, there are mainly two categories for the strain-based methods: detection of damage-induced strains and strain mapping (Güemes et al. 2020). The first method uses distributed sensors to catch strains located at the damaged area. This approach is simple and robust but has quite limited coverage, since damage is only detectable if a strain gauge is located exactly at the location of damage (Güemes et al. 2018). Thus, this approach is not realistic to monitor an entire structure using the traditional discrete strain measuring equipment. However, the development of distributed fibre optic sensors

has significantly increased the monitoring coverage. Bado and Casas (2021) provided a comprehensive review of the recent application of distributed optical fiber sensors on civil engineering structures. The other method, strain mapping, does not require sensors to be place right at the location of damage. Basically, the occurrence of local damage will result in strain redistribution, and the changes in the strain field will be analyzed by sophisticated algorithms to detect and locate the damage (Güemes et al. 2018). However, local cracks might have little impact to the global strain field, and thus are very difficult to detect (Güemes et al. 2020).

Guided wave monitoring is one of the most popular research topics in the last 10 years (Cawley 2018, Güemes et al. 2020, Kralovec and Schagerl 2020). Through analyzing the ultrasonic mechanical wave propagation within bounded structural media, it can detect relatively small damage in a large area using just a small number of transducers. However, due to the dispersive nature of the guided waves, the computational cost related to this method is generally high (Mitra and Gopalakrishnan 2016). Therefore, guided wave-based monitoring has been successfully applied to one-dimensional structures such as pipes, rails, cables, truss members and reinforcing bars. Further research is still need to for it to be implemented on more complex structures (Mitra and Gopalakrishnan 2016, Cawley 2018).

VBDD methods have drawn significant attention since the 1970s (Cawley 2018). The principle of the VBDD method is that damage can be detected and located through monitoring changes in a structure's dynamic response to imposed or ambient excitation forces (Zhou 2006). Similar to the guided wave monitoring method, VBDD has the potential to assess the integrity of the whole structure using a small number of sensors (Cawley 2018, Pepe et al. 2019). However, VBDD methods are more sensitive to changes in environmental factors, which makes it harder to identify small defects. Only severe damage is detectable in real-life applications (Cawley 2018, Güemes et al. 2020). This situation can potentially be improved by adopting artificial intellegence such as machine learning and deep learning into the diagnostics algorithm. Avci et al. (2021) conducted a comprehensive review of the recent applications of machine learning and deep learning methods used for VBDD in civil structures. It has been proven that machine learning and deep learning are more suitable to deal with fuzzy and noise-contaminated data than traditional data processing methods. Interest has been particularly drawn to 1D and 2D

convolutional neural networks (one type of deep learning algorithm), since they are extremely easy to train and have high computational efficiency (Avci et al. 2021).

AE and electromagnetic technologies were originally developed as NDT methods, but they can also be attached to the structure permanantly and thus be converted to SHM systems (Mba 2006, Amafabia et al. 2017, Cawley 2018). There are several review papers published about the advancements and applications of AE in SHM (Wevers and Lambrighs 2009, Behnia et al. 2014, Manthei and Plenkers 2018, Khan 2018, Calabrese and Proverbio 2020). Strantza et al. (2015) evaluated the crack detection capabilty of AE and other NDT methods on metallic structures, and concluded that all the tested methods can serve as long-term SHM methods and identify the crack locations effectively. Electromagnetic based SHM methods mainly consist of electromechanical impedance (EMI) and eddy current (EC) methods. The development of EMI techiniques for SHM is discuss in Chapters 1 to 7 of the book "Smart Materials in Structural Health Monitoring, Control and Biomechanics" (Bhalla and Soh 2012). Cirp et al. (2019) reviewed the state-of-art damage classification methodologies for EMI SHM technique and proposed an improved classification method using neural networks and self-organizing maps. The state-of-art development and applications of eddy current testing have been summarized in a few review papers (Ghoni et al. 2014, Sophian et al. 2017, AbdAlla et al. 2019).

Detailed comparisons of the commonly used SHM methods are provided in Table 2.1; a surface strain-based technique is being experimentally evaluated in this thesis.

2.2.5 Future of SHM

As shown in Table 2.1., there has not been an easy-to-use SHM method that can provide Level 4 monitoring of reinforced concrete structures. The surface strain-based SHM technique, if proven to be effective, would fill this gap. It also can be noted from the table that each SHM method currently has its own advantages and limitations and thus no SHM method is sufficient to monitor an entire full-scale structure on its own. Although breakthroughs can occur at any time, a more practical approach at the moment is through the combination of different techniques (Li et al. 2014, Xiang et al. 2018, Kralovec and Schagerl 2020). This approach is commonly referred to as data fusion or multiple-sensor approach. Kralovec (2020) reviewed this topic and concluded that a reliable multi-sensor SHM system can be created by combining static (i.e. strain-based or

electrical impedance tomography) and dynamic (i.e. vibration-based, EMI, guided waves, and acoustic emission) damage assessment methods. Khodaei and Aliabadi (2016) hold similar opinions and experimentally validated a multi-sensor system using guided waves, EMI and weighted energy arrival method as a Level 3 SHM system. Combined with structural analysis data, future multi-sensor approaches have the potential to form a robust system that can reach the highest level of monitoring (i.e., be able to estimate current capacity and remaining service life). However, further research is still required to identify the optimal combinations and analysis algorithms (Kralovec and Schagerl 2020).

A challenge for the development of a multi-sensor approach or SHM in general is that various techniques have been tested on very different structures, which makes it difficult to compare these methods side by side (Das and Saha 2018). To address this issue, the North American task group was formed in 1999 by the International Association for Structural Control (IASC) and American Society of Civil Engineers (ASCE). The task group designed a benchmark structure, which was a 2-bay by 2-bay steel-frame structure, and tested various existing SHM methods on this structure (Dyke et al. 2002, Johnson et al. 2002). Over the years, more researchers have participated in the benchmark study. A review of the SHM techniques implemented on the benchmark structure was provided by Das (2018). However, it is unclear why the task group has disappeared and has not developed any other benchmark structures. Future benchmark structures should be more complex and comparable to real-life structures, and benchmark studies would require worldwide collaborations from the researchers. Such benchmark studies would make objective comparisons of different SHM techniques possible and thus promote the development of SHM guidelines and standards (Zhou et al. 2013).

Table 2.1. Comparisons of main SHM techniques and the surface-strain based SHM technique.

SHM Technique	Suitable Usage	Rytter Level*	Main Sensor Type	Strengths	Drawbacks	Application	Reference
Surface Strain-based	Corroded Reinforced concrete beams	4	Any type of strain gauges	Easy principles; High sophistication;	Only suitable for local damage detection	Laboratory experiments on corroded RC beams	
Strain-based	Global monitoring	2, 3	Various kinds of strain gauges	Simple and robust	Large number of sensors required; Difficult procedures for installation	Real-life applications on buildings, bridges, tunnels, pipes, and wind turbines	(Güemes et al. 2018, 2020, Bado and Casas 2021)
Vibration-based damage detection	Global monitoring for large damage on various types of structures	2	Accelerometers	Full structural coverage with a small number of sensors	Sensitive to environmental noise; Only severe damage detectable	Many real-life applications on various bridges, concrete, steel frame, masonry, and composite buildings	(Peeters and De Roeck 2001, Brownjohn et al. 2011, Avci et al. 2021)
Guided Waves	One dimensional structure such as pipes, rail, cables, truss structures, and concrete rebar	2	Various actuation and sensing transducers: PZT wafer, FO sensors, and non-contact laser Doppler vibrometers	Cheap; Large coverage with less transducers; Non-sensitive to low Frequency noise; capable of detecting small defects	Dispersive in nature; Complicated analysis for 2D or 3D structures	Commercialized on one-dimensional structures	(Mitra and Gopalakrishnan 2016, Cawley 2018, Güemes et al. 2020)
Acoustic Emission	Propagation of cracks in all sorts of structures: metallic, RC, and composite	2	AE sensors (FBG or PZT based)	High sensitivity; Capable of remotely detecting damage; Not sensitive to environmental vibration noise	Can only be applied if structural components are adequately stressed; Difficult to detect existing non propagating defects; Sensitive to friction noise	Many industrial applications including bridges, pressure vessels, storage tanks, aircraft, concrete, steel and composite structures	(Wevers and Lambrighs 2009, Khan 2018, Cawley 2018, Tonelli et al. 2020)
Electro-Mechanical Impedance	Any type of damage in mechanical, civil or even biological fields	2	PZT transducer	Sensitive to small defects; Simple data acquisition; Immune to mechanical, electrical and electro-magnetic noise	Limited sensing range; Not capable of evaluating whole structural integrity; Need to choose appropriate frequency range; Need to compensate for temperature change	Steel beam, concrete structures, composite reinforced masonry walls, steel bridge joints and pipe joints	(Bhalla and Soh 2012, Li et al. 2014, Na and Baek 2018, Junior et al. 2020)
Eddy Currents	Cracks on electro-conductive structures	4	Eddy current sensor	No contact needed; no need of special specimen preparation	Limited to electro-conductive materials; small coverage area	Metal structures, aircraft	(Strantza et al. 2015, Jiao et al. 2016, AbdAlla et al. 2019)

* Rytter levels 1 to 4 correspond to increasing levels of sophistication in SHM diagnostics. Levels 1 to 3 indicates the SHM system has the ability to identify, locate, and quantify the damage respectively, while a level 4 SHM system can perform prognostics in addition to the information provided by levels 1 through 3 (Rytter 1993).

Lack of comprehensive SHM guidelines and standards has been widely acknowledged as one of the main reasons for the slow transition from research to real-life applications of SHM (Del Grosso 2014, Li et al. 2014, Yang et al. 2017). The first guideline for this subject was published by Intelligent Sensing for Innovative Structures (ISIS) of Canada in 2001 (Mufti). This guideline provides a comprehensive state-of-the-art review of the SHM technologies at that moment. However, this guideline has never been updated and no new standard has been published in Canada. Several other guidelines or standards for SHM have been published around the world. Moreu et al. (2018) has tabulated and compared the codes, standards and guidelines published in Australia, China, Canada, European Union, UK, Switzerland, and the United States. Although most of the standards are not compulsory, they can promote the implementation and code development for SHM (Moreu et al. 2018). It is worth mentioning that China has published a series of codes and standards for SHM including DB/T29-208-2011, CECE 333:2012, JGJ/T 302-2013, JT/T 1037-2016, and GB 50982-2014. Yang et al. (2017) have reviewed and discussed the main features of these five standards. Among these, GB 50982-2014 is the first and exclusive national code that enforces the implementation of SHM on high-rise (>250 m) and long-span (single span >100 m) structures (GB 50982 2014). Many representative applications of SHM on large-scale structures are available now in China, which demonstrates that a national code is a milestone for closing the gap between research and practical applications of SHM (Yang et al. 2017, Cawley 2018). Del Grosso (2014) proposed that a top-down approach could be used to develop a new generation of standards for SHM. Moreu et al. (2018) suggested that when the United States and other countries are developing their SHM codes in the future, they could borrow elements and lessons learned from the Chinese SHM code.

2.3. Economic Studies about SHM

It has long been recognized that wide industrial adoption of SHM systems is largely driven by its economic benefits (Farrar and Worden 2007, Cawley 2018, Sousa et al. 2019). Many research studies claim that, besides life-safety benefits, the implementation of SHM can also provide economic benefits (Farrar and Worden 2007, Harms et al. 2010, Yan et al. 2017a, Manco et al. 2021). However, how to quantify the economic benefits remains an open research problem (Zhang et al. 2021), and this problem became a focus of study only after 2010 (Qin et al. 2015, Long et al. 2020). The implementation and continuous operation of SHM systems would

certainly cause additional costs to the structural owners. Meanwhile, savings can usually be generated in the total life-cycle costs (LCC) of the structures. This is because the additional information provided by the SHM systems can assist the operators and engineers to optimize the inspection and maintenance strategies, and thus structures may have fewer scheduled inspections, timely maintenance, shortened down time, and eventually prolonged lifespan (Agusta et al. 2019, Larsson Ivanov et al. 2021). To evaluate the value of an SHM system is to evaluate the value of information (VOI) brought by the system (Klerk et al. 2019). As early as 2011, Christensen et al. proposed a VOI framework to quantify the value of SHM systems. The framework considered the different uncertainties associated with different SHM systems and adopted a combination of reliability analysis, decision theory and Bayesian analysis (Christensen et al. 2011). The method used is comparable to the state-of-the-art guidelines (Diamantidis et al. 2019) and research (Klerk et al. 2019, Zambon et al. 2020, Larsson Ivanov et al. 2021). A hypothetical reinforced concrete beam was used to demonstrate that the implementation of a standard SHM system could result in 6.61% reduction in the annualized LCC, while an enhanced SHM system could result in savings of 18.7%. However, this framework has never been validated experimentally.

Sebastian Thöns started to apply LCC and VOI analysis to SHM in 2013 (Thöns 2013, Thöns and Faber 2013, Thöns et al. 2013). He then became the chair of the scientific networking project, COST Action TU1402, in 2014. COST Action TU1402 was formed by a joint group of researchers and practitioners from 29 European countries, as well as China, USA and Australia and aimed to quantify the value of SHM. Although the economic studies started much later than the technical developments, the formation of TU1402 has significantly promoted the development process in this field. Within the active period of the project, from March 2014 to March 2019, the members of TU 1402 published 80 peer reviewed papers in total, held many workshops and developed three guidelines for operators, practicing engineers and scientists (Diamantidis et al. 2019, Sousa et al. 2019, Thöns 2019).

These guides were developed based on the results over the four-year of operation of this project and aimed to standardize the decision process of whether to pursue more Structural Health Information (SHI). In this context, SHI can refer to any additional information related to the health of a structure. It is not limited to the data gathered from SHM systems, but also from NDT, load testing, or other forms of inspections. But the value of SHM can certainly be quantified

based on the framework proposed in these guidelines. The guideline for operators recommends the use of SHI value analyses to structure owners due to its benefits in cost savings, life-safety, and sustainability. This guide contains a tabulated summary of the case studies performed on types of structures including buildings, dikes, bridges, offshore wind-parks, and roofs. For these various structural types, the value of SHI was estimated to be 10 to 90% of the expected total cost of the structure (Sousa et al. 2019). The guideline for practicing engineers recommends using the value of information (VOI) approach to quantify the value of SHI and discusses how to use the results for decision making (Diamantidis et al. 2019). The last guideline targets scientists and contains the most mathematical details about the standardized framework for quantifying the value of SHI (Thöns 2019).

After the end of the TU1402 project, the VOI approach has been continuously used and improved by many researchers (Zambon et al. 2020, Skokandić and Mandić Ivanković 2020, Sykora et al. 2020, Larsson Ivanov et al. 2021, Khan et al. 2021). For instance, Sykora et al. (2020) and Khan et al. (2021) performed VOI analysis for monitoring historic masonry structures and testing chloride content in reinforced concrete bridges, based on the framework developed by TU1402. Zambon et al. (2020) conducted a case study on a concrete bridge pier crosshead using a novel VOI framework that considered tiered assessments. A common conclusion from the recent research is that the value of SHM deployment is mostly affected by the uncertainties associated with the monitored infrastructure. Even an SHM system with lower accuracy can offer a high return rate when the structure is associated with high risks, but its value can be low or even negative for a very stable structure (Sousa et al. 2019, Bolognani et al. 2019, Klerk et al. 2019, Larsson Ivanov et al. 2021, Khan et al. 2021).

2.4. Strain Measuring Equipment

2.4.1. Introduction

Strain is a critical factor for the SHM technique being evaluated in this research study. Thus, four of the most prevalent strain measurement techniques are reviewed here, including mechanical strain gauges, electrical strain gauges, fiber optic sensors (FOS), and digital image correlation (DIC). The developmental history, working principles, state-of-the-art capability, advantages, and disadvantages of these strain measuring methods are discussed in this section.

2.4.2. Mechanical Strain Gauges

The first mechanical strain gauge was invented by Charles Huston in 1879 (Isah et al. 2020). It was designed to measure the elongation or contraction of a length on the surface of a specimen. This type of gauge usually consists of an invar main beam with two locating points. The movements of the locating points are measured by a dial or digital gauge (Brooks 2015). Then, the average strain can be calculated using the measured length change divided by the total gauge length. Generally, longer gauge lengths provide higher sensitivities in strain measurements. Figure 2.2 shows several dial-version gauges with different gauge lengths and their corresponding sensitivities (Brooks 2015). Also, digital gauges can provide higher sensitivity than dial gauges. Table 2.2 compares the sensitivity of dial and digital gauges with various gauge lengths (MeasureX 2015). The typical gauge length used for concrete laboratory testing is 200 mm (Brooks 2015).

Mechanical strain gauges can work in extremely hazardous environments including high temperature and high humidity. It is cost-effective considering it is reusable. Also, they are easy to use since they do not require any surface preparation (Brooks 2015, Jia et al. 2015). However, the attachment of mechanical strain gauges can produce undesired stress concentrations at the contact points (Khoo et al. 2016). They are also subject to the shortcoming of not being as accurate and easily damaged when a specimen breaks (Huang et al. 2010, Motra et al. 2014). Additionally, it is difficult to track strain changes at different locations simultaneously using mechanical strain gauges.

Table 2.2. Comparison of the sensitivities of mechanical strain gauges with dial and digital readings (MeasureX 2015).

Gauge Length (mm)	Sensitivity for Dial Gauges (με)	Sensitivity for Digital Gauges (με)
100	16	8
150	10.7	5.3
200	8	4
250	6.4	3.2
300	5.3	2.7
400	4	2
500	3.2	1.6

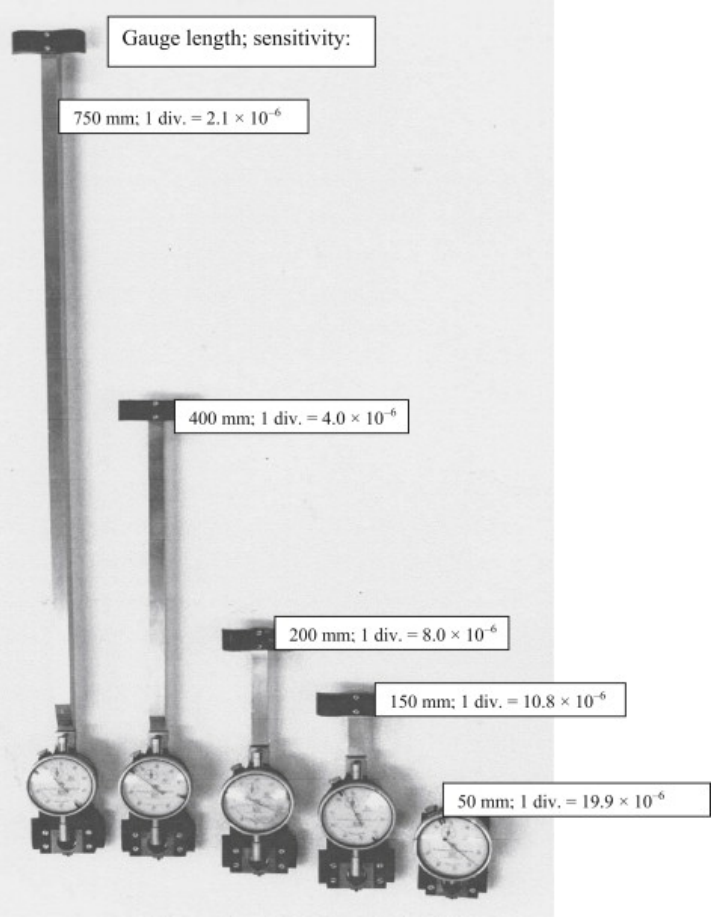

Figure 2.2. Mechanical strain gauges with various gauge lengths and their corresponding sensitivities (Brooks 2015). Copyright © Elsevier. Used with permission.

2.4.3. Electrical Strain Gauges

Electrical strain gauges were invented by Edward E. Simmons and Arthur C. Ruge in 1938 and they have been the most widely used strain determination method since then, due to the advantages of being cost-effective, robust and accurate (Huang et al. 2010, Jia et al. 2015, Isah et al. 2020). This type of gauge usually consists of a metallic foil pattern supported by an insulating backing. The backing is attached to the test specimen using a suitable adhesive, so the electrical strain gauge will deform along with the test specimen. The deformations will lead to linear changes in the foil's electrical resistance, which are continuously being measured by a reading unit (Omega 2016). Thus, the resolution of electrical strain gauges depends on the sensitivity of the reader unit to the small changes in the electrical resistance of the foil grid. A typical electrical

strain gauge can typically measure strain in micro-strain (με), which is $\varepsilon \times 10^{-6}$ (Isah et al. 2020). Although this type of gauge is generally considered more reliable than the other strain measurement methods, the existence of an electromagnetic field or change in temperature can affect its strain measurement (Yin et al. 2007, Guan et al. 2011, Isah et al. 2020). Moreover, when it is applied to the surface of concrete, its accuracy is affected by the non-homogeneity of concrete and the roughness of the concrete surface; thus, factors including the gauge length, change of temperature and aging of the gauges must be considered (Guan et al. 2011, Isah et al. 2020).

Guan et al. (2011) performed a laboratory experiment to test the accuracy of using electrical strain gauges to measure concrete surface strains. It was found that, unlike for a homogeneous material, the length of the electrical strain gauges had a major impact on the accuracy of the measurements: the longer the gauge, the higher the accuracy. More specifically, 100 mm, 200 mm, and 300 mm gauges had errors of 9%, 7%, and 5%, respectively (Guan et al. 2011). The errors increased to 22% and 16% for the 100- and 200-mm long gauges, respectively, 90 days after they were adhered, which suggests that aging caused a significant decrease in the accuracy of the electrical strain gauges (300 mm gauges were not included in the aging test).

2.4.4. Fibre Optic Sensors

Fiber optic technology was originally developed for long distance telecommunication in the 1970's (Güemes and Sierra-Pérez 2013). Optical fibres, usually made from silica, have the ability to transmit light with very little energy loss. Further developments in the field of optoelectronics allowed optical fibres to be used to make sensors for measuring physical, chemical, electrical and biological parameters (Michie 2000, Güemes and Sierra-Pérez 2013). In the field of SHM, fibre optic strain sensors are of particular interest to researchers. Fibre optic strain sensors can be divided into three categories based on their operating principle: interferometric, grating-based, and distributed (Di Sante 2015). An overview of the major sensor types is provided in Figure 2.3.

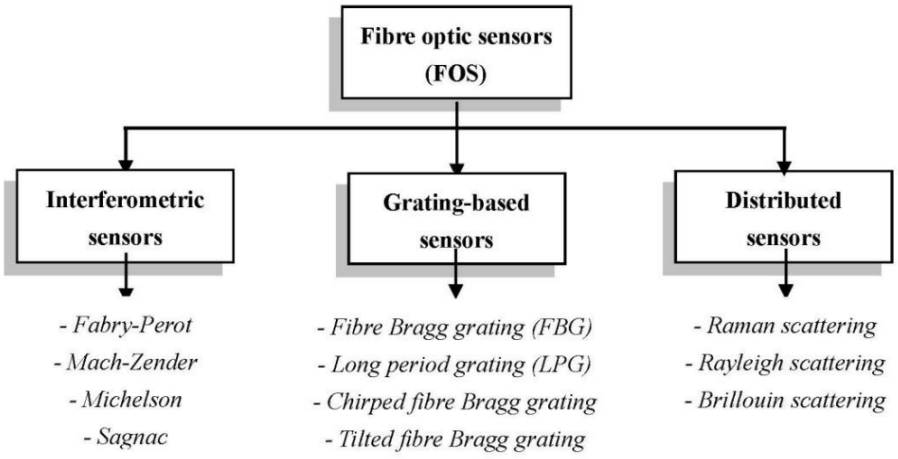

Figure 2.3. Overview of the categorization of major fibre optic strain sensor types (Di Sante 2015). Copyright © Multidisciplinary Digital Publishing Institute (MDPI) under Creative Commons Attribution (CC BY) License.

Sensors using different operating principles also have different measuring capabilities, as demonstrated in Figure 2.4. Interferometric sensors are also called single point sensors, as they can only pick up strain changes at a single location, similar to electrical strain gauges. However, these sensors can offer extremely high resolution in strain measurement (can exceed 1 με) (Di Sante 2015). The FOSs are generally known for having the multiplexing capability (Yin et al. 2007, López-Higuera et al. 2010, Abdo 2014, Paliwal and John 2017, Isah et al. 2020). This is actually referring to the grating based or distributed sensors, not the interferometric sensors. The grating-based sensors are quasi distributed. The most extensively researched type of quasi distributed sensor, the Fiber Bragg Grating (FBG) sensor, can have up to 1000 localized sensors placed at intervals along the fiber length (Güemes et al. 2018). Typically, FBG sensors can measure strains up to ±15000 με with an approximate resolution of 1 με (Loupos and Amditis 2017). Over the last two decades, the distributed sensors have gained more and more interest from researchers. In the distributed FOS systems, the fiber itself works simultaneously as sensors to detect change of temperature or strain and as transmitter of the information (Di Sante 2015, Güemes et al. 2018). This type of sensor can have a sensing length up to 150 km, which means they have great potential in monitoring large scale structures (Di Sante 2015). The resolution, however, varies with the sensing length and the acquisition rate. One of the cutting edge distributed sensors that is available commercially, NEUBRESCOPE NBX-8200 (Neubrex,

Japan), offers a spatial resolution of 20 cm with accuracy of 10 με, over a sensing length range of 50 m to 3 km (Neubrex 2020).

In addition to the multiplexing capability offered by the grating based and the distributed sensors, FOSs in general offer several other advantages. First, FOSs are extremely small and light. The optical fibres have a diameter of 125 μm, which is about the same thickness as a human hair. (Güemes and Sierra-Pérez 2013). Also, they are unaffected by electrical and magnetic noise, and they are safe for operation in explosive and hazardous environments. The disadvantages include sensitivity to ambient conditions that affect light intensity such as light source, dust, moisture, smoke (Abdo 2014).

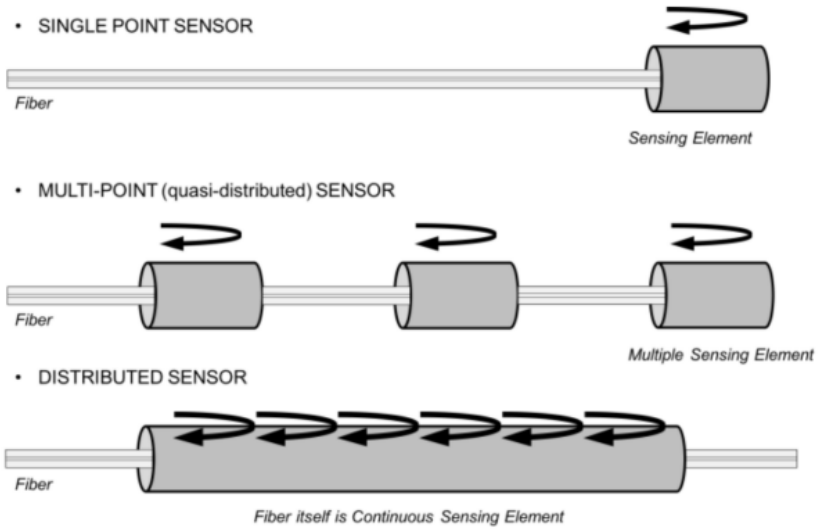

Figure 2.4. Demonstration of measuring capabilities of single point (interferometric sensors), quasi-distributed (grading-based sensors) and distributed sensors (Güemes et al. 2018). Copyright © MDPI under Creative Commons Attribution (CC BY) License.

2.4.5. Digital Image Correlation (DIC)

The Digital Image Correlation technique was first proposed in the 1980s (Yamaguchi 1981, Peters and Ranson 1982, Sutton et al. 1983). It is a non-contact optical method for full-field displacement and strain measurements. Due to the need for the full-field measurements, the DIC technique has been developed quickly and applied widely over the last a couple of decades (Hild and Roux 2006, Pan 2018, Pereira and D'Almeida 2019).

A DIC system is generally composed of digital cameras, lenses with different focal lengths, and a personal computer with analysis software installed (Pereira and D'Almeida 2019). In preparation for the DIC technique, a high contrast speckle pattern needs to be deposited on the surface of the object. Then, a series of digital, high resolution images are taken by one or more cameras to capture the changes of the speckle pattern before and after deformation (Hensley et al. 2017). These images are analyzed with correlation-based matching algorithms to calculate full-field displacement in pixels, which later is converted to standard units like micrometres (Pan 2018). Even though the principle of the DIC technique is relatively simple compared to other optical interferometry methods, it still requires a substantial amount of computation. Thus, the DIC algorithms have gradually evolved and have become less complex and more accurate (Chen et al. 2013, Khoo et al. 2016, Pereira and D'Almeida 2019). Besides the analyzing algorithms, the accuracy of the DIC systems also depends on the following factors: the digital image resolution, the size of the specimen, the distance between camera and specimen, the focal length of the lens, and the application of the speckle pattern (Cintrón and Saouma 2008, Khoo et al. 2016). The accuracy for the most advanced DIC systems is considered to be a few micrometers (Li et al. 2017).

While other techniques like mechanical and electrical strain gauges can only provide measurements in one dimension within a fixed gauge length, the DIC technique can measure displacements and strains in two dimensions if one camera is used and in three dimensions if two or more cameras are used. Although the DIC system has a higher up-front cost, its operational cost is near zero. Other advantages of the DIC technique include high strain limits, flexible and easy implementation, and insensitivity to environmental noise (Huang et al. 2010, Khoo et al. 2016, Pan 2018). However, the results obtained by the DIC system can be considered acceptable for many applications, but not accurate (Cintrón and Saouma 2008). Therefore, the DIC system is more commonly used in situations where the object's deformation is large (Hensley et al. 2017, Pereira and D'Almeida 2019).

2.4.6. Summary

Mechanical and electrical strain gauges are classic strain measuring tools with affordable price and high reliability. However, a mechanical strain gauge is unable to monitor strain changes at

multiple locations simultaneously; thus, it is deemed unsuitable for the SHM technique being tested in this research study. FOSs and the DIC system are relatively new technologies, but both are extensively researched and can measure in micro strains at their optimum conditions. The FOS has a unique advantage in measuring large-scale structures due to its multiplexing capabilities (Di Sante 2015, Isah et al. 2020). However, the lab experiment conducted in the current study was designed using small-sized beams. Also, the FOSs have not been fully commercialized yet; thus, there is a limited number of suppliers on the market. Although the optical fibres are supposed to be extremely cheap, the unit price of a semi-distributed sensor with 1 m sensing length was quoted as $145 by Yieldpoint Inc. and $273 by Hoskin Ltd., which is very high-priced for one-time use. Thus, the FOS was ruled out for this experiment as well. Finally, this lab experiment proceeded with two strain measuring techniques: electrical strain gauges and the DIC system. The purpose of testing with two different methods was to demonstrate how the different levels of accuracy of the obtained SHM data can affect the evaluated reliability index of the monitored structure.

2.5. Accelerated Corrosion Using the Impressed Current Method

2.5.1. Introduction

The corrosion of reinforcing bars is the biggest threat to the integrity of reinforced concrete structures, as it can cause cracking in concrete, decrease in structural capacity due to loss of bond and loss of effective area of the reinforcing bars, and in extreme cases, it can even lead to the failure of the structure (Palumbo 1991, Malumbela et al. 2010, Zhang et al. 2012, Hong et al. 2020). Compounding general corrosion issues, in cold regions like Canada, the increased use of de-icing salts containing chloride ions accelerates the corrosion of reinforcing bars and the deterioration of bridges, roadways, and other structures (Palumbo 1991, Fu et al. 2018). It has been estimated that the annual direct cost of corrosion, which is defined as the cost to the owner, is about $41 billion in Canada (Shipilov 2016), and $2.5 trillion globally (Koch et al. 2016). The indirect cost, which considers the cost to the user and the environment, is much more complex and difficult to quantify. A systematic study conducted through the collaboration of the U.S. Federal Highway Administration (FHWA), National Association of Corrosion Engineers (NACE)

International, and CC Technologies conservatively estimated the indirect cost of corrosion to be approximately equal to the direct cost of corrosion (Koch et al. 2016).

Studying corrosion mechanisms, their development, and their consequences through laboratory-conducted experiments is critical in generating information to increase structural safety and decrease the economic loss associated with corrosion (Stansbury and Buchanan 2000). However, corrosion can take years to develop in natural environments (Malumbela et al. 2012) and, thus, the corrosion of reinforcement in beams in laboratory experiments is generally accelerated by means of an impressed current. This method is time efficient, cost effective and easy to control (Ahmad 2009), but it has been criticized by several researchers for resulting in different surface characteristics than those obtained under natural circumstances, meaning that specimens corroded through the impressed current method might not represent the behaviour of in-service structural members accurately (Yuan et al. 2007, Ahmad 2009, Fu et al. 2018).

An alternative way to accelerate the corrosion of reinforced concrete is called the artificial environment method and was developed by Yuan et al. (2007). This method accelerates the corrosion process by placing the specimen in a chamber where environmental factors including high and low temperatures, dry and wet conditions, rainfall, salt spray, and ultraviolet light can be simulated and repeated in accelerated cycles (Yuan et al. 2007). The characteristics of corrosion occurring under an artificial climate environment are very similar to those occurring under a natural environment (Yuan et al. 2007, Dai et al. 2020); however, the time required to generate corrosion can only be reduced by a certain extent. For example, according to Dai et al. (2020), 167 days were spent to achieve a 2% mass loss of the reinforcing bars using the artificial environment method. Thus, this method was considered to be unrealistic for achieving a high degree of corrosion in limited timeframe (Dai et al. 2020). Therefore, the impressed current method remains to be the most practical method for accelerating the corrosion process. This section discusses its principle, setup, methods of estimation, advantages, and disadvantages.

2.5.2. Principles of Corrosion and the Impressed Current Method

Corrosion of metals in nature is the chemical or electrochemical reaction between a metal and its environment, which causes the degradation of the metals (Cicek and Al-Numan 2011). Although

concrete has a high pH, which naturally prevents the reinforcing bars from corrosion when it is intact (Palumbo 1991), the use of de-icing salt can serve as an electrolyte and accelerate the electrochemical corrosion of the steel bars. Electrochemical corrosion of metals under aqueous electrolytes can occur in both acidic and alkaline environment.

The oxidization of iron may be written as follow:

$$Fe \rightarrow Fe^{2+} + 2e^{-} \tag{2.1}$$

Then, under acidic environment, the freed electrons are consumed by the surrounding hydrogen ions forming hydrogen (Jones 1996):

$$2\,H^{+} + 2e^{-} \rightarrow H_2 \tag{2.2}$$

Under aqueous alkaline environment, the reaction and the products of the redox reaction are a bit different (Jones 1996):

$$2\,H_2O + 2e^{-} \rightarrow H_2 + 2OH^{-} \tag{2.3}$$

Since iron can exist in two oxidation states (+2 or +3), Fe^{2+} can be further oxidized to Fe^{3+}(Jones 1996):

$$Fe^{2+} + 3H_2O \rightarrow Fe(OH)_3 + 3H^{+} + e^{-} \tag{2.3}$$

Since the electrons have a negative charge, the liberated electrons can change the potential at the surface of the metal. A negative potential means the electrochemical reaction in Equation 2.2 does not happen fast enough and there are excess electrons accumulated at the surface. The accumulated electrons will slow down the degradation rate of the metal (Jones 1996). A positive potential, on the other hand, means there is a deficiency of electrons generated by Equation 2.1. The higher the potential, the greater the deficiency, and the faster the degradation of the metal will happen (Jones 1996). Therefore, the surface potential can be measured and used as an indicator of the corrosion rate (Jones 1996). Based on these principles, an external power supply can be connected to the reinforcing bar to either protect the metal from corrosion or to accelerate

the corrosion through altering the surface potentials. This method is called the impressed current method.

For corrosion of metals in aqueous electrolytes, the final reaction products can be described as a function of potential and the pH of the environment in a Pourbaix diagram as shown in Figure 2.5 (Barthel and Deiss 2021).

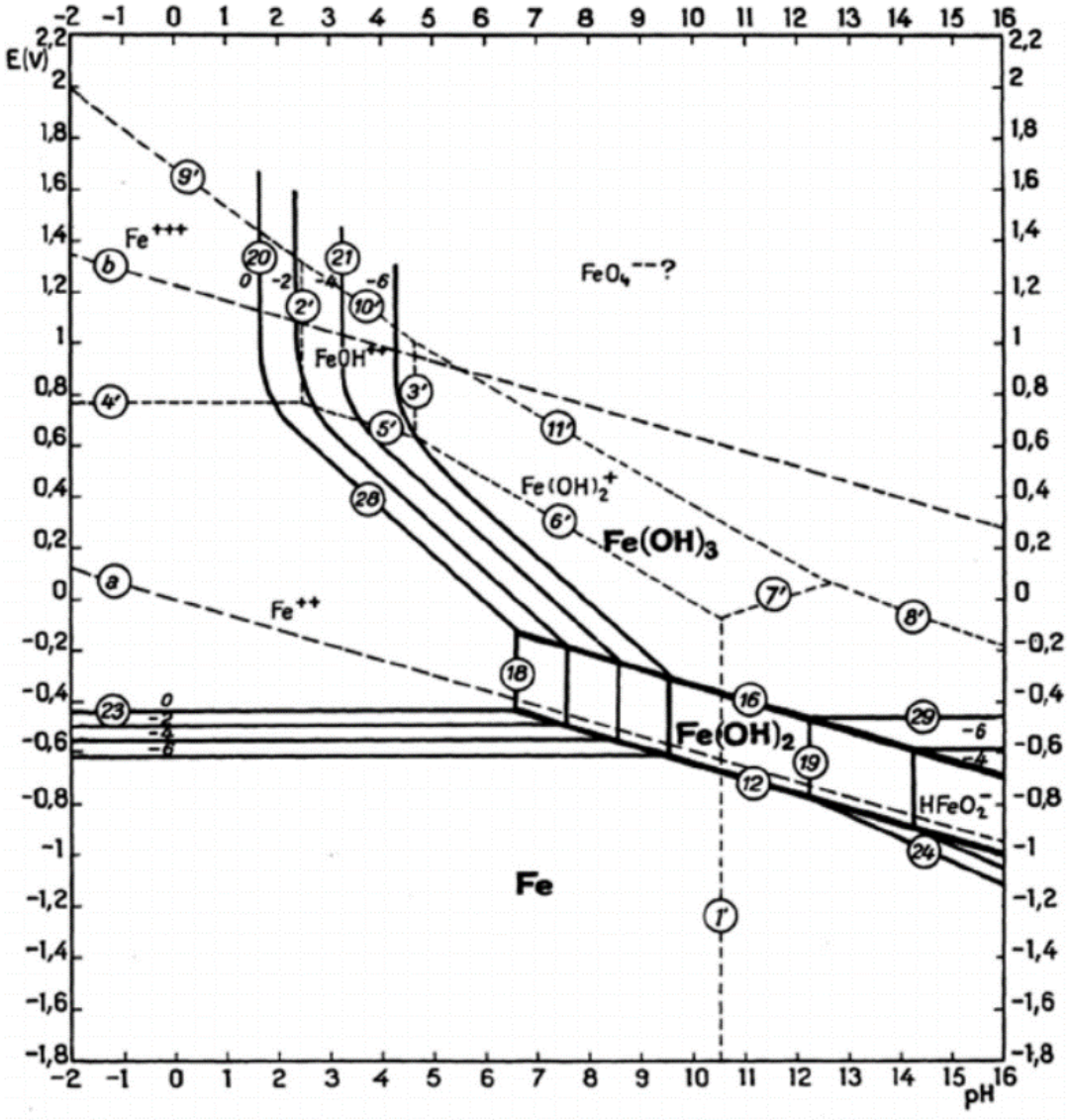

Figure 2.5. A Pourbaix diagram for Fe under aqueous alkaline environment (Barthel and Deiss 2021). Copyright © Wiley Online Library under Creative Commons Attribution (CC BY) License.

2.5.3. Setup of the Impressed Current Method

The setup of the impressed current method simulates an electrolyte cell, which includes a DC power supply, a cathode, an anode and an electrolyte (Palumbo 1991, Ahmad 2009). The anode is simply the steel bar that needs to be corroded (Malumbela et al. 2012). During the corrosion process, the steel bar is being forced to lose electrons, thus it is connected to the cathode of the DC power supply. The counter electrode, which is connected to the anodes of the DC power supply, has a wide range of options to choose from. In terms of material, it can be made of stainless steel, copper and titanium, for their excellent electrical conductivity. As for the shape of the counter electrodes, bars, plates or meshes of the previously mentioned metals have been reported in literature without posing any differences in the corrosion results (Malumbela et al. 2012). Lastly, the electrolyte is used to enable the current flow between the specimen and the counter electrode (Ahmad 2009). A common practice is to submerge the specimen in a NaCl solution with concentration ranges from 3% to 5%. The chloride solution not only provides electrical contact, but also breaks the thin protective film on the surface of the specimen once they penetrate the concrete cover (Palumbo 1991). Some researchers have also tried adding 2% to 5% NaCl by weight of cement into the concrete mixture during the casting of the specimens, which will save the time for the diffusion of the chloride irons (El Maaddawy and Soudki 2003, Imam et al. 2015). However, the specimens still need to be submerged in an electrolyte or be placed in a 100% humidity chamber to ensure the flow of current.

An illustration of a typical set up for using the impressed current method to corrode an RC beam is shown in Figure 2.6.

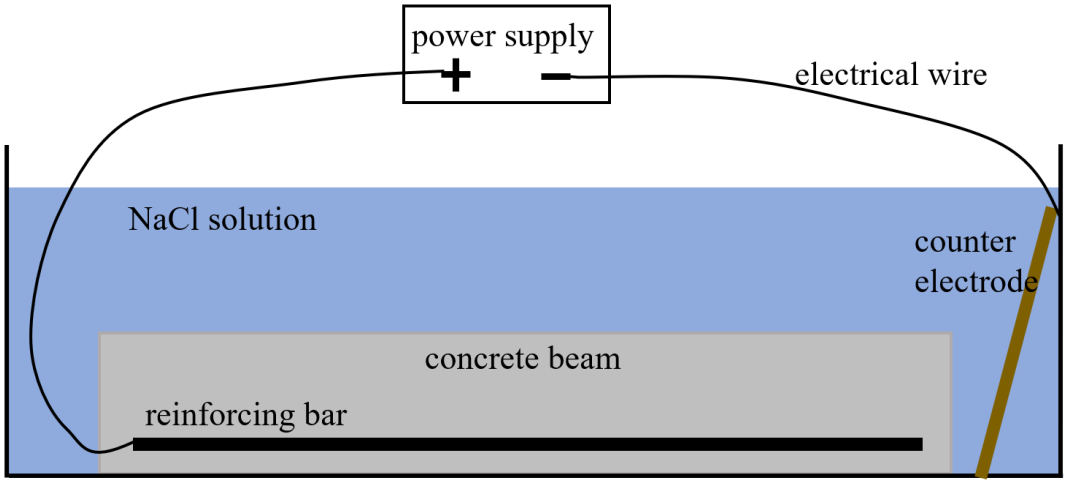

Figure 2.6. An illustration of a typical setup for the impressed current method.

2.5.4. Estimation of the Degree of Corrosion

Faradays' law can provide a theoretical estimation of the mass loss of steel due to corrosion, assuming all the applied current is engaged in the corrosion reaction (Ahmad 2009, Hong et al. 2020):

$$M = \frac{WI_{app}T}{nF} \tag{2.3}$$

where M is the mass loss of steel per unit surface area (g/cm^2), W is the atomic weight of steel (56 g/mol), I_{app} is the applied current density (A/ cm^2), T is the total time that the current has been applied (s), n is the number of equivalents exchanged, and F is Faraday's constant, which equals 96487 A·s/mol.

Malumbela et al. (2012) compared the data from 11 research studies in the literature. They concluded that the accuracies of using Faraday's law to predict mass loss due to corrosion varied between underestimating -6.7% and overestimating 23.9%. The average difference between predicted and actual mass loss was 1.3% with a standard deviation of 3.6%. It was also discovered that the actual corrosion tends to be consistently less than predicted at higher levels of corrosion. This might be related to the massive accumulation of corrosion products on the surface of the steel bar, thus inhibiting further corrosion (Malumbela et al. 2012).

The impressed current method works regardless of the level of the current densities being used. While 100 to 2000 $\mu A/cm^2$ are commonly used by researchers (Malumbela et al. 2012), Almusallam & Al-gahtani (1996) used a current density as high as 10400 $\mu A/cm^2$ in order to achieve the target amount of corrosion in time. In a natural environment, the current density is typically between 0.1 and 10 $\mu A/cm^2$ (Malumbela et al. 2012). Assuming an average current density of 3 $\mu A/cm^2$ under natural conditions, and an impressed current of 10400 $\mu A/cm^2$ in the laboratory, the corrosion in the lab is 3467 times faster than in the natural environment. In other words, ten years of corrosion can be achieved within one day using the impressed current method.

2.4.5. Advantages and Disadvantages

The prominent advantage of the impressed current method is its ability to achieve a high degree of corrosion in a very short period of time. The corrosion rate is not only high, but also can be easily adjusted through tuning the current intensity and the power-on time (Yuan et al. 2007, Ahmad 2009, Hong et al. 2020). In addition, the corrosion results are very predictable and highly repeatable, which makes this method ideal for laboratory experiments (Fu et al. 2018).

However, some researchers have pointed out that the distribution of the corrosion product on the surface of the reinforcing bar achieved by the impressed current method is different from that achieved when corroded under the natural environment (Yuan et al. 2007, Ahmad 2009, Fu et al. 2018). The corrosion grows evenly around the rebar perimeter when subjected to an impressed current, while under natural conditions, the corrosion tends to be greater on the side closest to the surface of the concrete (Yuan et al. 2007, Fu et al. 2018). Due to this difference in surface characteristics, the specimen corroded using the impressed current method may not be fully representative of the naturally corroded structural members in-service (Fu et al. 2018).

Moreover, there have been some controversies regarding the effects of using different levels of current density (Malumbela et al. 2012). Although it has been proven that target corrosion degree can be achieved regardless of the level of the current density being used, the same degree of corrosion caused by a different level of current density may result in different degrees of cracking of the beams, and therefore leads to different ductility and load bearing capacities. A couple of studies have shown that higher current densities are more detrimental to the corroded

beams (Mangat and Elgarf 1999, El Maaddawy and Soudki 2003), while other studies suggested the opposite (Alonso et al. 1998, Malumbela et al. 2010). It was suggested that this topic should be investigated further (Malumbela et al. 2012).

2.6. Summary

From a technical perspective, various SHM technologies have been developed and improved rapidly over the last few decades; however, the transition from research to field deployment is difficult. A major reason for this issue is that, currently speaking, no technology is perfect. A review of the state-of-the-art SHM technologies shows that most of the SHM methods provide Level 2 monitoring, which means they can identify the existence and location of the damage, but they can not quantify the severity of the damage, not to mention provide prognostics of the structure. Currently, there has not been an SHM method that can perform Level 4 monitoring of reinforced concrete structures. The surface strain-based method, if proven to be effective, would fill this gap. This method is suitable for local damage detection, and thus, it has the potential to be paired with other Level 2 global damage detection methods to form a robust and sophisticated SHM system. Such a combined SHM system would have an advantage compared to each individual SHM method and is likely to promote real-life applications of SHM.

The economic study related to SHM has drawn significant attention over the last ten years, because it has been commonly acknowledged that, for the wide adoption of SHM, it is critical to demonstrate the quantified SHM value to the structural owners. The economic value of SHM comes from the provided additional information which can be used to optimize the maintenance strategy and cause savings in the structure's life-cycle cost. The VOI is a commonly used concept in quantifying the economic value of SHM. It is defined as the difference between the expected life-cycle costs of the structure without and with the SHM information (Zonta et al. 2014). VOI is easy to define, but difficult to demonstrate, as each structure is in a different condition. A simple SHM system applied on a high-risk structure may result in high returns, but a sophisticated SHM system applied on a stable structure may even yield a negative VOI. More case studies applying VOI approach on various types and conditions of structures would be beneficial to provide a more comprehensive and objective description of the value of SHM systems. Christensen et al. (2011) proposed a VOI framework to compare the value of SHM

systems with different levels of sophistication, followed by a demonstration using a hypothetical reinforced concrete beam. In the latter part of this thesis, data obtained from the experimental results are used to demonstrate the framework, and the estimated savings associated with using a standard and enhanced SHM system are compared to the actual costs of the SHM instruments to see if the investment is economically justified.

The literature review also compared four types of strain measuring equipment commonly used in SHM, including the mechanical strain gauge, electrical strain gauge, FOS, and DIC. It was found that the mechanical strain gauge was unsuitable for the experiment conducted in this research study due to its lack of ability to measure strains at multiple locations simultaneously. FOS has gained a lot of popularity in research due to its multiplexing capability. However, the multiplexing capability is not critical to this experimental study, and the commercialized FOSs are more than ten times more expensive than electrical strain gauges. Therefore, this lab experiment proceeded with using electrical strain gauges and the DIC system.

Lastly, the principle of corrosion and the techniques used to accelerate the corrosion of reinforced concrete in a laboratory environment were reviewed. The impressed current method is the only feasible method that can induce a large amount of corrosion in a reasonable timeframe; however, it was found that the resulting distribution of the corrosion product might be different from that produced in the natural environment. The state-of-the-art advancements in accelerated corrosion using the impressed current method have been adopted into the experimental design, and it is important to be aware that the difference in the distribution of corrosion product might alter the mechanical properties of the specimen, such as the debonding behaviour and beam's capacity.

CHAPTER 3 METHODOLOGY

3.1. Overview

For this research project, a laboratory experiment on nine small-scale reinforced concrete beams was conducted. These beams were cast in three batches, with each batch subjected to accelerated corrosion by the impressed current method to achieve a different amount of weight loss in the reinforcing bars. Four-point loading tests were performed before and after corrosion. During these tests, the beams were monitored by electrical strain gauges and a DIC system using the surface strain-based SHM technique described by Christensen et al. (2011). As a Level 4 SHM technique, its purpose was to accurately estimate the effective reinforcing bar area and the remaining beam capacity due to corrosion. The estimates obtained from the SHM system were compared to the experimental results to evaluate the effectiveness of the proposed SHM technique. The experimental data were also used in reliability and economic analyses to demonstrate the value of SHM systems with different levels of uncertainty. In order to create an enhanced monitoring system with low levels of uncertainty, a cover meter was used to determine the location of the reinforcing bars with greater certainty. The SHM system considering strain data alone was called the standard SHM system, while the cover meter was combined with the strain measuring equipment to create an enhanced monitoring system.

This chapter describes the methodologies used for the laboratory experiment and the following technical and economic analyses in detail. Section 3.2 describes the experimental program including specimen preparation, the monitoring equipment and procedures, the accelerated corrosion process using the impressed current method, and loading test procedure. Section 3.3 explains the theoretical principles of the SHM technique, and the methodologies for the reliability and economic analyses are presented in Section 3.4 and 3.5, respectively.

3.2. Experimental Program

3.2.1. Specimen Preparation

The experimental program consisted of testing nine small-scale reinforced concrete beams, which were cast in three batches. Each batch comprised three beams and 12 companion concrete cylinders. The dimensions of the beams are shown in Figure 3.1, while the concrete mix designs are given in Table 3.1. The design for beams in batches 2 and 3 differed from that of Batch 1, as explained later in this section.

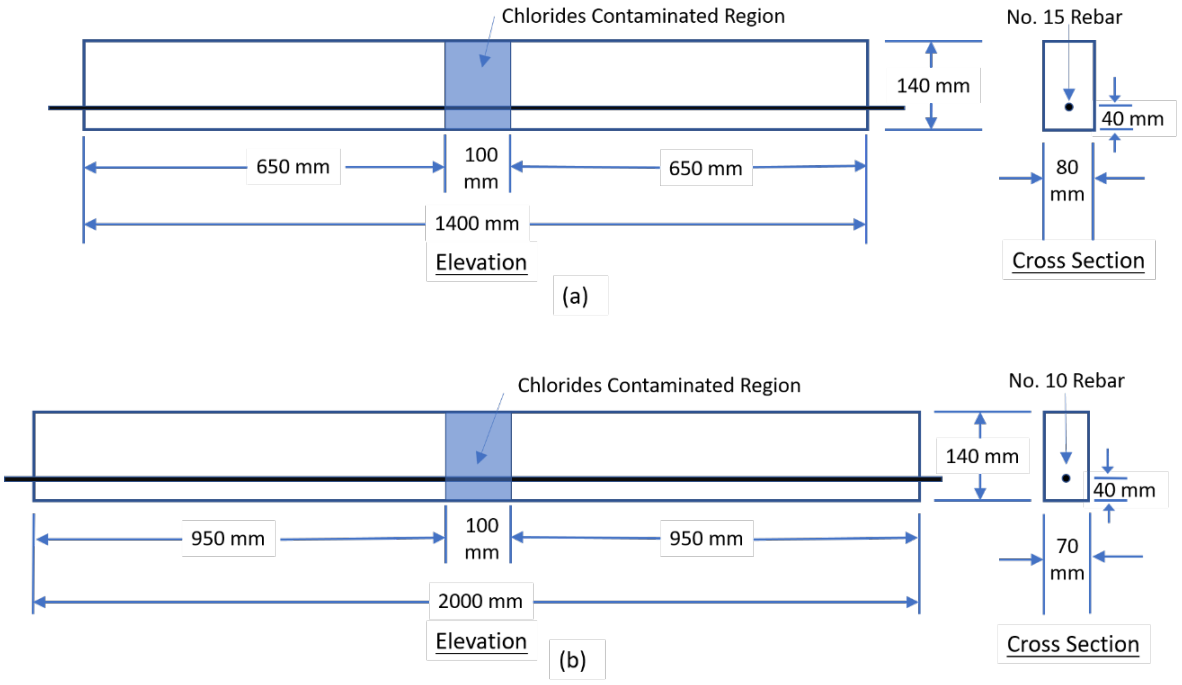

Figure 3.1. Configuration of beams used for the experimental program: (a) Batch 1; and (b) Batches 2 and 3.

Table 3.1. Concrete mix designs, specified as mass ratios.

Batch 1 Mix Design					
Water	Cement	Sand	Gravel	Superplasticizer	Sodium Chloride*
0.40	1.00	1.65	2.92	0.01	0.05
Batch 2&3 Mix Designs					
Water	Cement	Sand	Gravel	Superplasticizer	Sodium Chloride*
0.55	1.00	2.37	1.58	0.003	0.05

*Sodium chloride was only added to the middle section for controlled corrosion.

In general, beams in all three batches had small cross sections, so pea gravel with grain sizes ranging from 3.2 mm to 9.5 mm (1/8 to 3/8 inches) was used as coarse aggregate. The sand available in the structural laboratory was used as fine aggregate. Superplasticizer (Supercizer 5, Fritz-Pak Corporation, Dallas, TX) was used to increase the workability of the concrete mixture. A single No. 15 steel reinforcing bar with a nominal yield strength of 400 MPa was used as the flexural reinforcement for Batch 1 beams. The reinforcing bars protruded from both ends of the beams for the convenience of connecting to the DC power supply for the accelerated corrosion process using the impressed current method. The mechanical properties of the steel bar and concrete used for each batch of beams were determined through companion specimen tests in laboratory. The results are summarized in Appendix A.

The casting of each batch of beams was completed on two separate days, with 48 hours in between. On the first day, the ordinary concrete mix (without sodium chloride) was used to cast all but the middle sections of the beams (see Fig 3.1). The middle sections were left empty and were separated from the ends by plastic blockers while the end sections were being cast. The blocker was cut into three pieces with a hole in the middle to allow the bar to pass through it, as shown in Figure 3.2 (a). Then these blockers were screwed to the bottom and sides of the wooden forms. Some preparation work was done prior to mixing the concrete. The required mass of each ingredient was calculated based on the beam configuration, assuming 30% waste, and the wooden beam molds were covered with a thin layer of debonding oil (AR Rich-Cote, Acrow-Richmond, Toronto). Then the pre-measured ingredients were mixed using a drum mixer with 9 ft^3 capacity (Model C9-CE, Monarch Industries, Winnipeg) in the order of coarse aggregate, sand, cement. The dry materials were mixed for about 2 minutes before water was added gradually to the mixer. The superplasticizer and sodium chloride (if needed) were added last. Then, the concrete was mixed for another five minutes. This was followed by a slump test, conducted as specified in ASTM C143/C143M-15 (ASTM 2015), to ensure the mixture met the required consistency. The slump test results are presented in Appendix A. After the slump test, the concrete mixture was poured into the molds in three layers, while the molds were sitting on a concrete vibrating table. Lastly, the beams were covered with damp cloths to prevent moisture loss.

After the concrete in the ends of the beams had cured for 48 hours, the plastic blockers were removed. Bonding adhesive (Sikadur 32 Sika Inc., Canada) was applied to the concrete surfaces at the cold joints. The concrete mixing process was the same as before. The mix was poured into the middle section of the beam in three layers, and each layer was rodded 25 times. In order to measure the concrete strength and modulus, 12 companion concrete cylinders were cast from the concrete mixture containing NaCl because the middle sections were the critical regions for the loading tests. The beams and companion cylinders were covered with damp cloths and left to cure for another 48 hours before demolding. After demolding, they were transferred to a 100% humidity chamber for curing.

(a) (b)

Figure 3.2. (a) Blocker design for Batch 1; (b) The beam moulds showing the modified blocker design for Batch 2 and Batch 3.

After preparing and testing the Batch 1 beams, it was determined that several factors could be improved. Firstly, the concrete mixture had a slump of 40 mm, which was lower than desired and made proper consolidation difficult. This resulted in honeycombing in the concrete, as shown in Figure 3.3. These beams also failed in shear instead of flexure at the end of the post-corrosion loading tests due to the relatively high reinforcement ratio. The reinforcement ratio used by the

Batch 1 beams was $\frac{200\ \text{mm}^2}{80\ \text{mm}\times 140\ \text{mm}} = 0.0179$. Although this less than the maximum allowable reinforcement ratio specified by CSA A23.3-14 (2014), which is 0.025, the cross-sectional area of the beams was too small to fit in any shear reinforcement. As a result, the shear resistances of the beams were lower than the bending moment resistance. Moreover, the blockers did not perform as desired. Some concrete seeped through the holes in the blockers and covered the screws, which made them extremely difficult to remove. Lastly, the bonding adhesive, Sikadur 32, had a very high ability to bond surfaces. Even though de-bonding oil had been applied to the wooden forms, pieces of the form adhered to the beams where the bonding adhesive had been applied and they became inseparable. This is apparent in Figure 3.3.

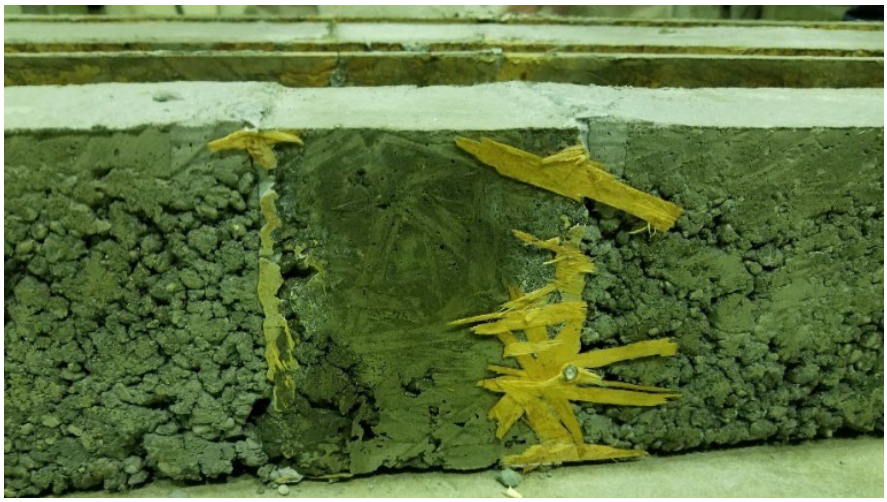

Figure 3.3. Side surface of the middle region of a beam from Batch 1, showing honeycombing in the concrete.

Based on the factors listed above, the mix design and configuration for the following batches of beams were modified, as shown in Table 3.1 and Figure 3.1 (b). The mix design for Batches 2 and 3 had a higher water cement ratio of 0.55, higher water percentage of the total mixture, and a smaller amount of gravel. The beam length for Batches 2 and 3 was increased to 2.0 m and the reinforcing bar size was decreased to a No. 10 bar to ensure that the beams would fail in flexure. Since there was less reinforcement in these beams, the neutral axis (N.A.) location moved upward. To ensure that the compression region was deep enough for the installation of the desired number of strain gauges, the beam width was also decreased. Thick Styrofoam blockers were used instead of the plastic ones because the Styrofoam could be removed more easily by being broken up and blown out with compressed air. Also, wax paper was used to line the forms

in the middle section where the bonding adhesive was used to prevent the beams from adhering to the forms. These changes made to Batches 2 and 3 resolved all the issues encountered in Batch 1. However, the wax paper wrinkled after being exposed to moisture in the concrete, which caused the side surfaces of the beams to be uneven, as shown in Figure 3.4.

After the beams had cured for 28 days, they were taken out of the humidity chamber and had their surfaces were prepared for monitoring during the load test. Both the electrical strain gauges and the DIC system required a clean and smooth surface on which to work, so an angle grinder was used to grind and polish the side surfaces of the concrete beams in the middle sections. After this, the dust and debris generated by the grinding process were removed using compressed air, and each surface was wiped clean using a non-woven sponge and Acetone. As shown in Figure 3.4, the processed surface in the middle was smooth and clean, whereas outside of this region, the surface was still wrinkled.

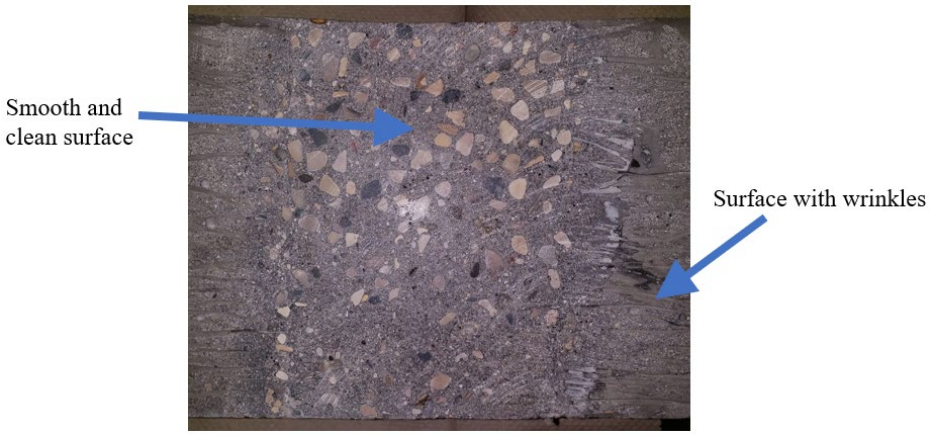

Figure 3.4. A photo of the side surface of a beam from Batch 3 in the middle region, showing wrinkling on the surface and the finish after smoothing and cleaning.

3.2.2. Instrumentation

The instruments used to monitor the beams during the load tests included electrical strain gauges, a DIC system, and a cover meter. Except for the pre-corrosion load test for Batch 1 and the second post-corrosion load test for Batch 2, the beams were monitored by electrical strain gauges on one side and by the DIC on the other side. Only electrical strain gauges were used to monitor one side of the beams during the pre-corrosion load test for Batch 1, because this was the original plan for the experiment. Then starting from the post-corrosion load tests, the DIC system was

used to monitor the other side of the beams. Lastly, the purpose of using electrical strain gauges to monitor both sides of the beams during the second post-corrosion load test for Batch 2 was to verify the existence of eccentric loading and to control variables The cover meter was used to locate the reinforcing bars for all the load tests.

Electrical Strain Gauges

Four electrical strain gauges were applied to one of the side surfaces of each beam, oriented to measure longitudinal strain during the pre-corrosion and post-corrosion load tests. A second post corrosion load test was conducted on Batch 2 beams, for which eight electrical strain gauges were applied, four on each side. These strain gauges were placed in the middle section of the beams where the reinforcing bars were corroded.

For Batch 1, gauges were attached in both the compression and tension zones, as shown in Figure 3.5 (a). However, it was discovered that the gauges in the compression zones were more durable and yielded more reliable data, which may have been due to the extreme local tensile strains at the crack locations. Also, gauges in the tension zone were more prone to damage during the corrosion process because the accumulated rust from the corroding rebar caused the beams to crack, allowing the rust to cover the strain gauges. Therefore, for Batches 2 and 3, all gauges were placed in the compression zone. Due to the limitations of space, one of the gauges was attached to the top surface close to the edge, as shown in Figure 3.5 (b). The exact locations of the attached strain gauges are described in Appendix B.

Since concrete is a non-homogeneous material, electrical strain gauges with a gauge length five times the largest grain of the aggregate were selected. Thus, electrical strain gauges with a 60 mm gauge length (model PL-60-11-3LJCT-F, Tokyo Sokki Kenkjujo Co. Ltd., Japan) were used to even out the non-homogeneous effect of the concrete. This type of strain gauge can measure strain up to 0.02 (Tokyo Measuring Instruments Lab 2021), and in the actual measurement, they had a precision of 2 micro strain (2×10^{-6}).

(a) (b)

Figure 3.5. (a) Illustration of electrical strain gauge locations for Batch 1 and (b) for Batches 2 and 3.

The type of adhesive used to attach the strain gauges for Batch 1 was CN-E, made by the same manufacturer that made the strain gauges (Figure 3.6 (a)). For Batch 2, a different adhesive, Gorilla Super Glue, was used (Figure 3.6 (b)), but it did not work well, even though it had the same main ingredients as the CN-E. As a result, CN-E was used again for Batch 3. Also, as described below, Batch 2 beams were not tested to failure during the first post-corrosion load test. After the first post-corrosion load test, the previously attached electrical strain gauges were ground off, and new ones were attached using the CN-E adhesive for the second post-corrosion load test.

(a) (b)

Figure 3.6. (a) CN-E adhesive used for Batches 1 and 3; (b) Gorilla super glue used for Batch 2.

DIC System

As previously mentioned, during the load tests, strains were measured on one side of the beams using the electrical strain gauges, and on the other side using the DIC system (model VIC-3D and VIC-2D, Correlated Solutions Inc., US). DIC is a non-contact optical method that measures in-plane displacements and strains by tracking the relative movement of painted dots on a surface. As a preparation, the surface was first painted white using spray paint (340 G in flat white, Tremclad®, Canada) and left to dry for 24 hours. Then a contrasting speckle pattern, as shown in Figure 3.7, was hand drawn on the white surface using a fine tip marker. These dots had a diameter of approximately 1 mm and the spacing was also approximately 1mm.

Figure 3.7. Contrasting speckle pattern on the middle section of a beam for the DIC system.

The idea of monitoring the second side of the beams using the DIC system was proposed after the pre-corrosion load tests for Batch 1 had been conducted. Therefore, DIC data for the pre-corrosion load tests for this batch of beams were not obtained. The set-up for the DIC system used in the post-corrosion load tests for Batch 1 is shown in Figure 3.8. Two cameras were used; thus, the collected data were analyzed using the DIC 3D software. However, the orientation of the beams in the test machine was changed to accommodate the longer beams for Batches 2 and 3, and only one camera was used due to spatial limitations, as seen in Figure 3.9. The data for these beams were analyzed using the DIC 2D software. The 2D system measured displacements and strains in two dimensions, which was adequate for the purposes of this research study. The advantage of a 2D system is that it has higher resolution. According to the manufacturer, the 3D

system has a strain resolution of 100 microstrain, while the 2D system has a resolution between 10 and 50 microstrain (Correlated Solutions Inc. 2018).

Figure 3.8. DIC system set-up for Batch 1 beams.

Figure 3.9. DIC system set-up for Batch 2 and Batch 3 beams.

Cover meter

In addition to the strain monitoring equipment used during the loading tests, a cover meter was also used prior to conducting the loading tests to reduce the uncertainty in the location of the reinforcing bars. A cover meter (Proceq Profometer 5^{+}, Proceq Inc, USA), as shown in Figure 3.10, was borrowed from ISL Engineering and Land Services Ltd. This device utilizes the pulse-induction method, and its accuracy is reported to be ±2 mm or 5%, whichever is greater (Proceq 2007).

Figure 3.10. Using the Proceq Profometer 5+ to measure the rebar cover depth of a beam.

3.2.3. Corrosion Procedure

Following the pre-corrosion loading tests, the beams were subjected to accelerated corrosion using the impressed current method. The objective was to only corrode the middle 100 mm section of the reinforcing bars to achieve weight losses of 30%, 20% and 10% for Batches 1, 2 and 3, respectively. As described earlier, NaCl had already been added to the concrete mixture in the middle sections, so that area was more prone to corrosion than the rest of the beam.

The experimental setup for the accelerated corrosion process is shown in Figure 3.11. The cathode of a 30 V DC power supply (UK3005-H, iiBro, China) was connected to one end of the reinforcing bar, and the anode was connected to a counter electrode. In this case, a sheet of copper mesh served as the counter electrode and was wrapped around the middle 100 mm section of the beam. This measure was used to further ensure that corrosion would be concentrated in the middle section. A thick layer of wet cotton towel was wrapped outside the copper mesh, and the moisture served as an electrolyte that provided for a continuous electrical circuit between the anode and the cathode and through the beam. If the cotton cloth were to get drier, the resistance of the circuit would increase, and it would require higher voltage to maintain the same current through the system. Therefore, to prevent the moisture from evaporating, the beams were placed inside a curing room, where the relative humidity was 100%. A 5% sodium chloride solution was added to the cloth daily to maintain optimum conductivity.

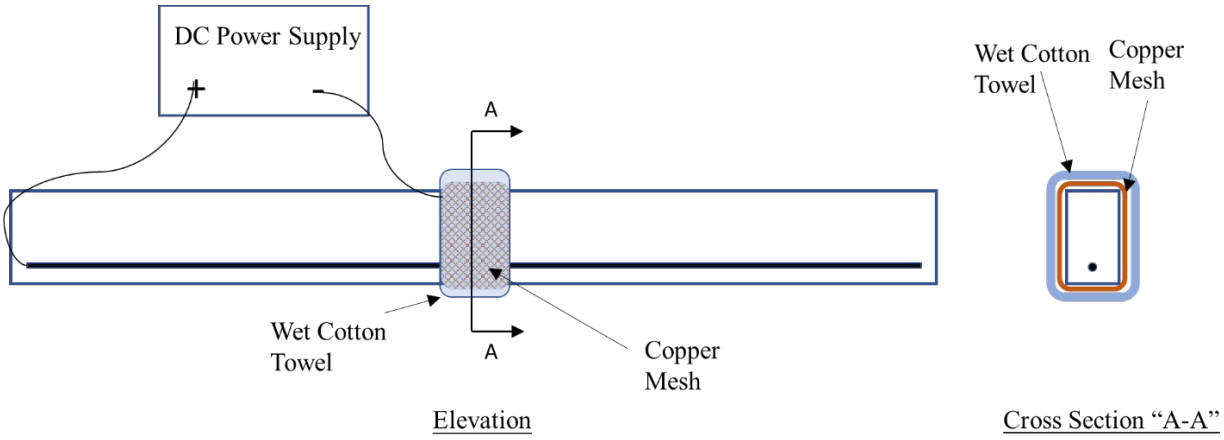

Figure 3.11. Setup for accelerated corrosion, shown in elevation and cross-section.

Preliminary Test

A short 200 mm long beam with the same cross-sectional dimensions as the Batch 1 beams was used to test the corrosion procedure first and served as a preliminary test; it is shown in Figure 3.12 (a). The target weight loss in the middle 100 mm length of rebar for this test was 10%. The average current that went through the circuit was 50 mA, which was the maximum constant current that could be maintained by a 30 V DC power supply. The surface area of the section of the steel bar to be corroded was $\pi(16\text{ mm})(100\text{ mm}) = 5026.5\text{ mm}^2$. Thus, the current density can be calculated as $\frac{50\text{ mA}}{5026.5\text{ mm}^2} = 0.00995\frac{\text{mA}}{\text{mm}^2} = 995\frac{\mu\text{A}}{\text{cm}^2}$. Based on the literature review, current densities from 100 to 2000 $\frac{\mu\text{A}}{\text{cm}^2}$ are commonly used for the impressed current method (Malumbela et al. 2012). The current density used in this experiment was in the middle of that range. The time duration required for the corrosion process was calculated based on Faradays' law:

$$M = \frac{WI_{app}T}{nF} \tag{3.1}$$

where M is the mass loss of steel per unit surface area (g/ cm^2), W is the atomic weight of steel (56 g/mol), I_{app} is the applied current density (0.995 mA/ cm^2), T is the time period (s) that must be solved for, n is the number equivalents exchanged (2 for Fe), and F is Faraday's constant (96487 A·s/mol)

According to Faraday's law, the theoretical duration for the corrosion process to achieve the target weight loss was 12 days (287 hrs). A sample calculation demonstrating Faraday's law is provided in Appendix C. After applying the current for 287 hrs, the corroded reinforcing bar was extracted and cleaned. The reinforcing bar was extracted by breaking the beam using a hammer. The corrosion product was removed from the steel bar sections using the chemical method described in ASTM G1 (2017). The procedure of the chemical method involves immersing the corroded steel bar in hydrochloric acid solution for 10 mins. The solution was made by adding 500 mL hydrochloric acid (HCL, sp gr 1.19), 3.5 g hexamethylene tetramine, and distilled water to make 1 litre. Figure 3.12 (b) shows the corroded steel bar being cleaned in the HCL solution.

The preliminary test validated that the corrosion method was able to concentrate the corrosion in the target area. All corrosion occurred within a 160 mm length. The middle 100 mm section experienced uniform severe corrosion, and the remaining 60 mm was slightly corroded, as shown in Figure 3.12 (c). The average weight loss of the middle section was 11.2 %, which was close to the expected value.

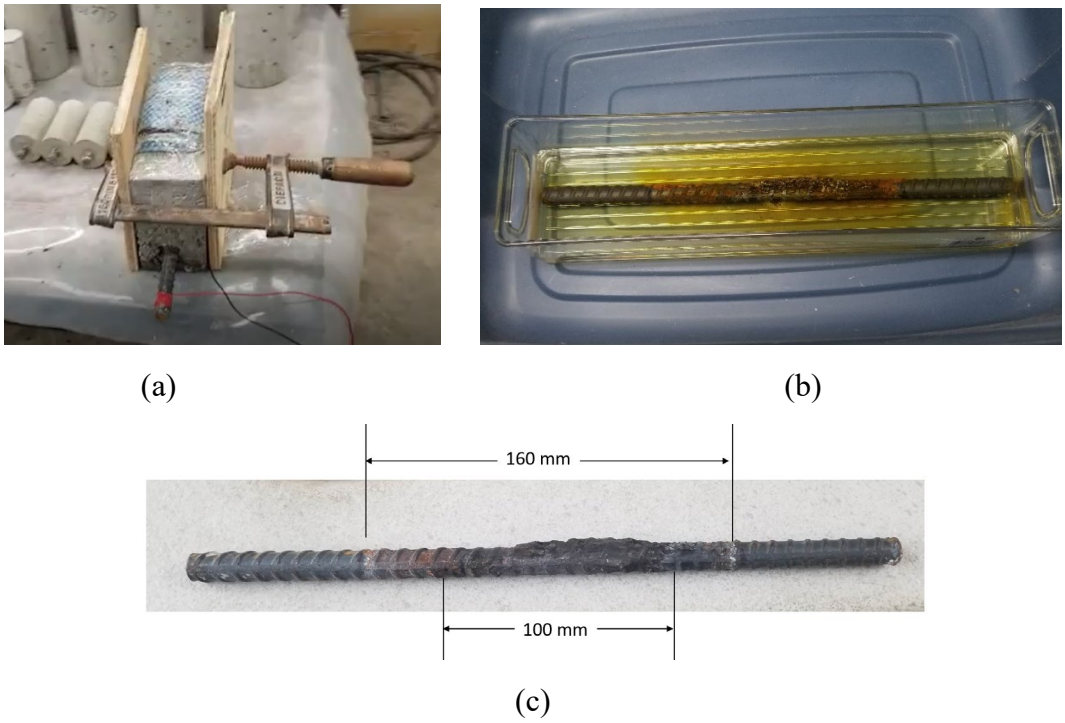

Figure 3.12. (a) Preliminary test for the accelerated corrosion on the short beam; (b) Cleaning process for the corroded steel bar in the preliminary test; (c) Cleaned steel bar in the preliminary test.

Corrosion of the Beams

The targeted weight loss and the estimated total amount of current required to meet the target for each batch of beams is shown in Table 3.2. An average current of 50 mA was used for all beams. Based on the calculations using Faraday's law, Batch 1, 2 and 3 were corroded for 35.9, 12.2 and 6.1 days, respectively. The current rate was selected based the limitaions of the circuit resistances and the voltage capacity of the DC power supply. The resistance of the circuit connecting each beam was similar, and 20 V was required to maintain the constant 50 mA current when the cotton towel was fully saturated. The DC power supply could provide a maximum of 30 V; therefore, 10 V were left as contingency in case the resistance of the circuit increased when the cotton towel got drier.

Table 3.2. Corrosion target and current requirement for each batch of beams.

Batch Number	Rebar Size	Target Weight Loss	Estimated Required Current (A · hr)	Required Duration of Corrosion (day)
Batch 1	No.15	30%	43.0	35.9
Batch 2	No.10	20%	15.3	12.2
Batch 3	No.10	10%	7.31	6.1

After corrosion was completed, the DIC surfaces were repainted due to the corrosion stains. Electrical strain gauges were checked for integrity and replaced if they had lost connection. Following the post-corrosion load test, the reinforcing bars were extracted and cleaned following the same procedure as was used in the preliminary test. Then, the middle 100 mm sections were cut off using a table saw and weighed using a scale with a precision of 0.1 g. Their weights were compared to the weight of the uncorroded reinforcing bar, and thus, the actual percentage weight losses were determined.

3.2.4. Loading Test Set-up and Procedures

Four-point loading tests, set up as shown in Figures 3.13 and 3.14, were performed on the beams before and after corrosion using an Instron 600DX Universal Testing Machine (UTM) with a capacity of 600 kN. With this specific loading setup, the impact of potential loss of bond due to corrosion was minimized. Since corrosion was concentrated in the middle 100 mm section, the rest of the reinforcing bar maintained its original bond strength. The use of the four-point loading

set-up created a constant moment region within a 200 mm length centered at mid-span; therefore, bonding was not required in the corroded sections.

Figure 3.14 shows a beam being monitored by the DIC system and electrical strain gauges during a loading test. In this figure, the left-hand side surface of the beam is painted with a speckle pattern and is being monitored by the DIC system. The right-hand side has electrical strain gauges attached and is connected to a data acquisition (DAQ) system.

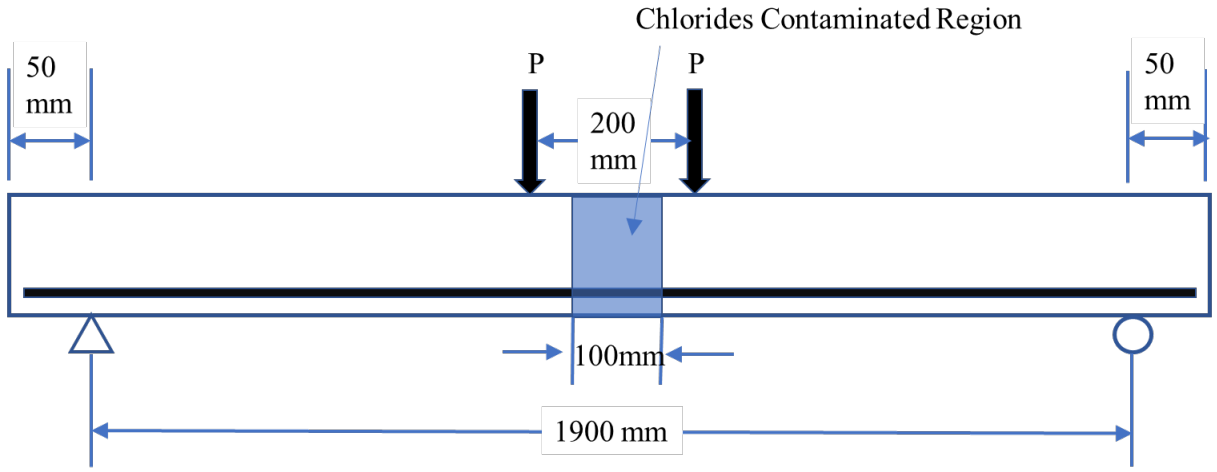

Figure 3.13. Four-point loading test set-up.

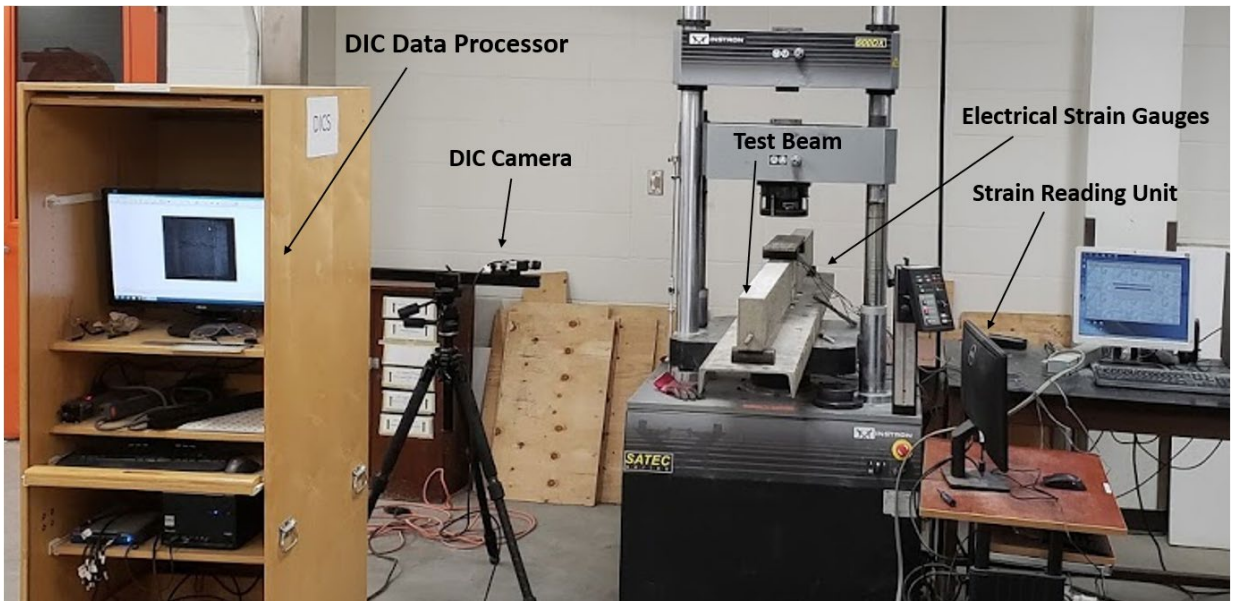

Figure 3.14. The experimental set-up, showing a beam being monitored by the DIC system and electrical strain gauges during a loading test.

Each beam was loaded multiple times during the pre-corrosion and post-corrosion loading tests and results from multiple tests were averaged. For each loading cycle, the beam was loaded to its cracking load (approximately 4 kN for Batch 1 beams and 2 kN for Batch 2 and Batch 3 beams) at a constant rate of 3 kN/min. The machine held the cracking load for approximately 30 seconds. After this, the load was increased at the same rate pausing at 1 kN intervals until the end of the elastic region was reached (approximately 10 kN for Batch 1 beams and 5 kN for Batch 2 and Batch 3 beams). This was to ensure the beams had been fully cracked. The end of elastic region was taken as the yielding of steel. Taking Batch 3 as an example, the loads were held at 2 kN, 3 kN, 4 kN and 5 kN. A sample calculation showing the theoretical cracking load and the end of elastic region is provided in Appendix D.

The beams were unloaded completely at the end of each loading cycle, then the same loading procedures were repeated at least three times to get averaged results.

At the end of the post-corrosion loading tests, the beams were loaded to failure at a uniform rate of 3 kN/min. The failure was detected by the loading machine and was defined as the point at which when the beam's capacity dropped 20% from the maximum that had been reached.

The pre-corrosion loading tests or post-corrosion loading tests on all three beams from each batch were completed on the same day. Then, their corresponding companion specimens were tested either on the same day or the following day to determine the mean and standard deviation of their strength and modulus. Twelve companion specimens were prepared for each batch of beams; six of them were tested after the pre-corrosion loading test, and six were tested after the post-corrosion loading test. A compressometer with a dial gauge was attached to the concrete cylinders for the compression tests to determine the elastic modulus. The compressometer measures displacements with a precision of 0.0025 mm (0.0001'') within a gauge length of 101.6 mm (four inches). The loading rate for the compression test was 0.25 MPa/s, which complied with the loading rate specified by CSA A23.2-14 (2014). The compressive test results are listed in Appendix A.

3.3. Theoretical Principles of the Surface Strain-based SHM Technique

3.3.1. The Original Theory Using Two Strain Readings

The theoretical principles of the surface strain-based SHM technique were first described by Christensen et al. (2011). Assuming that the reinforced concrete beam has a linear strain distribution on the side surface when subjected to a certain load and the strains can be measured accurately, the effective cross-sectional area of the reinforcing bar can be calculated simply using the readings from two strain gauges and principles of mechanics of materials. The following paragraphs provide a step-by-step description of the procedure.

As shown in Figure 3.15. (a), two strain gauges are located at the midspan of the beam (where the bending moment is the largest) at different depths, d_1 and d_2, respectively. A strain diagram, Figure 3.15 (b), can be constructed using the data provided by these strain gauges. Since ΔABO and ΔCDO are similar triangles, we can obtain the following relationship:

$$\frac{\varepsilon_1}{\varepsilon_2} = \frac{c-d_1}{d_2-c} \tag{3.2}$$

where ε_1 and ε_2 are the strain readings provided by the gauges at depths of d_1 and d_2. The distance from the top of the beam to the neutral axis, c, can be calculated by rearranging the equation above:

$$c = \frac{\varepsilon_1 d_2 + \varepsilon_2 d_1}{\varepsilon_1 + \varepsilon_2} \tag{3.3}$$

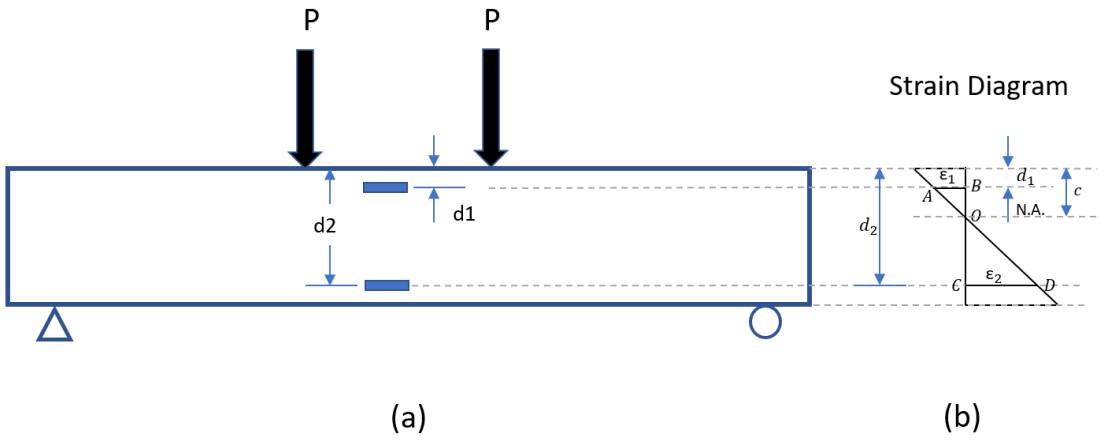

Figure 3.15. (a) Beam being monitored with two strain gauges; and (b) the strain diagram showing the relationship of the similar triangles.

Based on the principles of mechanics of materials, the neutral axis is located at the centroid of the cross-section as long as the beam is still under elastic deformation. Using the cracked transformed cross-section shown in Figure 3.16, the distance from the top of the beam to the centroid, $\bar{y}$, can be calculated as

$$\bar{y} = \frac{(bc)\frac{c}{2} + A_t d}{bc + A_t} \tag{3.4}$$

where b is the width of the beam, d is the distance from the top surface to the rebar location, and A_t is the transformed rebar area. Equation 3.4 is valid only if the beam is fully cracked (i.e. cracked from the bottom of the beam up to the neutral axis location). If the applied load is not high enough to fully crack the beam, the location of the centroid would be lower than the location of the neutral axis. However, the applied load can not be too high either. The strain distribution would not be linear if the beam reaches the inelastic deformation zone. Therefore, theoretically the optimum level of the applied load should result in the beam reaching the higher end of the elastic zone. When the beam is fully cracked under the elastic deformation range, $c = \bar{y}$, Equation 3.4 can be rearranged to obtain the transformed rebar area, A_t.

$$A_t = \frac{bc^2}{2(d-c)} \tag{3.5}$$

The transformed rebar area is defined as the actual rebar area times the modular ratio. The modular ratio, n, is the ratio of the Young's modulus of steel to that of concrete. Therefore, the actual steel bar area can be calculated as:

$$A_s = \frac{A_t}{n} \tag{3.6}$$

This actual rebar cross-sectional area, A_s, is the effective area left after corrosion. Therefore, it can be used to estimate the bending moment capacity, M_u as follows:

$$M_u = A_s f_y d - \frac{A_s^2 f_y^2}{2b\alpha_1 f_c'} \tag{3.7}$$

where f_y and f_c' are the yielding stress of steel and the specified compressive strength of concrete, respectively, b is the width of the cross-section, and α_1 is the Whitney stress block parameter which is calculated based on f_c'..

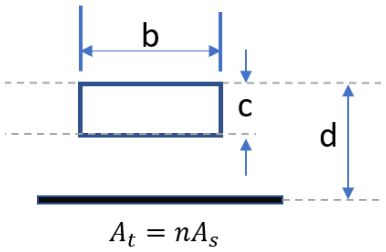

Figure 3.16. The cracked transformed section used to find centroid.

3.3.2. Locating the Neutral Axis Using Multiple Strain Readings

Section 3.3.1. provided a walk-through of the principles of the proposed SHM technique considering the simplest scenario, for which only two strain readings were obtained. In that case, assuming the beam is under elastic deformation and the surface strains are distributed linearly, the similar triangle method was used to find the neutral axis location. However, during the experimental program, additional electrical and DIC strain readings were obtained to increase the reliability of the data. Thus, the similar triangle method was not adequate to calculate the N.A. location. Instead, the N.A. could be located using a linear best fit function obtained by applying the least squares method, in which the strain gauge locations and readings can be taken as the x- and y-coordinates respectively, as shown in Figure 3.17. The x-intercept of the derived best fit trendline is the estimated N.A. location.

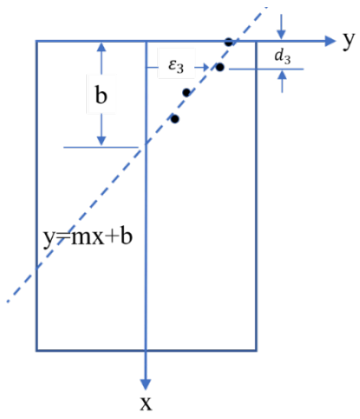

Figure 3.17. Illustration of finding the N.A. location using the best fit function through multiple strain readings.

When combining data from the two faces to locate the N.A., three different methods were proposed and tested to find the optimal analysis procedures. The alternative methods are explained below and illustrated in Figure 3.18. Sample Calculations are given in Appendix E.

- Method 1: Obtain the best fit function for the DIC and the ESG sides separately, then take an average between the two N.A. locations.
- Method 2: Merge the data from the two sides into one data set, and then apply best fit.
- Method 3: Firstly, obtain the best fit function for the DIC side, then use this function to interpolate the DIC strains at the same depths as the ESGs. Next, find the average of the interpolated DIC readings and the corresponding ESG readings. Lastly, find the best fit function using the averaged strains.

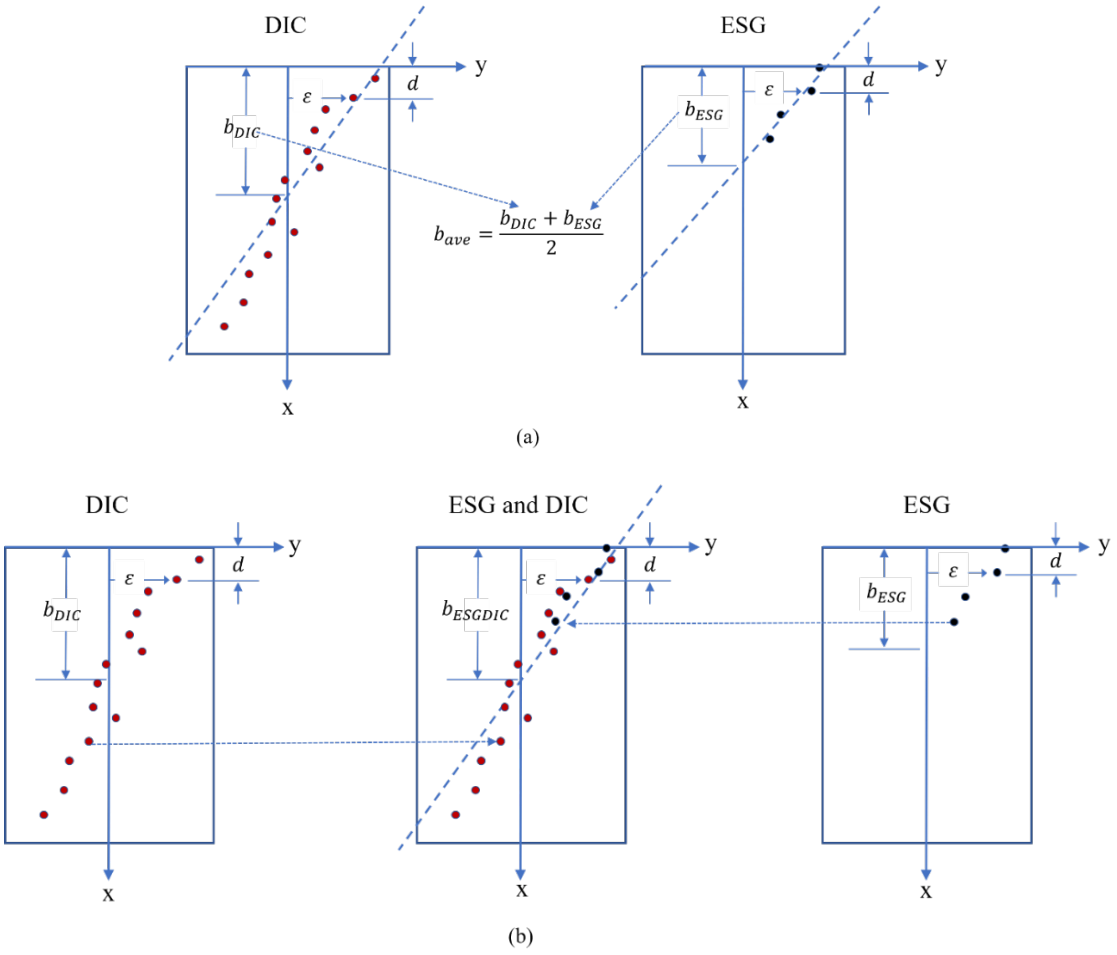

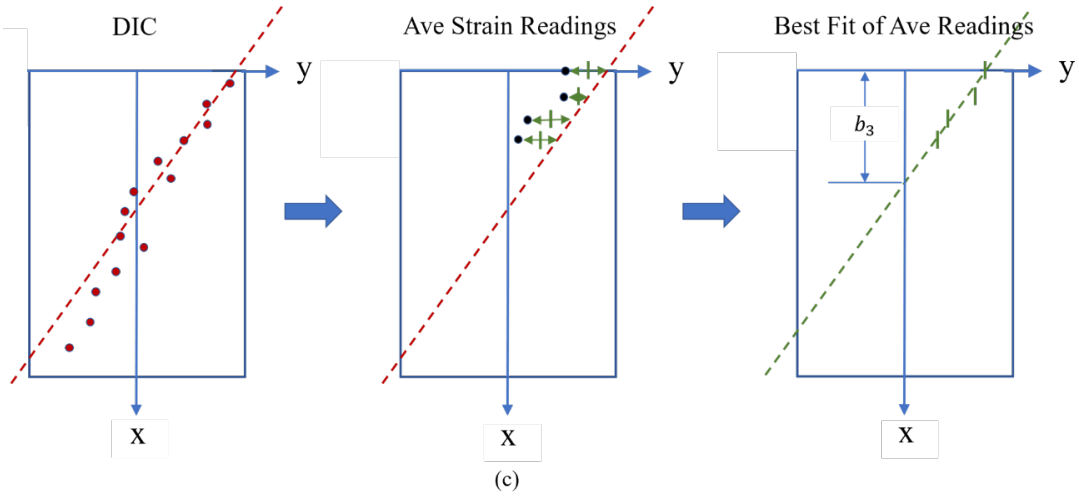

Figure 3.18. Illustration of locating neutral axes using the integrated data from two faces: (a) Method 1; (b) Method 2; and (c) Method 3.

If the two faces are perfectly complementary to each other, or in other words, the estimated neutral axis locations on the two faces are equal in distance and opposite in direction from the theoretical N.A. location, then Method 1 should be effective. Method 2 should work well when the number of measurement locations on both sides is similar, as was the case for the second post-corrosion load test for Batch 2, for which both sides were monitored by four electrical strain gauges. In the other load tests, however, the number of extensometers on the DIC side was significantly larger than the number of electrical strain gauges, and thus, the results might be partial to the DIC data. Method 3 is the most complicated procedure, but it might be able to overcome the weighting issue associated with Method 2.

3.4. Methodology for the Reliability Analysis

3.4.1. Reliability Analysis

One way to quantify a structure's level of safety is through the reliability index, which is defined as follows (Frangopol and Messervey 2011):

$$\beta = \frac{\mu_R - \mu_L}{\sqrt{\sigma_R^2 + \sigma_L^2}} \tag{3.8}$$

where μ_R and μ_L are the mean values of resistance and load effect, respectively, and σ_R and σ_L are their corresponding standard deviations. This equation assumes that the two variables are normally distributed.

The reliability indexes were calculated using Equation 3.8 based on the monitoring data provided by the standard and enhanced SHM systems separately. For this research study, μ_R was the estimated moment resistance of the monitored beams. μ_L was considered to be the maximum allowable moment that can be applied to the beams. In reality, μ_L should be taken as the design load of the structure. However, under the circumstances of this lab experiment, an assumed value was needed. To make the assumption more reasonable, μ_L was taken as the largest integer value of the moment in kN·m smaller than a beam's factored design resistance calculated based on CSA A23.3-14 (2014). μ_R was re-calculated after the beams had been corroded, but μ_L was assumed to be the same, because it was intended to evaluate whether the beams still had adequate level of safety after corrosion. Since the loads were applied by a universal testing machine in a laboratory setting, the standard deviation of the applied moment, σ_L, was approximated to be zero. Lastly, the standard deviation of the moment resistance, σ_R, was calculated as an accumulation of the standard deviations of all the independent variables used in the process of calculating the mean beam resistance.

For the purpose of illustrating this process, assume that a function $f(x_1, x_2, \ldots, x_n)$ is based on n independent variables. Also assume each variable follows a normal probability distribution and has a standard deviation, σ_{xi}. Then, the standard deviation of the result of this function can be calculated using Equation 3.9 (Nowak and Collins 2000):

$$\sigma_{f(x_i)} = \sqrt{\sum_{i=1}^{n} \left(\frac{\partial f}{\partial x_i}\right)^2 \times {\sigma_{x_i}}^2} \tag{3.9}$$

Taking the calculation of the transformed area, A_t, as an example, A_t is calculated based on three variables: the beam width, b; the neutral axis location, c; and the rebar location, d, as shown in Equation 3.10:

$$A_t = \frac{bc^2}{2(d-c)} \tag{3.10}$$

Assuming that the standard deviations of b, c, and d have already been obtained and denoted as σ_b, σ_c, and σ_d, then the standard deviation of the transformed area, σ_{A_t}, can be calculated as:

$$\sigma_{A_t} = \sqrt{\left(\frac{c^2}{2(d-c)}\right)^2 {\sigma_b}^2 + \left(\frac{2bcd-bc^2}{2(d-c)^2}\right)^2 {\sigma_c}^2 + \left(\frac{-bc^2}{2(d-c)^2}\right)^2 {\sigma_d}^2} \tag{3.11}$$

Therefore, it is critical to identify the standard deviation of each individual variable. The methods used are described in Section 3.4.2.

After the mean and standard deviation of the estimated beam resistance were determined, probability distribution diagrams were constructed using the following formula for a normal probability distribution (NIST/SEMATECH 2012) to illustrate the probabilities of failure associated with different monitoring systems:

$$P(x) = \frac{1}{\sigma_R\sqrt{2\pi}} e^{\frac{-(x-\mu_R)^2}{2\sigma_R{}^2}} \tag{3.12}$$

An example probability distribution diagram, associated with alternative monitoring systems, is shown in Figure 3.19. The probability distribution curve for the enhanced monitoring system is narrower than that of the standard monitoring system, because enhanced monitoring produces more certainty about the estimated mean resistance. The area below the curve to the left of the applied moment indicates the probability of failure. Thus, for the enhanced monitoring system to get the same probability of failure as the standard monitoring system, the beam would be allowed to remain in service and deteriorate for a longer period of time.

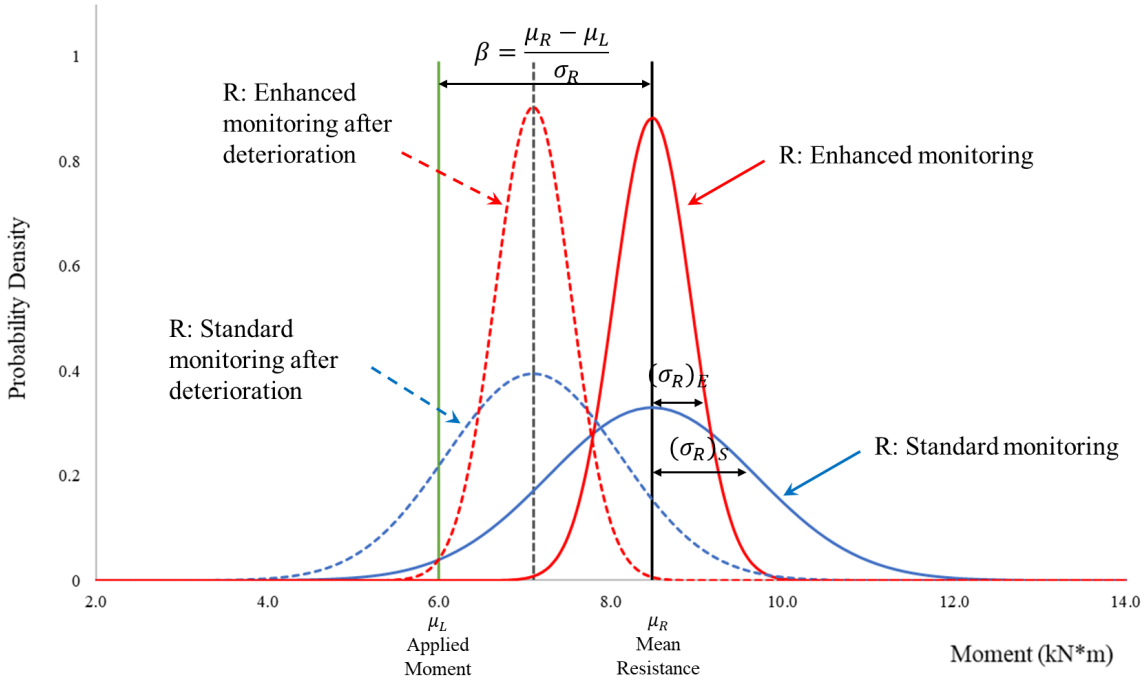

Figure 3.19. Probability distribution diagram of a beam's flexural capacity associated with standard and enhanced monitoring systems.

3.4.2. Determination of the Standard Deviations of Variables

All the variables used in this research study were assumed to follow a normal probability distribution that could be represented by its mean and standard deviation. The standard deviations were determined in three different ways, depending on the specific variable. The first way was based on the precision of the instrument used to make the measurement. It was assumed that the precision of a measurement device corresponded to the 90% confidence limits, which lie 1.645 standard deviations from the mean. For instance, beam width was measured using a ruler with 1 mm precision, so the standard deviation of beam width was $\frac{1\,mm}{1.645} = 0.606\,mm$.

The second way to determine a variable's standard deviation was through experimental statistics. The mechanical properties of steel and concrete were determined through testing the companion specimens in the lab. The standard deviation of the material properties was then calculated directly using the test results. Detailed results can be found in Appendix A. Another property that was determined through statistics was the estimated neutral axis locations. While a certain load was being held during the load test, strain data were obtained with a sampling rate of 1/s. Each set of strain data corresponded to an estimated neutral axis location. Thus, since each load was held for approximately 30 s, 30 neutral axis locations were obtained. The mean and standard deviation of the estimated neutral axis locations were then determined through the statistical method.

Lastly, if a variable was neither measured directly nor obtained through laboratory testing, then its standard deviation was determined through literature references. For instance, without the help of a cover meter, the tolerance for the cover depth over the reinforcing steel in a reinforced concrete beam is ± 12 mm as specified by CSA A23.1 (2014). This was assumed to correspond to the 90% confidence limit. Considering the Young's modulus of reinforcing steel, Mansour et. al (1984) reviewed the test results for 300 samples, and concluded a weighted average coefficient of variation to be 0.031. Thus, for a steel bar with a modulus of 200 GPa, the standard deviation was estimated to be 6.2 GPa.

A list of variables used to determine a beam's moment capacity and their corresponding standard deviations are presented in Table 3.3.

Table 3.3. List of variables and their corresponding standard deviations.

Symbol	Variable Definition	Standard Deviation	Source
c	Estimated N.A. Location	varies	Experimental Statistics
f'_c	Concrete Compressive Strength	varies	Experimental Statistics
E_c	Concrete Young's Modulus	varies	Experimental Statistics
f_y	Steel Yield Strength	varies	Experimental Statistics
Es	Steel Young's Modulus	6.2 MPa	Literature (Mansour et.al, 1984)
d_b	Rebar Diameter	0 mm	Assumed to be very small
b	Beam Width	0.608 mm	Ruler Precision (±1 mm)
h	Beam Height	0.608 mm	Ruler Precision (±1 mm)
cc	Concrete Cover Thickness	7.3 mm (standard) 1.2 mm (enhanced)	Literature (CSA A23.1, 2014) Cover Meter Precision (±2 mm)

3.5. Methodology for the Economic Analysis

The economic values associated with implementing the standard and enhanced SHM systems were quantified using the VOI approach assuming the beams tested in the laboratory were the edge beams on the University Bridge in Saskatoon, SK. The edge beam is one of the most easily corroded structural members of a bridge, since it does not have waterproof surfacing like the bridge deck does (Racutanu 1999). Without the help of any SHM systems, the current replacement cycle of edge beams is 45 years on average, and the cost of replacement (including demolition and reconstruction) is around $820/meter (Mattsson et al. 2007). Assuming a 5% inflation rate, the replacement cost of edge beams is equivalent to $1624/meter in 2021. The university bridge has a length of 378 metres (City of Saskatoon 2020), so the total cost to replace the edge beams on both sides of the bridge is $378\,m \times 2 \times \$1624/m = \$1{,}227{,}744$. This value was assumed to be the total life cycle cost of the edge beams without SHM monitoring.

Assume that the present time is 45 years into the service life of this bridge. Without the information provided by any SHM system, a bridge inspector may decide to replace all the edge beams due to the uncertainty of the deterioration condition of the beams. However, if an SHM system was implemented to reduce the uncertainty in the actual condition of the beams, they may be allowed to remain in service, thus extending their service lives, if they were found to have an adequate level of safety, defined as possessing a reliability index that exceeds a critical value. In

structural assessment, the target reliability index is commonly taken as 2 to 4 (Frangopol and Messervey 2011). In this research, a lower reliability index of 2 was adopted as the critical value, $\beta_{critical}$.

The reliability indexes obtained for the beams using the information provided the standard and enhanced monitoring systems were compared to the critical value. If the reliability index for the beam was less than $\beta_{critical}$, the beam was assumed to be taken out of service immediately. On the other hand, if the reliability index for the beam was greater than $\beta_{critical}$, the beam was assumed to remain in service and continue to deteriorate while being monitored continuously until its reliability index dropped to the minimum acceptable value, $\beta_{critical} = 2$. The minimum allowable mean resistance of the structure, μ_{Rallow}, was calculated by rearranging Equation 3.8 above:

$$\mu_{Rallow} = \beta_{critical} \times \sqrt{\sigma_R^2 + \sigma_L^2} + \mu_L \tag{3.13}$$

After obtaining the minimum allowable resistance, μ_{Rallow}, the minimum allowable reinforcing bar area due to corrosion, A_{allow}, could be solved using Equation 3.7 earlier and taking $M_u = \mu_{Rallow}$.

The maximum allowable mass loss of reinforcement was calculated as:

$$M = (A_s - A_{allow}) l \rho \tag{3.14}$$

where A_s was the current reinforcing bar area estimated by the SHM system, l was the length of the corroded section, and ρ was the density of the steel. Then, the mass loss was transformed into the additional service life by rearranging Faraday's law:

$$T = \frac{MnF}{WI} \tag{3.15}$$

where M is the mass loss at the reinforcement per unit surface area (g/ cm^2), W is the atomic weight of steel (56 g/mol), I is the current density in natural corroding condition (A/ cm^2), T is the time period (s) that must be solved for, n is the number equivalents exchanged (2), and F is Faraday's constant (96487 A·s/mol). The corrosion of metal is a process by which the metal loses its electrons to the surrounding environment; thus, it will generate a weak electric current, and this current can be used to quantify the speed of the corrosion. In a natural environment, the

current density is typically between 0.1 and 10 μA/cm^2 (Malumbela et al. 2012). For this research study, a high current density of 10 μA/cm^2 was assumed to give the most conservative estimates of the extended service lives. The extended service life is inversely proportional to the assumed current density. For example, if 5 μA/cm^2 was assumed instead of 10 μA/cm^2, the calculated additional service life would be doubled. It is important to recognize that the calculated values were just predictions made for the purpose of the economic analyses. In reality, the beam would be monitored consistently, so they would be taken out of service based on their real-time conditions.

For a beam with an extended life-span, its total life cycle cost may be the same as the unmonitored beam with a service life of 45 years, but the total cost is distributed over a longer period of time. Thus, the one that has a longer life-span clearly has more economic benefits. Therefore, it is appropriate to estimate the value based on the annual worth of life cycle costs (AWLCC), which is calculated using the following formula (ASTM 2017):

$$AWLCC = \frac{P[i(1+i)^y]}{(1+i)^y-1} \tag{3.16}$$

where P stands for the present value of the total life cycle cost; i is the discount rate (assumed to be 5%); and y is the compounding period, which is equal to the expected life span of the structure, in years.

The values of SHM systems with different levels of uncertainty were quantified by comparing the AWLCC calculated based on the information available in the following three scenarios: 1. No SHM system; 2. Implementation of a standard SHM system; and 3. Implementation of an enhanced SHM system.

CHAPTER 4 EVALUATION OF THE PRACTICAL EFFECTIVENESS OF THE SURFACE STRAIN-BASED SHM TECHNIQUE

4.1. Overview

The prerequisite to evaluating the effectiveness of the proposed SHM technique is to find the best possible procedures for implementing such a technique. Despite the simplicity and the rationality of the theory of the SHM technique being tested, its practical effectiveness could be affected by many factors and could potentially be improved via certain modifications to the procedures of data collection and analysis. Preliminary analyses were conducted during the time gaps between the load tests, and the results of the antecedent load test were used to make modifications in the data collection and analysis procedures used for the following load test. The preliminary analysis focused on investigating the optimal sensor locations and the optimal applied load level for the beams; the results of these analyses are presented in Appendix F. It was found that more reliable strain data were obtained when the electrical strain gauges were placed in the compression zone, in the same plane (i.e., not on the top of the beams), and ideally not too close to the neutral axis. Moreover, a higher applied load (but within the beam's elastic deformation region) is recommended because the disparity between the neutral axis location estimated using data from the two sides of the beam was reduced by applying higher loads.

For the preliminary analyses, N.A. locations were estimated using strain data from each face separately. The accuracy of the estimates was not ideal, and it was found that the estimates from the two faces generally lay on opposite sides of the theoretical N.A. location. Therefore, it was suspected that the estimates from two sides were complimentary to each other and that estimates obtained using combined data from the two faces would be better. After all load tests were completed, the data were processed once again systematically using the data from the two faces

combined. Three different methods for combining the data from the two faces were employed, as described in Section 3.3.2, and the performance is discussed in Section 4.4. The coefficient of determination (R^2) and the standard deviation of the estimated N.A. locations were also calculated and referenced for selecting the optimal results, which corresponded to the procedures required to produce the maximum effectiveness of the strain-based SHM technique. The effectiveness of the proposed SHM technique was then evaluated based on the accuracy in estimating the N.A location, the steel bar cross-sectional area, and the beam capacity. The estimated values were compared to the actual or theoretically calculated values, as shown in Figure 4.1.

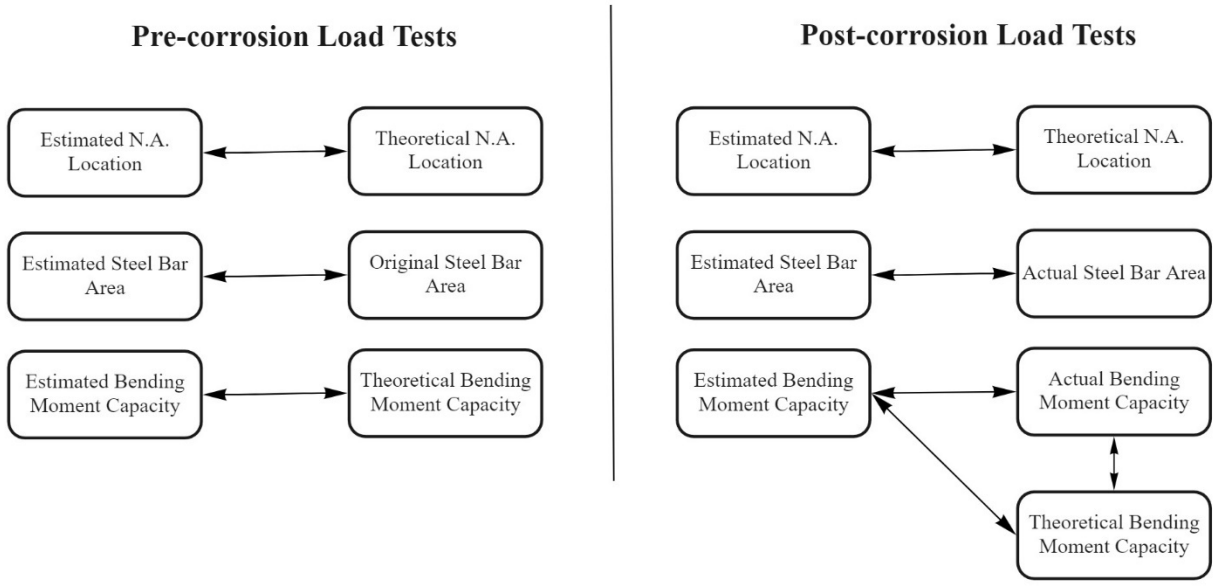

Figure 4.1. Comparisons used to evaluate the effectiveness of the surface strain-based SHM technique in the pre- and post-corrosion load tests.

In the pre-corrosion load tests, the actual steel bar areas were known values, equal to the original cross-sectional areas of the steel bars. Theoretical N.A. locations and bending moment capacities were calculated based on the known steel bar areas. The estimated steel bar area obtained using the SHM data was compared to the original steel bar area, whereas the estimated N.A. location and bending moment capacity were compared to theoretical values. In the post-corrosion load tests, the actual steel bar area and bending moment capacity were obtained directly from the experiments. The theoretical N.A. location and bending moment capacity were calculated based on the actual steel bar area. The SHM estimates were compared to these actual and/or theoretical

values as shown in Fig 4.1. The actual bending moment capacity was also compared to the theoretically calculated one to demonstrate the difficulty in estimating the actual capacity of reinforced concrete beams.

All the experimental data required to calculate the SHM estimates and to evaluate the effectiveness of the SHM technique are presented in Section 4.2. The theoretically calculated values are presented in Section 4.3. The estimates of the N.A. locations, steel bar areas, and beam capacities are compared to the theoretical and/or experimental values in Section 4.4. Finally, the effectiveness of the proposed SHM technique is summarized in Section 4.5.

4.2. Measured Data

4.2.1. Introduction

This section presents the data obtained from the experimental program, including the measured material properties, the measured beam dimensions and reinforcing bar locations, samples of the raw strain data, as well as the actual failure loads of the beams. All these data were essential for the following analyses. The measured material properties and beam dimensions were critical to the calculation of theoretical N.A. locations and the prediction of the flexural capacities. The N.A. locations were estimated using the strain readings and their corresponding locations. The actual failure loads were used as the evaluation criteria for the effectiveness of the SHM method.

4.2.2. Material Properties

Twelve companion concrete cylinders were cast for each batch of beams, six of which were tested at the time of the pre-corrosion load test; the other six were tested at the time of the post-corrosion load test to determine the concrete compressive strength and modulus. Three samples were cut from each steel bar and tested to determine the bar's tensile strength. A nominal modulus of 200 GPa was assumed for the steel, and the yield strength and ultimate tensile strength were determined by the Instron 600DX UTM internal software. The averaged results of the steel bar tensile tests and concrete compressive tests are listed in Tables 4.1 and 4.2, respectively. The detailed test result of each specimen is provided in Appendix A. The moduli of steel and concrete were critical variables used in the calculation of the theoretical N.A. locations and the effective cross-sectional areas of the reinforcing bars. The strengths of these materials were mainly used for predicting the beams' cracking loads, their elastic limits, and their ultimate

capacities. Furthermore, the standard deviations of these material properties were used in the reliability analyses, which are discussed in Chapter 5.

Table 4.1. Summary of measured steel bar tensile properties.

Steel Bar #	Yield Strength (MPa)		Ultimate Strength (MPa)		Beam #
	Mean	Standard Deviation	Mean	Standard Deviation	
No.15 bar	482.3	1.1	607.4	0.9	Batch 1, Beam 1 Batch 1, Beam 2 Batch 1, Beam 3
No.10 bar-1	444.9	1.0	666.9	1.2	Batch 2, Beam 1 Batch 2, Beam 2
No.10 bar-2	448.6	1.3	664.8	3.6	Batch 2, Beam 3 Batch 3, Beam 1
No.10 bar-3	437.3	1.9	649.3	2.0	Batch 3, Beam 2 Batch 3, Beam 3

Table 4.2. Summary of measured concrete compression properties.

Loading Test	Age of Specimens (days)	Strength (MPa)		Modulus (GPa)	
		Mean	Standard Deviation	Mean	Standard Deviation
Batch 1 Pre-corrosion	28	55.9	2.0	32.9	1.5
Batch 1 Post-corrosion	110	45.1	7.1	33.0	1.7
Batch 2 Pre-corrosion	28	36.9	0.8	25.1	0.7
Batch 2 Post-corrosion*	42	36.9	0.8	25.1	0.7
Batch 2 Second Post-corrosion	160	41.3	1.1	22.7	0.7
Batch 3 Pre-corrosion	28	38.3	1.1	22.8	1.1
Batch 3 Post-corrosion	36	39.2	1.1	23.1	0.7

*Since the companion concrete cylinders were only tested at the second post-corrosion loading test, concrete properties in the post-corrosion load test were assumed to be identical to those in the pre-corrosion load test.

A second post-corrosion load test for Batch 2 was conducted because not much useful information could be concluded from the original post-corrosion load test. Thus, the six companion concrete cylinders prepared for the original Batch 2 post-corrosion load test were saved for the second one, and the concrete properties in the original post-corrosion load tests were assumed to be the same as those in the pre-corrosion load test. The gap between the pre-corrosion load test and the original post-corrosion load test was only two weeks, and the gap between the second post-corrosion load test and the original one was three months.

4.2.3. Measured Beam Configurations

The design configurations for the beams are shown in Figure 3.1; however, the actual configurations of the fabricated beams may vary considerably, for which reason CSA A23.3-14 specifies a ±12 mm tolerance for beam height, width, and concrete cover thickness (CSA 2014). To decrease the uncertainties in the beam dimensions, a tape measure with a precision of 1 mm was used to measure the beam height and width, and a cover meter (model Profometer 5^{+}, Proceq SA, Switzerland) with a precision of 2 mm was used to measure the concrete cover depth. The uncertainty of reinforcing bar locations was also decreased drastically since they were calculated using the beam heights and the cover depths.

The measured beam dimensions are displayed in Table 4.3. Because a grinder was used to smooth the concrete surfaces of the beams in Batches 2 and 3, there were differences in the beams' widths and heights before and after corrosion. The reinforcing bars' cross-sectional areas in the pre-corrosion load tests were taken to be the nominal areas of the bars used for the beams. To determine the remaining area in the post-corrosion load tests, the bars were extracted and cleaned following the procedure specified in ASTM G1. The weight loss of the middle 100 mm section was measured and used to calculate the loss of cross-sectional area.

Table 4.3. Measured beam dimensions.

Batch #	Beam #	Width (mm)	Height (mm)	Concrete Cover Thickness (mm)	Rebar Location* (mm)	Rebar Area (mm^2)
Batch 1 Pre-corrosion	Beam 1	80	140	31	101	200
	Beam 2	80	140	33	99	200
	Beam 3	80	140	33	99	200
Batch 1 Post-corrosion	Beam 1	80	140	31	101	190
	Beam 2	80	140	33	99	165
	Beam 3	80	140	33	99	179
Batch 2 Pre-corrosion	Beam 1	73	142	33	103	100
	Beam 2	72	142	33	103	100
	Beam 3	73	138	30	102	100
Batch 2 Post-corrosion	Beam 1	72	142	33	103	78
	Beam 2	72	142	33	103	80
	Beam 3	73	138	30	102	80
Batch 2 Second Post-corrosion	Beam 1	72	142	33	103	78
	Beam 2	71	141	33	102	80
	Beam 3	72	136	30	100	80
Batch 3 Pre-corrosion	Beam 1	72	139	34	99	100
	Beam 2	70	140	34	100	100
	Beam 3	72	140	33	101	100
Batch 3 Post-corrosion	Beam 1	71	140	34	100	88
	Beam 2	70	140	34	100	86
	Beam 3	70	140	33	101	90

* Reinforcing bar location is measured from the bottom surface of the beam to the bottom surface of the bar.

4.2.4. Strain Data

This section provides samples of raw strain data obtained from the electrical strain gauge (ESG) data acquisition (DAQ) system and the DIC analysis software.

The raw data provided by the ESG DAQ system were in the form of Excel spreadsheets containing strain readings from each strain gauge along with the corresponding time and loads. As an example, the raw data for the first cycle of the post-corrosion load tests for Batch 3 Beam 3 is provided in Appendix G, and the changes of strain are plotted in Figure 4.2. The strain values at each gauge location increased linearly as the load increased from 0 to 4 kN. This was expected since the beam was still within the elastic deformation region. The neutral axis locations were calculated by combining the strain data with their corresponding gauge locations, which were measured using a tape measure with a precision of 1 mm. The measurements of the gauge locations are provided in Appendix B.

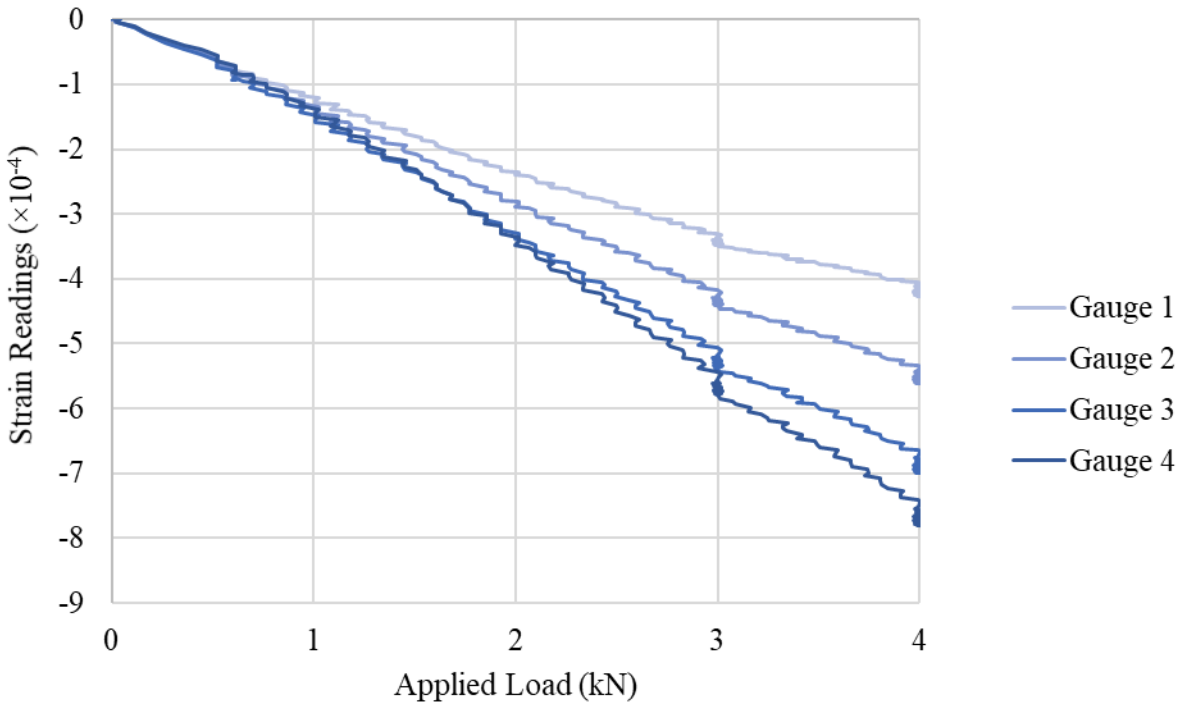

Figure 4.2. ESG readings plotted against increasing loads from the post-corrosion load test for Batch 3 Beam 3 Cycle 1

As for the DIC system, high resolution photos were taken at one second intervals throughout the loading process. Afterwards, the photos were imported to the DIC 3D (for Batch 1) or 2D (for Batches 2 and 3) software to analyze the displacements of the black dots painted on the side surfaces. Then the strains were calculated in the software as secondary analyses using the displacement data. To extract the strain data at certain locations, virtual extensometers can be drawn at any location and in any direction within the patterned area. A screen capture of the

strain field on the side surface with numerous virtual extensometers on it is shown in Figure 4.3 (a). The averaged strains over the length of the extensometers can be calculated and exported to an Excel spreadsheet with corresponding time stamps. The DIC system was not connected to the UTM, so the exported data did not contain the corresponding applied load. The DIC strain data from the same load test as the one used for Figure 4.2 are plotted with respect to time in Figure 4.3 (b). The DIC data in this figure appears to level off rather than continue to increase because the applied loads were held constant at 3 kN and 4 kN for a period of time. Only the ESG DAQ system was connected to the loading machine, and thus only the ESG strain readings were correlated to the applied loads. Fortunately, both systems provided time stamps for the measured strain readings. Thus, the N.A. locations derived using the DIC data were correlated to the applied loads through the time stamps. Strain measurements are plotted against applied load in Figure 4.3 (c). In this figure, the DIC strains increase linearly as the load increases. However, the top extensometer "E0" was in a the similar location to Gauge 3 on the ESG side, but the DIC reading was much smaller than the ESG one.

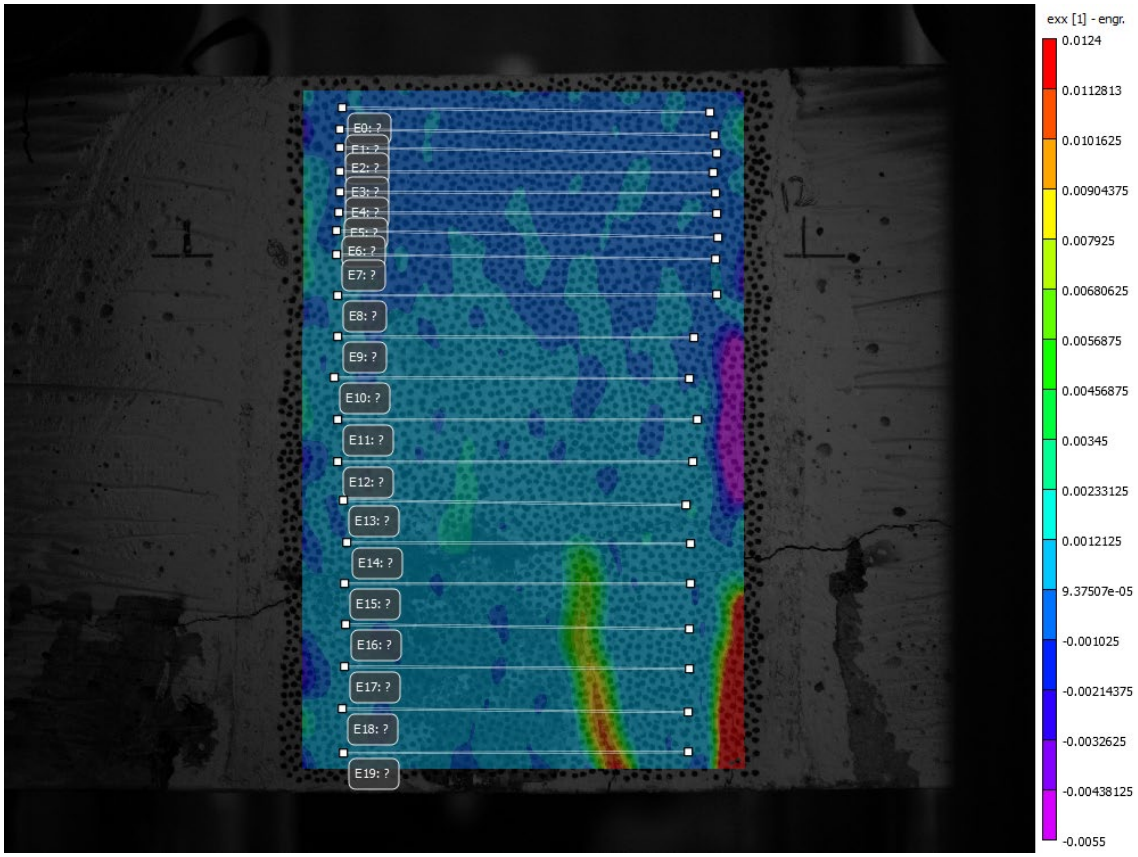

(a)

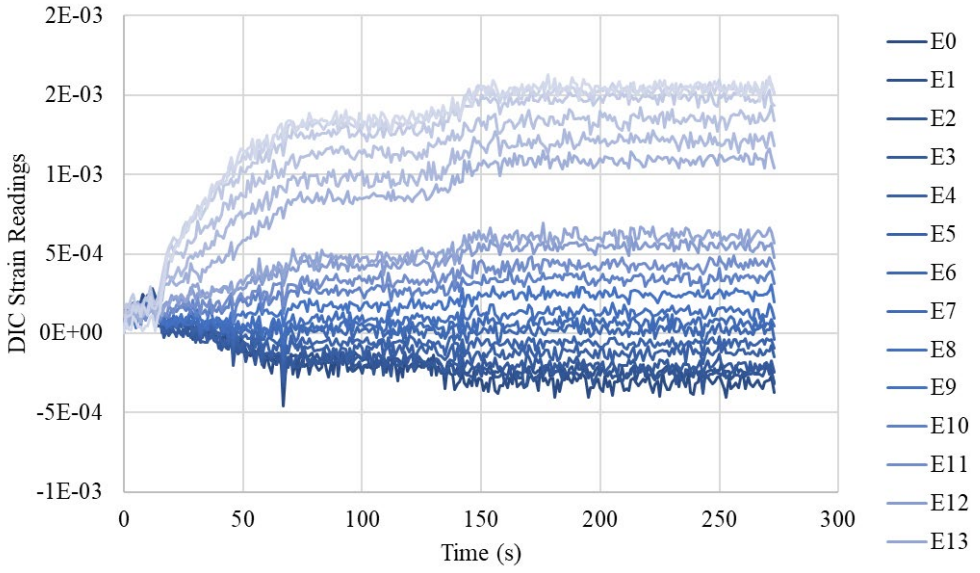

(b)

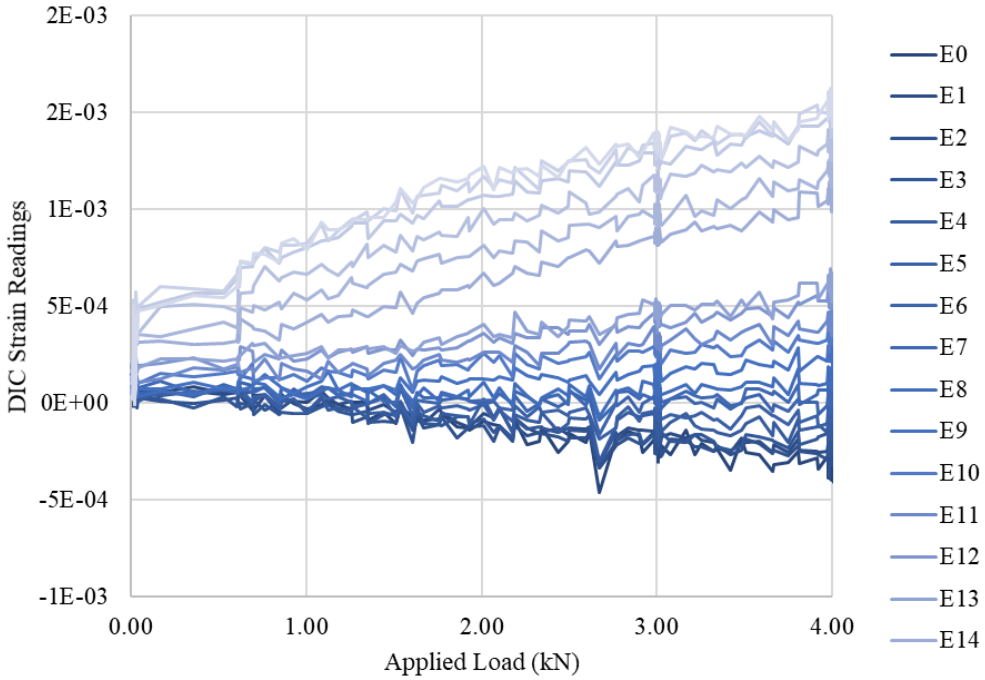

(c)

Figure 4.3. DIC Analysis from post-corrosion load test for Batch 3 Beam 3 Cycle 1: (a) strain field on the side surface of the beam when the applied load was 3 kN, with numerous virtual extensometers defined, (b) a plot of the average strain along each virtual extensometer against time, and (c) a plot of the average strain along each virtual extensometer against applied load.

To obtain the locations of these virtual extensometers, the same screen capture was imported into ImageJ2 (Rueden et al. 2017), which is an open-source software designed for scientific image processing. This software can measure the pixel length between two points on a picture and convert it to any given unit after setting scales using a known reference. Thus, its precision can potentially be as high as 0.001 mm. However, to achieve such high precision, it would require the scale reference to be measured with equal precision, which is quite impossible. The scale reference was measured using a tape measure with a precision of 1 mm. Therefore, the precision of ImageJ derived lengths was assumed to be 1 mm in subsequent analyses.

By comparing the strain diagrams for ESG (Figure 4.1) and DIC (Figure 4.2 (b)), it is obvious that the ESG data have a much lower level of fluctuations. The higher noise in the DIC readings might be due to lower precision compared to the ESGs, and other environmental factors such as vibrations of the loading machine, dust in the air, and lighting conditions in the lab.

4.2.5. Measured Failure Loads of the Beams

The loads that ultimately broke the beams and their corresponding failure modes in the post-corrosion load tests are summarized in Table 4.4. Beams in Batch 1 failed in shear due to the relatively high reinforcement ratio and the lack of shear reinforcement. The design for beams in Batches 2 and 3 was adjusted to reduce the amount of reinforcement, and thus, they failed in flexure as desired. The actual failure loads are used to evaluate the accuracy of the SHM estimates of bending moment capacity in Section 4.5.

Table 4.4. Actual failure loads of the beams.

Batch #	Beam #	Actual Failure Load (kN)	Failure Mode
Batch 1	Beam 1	14.8	Shear
	Beam 2	12.0	Shear
	Beam 3	17.5	Shear
Batch 2	Beam 1	12.2	Flexure
	Beam 2	9.9	Flexure
	Beam 3	9.8	Flexure
Batch 3	Beam 1	11.3	Flexure
	Beam 2	12.4	Flexure
	Beam 3	12.7	Flexure

4.2.6. Measured Loss of Steel Bar Areas due to Corrosion

After the beams had been loaded to failure in the post-corrosion load tests, the corroded reinforcing bar were extracted, cut, and cleaned following the procedures described in Section 3.3.3. In percentage terms, the actual loss of steel bar area was assumed to be equivalent to the loss of mass, which was determined by comparing the remaining mass of the middle 100 mm length of bar to that of the uncorroded steel bar of the same length. Table 4.5. summarizes the actual mass losses for all of the beams.

The corrosion levels achieved for Batches 2 and 3 were very close to the target values. However, the mass losses achieved for Batch 1 beams were much lower than expected. This may have been caused by the corrosion not being concentrated in the middle 100 mm section. Since Batch 1 beams used a larger bar size, more rust was generated for the same percentage of mass loss. Thus, large horizontal cracks formed on these beams, and sodium chloride solution may have penetrated these cracks, leading to corrosion taking place over a greater bar length. However, the first specimen in Batch 1 experienced an extremely low amount of corrosion. During the corrosion of Batch 1 beams, the resistance of beam 1 suddenly dropped in the middle of the process, so a short-circuit in the electrical circuit is suspected. However, the location of the short-circuit could not be identified through inspection.

Table 4.5. Target and actual mass loss for each beam.

Batch #	Beam #	Target Weight Loss	Actual Weight Loss
Batch 1	Beam 1	30%	5.1%
	Beam 2	30%	17.7%
	Beam 3	30%	10.5%
Batch 2	Beam 1	20%	21.7%
	Beam 2	20%	20.3%
	Beam 3	20%	20.2%
Batch 3	Beam 1	10%	11.5%
	Beam 2	10%	13.6%
	Beam 3	10%	9.8%

4.3 Theoretically Calculated Values

To evaluate the effectiveness of the proposed SHM technique, the estimated N.A. locations, effective steel bar areas, and the bending moment capacities were compared to the actual or theoretical values. The measured actual steel bar areas were known values in both pre- and post-corrosion load tests. Before corrosion, the nominal steel bar area was 200 mm^2 for beams in Batch 1, and 100 mm^2 for beams in Batches 2 and 3. The measured actual remaining steel bar areas after corrosion were summarized in Section 4.2.6. Theorical N.A. locations and bending moment capacities were calculated based on the actual steel bar areas, measured beam configurations, and material properties presented in Sections 4.2.2 and 4.2.3.

Tables 4.6 to 4.12 summarize the calculated theoretical values of N.A. locations and bending moment capacities for the beams in each load test, along with the associated variables used for the calculations, including the material properties, beam configurations, and effective reinforcing bar areas. The load capacity for shear failure was also calculated and compared to the load capacity for flexural failure. Based on the calculations, Batch 1 beams were governed by shear failure, which was validated by the experiments. It would be unreasonable to compare the SHM predicted flexural capacity to the actual capacity if the beams failed in shear. Thus, in subsequent sections, the beam's shear capacity was estimated using SHM data and compared to the actual and theoretical values for Batch 1. Beams in batches 2 and 3 failed in flexure as planned. Sample calculations are provided in Appendix D.

Table 4.6. Theoretically calculated values for strength and neutral axis location for Batch 1 beams for the pre-corrosion load test, along with measured or assumed values for the required variables.

Property Category	**Property**	**Beam 1**	**Beam 2**	**Beam 3**
Material Properties	concrete strength (MPa)	55.9	55.9	55.9
	concrete modulus (GPa)	32.9	32.9	32.9
	steel yield strength (MPa)	482	482	482
	steel modulus (GPa)	200	200	200
Beam Configurations	width （mm）	80	80	80
	depth (mm)	140	140	140
	concrete cover depth (mm)	31	33	33
	depth to rebar, d (mm)	103	101	101
	original steel bar area (mm^2)	200	200	200
Corrosion Condition	corrosion percentage	0%	0%	0%
	effective steel area (mm^2)	200	200	200
Theoretical Values	elastic neutral axis location (mm)	42.3	41.7	41.7
	bending moment capacity (kN·m)	8.38	8.19	8.19
	load capacity for flexural failure (kN)	30.5	29.8	29.8
	load capacity for shear failure (kN)	24.6	24.6	24.6

Table 4.7. Theoretically calculated values for strength and neutral axis location for Batch 1 beams for the post-corrosion load test, along with measured or assumed values for the required variables.

Property Category	**Property**	**Beam 1**	**Beam 2**	**Beam 3**
Material Properties	concrete strength (MPa)	45.1	45.1	45.1
	concrete modulus (GPa)	33.0	33.0	33.0
	steel yield strength (MPa)	482	482	482
	steel modulus (GPa)	200	200	200
Beam Configurations	width （mm）	80	80	80
	depth (mm)	140	140	140
	concrete cover depth (mm)	31	33	33
	depth to rebar, d (mm)	103	101	101
	original steel bar area (mm^2)	200	200	200
Corrosion Condition	corrosion percentage	5.1%	17.7%	10.5%
	effective steel area (mm^2)	190	165	179
Theoretical Values	elastic neutral axis location (mm)	41.4	38.8	40.0
	bending moment capacity (kN·m)	7.76	6.74	7.23
	load capacity for flexural failure (kN)	28.2	24.5	26.3
	load capacity for shear failure (kN)	22.1	22.1	22.1

Table 4.8. Theoretically calculated values for strength and neutral axis location for Batch 2 beams for the pre-corrosion load test, along with measured or assumed values for the required variables.

Property Category	**Property**	**Beam 1**	**Beam 2**	**Beam 3**
Material Properties	concrete strength (MPa)	36.9	36.9	36.9
	concrete modulus (GPa)	25.1	25.1	25.1
	steel yield strength (MPa)	445	445	449
	steel modulus (GPa)	200	200	200
Beam Configurations	width （mm）	73	72	73
	depth (mm)	142	142	138
	concrete cover depth (mm)	33	33	30
	depth to rebar, d (mm)	103	103	102
	original steel bar area (mm^2)	100	100	100
Corrosion Condition	corrosion percentage	0%	0%	0%
	effective steel area (mm^2)	100	100	100
Theoretical Values	elastic neutral axis location (mm)	37.8	38.0	37.6
	bending moment capacity (kN·m)	4.14	4.13	4.12
	load capacity for flexural failure (kN)	9.73	9.72	9.70
	load capacity for shear failure (kN)	18.5	18.3	18.0

Table 4.9. Theoretically calculated values for strength and neutral axis location for Batch 2 beams for the first post-corrosion load test, along with measured or assumed values for the required variables.

Property Category	**Property**	**Beam 1**	**Beam 2**	**Beam 3**
Material Properties	concrete strength (MPa)	36.9	36.9	36.9
	concrete modulus (GPa)	25.1	25.1	25.1
	steel yield strength (MPa)	445	445	449
	steel modulus (GPa)	200	200	200
Beam Configurations	width （mm）	72	72	73
	depth (mm)	142	142	138
	concrete cover depth (mm)	33	33	30
	depth to rebar, d (mm)	103	103	102
	original steel bar area (mm^2)	100	100	100
Corrosion Condition	corrosion percentage	22%	20%	20%
	effective steel area (mm^2)	78	80	80
Theoretical Values	elastic neutral axis location (mm)	34.5	34.8	34.4
	bending moment capacity (kN·m)	3.31	3.37	3.36
	load capacity for flexural failure (kN)	7.79	7.92	7.92
	load capacity for shear failure (kN)	18.3	18.3	18.0

Table 4.10. Theoretically calculated values for strength and neutral axis location for Batch 2 beams for the second post-corrosion load test, along with measured or assumed values for the required variables.

Property Category	**Property**	**Beam 1**	**Beam 2**	**Beam 3**
Material Properties	concrete strength (MPa)	41.3	41.3	41.3
	concrete modulus (GPa)	22.7	22.7	22.7
	steel yield strength (MPa)	445	445	449
	steel modulus (GPa)	200	200	200
Beam Configurations	width （mm）	72	71	72
	depth (mm)	142	141	136
	concrete cover depth (mm)	33	33	30
	depth to rebar, d (mm)	103	102	100
	original steel bar area (mm^2)	100	100	100
Corrosion Condition	corrosion percentage	22%	20%	20%
	effective steel area (mm^2)	78	80	80
Theoretical Values	elastic neutral axis location (mm)	35.9	36.2	35.6
	bending moment capacity (kN·m)	3.34	3.36	3.32
	load capacity for flexural failure (kN)	7.86	7.90	7.81
	load capacity for shear failure (kN)	19.3	18.9	18.5

Table 4.11. Theoretically calculated values for strength and neutral axis location for Batch 3 beams for the pre-corrosion load test, along with measured or assumed values for the required variables.

Property Category	**Property**	**Beam 1**	**Beam 2**	**Beam 3**
Material Properties	concrete strength (MPa)	38.3	38.3	38.3
	concrete modulus (GPa)	22.8	22.8	22.8
	steel yield strength (MPa)	449	437	437
	steel modulus (GPa)	200	200	200
Beam Configurations	width （mm）	72	70	72
	depth (mm)	139	140	140
	concrete cover depth (mm)	34	34	33
	depth to rebar, d (mm)	99	100	101
	original steel bar area (mm^2)	100	100	100
Corrosion Condition	corrosion percentage	0%	0%	0%
	effective steel area (mm^2)	100	100	100
Theoretical Values	elastic neutral axis location (mm)	38.5	39.2	39.0
	bending moment capacity (kN·m)	4.00	3.94	3.99
	load capacity for flexural failure (kN)	9.40	9.27	9.40
	load capacity for shear failure (kN)	18.2	17.8	18.3

Table 4.12. Theoretically calculated values for strength and neutral axis location for Batch 3 beams for the post-corrosion load test, along with measured or assumed values for the required variables.

Property Category	Property	Beam 1	Beam 2	Beam 3
Material Properties	concrete strength (MPa)	39.2	39.2	39.2
	concrete modulus (GPa)	23.1	23.1	23.1
	steel yield strength (MPa)	449	437	437
	steel modulus (GPa)	200	200	200
Beam Configurations	width （mm）	71	70	70
	depth (mm)	140	140	140
	concrete cover depth (mm)	34	34	33
	depth to rebar, d (mm)	100	100	101
	original steel bar area (mm^2)	100	100	100
Corrosion Condition	corrosion percentage	11.5%	13.6%	9.8%
	effective steel area (mm^2)	89	86	90
Theoretical Values	elastic neutral axis location (mm)	37.0	36.8	37.7
	bending moment capacity (kN·m)	3.63	3.46	3.64
	load capacity for flexural failure (kN)	8.53	8.15	8.56
	load capacity for shear failure (kN)	18.3	18.0	18.0

4.4. Estimated N.A. Locations Considering Combined Data from Two Faces

As discussed in Section 4.1, a preliminary analysis was performed to optimize the procedures used to estimate the neutral axis locations from measured strain data. The accuracy of the estimated N.A. locations considering the strain data from each individual face has been presented and discussed in Appendix F. From those preliminary analysis results, the optimal gauge locations and level of the applied load were identified. The results also suggested that estimates obtained using the combined data from two faces were more accurate and reliable. Therefore, the three different methods for combining the data from two faces, as described in Section 3.3.2, were applied to find the estimated N.A. locations, and the results are compared and discussed in

this section. Unreliable data identified by the preliminary analyses were excluded from these analyses. A detailed sample calculation of using a best fit function to find the estimated N.A. location and the corresponding coefficient of determination (R^2) is provided in Appendix E. This sample calculation was performed using strain data at one instant in time. Since the applied load was maintained at a certain level for 30 to 60 seconds, the estimated N.A. locations and corresponding coefficients of determination presented in this section correspond to the average values over the period that the load was held constant. The standard deviation was also calculated based on the variation of the instantaneous values for the estimated N.A. location obtained during this time period. Due to the large amount of calculation required, the analyses were automated in Python. The sample Python codes are provided in Appendix H.

The best estimates for each load test are highlighted in the tables in this section; these were used to estimate the effective steel bar areas and predict the remaining bending moment capacities in Section 4.5. In reality, the actual condition of the beams would be unknown, so the best estimates were not selected based on how close they were to the theoretical values, but were rather based on the standard deviation and coefficient of determination of the results as if the theoretical values were unknown. In theory, estimates with the lowest standard deviation and high coefficient of determination should be more accurate. Thus, these two factors were used for screening the optimum results.

4.4.1. Batch 1 Pre-corrosion Load Test

Only one side of the Batch 1 beams was monitored during the pre-corrosion load tests. Thus, this batch did not have the two face combined estimates. Based on the preliminary analysis presented in Appendix F, data obtained from the tension zone were not reliable, so the best estimates were selected among the results obtained using the data in the compression zone only ("ESG_cmprs") and the data in the compression zone and excluding the top gauges ("ESG_G2&G3").

The estimated N.A. locations using these two data groups and their corresponding coefficients of determination and standard deviations are presented in Table 4.13. The estimate with the lowest standard deviation for each beam is highlighted in green (also noted with double asterisks), and the estimate with the highest coefficient of determination is highlighted in yellow (also noted with a single asterisk). These cells were selected using the conditional formatting function in Excel. Since the number of decimal places displayed was fixed, some values may appear to be

the same but only one of them was highlighted. Since the "ESG_G2&G3" data group only contained data from two gauges, both data points were located on the line, and the coefficients of determination were equal to unity for all the corresponding estimates for this data group. Thus, the coefficients of determination were not used to identify the best estimates for this data group, and the coefficient of determination criterion was restricted to the "ESG_cmprs" data group.

The estimated N.A. locations for this set of load tests are plotted against their corresponding coefficient of determination and standard deviation values in Figures 4.4 (a) and (b), respectively. The calculated theoretical N.A. locations are also shown in the figures. It was expected that the accuracy of the estimates would increase as the coefficient of determination increased and as the standard deviation decreased. However, these trends were not observed for this set of load tests when considering the estimates provided by each data group separately. It might because all the coefficients of determination were quite high for this set of the load tests (>0.97) and the standard deviations were quite low (<0.7 mm). The estimates were also close to the theoretical values. The estimates provided by the "ESG_cmprs" data group were within 3 mm of the theoretical values. The "ESG_G2&G3" estimates had higher differences and higher standard deviations. Thus, comparing the estimates made by these two data groups, estimates with lower standard deviations would also be more accurate.

For Beams 1 and 2, the estimate with the lowest standard deviation was closer to the theoretical value than the estimate with the highest coefficient of determination. For Beam 3, since there were only two strain gauges located in the compression zone, coefficient of determination could not be applied as the selection criteria. Overall, using standard deviation as the criterion for selecting the best estimate was observed to be more robust and provided better estimates based on the results from this set of load tests.

Table 4.13. Batch 1 pre-corrosion load test N.A. locations in mm, and the corresponding coefficients of determination and standard deviations.

Beam #	Load	Cycle #	ESG_cmprs			ESG_G2&G3			Theoretical
			Mean	R^2	STDV	Mean	R^2	STDV	
Beam 1	5 kN	Cycle 1	44.81	1.00	0.29	45.43	1.00	0.32	42.90
		Cycle 2	39.54	0.99	0.11	41.80	1.00	0.15	42.90
	6 kN	Cycle 1	44.61	*1.00	0.25	45.17	1.00	0.24	42.90
		Cycle 2	39.89	0.99	0.09	42.23	1.00	0.11	42.90
	7 kN	Cycle 1	43.73	1.00	0.34	44.50	1.00	0.26	42.90
		Cycle 2	39.99	0.99	0.11	42.41	1.00	0.09	42.90
	8 kN	Cycle 1	43.03	1.00	0.08	43.97	1.00	0.11	42.90
		Cycle 2	39.82	0.99	0.10	42.48	1.00	**0.08	42.90
Beam 2	5 kN	Cycle 1	41.71	0.97	0.28	49.34	1.00	0.27	42.30
		Cycle 2	43.94	0.97	0.08	51.22	1.00	0.23	42.30
		Cycle 3	44.26	0.98	0.14	51.63	1.00	0.38	42.30
	6 kN	Cycle 1	41.89	0.97	0.18	49.35	1.00	0.24	42.30
		Cycle 2	43.86	0.98	0.07	50.76	1.00	0.19	42.30
		Cycle 3	44.10	0.98	0.08	50.93	1.00	0.21	42.30
	7 kN	Cycle 1	42.92	0.97	0.10	49.90	1.00	0.14	42.30
		Cycle 2	43.90	0.98	0.07	50.27	1.00	0.15	42.30
		Cycle 3	44.11	0.98	0.07	50.31	1.00	0.18	42.30
	8 kN	Cycle 1	43.20	0.98	**0.06	49.95	1.00	0.16	42.30
		Cycle 2	44.02	0.98	0.06	50.25	1.00	0.15	42.30
		Cycle 3	44.07	*0.98	0.06	50.08	1.00	0.15	42.30
Beam 3	5 kN	Cycle 1	N/A	N/A	N/A	47.87	1.00	0.67	42.30
		Cycle 2	N/A	N/A	N/A	48.14	1.00	0.48	42.30
		Cycle 3	N/A	N/A	N/A	46.25	1.00	0.60	42.30
	6 kN	Cycle 1	N/A	N/A	N/A	46.35	1.00	0.65	42.30
		Cycle 2	N/A	N/A	N/A	47.15	1.00	0.61	42.30
		Cycle 3	N/A	N/A	N/A	45.26	1.00	0.46	42.30
	7 kN	Cycle 1	N/A	N/A	N/A	45.28	1.00	0.38	42.30
		Cycle 2	N/A	N/A	N/A	45.97	1.00	0.39	42.30
		Cycle 3	N/A	N/A	N/A	44.42	1.00	0.31	42.30
	8 kN	Cycle 1	N/A	N/A	N/A	42.92	1.00	0.66	42.30
		Cycle 2	N/A	N/A	N/A	44.43	1.00	0.34	42.30
		Cycle 3	N/A	N/A	N/A	43.30	1.00	**0.26	42.30

Note: * Estimate with the highest coefficient of determination for each beam is highlighted in yellow.

** Estimate with the lowest standard deviation for each beam is highlighted in green.

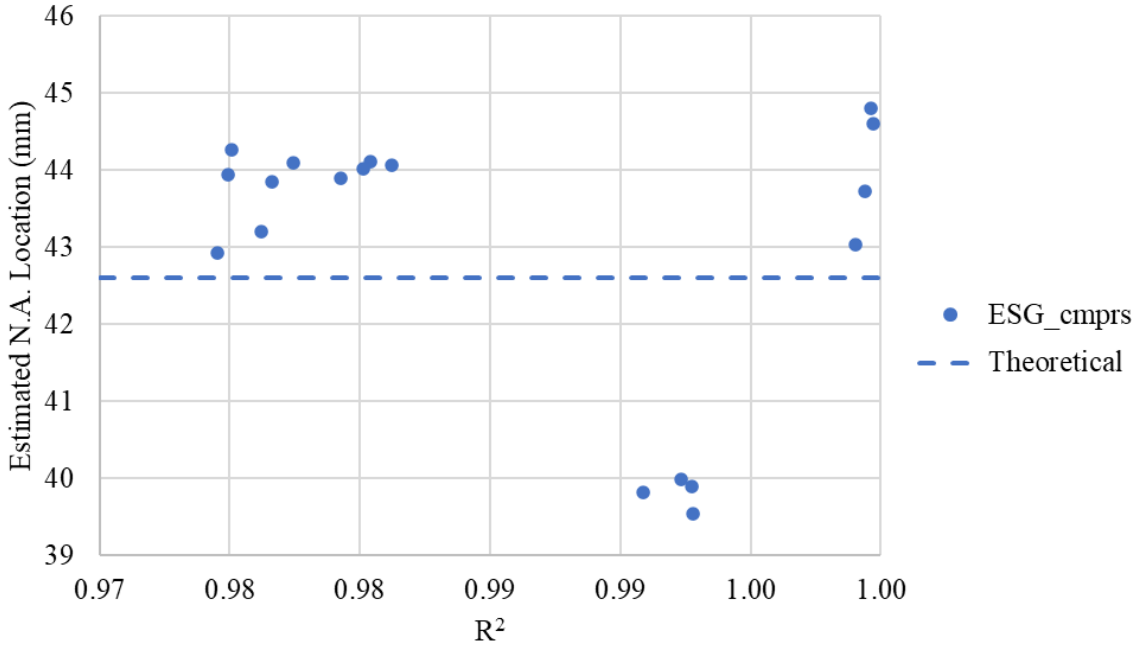

(a)

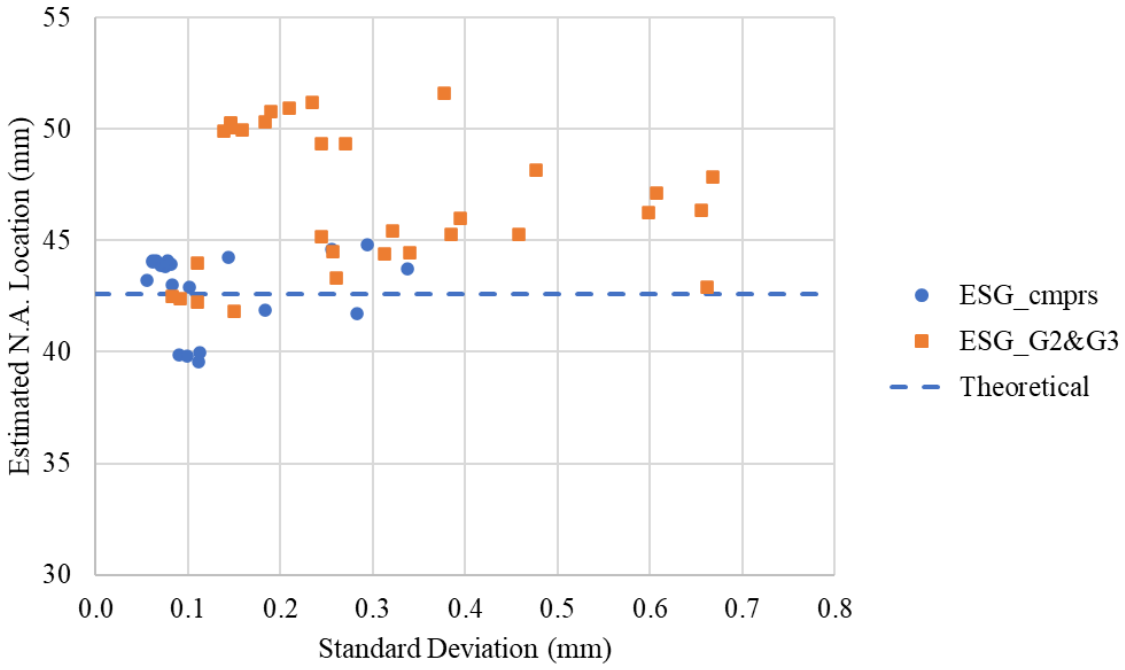

(b)

Figure 4.4. Batch 1 pre-corrosion load test N.A. locations, plotted against (a) the corresponding coefficients of determination, and (b) the corresponding standard deviations.

4.4.2. Batch 1 Post-corrosion Load Test

The preliminary analysis for Batch 1 post-corrosion load tests investigated the reliability of data from the DIC gauges in the tension zone and the old electrical strain gauges attached prior to corrosion. It was found that using the strains from the tension zone had a negative effect on the accuracy of the estimated N.A. location, while the use of data from the old electrical strain gauges did not have an obvious effect. Therefore, the DIC data in the compression zone ("DIC_cmprs") and all the ESG data ("ESG_all") were combined to find the estimated N.A. locations using the three methods. Estimates obtained considering data from each face individually and considering data from two faces combined using the three methods described in Section 3.2.2 are summarized in Table 4.14.

In Table 4.14., conditional formatting was applied to highlight the highest coefficient of determination in yellow and the lowest standard deviation in green for each beam. Estimates obtained using "ESG_all" and "Method 3" were excluded from the selection based on coefficients of determination, since fewer electrical strain gauges were used in the post corrosion load tests (3 for Beam 1, 4 for Beam 2, and 2 for Beam 3). Estimates obtained using Method 1 did not have coefficients of determination, since they were obtained by taking an average of the estimates from two faces directly. In the end, selection of the best estimates using coefficient of determination were restricted to "DIC_cmprs" and "Method 2". The estimates made by "ESG_cmprs" generally had higher coefficients of determination than "Method 2". This means the strains were more linearly distributed on each single face but were not identical on the two faces. However, the DIC estimates had much higher standard deviations than the ESG estimates. Estimates using "ESG_all" had the lowest standard deviations among all five different combinations, and the estimates considering data from two faces combined had higher standard deviations than considering ESG data alone, probably due to the high noise from the DIC data. Since it was speculated from the preliminary analysis that the two face combined data should be able to provide more accurate estimates, the estimate that had the lowest standard deviation among Methods 1 to 3 were highlighted in blue, and they were all from Method 3. Comparing the estimated N.A. locations corresponding to the highlighted cells to the theoretical N.A. location for each beam, it can be observed that, for Beams 1 and 2, estimates selected based on the standard deviations were better than those selected based on the coefficients of determination, and the two face combined data resulted in better estimates than using electrical strain gauges

alone, even though the two face combined estimates had higher standard deviations. For Beam 3, “DIC_cmprs” provided the best estimate; however, it did not differ much from the other two estimates.

The estimated N.A. locations for this set of load tests are plotted against the corresponding coefficient of determination and standard deviation values in Figures 4.5 (a) and (b), respectively. The outliers, such as the estimates made for Beam 2 Cycle 1, were omitted from the figure due to the limited boundary of the axes. It can be observed that the estimates show a convergence trend to the theoretical values as the coefficient of determination increases and as the standard deviation decreases.

Table 4.14. Batch 1 post-corrosion load test N.A. locations in mm, and the corresponding coefficients of determination and standard deviations.

Beam #	Load	Cycle #	DIC_cmprs			ESG_all			Method 1			Method 2			Method 3			Theoretical
			Mean	R^2	STDV	Mean	R^2	STDV	Mean	R^2	STDV	Mean	R^2	STDV	Mean	R^2	STDV	
Beam 1	5 kN	Cycle 1	61.93	0.69	12.00	41.01	1.00	0.09	51.47	N/A	8.48	57.05	0.63	9.02	49.58	1.00	4.18	42.00
		Cycle 2	49.88	*0.96	1.57	38.67	1.00	0.11	44.27	N/A	1.11	49.56	0.71	1.33	44.42	1.00	***0.69	42.00
		Cycle 3	47.96	0.93	5.25	38.69	1.00	0.09	43.32	N/A	3.71	50.43	0.67	5.79	43.53	1.00	2.36	42.00
		Cycle 4	40.59	0.72	1.98	39.11	1.00	0.07	39.85	N/A	1.40	39.37	0.91	1.15	39.74	1.00	0.87	42.00
		Cycle 5	51.11	0.77	4.04	39.85	1.00	0.09	45.48	N/A	2.86	46.30	0.88	2.94	44.49	1.00	1.49	42.00
	6 kN	Cycle 1	61.28	0.77	6.51	40.97	1.00	0.08	51.13	N/A	4.60	54.19	0.75	2.92	49.05	1.00	1.79	42.00
		Cycle 2	49.70	0.95	2.64	38.83	1.00	0.09	44.27	N/A	1.87	48.20	0.81	2.08	44.09	1.00	1.13	42.00
		Cycle 3	48.56	0.93	3.01	38.88	0.99	**0.06	43.72	N/A	2.13	48.85	0.78	2.42	43.68	1.00	1.25	42.00
		Cycle 4	41.42	0.75	3.34	39.33	1.00	0.09	40.38	N/A	2.36	39.25	0.92	2.00	40.15	1.00	1.34	42.00
		Cycle 5	50.75	0.74	6.27	39.93	1.00	0.07	45.34	N/A	4.43	43.55	0.90	3.06	43.88	1.00	2.09	42.00
Beam 2	5 kN	Cycle 1	-296.91	0.54	5804.73	31.55	0.97	**0.07	-132.68	N/A	4104.57	-162.93	0.03	208.83	70.47	0.98	6.32	39.30
		Cycle 2	49.23	0.94	1.88	30.09	0.96	0.20	39.66	N/A	1.34	68.14	0.29	4.37	39.92	0.99	0.74	39.30
		Cycle 3	49.03	0.98	2.08	31.46	0.97	0.16	40.25	N/A	1.48	70.65	0.33	3.93	40.47	0.99	***0.74	39.30
		Cycle 4	46.41	0.95	2.18	29.58	0.21	0.16	38.00	N/A	1.55	-865.74	0.00	1703.62	41.07	0.73	1.06	39.30
		Cycle 5	49.09	0.95	6.98	30.14	0.21	0.17	39.61	N/A	4.94	-1331.97	0.00	5738.69	42.53	0.72	2.35	39.30
	6 kN	Cycle 1	223.88	0.63	146.83	31.74	0.97	0.10	127.81	N/A	103.82	1139.36	0.01	7782.03	64.40	0.98	4.19	39.30
		Cycle 2	49.28	0.94	2.78	30.75	0.97	0.11	40.02	N/A	1.97	61.61	0.41	4.62	39.81	0.99	1.02	39.30
		Cycle 3	49.23	*0.99	2.66	31.92	0.98	0.11	40.57	N/A	1.89	60.53	0.50	2.67	40.28	0.99	0.78	39.30
		Cycle 4	46.84	0.95	2.52	30.03	0.21	0.15	38.44	N/A	1.79	314.07	0.00	2949.78	41.29	0.71	1.27	39.30
		Cycle 5	53.25	0.94	10.49	30.52	0.21	0.15	41.89	N/A	7.42	378.88	0.01	566.18	43.54	0.65	3.26	39.30
Beam 3	5 kN	Cycle 1	57.70	0.82	4.62	48.89	1.00	0.32	53.30	N/A	3.27	76.73	0.47	9.22	53.60	1.00	2.32	40.60
		Cycle 2	48.42	0.95	2.08	53.12	1.00	0.37	50.77	N/A	1.49	51.77	0.89	2.42	50.38	1.00	***1.25	40.60
		Cycle 3	58.95	0.69	10.72	53.19	1.00	0.53	56.07	N/A	7.59	67.96	0.63	13.12	55.67	1.00	4.89	40.60
	6 kN	Cycle 1	55.11	0.83	3.06	48.82	1.00	**0.31	51.97	N/A	2.18	64.83	0.67	4.34	52.10	1.00	1.52	40.60
		Cycle 2	48.48	*0.96	2.37	53.22	1.00	0.38	50.85	N/A	1.69	50.44	0.95	2.70	50.56	1.00	1.43	40.60
		Cycle 3	55.88	0.76	9.12	53.50	1.00	0.40	54.69	N/A	6.45	59.88	0.78	9.32	54.29	1.00	4.21	40.60

Note: * Estimate with the highest coefficient of determination for each beam is highlighted in yellow.

** Estimate with the lowest standard deviation for each beam is highlighted in green.

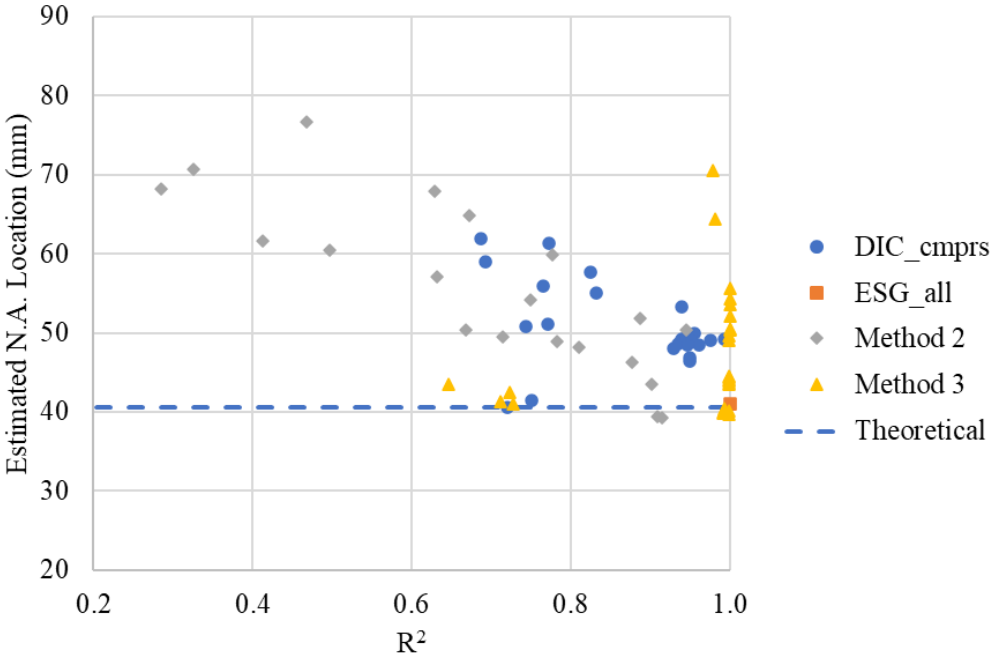

(a)

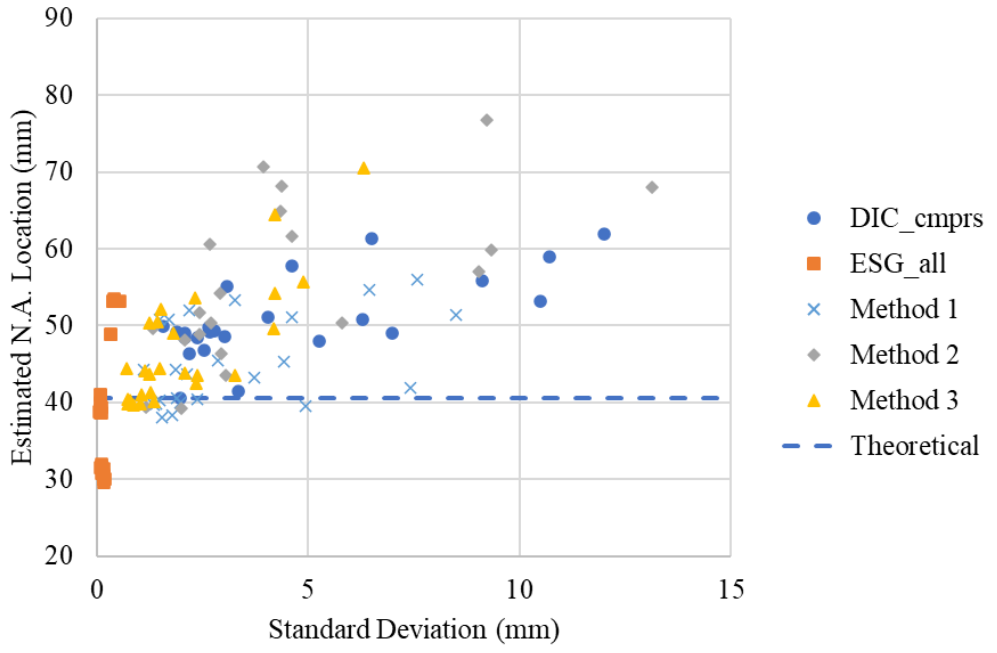

(b)

Figure 4.5. Batch 1 post-corrosion load test N.A. locations, plotted against (a) the corresponding coefficients of determination, and (b) the corresponding standard deviations.

4.4.3. Batch 2 Pre-corrosion Load Test

Based on the preliminary analysis results, the most reliable data groups for this set of loading tests were “DIC_ cmprs” on the DIC side and “ESG_23” on the ESG side. The estimated N.A. locations considering these two data sets individually and combined are presented in Table 4.15 along with their corresponding coefficients of determination and standard deviations.

The same conditional formatting used in the previous tables was applied. The highest coefficient of determination obtained for each beam is highlighted in yellow. Again, since data from only two electrical strain gauges were considered for “ESG_G2&G3” and “Method 3” estimates, their coefficients of determination could not be used to select the best estimates. Between “DIC_cmprs” and “Method 2”, “DIC_cmprs” provided higher coefficients of determination. Method 2 involves merging the strain data and locations from the two faces into one data set and finding the best fit line. A low coefficient of determination means the data do not fit well on the same line. Therefore, it can be inferred that the two faces had different strain distributions during the loading tests.

The lowest standard deviation obtained for each beam among all five data combinations is highlighted in green, and the lowest value among the two-face combined data analyses is highlighted in blue. Similar to the previous batch, using ESG data alone provided the most stable estimates, and among the two-face combined data analyses, Method 3 was the best. The theoretical N.A. location was calculated to be around 38 mm below the top surface of the beam for all these beams. Comparing the estimated N.A. locations associated with the highlighted cells to the theoretical values, it is evident that the closest estimates were in blue, green, and yellow for Beams 1 to 3, respectively. Thus, from this set of the load tests, there is no way to conclude the best screening method to obtain the optimum result.

The estimated N.A. locations for this set of load tests are plotted against the corresponding coefficient of determination and standard deviation values in Figures 4.6 (a) and (b), respectively. Since these estimates were high and varied widely, the figures show a clear trend of converging to the theoretical values as the coefficient of determination increases and as the standard deviation decreases. This verifies that both coefficient of determination and standard deviation can be used for selecting the best estimate. However, it is noted that coefficient of determination is sensitive to the number of data points used to find the best fit function.

Table 4.15. Batch 2 pre-corrosion load test N.A. locations in mm, and the corresponding coefficients of determination and standard deviations.

Beam #	Load	Cycle #	DIC_cmprs			ESG_G2&G3			Method 1			Method 2			Method 3			Theoretical
			Mean	R^2	STDV	Mean	R^2	STDV	Mean	R^2	STDV	Mean	R^2	STDV	Mean	R^2	STDV	
Beam 1	3 kN	Cycle 1	72.79	0.91	8.43	101.62	1.00	30.04	87.21	N/A	22.06	207.26	0.02	863.72	76.56	1.00	7.84	37.8
		Cycle 2	92.42	0.75	12.12	98.61	1.00	25.60	95.51	N/A	20.03	-221.05	0.01	360.32	92.70	1.00	12.94	37.8
		Cycle 3	69.02	0.90	8.43	102.74	1.00	27.54	85.88	N/A	20.37	120.26	0.09	43.19	75.32	1.00	7.99	37.8
	4 kN	Cycle 1	66.98	0.95	6.67	65.91	1.00	2.92	66.44	N/A	5.15	114.60	0.11	30.76	66.43	1.00	4.82	37.8
		Cycle 2	90.18	0.91	10.86	66.34	1.00	2.93	78.26	N/A	7.95	4316.53	0.00	17166.45	81.87	1.00	7.31	37.8
		Cycle 3	61.34	0.92	7.94	69.05	1.00	2.84	65.20	N/A	5.96	79.19	0.30	19.10	63.75	1.00	5.58	37.8
	5 kN	Cycle 1	58.97	0.97	5.19	59.67	1.00	1.45	59.32	N/A	3.81	77.68	0.28	15.26	59.08	1.00	3.49	37.8
		Cycle 2	77.55	0.85	8.39	60.39	1.00	1.14	68.97	N/A	5.99	202.08	0.02	627.13	70.92	1.00	5.04	37.8
		Cycle 3	54.75	0.96	5.35	62.51	1.00	1.04	58.63	N/A	3.85	62.40	0.58	10.02	57.56	1.00	3.42	37.8
	6 kN	Cycle 1	58.69	*0.97	4.28	57.99	1.00	0.43	58.34	N/A	3.04	71.14	0.42	7.89	58.31	1.00	2.56	37.8
		Cycle 2	73.05	0.88	6.16	58.87	1.00	**0.36	65.96	N/A	4.37	140.82	0.05	39.58	67.17	1.00	3.31	37.8
		Cycle 3	53.24	0.97	3.09	60.94	1.00	0.65	57.09	N/A	2.24	57.44	0.76	4.07	56.25	1.00	***2.03	37.8
Beam 2	3 kN	Cycle 1	-1.18	0.87	3.38	29.24	1.00	1.03	14.03	N/A	2.50	18.23	0.46	1.09	20.46	1.00	1.25	38.0
		Cycle 2	-25.19	0.90	10.80	36.51	1.00	0.84	5.66	N/A	7.66	14.36	0.34	1.51	17.11	1.00	2.39	38.0
		Cycle 3	-5.66	0.75	10.39	37.68	1.00	0.80	16.01	N/A	7.37	18.69	0.39	1.98	23.24	1.00	2.50	38.0
		Cycle 4	-31.84	0.83	18.23	38.28	1.00	0.80	3.22	N/A	12.90	15.26	0.19	1.12	18.31	1.00	1.97	38.0
	4 kN	Cycle 1	2.74	0.90	2.23	31.95	1.00	0.65	17.35	N/A	1.65	20.76	0.44	0.83	23.66	1.00	0.92	38.0
		Cycle 2	-13.37	0.92	7.53	38.61	1.00	0.45	12.62	N/A	5.33	17.11	0.36	0.78	21.51	1.00	1.09	38.0
		Cycle 3	2.72	0.84	3.21	39.53	1.00	0.36	21.13	N/A	2.29	20.73	0.42	0.85	26.22	1.00	1.04	38.0
		Cycle 4	-23.23	0.91	13.13	40.03	1.00	0.35	8.40	N/A	9.29	18.10	0.19	0.88	23.26	1.00	1.51	38.0
	5 kN	Cycle 1	8.12	0.91	1.90	35.76	1.00	1.21	21.94	N/A	1.59	22.86	0.45	0.73	26.99	1.00	1.01	38.0
		Cycle 2	-2.81	0.94	4.07	39.86	1.00	0.28	18.52	N/A	2.88	19.82	0.39	0.71	25.29	1.00	0.88	38.0
		Cycle 3	7.64	0.88	2.91	40.50	1.00	0.22	24.07	N/A	2.07	22.45	0.43	1.01	28.43	1.00	1.13	38.0
		Cycle 4	-4.12	0.96	7.37	40.87	1.00	0.20	18.37	N/A	5.21	20.91	0.22	1.20	27.09	1.00	1.46	38.0

Table 4.15. Continued.

Beam 2	**6 kN**	Cycle 1	8.40	0.91	2.53	36.30	1.00	0.37	22.35	N/A	1.81	23.16	0.45	0.87	27.47	1.00	***0.68	38.0
		Cycle 2	1.04	0.95	3.14	40.74	1.00	0.18	20.89	N/A	2.23	20.74	0.40	0.73	26.60	1.00	0.91	38.0
		Cycle 3	9.62	0.89	2.45	41.14	1.00	0.16	25.38	N/A	1.73	23.55	0.43	0.88	29.86	1.00	0.94	38.0
		Cycle 4	5.96	*0.98	2.56	41.37	1.00	**0.13	23.66	N/A	1.82	22.13	0.27	0.75	28.39	1.00	1.02	38.0
Beam 3	**3 kN**	Cycle 1	31.04	0.99	2.93	79.80	1.00	17.78	55.42	N/A	12.74	32.09	0.92	2.73	40.40	1.00	2.49	37.6
		Cycle 2	27.45	0.97	2.40	56.43	1.00	2.98	41.94	N/A	2.70	28.72	0.90	2.12	35.57	1.00	1.88	37.6
		Cycle 3	19.12	0.96	2.47	74.64	1.00	9.51	46.88	N/A	6.95	23.65	0.57	1.57	31.07	1.00	1.64	37.6
	4 kN	Cycle 1	35.33	0.99	2.50	53.21	1.00	3.17	44.27	N/A	2.86	36.20	0.96	2.34	41.70	1.00	1.66	37.6
		Cycle 2	28.53	0.98	1.63	49.91	1.00	1.08	39.22	N/A	1.38	29.84	0.90	1.41	36.05	1.00	1.12	37.6
		Cycle 3	23.13	0.97	2.17	57.79	1.00	2.37	40.46	N/A	2.28	26.87	0.62	1.53	34.13	1.00	1.32	37.6
	5 kN	Cycle 1	36.37	1.00	1.62	47.10	1.00	0.93	41.74	N/A	1.32	36.95	0.97	1.65	40.88	1.00	1.02	37.6
		Cycle 2	29.54	0.99	1.72	46.93	1.00	0.65	38.23	N/A	1.30	30.80	0.90	1.39	36.41	1.00	1.04	37.6
		Cycle 3	25.03	0.99	2.24	52.14	1.00	1.17	38.59	N/A	1.79	28.32	0.64	1.69	35.05	1.00	1.55	37.6
	6 kN	Cycle 1	37.21	*1.00	1.92	44.90	1.00	0.28	41.05	N/A	1.37	37.55	0.95	1.88	40.83	1.00	1.04	37.6
		Cycle 2	30.11	0.99	1.75	45.35	1.00	**0.20	37.73	N/A	1.24	31.37	0.88	1.42	36.68	1.00	1.02	37.6
		Cycle 3	24.68	0.99	1.38	49.57	1.00	0.22	37.12	N/A	0.99	28.14	0.60	0.92	34.75	1.00	***0.90	37.6

Note: * Estimate with the highest coefficient of determination for each beam is highlighted in yellow.

** Estimate with the lowest standard deviation for each beam is highlighted in green.

*** Estimate with the lowest standard deviation among the two-face combined data analyses is highlighted in blue.

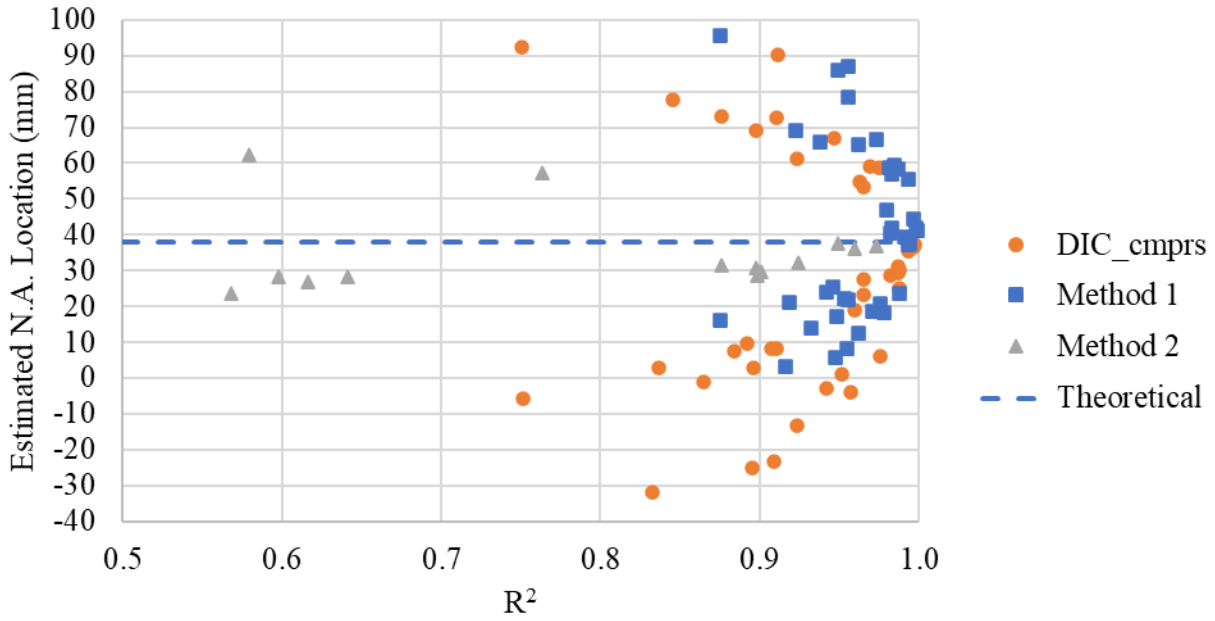

(a)

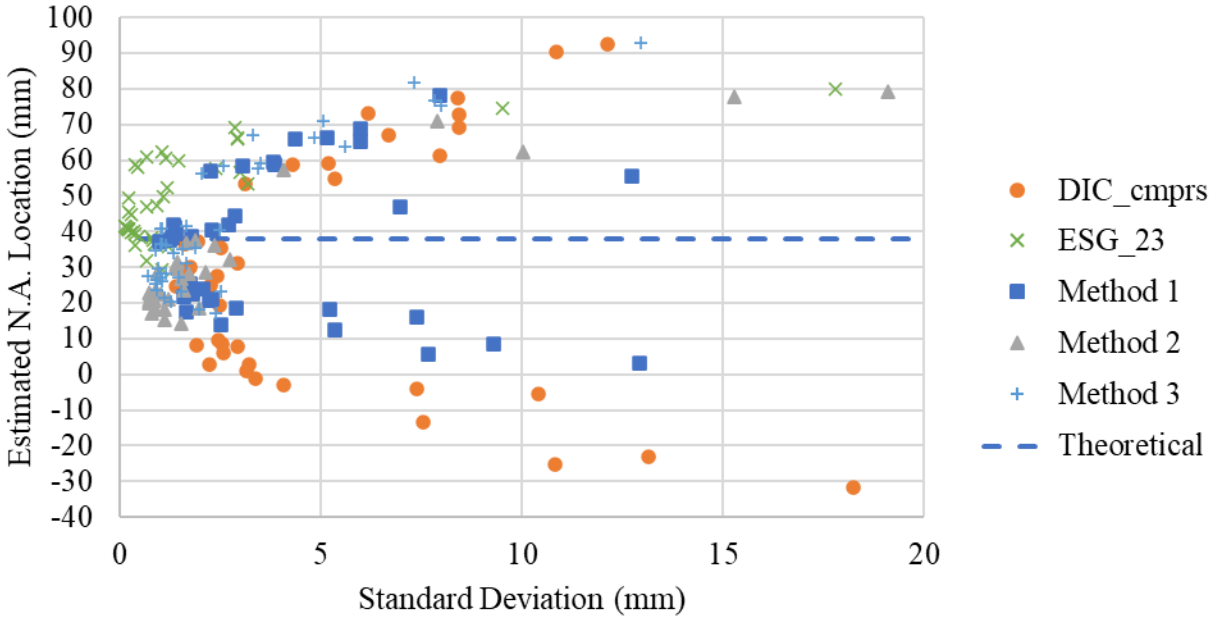

(b)

Figure 4.6. Batch 2 pre-corrosion load test N.A. locations, plotted against (a) the corresponding coefficients of determination, and (b) the corresponding standard deviations.

4.4.4. Batch 2 First Post-corrosion Load Test

In the post-corrosion load tests for Batch 2, each beam had three working electrical strain gauges. The DIC data in the compression zone ("DIC_cmprs") and all the ESG data ("ESG_all") were combined using Methods 1 to 3 to estimate the N.A. locations. The results and the corresponding coefficients of determination and standard deviations are presented in Table 4.16. The same conditional formatting used in the previous tables was applied. For Beam 1, the cell highlighted in yellow, which is the estimate that has the highest coefficient of determination, is the closest to the theoretical value. For Beam 2, the estimate with the highest coefficient of determination was obtained using Method 3, and it also had the lowest standard deviation among the estimates obtained using two-face combined data. This estimate is closer to the theoretical value than the estimate obtained using ESG data alone. For the last beam, the estimate with the lowest standard deviation among all five data combinations was from Method 2, and this estimate is better than the one selected based on the highest coefficient of determination (although still not close to the theoretical value).

The estimated N.A. locations for this set of load tests are plotted against the corresponding coefficient of determination and standard deviation values in Figures 4.7 (a) and (b), respectively. The same convergence trend is observed for this set of the load tests. Overall, however, the estimated N.A. locations from this set differed greatly from the theoretical values. As discussed in the preliminary analysis in Appendix F, the high difference might be due to the type of adhesive used to attach the strain gauges, the unevenness of the surface, and the slenderness of the beams (i.e., twisting). This batch of beams was not loaded to failure during this set of the load tests. The attached strain gauges and the DIC speckle pattern were ground off to create a smooth surface. Four new electrical strain gauges were attached on each side of the beam using the adhesive provided by the manufacturer of the gauges. Then, another set of loading tests was performed.

Table 4.16. Batch 2 first post-corrosion load test N.A. locations in mm, and the corresponding coefficients of determination and standard deviations.

Beam #	Load	Cycle #	DIC_cmprs			ESG_all			Method 1			Method 2			Method 3			Theoretical
			Mean	R^2	STDV	Mean	R^2	STDV	Mean	R^2	STDV	Mean	R^2	STDV	Mean	R^2	STDV	
Beam 1	3 kN	Cycle 1	130.91	0.13	543.26	18.40	0.54	0.73	74.65	N/A	384.14	60.46	0.17	106.70	8.38	0.45	4.19	34.50
		Cycle 2	-903.58	0.11	7698.02	-739.27	0.09	597.21	-821.42	N/A	5459.68	-148.53	0.25	94.88	-149.16	0.58	562.65	34.50
		Cycle 3	44.72	0.38	17.37	28.63	0.77	**0.10	36.67	N/A	12.28	91.64	0.12	11.09	29.39	0.77	0.53	34.50
		Cycle 4	33.48	0.74	6.85	-489.31	0.08	2757.72	-227.91	N/A	1950.01	36.06	0.82	6.04	80.01	0.74	8.98	34.50
	4 kN	Cycle 1	-76.67	0.07	569.82	21.72	0.57	1.01	-27.47	N/A	402.92	549.78	0.02	3309.68	15.83	0.53	2.68	34.50
		Cycle 2	162.51	0.30	157.13	124.07	0.57	4.11	143.29	N/A	111.14	-305.65	0.02	4286.31	257.95	0.48	29.44	34.50
		Cycle 3	48.59	0.56	9.59	29.29	0.78	0.12	38.94	N/A	6.78	89.82	0.18	5.19	30.59	0.79	***0.36	34.50
		Cycle 4	34.69	*0.87	4.22	158.42	0.22	17.67	96.55	N/A	12.85	40.41	0.83	5.78	65.45	0.83	5.27	34.50
Beam 2	3 kN	Cycle 1	72.45	0.71	11.27	57.56	0.91	0.87	65.00	N/A	7.99	54.91	0.98	2.75	56.47	0.98	1.93	34.80
		Cycle 2	20.28	0.85	6.67	71.27	0.94	2.61	45.77	N/A	5.06	23.72	0.93	3.84	36.85	0.99	3.15	34.80
		Cycle 3	26.92	0.73	10.66	73.12	0.95	3.70	50.02	N/A	7.98	26.79	0.93	4.37	40.01	0.99	3.69	34.80
	4 kN	Cycle 1	56.55	0.84	4.55	53.73	0.96	**0.22	55.14	N/A	3.22	49.74	0.98	1.72	51.44	0.99	1.03	34.80
		Cycle 2	18.93	0.93	3.37	59.37	0.98	0.80	39.15	N/A	2.45	23.07	0.92	2.26	35.39	1.00	1.66	34.80
		Cycle 3	21.37	0.89	3.25	60.16	0.98	0.89	40.77	N/A	2.38	25.24	0.92	1.94	37.35	*1.00	***0.40	34.80
Beam 3	3 kN	Cycle 1	-2028.67	0.14	10378.97	-19.15	0.84	1.66	-1023.91	N/A	7339.04	63.61	0.64	1.93	121.05	*0.92	4.31	34.40
		Cycle 2	46.69	0.32	574.14	-19.09	0.79	2.98	13.80	N/A	405.98	27.82	0.81	2.35	67.07	0.84	4.82	34.40
		Cycle 3	46.54	0.07	196.70	-20.56	0.77	3.28	12.99	N/A	139.11	27.75	0.72	2.54	81.44	0.71	5.75	34.40
		Cycle 4	22.14	0.12	79.06	-21.88	0.76	3.63	0.13	N/A	55.96	20.47	0.89	1.63	57.51	0.74	4.26	34.40
	4 kN	Cycle 1	-237.11	0.25	386.76	-29.70	0.67	1.05	-133.40	N/A	273.48	62.66	0.65	***0.92	128.15	0.82	8.05	34.40
		Cycle 2	-85.84	0.22	361.39	-45.12	0.61	1.85	-65.48	N/A	255.55	32.59	0.80	2.14	73.60	0.84	3.61	34.40
		Cycle 3	12.78	0.05	277.49	-52.36	0.58	3.97	-19.79	N/A	196.24	30.29	0.72	1.79	76.24	0.80	3.82	34.40
		Cycle 4	44.43	0.14	51.18	-56.75	0.55	4.32	-6.16	N/A	36.32	25.18	0.90	1.54	63.68	0.81	3.33	34.40

Note: * Estimate with the highest coefficient of determination for each beam is highlighted in yellow.

** Estimate with the lowest standard deviation for each beam is highlighted in green.

*** Estimate with the lowest standard deviation among the two-face combined data analyses is highlighted in blue.

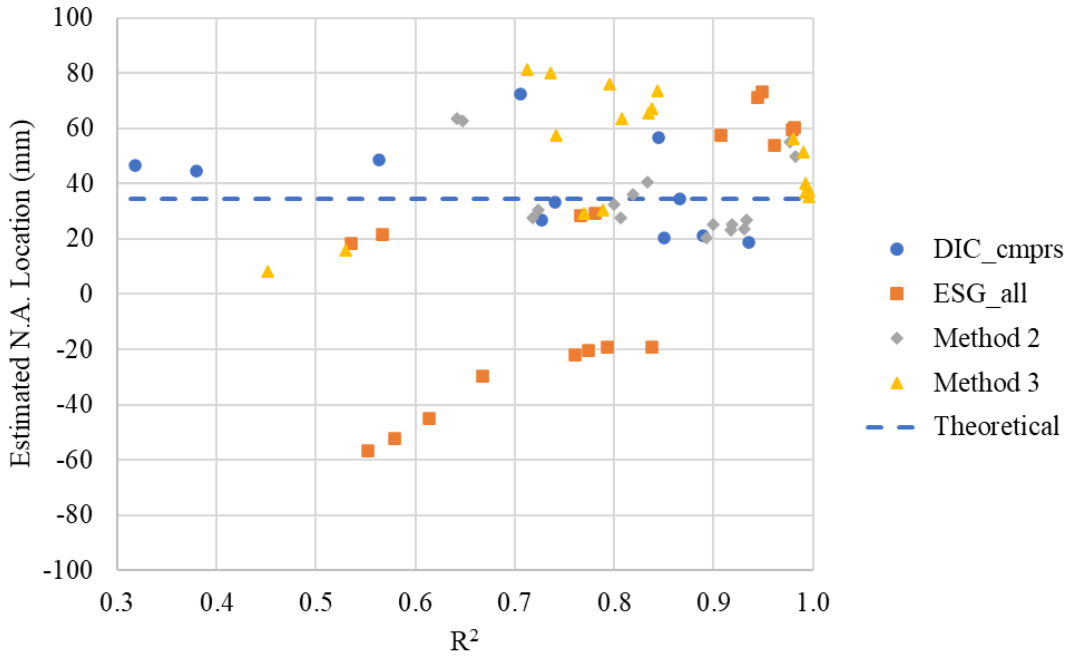

(a)

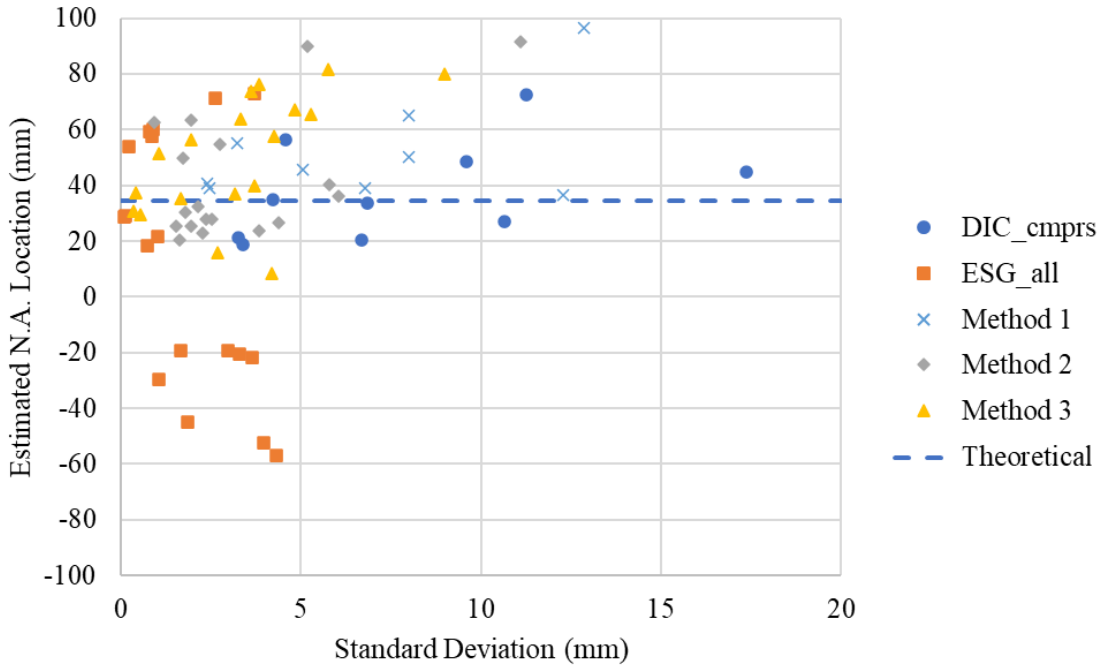

(b)

Figure 4.7. Batch 2 first post-corrosion load test N.A. locations, plotted against (a) the corresponding coefficients of determination, and (b) the corresponding standard deviations.

4.4.5. Batch 2 Second Post-corrosion Load Test

Based on the preliminary analysis results, the top gauges negatively affected the accuracy of the results, so the data from the top gauges were excluded when combining the data from two faces. The estimated N.A. locations and the corresponding coefficients of determination and standard deviations are presented in Table 4.17. The same conditional formatting rules described earlier were also applied to this table.

Since strain gauge locations were the same on both sides, the best fit line obtained using Methods 2 and 3 were the same. Also, the estimated N.A. locations and the corresponding standard deviations were the same. However, Method 2 resulted in much lower coefficients of determination compared to Method 3, because Method 2 used 6 data points to derive the best fit line and Method 3 only used three average strain values from the two faces. The coefficients of determination for the single face estimates were also quite close to one, which means the strains were linearly distributed on each face. However, low coefficients of determination for Method 2 indicates the strains on the two faces were different. The gauges were placed at the same locations on both sides. If the readings were the same, the coefficients of determination using Method 2 would be as high as the ones obtained using data from each individual face. If the difference in strain readings was caused by eccentric loading, it was expected that the estimates on the two faces would lie on opposite sides of the theoretical values. However, for this set of load tests, the estimates from both faces were consistently higher than the theoretical values, and the estimates made using two-face combined data were not obviously better than those obtained using data from each face individually. Therefore, it is suspected that the difficulty in obtaining accurate estimates was caused by more complicated mechanisms such as twisting due to the slenderness effect.

The estimated N.A. locations for this set of load tests are plotted against the corresponding coefficient of determination and standard deviation values in Figures 4.8 (a) and (b), respectively. The convergence trend was obvious from these figures. But this batch of the estimates did not get very close to the theoretical value even when the coefficients of determination were close to one and when the standard deviations were close to zero. Many estimates with high coefficients of determination still had high errors.

Table 4.17. Batch 2 second post-corrosion load test N.A. locations in mm, and the corresponding coefficients of determination and standard deviations.

Beam #	Load	Cycle #	Face 1			Face 2			Two Face Method 1			Two Face Method 2			Two Face Method 3			Theoretical
			Mean	R2	STDV	Mean	R2	STDV	Mean	R2	STDV	Mean	R2	STDV	Mean	R2	STDV	
Beam 1	3 kN	Cycle 1	74.28	1.00	3.52	65.07	0.95	2.09	69.68	N/A	2.80	68.67	0.60	2.51	68.67	0.98	2.51	35.90
		Cycle 2	57.88	1.00	1.40	78.70	0.97	1.87	68.29	N/A	1.64	70.20	0.15	1.75	70.20	0.98	1.75	35.90
		Cycle 3	65.59	1.00	1.42	69.84	0.98	1.19	67.71	N/A	1.30	68.07	0.38	1.26	68.07	0.99	1.26	35.90
		Cycle 4	62.04	*1.00	4.58	68.01	0.99	5.48	65.03	N/A	5.03	65.29	0.58	5.09	65.29	1.00	5.09	35.90
		Cycle 5	55.36	1.00	3.19	71.09	0.98	5.78	63.23	N/A	4.48	63.91	0.34	4.65	63.91	1.00	4.65	35.90
		Cycle 6	63.41	0.98	5.73	70.67	0.99	6.26	67.04	N/A	6.00	67.47	0.44	6.09	67.47	0.98	6.09	35.90
		Cycle 7	65.88	1.00	6.59	70.32	0.99	5.92	68.10	N/A	6.26	68.44	0.41	6.25	68.44	0.99	6.25	35.90
		Cycle 8	69.36	1.00	6.88	72.37	0.99	6.78	70.86	N/A	6.83	71.11	0.40	6.85	71.11	0.99	6.85	35.90
		Cycle 9	70.72	1.00	7.26	68.80	0.99	5.79	69.76	N/A	6.52	69.61	0.62	6.38	69.61	0.99	6.38	35.90
		Cycle 10	69.82	1.00	7.65	72.97	0.99	6.85	71.40	N/A	7.25	71.64	0.40	7.20	71.64	1.00	7.20	35.90
		Cycle 11	78.55	1.00	9.95	71.84	0.99	6.39	75.19	N/A	8.17	74.57	0.63	7.74	74.57	0.99	7.74	35.90
	4 kN	Cycle 4	52.73	1.00	0.60	58.32	0.99	0.33	55.52	N/A	0.47	55.67	0.75	0.44	55.67	1.00	0.44	35.90
		Cycle 5	48.25	1.00	0.52	60.24	0.99	0.37	54.25	N/A	0.45	54.55	0.52	0.46	54.55	1.00	0.46	35.90
		Cycle 6	52.47	0.99	0.45	58.98	0.99	0.40	55.72	N/A	0.42	55.97	0.64	0.41	55.97	0.99	0.41	35.90
		Cycle 7	52.67	1.00	2.08	57.74	0.99	2.01	55.20	N/A	2.04	55.47	0.63	2.06	55.47	1.00	2.06	35.90
		Cycle 8	54.48	1.00	2.47	58.56	0.99	2.26	56.52	N/A	2.36	56.74	0.64	2.37	56.74	1.00	2.37	35.90
		Cycle 9	55.28	1.00	2.42	56.47	0.99	2.12	55.87	N/A	2.27	55.92	0.82	2.26	55.92	1.00	2.26	35.90
		Cycle 10	54.75	1.00	2.40	58.80	0.99	2.39	56.78	N/A	2.40	57.01	0.62	2.41	57.01	1.00	2.41	35.90
		Cycle 11	58.77	1.00	3.05	57.69	0.99	2.37	58.23	N/A	2.71	58.16	0.83	2.66	58.16	1.00	2.66	35.90
	5 kN	Cycle 7	48.76	1.00	0.14	53.73	0.99	0.17	51.25	N/A	0.16	51.45	0.71	0.14	51.45	1.00	0.14	35.90
		Cycle 8	49.45	1.00	0.21	53.63	0.99	0.20	51.54	N/A	0.21	51.72	0.74	0.20	51.72	1.00	0.20	35.90
		Cycle 9	49.56	1.00	1.04	51.34	1.00	1.02	50.45	N/A	1.03	50.50	0.89	1.03	50.50	1.00	1.03	35.90
		Cycle 10	48.65	1.00	1.20	52.78	1.00	1.23	50.72	N/A	1.22	50.89	0.75	1.23	50.89	1.00	1.23	35.90
		Cycle 11	51.32	1.00	1.44	51.97	1.00	1.16	51.64	N/A	1.30	51.66	0.91	1.29	51.66	1.00	1.29	35.90

Table 4.17. Continued.

Beam #	Load	Cycle #	Face 1			Face 2			Two Face Method 1			Two Face Method 2			Two Face Method 3			Theoretical
			Mean	R2	STDV	Mean	R2	STDV	Mean	R2	STDV	Mean	R2	STDV	Mean	R2	STDV	
Beam 1	6 kN	Cycle 9	47.18	1.00	0.12	49.28	1.00	0.11	48.23	N/A	0.11	48.28	0.91	**0.10	48.28	1.00	**0.10	35.90
		Cycle 10	45.91	1.00	0.14	50.06	1.00	0.14	47.98	N/A	0.14	48.11	0.82	0.13	48.11	1.00	0.13	35.90
		Cycle 11	47.57	1.00	0.81	48.87	1.00	0.68	48.22	N/A	0.75	48.26	0.93	0.75	48.26	1.00	0.75	35.90
Beam 2	3 kN	Cycle 1	56.32	0.98	0.83	-37.80	0.75	2.78	9.26	N/A	1.81	-1219.92	0.00	685.20	-1219.92	0.06	685.20	36.20
		Cycle 2	53.17	0.99	0.47	235.00	0.54	47.60	144.08	N/A	24.04	81.58	0.49	2.49	81.58	0.99	2.49	36.20
		Cycle 3	50.18	0.99	2.03	185.01	0.67	82.94	117.59	N/A	42.48	73.56	0.56	7.72	73.56	1.00	7.72	36.20
		Cycle 4	52.92	0.99	2.92	326.51	0.45	1982.43	189.71	N/A	992.68	90.52	0.27	15.66	90.52	0.99	15.66	36.20
		Cycle 5	52.79	0.99	2.87	220.44	0.68	152.86	136.62	N/A	77.87	76.86	0.62	10.41	76.86	1.00	10.41	36.20
		Cycle 6	52.47	1.00	2.68	383.51	0.58	552.14	217.99	N/A	277.41	77.91	0.61	10.33	77.91	0.99	10.33	36.20
		Cycle 7	52.97	1.00	2.96	412.83	0.62	667.89	232.90	N/A	335.42	78.22	0.63	11.16	78.22	0.99	11.16	36.20
		Cycle 8	53.23	1.00	2.70	227.55	0.66	171.53	140.39	N/A	87.12	73.36	0.66	8.52	73.36	0.99	8.52	36.20
		Cycle 9	52.38	1.00	2.66	209.47	0.67	145.33	130.92	N/A	74.00	72.98	0.70	8.71	72.98	0.99	8.71	36.20
	4 kN	Cycle 3	46.59	0.99	0.13	90.43	0.96	2.85	68.51	N/A	1.49	59.71	0.79	0.64	59.71	1.00	0.64	36.20
		Cycle 4	47.22	0.99	0.22	105.11	0.95	3.79	76.17	N/A	2.00	64.56	0.56	0.87	64.56	1.00	0.87	36.20
		Cycle 5	46.56	1.00	1.04	81.51	0.97	7.61	64.03	N/A	4.33	57.73	0.85	2.55	57.73	1.00	2.55	36.20
		Cycle 6	46.54	1.00	1.17	85.70	0.96	10.08	66.12	N/A	5.62	58.37	0.84	3.00	58.37	1.00	3.00	36.20
		Cycle 7	46.54	1.00	1.12	83.15	0.97	9.35	64.85	N/A	5.23	57.82	0.85	2.86	57.82	1.00	2.86	36.20
		Cycle 8	47.05	1.00	1.17	78.55	0.97	8.81	62.80	N/A	4.99	56.32	0.83	2.72	56.32	1.00	2.72	36.20
		Cycle 9	46.50	1.00	1.08	78.00	0.97	8.29	62.25	N/A	4.69	56.08	0.86	2.62	56.08	1.00	2.62	36.20
	5 kN	Cycle 5	44.41	1.00	0.11	66.57	0.99	0.72	55.49	N/A	0.42	52.33	0.91	0.27	52.33	1.00	0.27	36.20
		Cycle 6	43.85	1.00	0.15	65.97	0.99	0.82	54.91	N/A	0.49	51.69	0.91	0.34	51.69	1.00	0.34	36.20
		Cycle 7	43.58	1.00	0.66	63.35	1.00	3.23	53.46	N/A	1.95	50.78	0.92	1.39	50.78	*1.00	1.39	36.20
		Cycle 8	44.19	1.00	0.60	60.82	0.99	2.75	52.50	N/A	1.67	50.01	0.89	1.19	50.01	1.00	1.19	36.20
		Cycle 9	43.66	1.00	0.61	60.25	0.99	3.16	51.96	N/A	1.89	49.61	0.92	1.33	49.61	1.00	1.33	36.20

Table 4.17. Continued.

Beam #	Load	Cycle #	Face 1			Face 2			Two Face Method 1			Two Face Method 2			Two Face Method 3			Theoretical
			Mean	R2	STDV	Mean	R2	STDV	Mean	R2	STDV	Mean	R2	STDV	Mean	R2	STDV	
Beam 2	6 kN	Cycle 7	41.79	1.00	0.10	55.40	1.00	0.51	48.59	N/A	0.30	47.08	0.95	0.23	47.08	1.00	0.23	36.20
		Cycle 8	42.66	1.00	**0.08	53.79	1.00	0.38	48.23	N/A	0.23	46.88	0.92	***0.16	46.88	1.00	***0.16	36.20
		Cycle 9	41.97	1.00	0.50	52.66	1.00	1.77	47.31	N/A	1.13	46.13	0.95	0.91	46.13	1.00	0.91	36.20
Beam 3	3 kN	Cycle 1	230.02	0.33	325.27	-72.68	0.97	3.41	78.67	N/A	164.34	571.63	0.02	5315.71	571.63	0.09	5315.71	35.60
		Cycle 2	54.06	1.00	0.27	-519.20	0.90	110.09	-232.57	N/A	55.18	96.46	0.40	1.70	96.46	1.00	1.70	35.60
		Cycle 3	53.17	1.00	1.08	-928.67	0.72	3840.56	-437.75	N/A	1920.82	88.53	0.49	8.83	88.53	1.00	8.83	35.60
		Cycle 4	53.65	1.00	1.36	-8131.10	0.62	34494.87	-4038.73	N/A	17248.11	97.16	0.40	13.02	97.16	1.00	13.02	35.60
		Cycle 5	53.40	1.00	1.41	-585.43	0.59	2697.69	-266.02	N/A	1349.55	96.88	0.40	13.11	96.88	1.00	13.11	35.60
		Cycle 6	56.94	1.00	1.65	-161.06	0.91	95.48	-52.06	N/A	48.56	124.40	0.26	25.53	124.40	1.00	25.53	35.60
		Cycle 7	58.21	0.98	1.98	619.24	0.70	4301.11	338.73	N/A	2151.54	116.06	0.34	20.94	116.06	0.99	20.94	35.60
		Cycle 8	51.44	1.00	1.32	-119.02	0.51	1278.00	-33.79	N/A	639.66	86.64	0.47	9.73	86.64	1.00	9.73	35.60
	4 kN	Cycle 3	50.48	1.00	0.18	231.44	0.91	11.33	140.96	N/A	5.76	73.34	0.64	0.44	73.34	1.00	0.44	35.60
		Cycle 4	50.22	1.00	0.17	248.89	0.90	15.51	149.55	N/A	7.84	74.31	0.63	0.62	74.31	1.00	0.62	35.60
		Cycle 5	49.56	1.00	0.85	214.14	0.91	84.81	131.85	N/A	42.83	70.98	0.67	4.04	70.98	1.00	4.04	35.60
		Cycle 6	51.96	1.00	1.17	434.10	0.56	1486.73	243.03	N/A	743.95	79.55	0.55	6.04	79.55	1.00	6.04	35.60
		Cycle 7	52.33	0.99	1.40	266.14	0.90	159.17	159.24	N/A	80.28	76.84	0.65	6.00	76.84	1.00	6.00	35.60
		Cycle 8	47.59	1.00	0.90	158.61	0.94	43.51	103.10	N/A	22.20	65.92	0.70	3.53	65.92	1.00	3.53	35.60
	5 kN	Cycle 5	47.71	1.00	**0.09	118.04	0.97	1.78	82.87	N/A	0.94	63.13	0.76	***0.24	63.13	1.00	***0.24	35.60
		Cycle 6	49.07	1.00	0.18	154.76	0.96	6.14	101.91	N/A	3.16	67.06	0.69	0.54	67.06	1.00	0.54	35.60
		Cycle 7	48.55	0.99	0.86	106.80	0.99	12.19	77.67	N/A	6.52	63.42	0.80	2.55	63.42	1.00	2.55	35.60
		Cycle 8	45.11	1.00	0.59	90.55	0.99	8.63	67.83	N/A	4.61	57.21	0.82	1.84	57.21	1.00	1.84	35.60
	6 kN	Cycle 7	46.27	0.99	0.52	77.05	1.00	1.35	61.66	N/A	0.94	56.17	0.88	0.48	56.17	1.00	0.48	35.60
		Cycle 8	43.62	1.00	0.39	70.56	1.00	2.56	57.09	N/A	1.47	52.34	0.89	0.87	52.34	*1.00	0.87	35.60
	7 kN	Cycle 8	38.55	1.00	1.82	50.06	1.00	4.90	44.30	N/A	3.36	43.01	0.95	2.83	43.01	1.00	2.83	35.60

Note: * Estimate with the highest coefficient of determination for each beam is highlighted in yellow.

** Estimate with the lowest standard deviation for each beam is highlighted in green.

*** Estimate with the lowest standard deviation among the two-face combined data analyses is highlighted in blue.

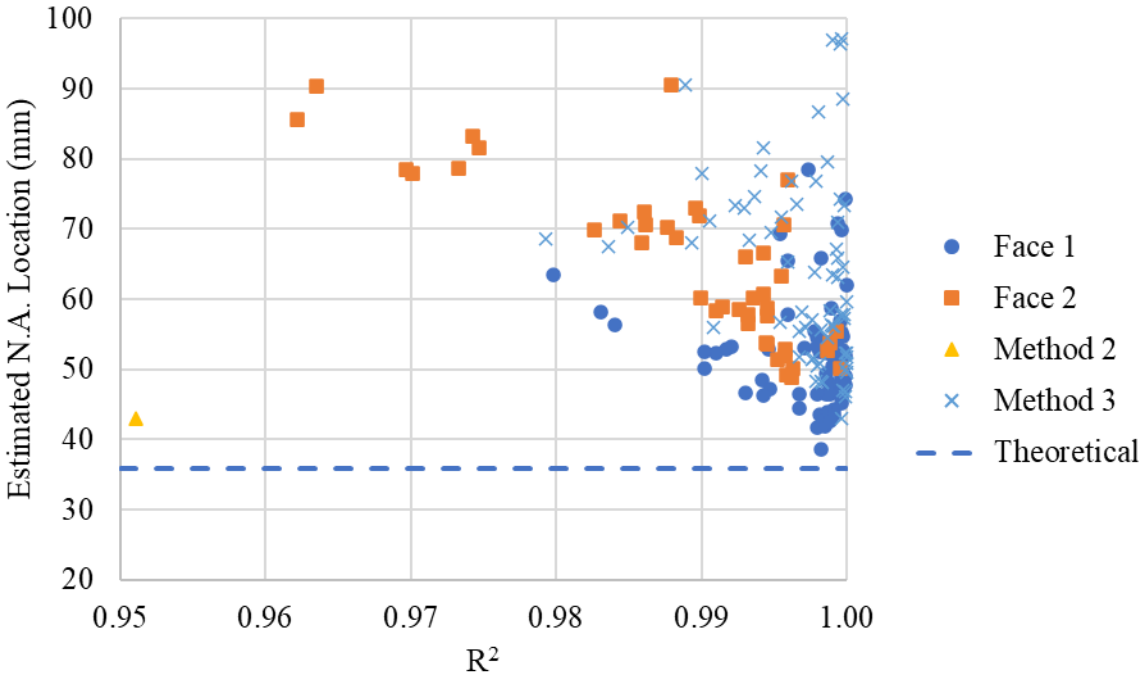

(a)

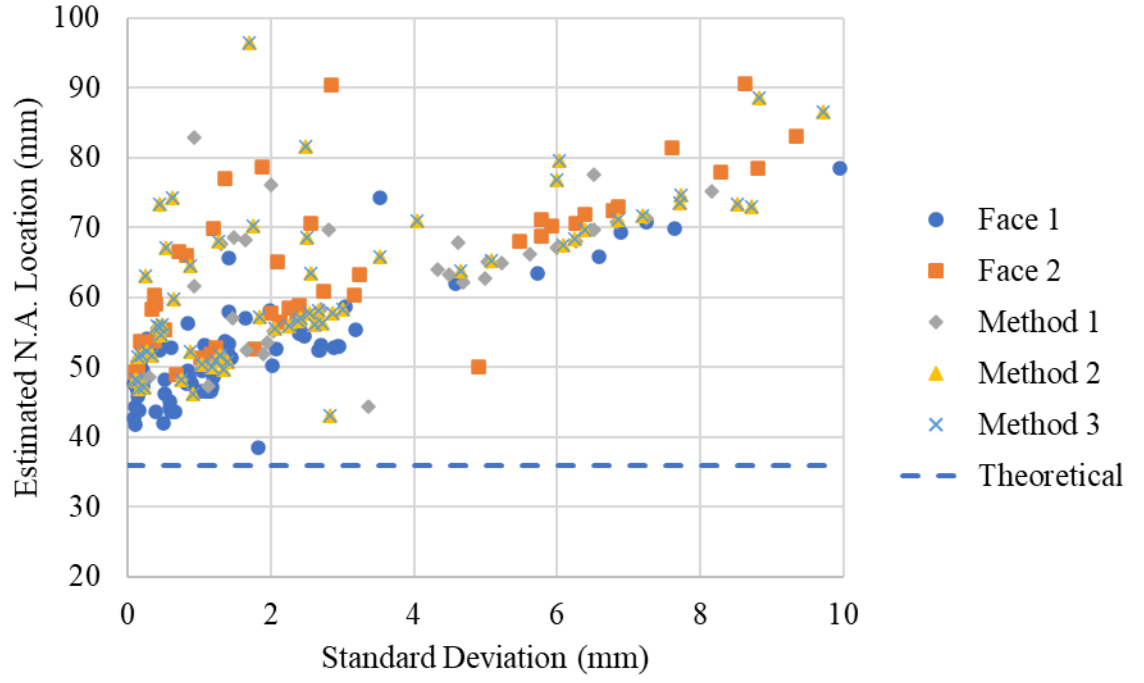

(b)

Figure 4.8. Batch 2 second post-corrosion load test N.A. locations, plotted against (a) the corresponding coefficients of determination, and (b) the corresponding standard deviations.

4.4.6. Batch 3 Pre-corrosion Load Test

Batch 3 beams did not have any issues with the surface smoothness and the type of adhesive used for the electrical strain gauges. The DIC data from the compression zone were combined with all the ESG data for the two-face combined analysis. The results and the corresponding coefficients of determination and standard deviations are presented in Table 4.18. The same formatting rules were applied to this table.

For all three beams, the estimates with the highest coefficients of determination were obtained using Method 3. The coefficients of determination for the estimates obtained using data from each face individually were also high, and the coefficients of determination for Method 2 estimates were low as usual indicating different strain distributions on the two faces. Estimates using ESG data alone had the lowest standard deviation except for Beam 1. For Beam 1, an estimate obtained using Method 2 had the lowest standard deviation, but it was less accurate than the estimate made by Method 3 which had the highest coefficient of determination. For Beams 2 and 3, the estimates closest to the theoretical values were in blue and green, respectively.

The estimated N.A. locations for this set of load tests are plotted against the corresponding coefficient of determination and standard deviation values in Figures 4.9 (a) and (b), respectively. It is obvious that the estimates converge to the theoretical value as the standard deviation of the estimates drops. However, the convergence trend for coefficients of determination is not as clear. Many estimates made by considering ESG data alone and two-face combined using Method 3 had coefficients of determination very close to one but still differed greatly from the theoretical N.A. location.

Table 4.18. Batch 3 pre-corrosion load test N.A. locations in mm, and the corresponding coefficients of determination and standard deviations.

Beam #	Load	Cycle #	DIC_cmprs			ESG_all			Method 1			Method 2			Method 3			Theoretical
			Mean	R^2	STDV	Mean	R^2	STDV	Mean	R^2	STDV	Mean	R^2	STDV	Mean	R^2	STDV	
Beam 1	3 kN	Cycle 1	13.49	0.99	1.59	124.47	0.97	7.80	68.98	N/A	4.69	24.72	0.42	1.00	29.60	*1.00	1.30	38.50
		Cycle 2	22.72	0.98	0.83	115.18	0.95	10.87	68.95	N/A	5.85	26.40	0.69	**0.66	36.69	1.00	0.73	38.50
		Cycle 3	23.91	0.97	0.96	115.93	0.95	9.65	69.92	N/A	5.31	29.98	0.58	1.07	37.74	1.00	1.17	38.50
	4 kN	Cycle 1	14.89	0.99	1.18	55.30	0.86	20.18	35.10	N/A	10.68	24.16	0.58	1.12	26.87	0.98	2.16	38.50
		Cycle 2	22.76	0.99	1.13	84.19	0.98	3.30	53.47	N/A	2.21	26.51	0.71	0.96	35.99	1.00	0.82	38.50
		Cycle 3	23.89	0.98	0.93	82.93	0.98	3.35	53.41	N/A	2.14	29.57	0.62	0.93	36.63	1.00	0.86	38.50
Beam 2	3 kN	Cycle 1	29.05	0.76	4.21	57.04	1.00	0.82	43.05	N/A	2.52	34.58	0.45	2.48	44.18	1.00	1.98	39.20
		Cycle 2	68.96	0.85	7.94	44.29	1.00	0.18	56.62	N/A	4.06	64.38	0.69	5.78	54.30	1.00	2.41	39.20
		Cycle 3	64.55	0.87	5.87	44.09	1.00	0.17	54.32	N/A	3.02	57.17	0.86	3.10	51.69	1.00	1.49	39.20
	4 kN	Cycle 1	32.16	0.87	1.71	56.99	1.00	2.61	44.58	N/A	2.16	36.28	0.55	***1.29	44.74	1.00	1.63	39.20
		Cycle 2	61.50	0.92	4.73	43.54	1.00	0.07	52.52	N/A	2.40	58.05	0.81	3.54	51.20	*1.00	1.67	39.20
		Cycle 3	59.69	0.92	5.13	43.43	1.00	**0.06	51.56	N/A	2.59	53.42	0.90	3.04	49.59	1.00	1.53	39.20
Beam 3	3 kN	Cycle 1	52.64	0.80	7.18	40.44	1.00	0.35	46.54	N/A	3.76	49.76	0.75	5.86	45.96	*1.00	3.02	39.00
		Cycle 2	65.37	0.91	7.08	36.94	1.00	0.12	51.15	N/A	3.60	78.37	0.19	14.34	51.21	1.00	2.99	39.00
		Cycle 3	75.87	0.83	8.61	36.27	1.00	0.14	56.07	N/A	4.38	88.59	0.15	12.42	54.10	1.00	2.58	39.00
	4 kN	Cycle 1	52.35	0.90	3.93	39.22	1.00	0.08	45.78	N/A	2.00	49.40	0.76	2.31	45.28	1.00	***1.50	39.00
		Cycle 2	64.18	0.93	5.59	36.79	1.00	0.06	50.48	N/A	2.83	72.20	0.25	9.27	50.11	1.00	2.20	39.00
		Cycle 3	70.83	0.88	5.12	36.29	1.00	**0.05	53.56	N/A	2.58	77.25	0.22	5.40	51.89	1.00	1.54	39.00

Note: * Estimate with the highest coefficient of determination for each beam is highlighted in yellow.

** Estimate with the lowest standard deviation for each beam is highlighted in green.

*** Estimate with the lowest standard deviation among the two-face combined data analyses is highlighted in blue.

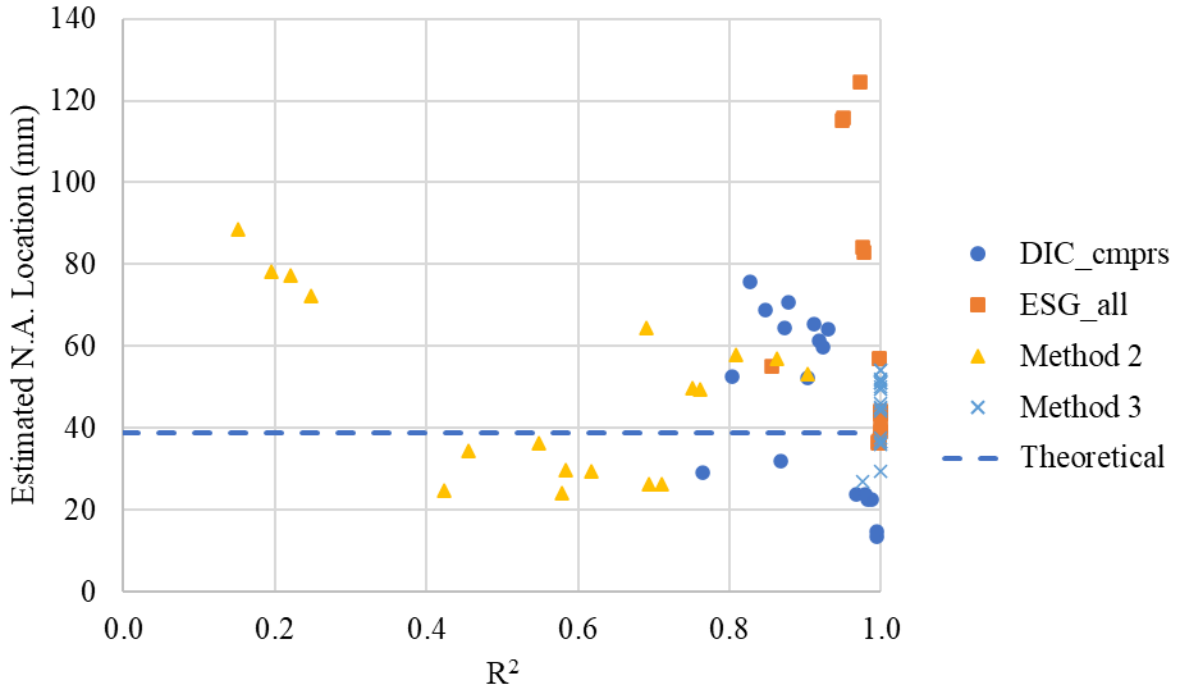

(a)

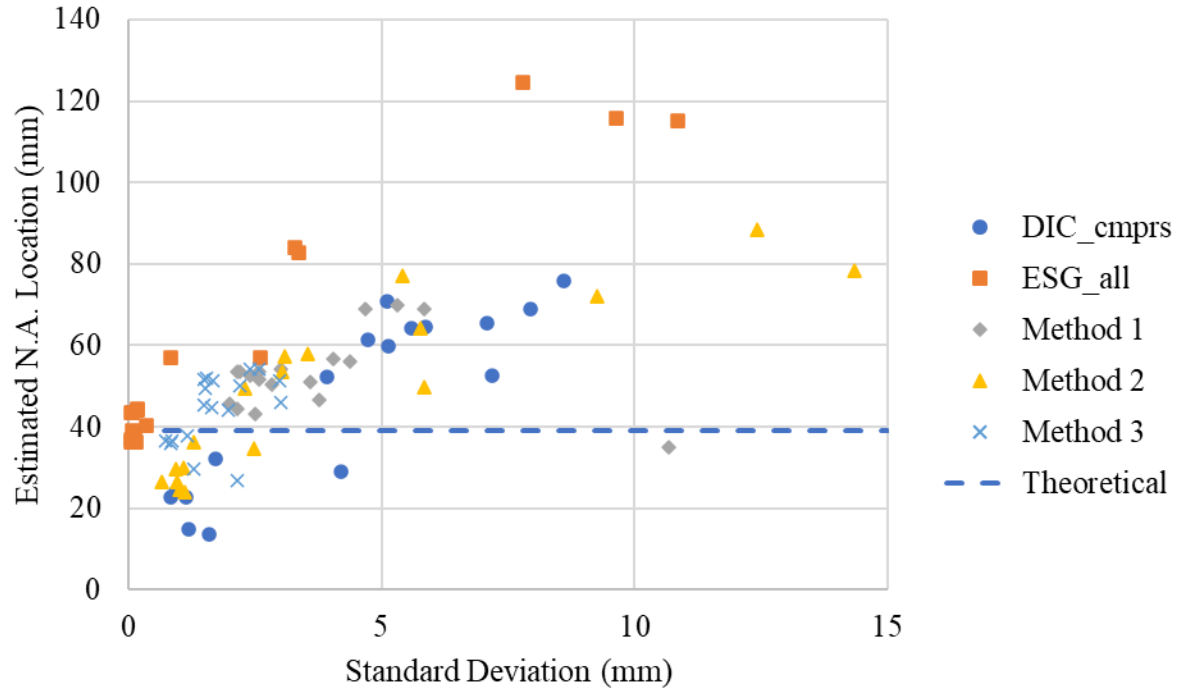

(b)

Figure 4.9. Batch 3 pre-corrosion load test N.A. locations, plotted against (a) the corresponding coefficients of determination, and (b) the corresponding standard deviations.

4.4.7. Batch 3 Post-corrosion Load Test

All electrical strain gauges were still functioning after corrosion. Similar to the analysis conducted for the pre-corrosion load test, the DIC data in the compression zone and all the ESG data were combined for the two-face analysis. The results and the corresponding coefficients of determination and standard deviations are presented in Table 4.19, in which the same conditional formatting rules were applied.

For this set of load tests, the estimates obtained using Method 3 consistently had the highest coefficients of determination, and the estimates obtained using ESG data alone had the lowest standard deviations. Among the estimates made by two-face combined data, the estimates with the lowest standard deviations were generated by Methods 1 or 3. Comparing estimated N.A. locations associated with the cells highlighted in three different colors to the theoretical values, for all three beams, the blue cells were the closest. This means the best estimates can be selected based on the lowest standard deviation among two-face combined estimates.

The estimated N.A. locations for this set of load tests are plotted against the corresponding coefficient of determination and standard deviation values in Figures 4.10 (a) and (b), respectively. The convergence trends are clear in both figures.

Table 4.19. Batch 3 post-corrosion load test N.A. locations in mm, and the corresponding coefficients of determination and standard deviations.

Beam #	Load	Cycle #	DIC_cmprs			ESG_all			Method 1			Method 2			Method 3			Theoretical
			Mean	R2	STDV	Mean	R2	STDV	Mean	R2	STDV	Mean	R2	STDV	Mean	R2	STDV	
Beam 1	3 kN	Cycle 1	32.58	0.86	2.10	75.67	0.97	1.91	54.12	N/A	2.00	41.34	0.43	1.23	52.29	0.99	2.04	37.00
		Cycle 2	29.47	0.90	2.05	65.25	0.99	1.00	47.36	N/A	1.52	39.02	0.43	1.30	45.86	1.00	1.40	37.00
		Cycle 3	25.55	0.90	2.22	64.28	0.99	0.90	44.92	N/A	1.56	36.82	0.36	1.11	45.36	1.00	1.71	37.00
		Cycle 4	32.05	0.96	1.40	63.45	0.99	0.85	47.75	N/A	1.13	39.35	0.52	0.84	46.49	1.00	1.28	37.00
		Cycle 5	25.63	0.95	1.28	57.04	0.99	0.71	41.33	N/A	1.00	34.33	0.49	0.74	40.67	1.00	0.91	37.00
		Cycle 6	29.31	0.99	1.31	49.04	1.00	0.89	39.18	N/A	1.10	34.42	0.83	0.88	36.51	1.00	0.56	37.00
	4 kN	Cycle 1	31.33	0.94	1.38	66.45	0.99	0.55	48.89	N/A	0.96	39.31	0.49	0.84	47.76	1.00	1.22	37.00
		Cycle 2	29.26	0.93	1.05	60.11	0.99	0.30	44.68	N/A	0.68	37.87	0.47	0.68	43.76	1.00	0.84	37.00
		Cycle 3	26.86	0.94	1.70	59.31	0.99	0.28	43.09	N/A	0.99	36.40	0.43	0.94	43.33	1.00	1.28	37.00
		Cycle 4	31.98	0.97	1.47	58.45	0.99	0.44	45.21	N/A	0.95	38.41	0.57	0.93	44.53	1.00	0.98	37.00
		Cycle 5	27.91	0.97	1.18	52.26	1.00	1.06	40.09	N/A	1.12	34.64	0.59	0.82	39.57	1.00	0.94	37.00
		Cycle 6	28.26	0.98	0.94	45.24	1.00	0.56	36.75	N/A	0.75	32.72	0.76	0.52	36.12	1.00	0.46	37.00
	5 kN	Cycle 4	31.76	0.98	0.99	54.78	1.00	0.92	43.27	N/A	0.96	37.62	0.63	0.65	42.61	1.00	0.85	37.00
		Cycle 5	27.97	0.98	1.38	49.38	1.00	0.66	38.68	N/A	1.02	34.07	0.64	0.81	38.32	1.00	0.69	37.00
		Cycle 6	28.27	0.98	0.98	44.34	1.00	**0.12	36.30	N/A	0.55	32.50	0.77	0.71	35.61	1.00	1.38	37.00
	6 kN	Cycle 4	31.84	0.99	0.70	51.97	1.00	0.39	41.91	N/A	0.54	37.00	0.65	0.49	41.71	1.00	0.50	37.00
		Cycle 5	29.16	0.99	0.84	47.42	1.00	0.53	38.29	N/A	0.69	34.35	0.68	0.46	38.21	1.00	***0.41	37.00
		Cycle 6	27.97	0.98	0.83	43.22	1.00	0.26	35.60	N/A	0.54	32.02	0.74	0.61	35.55	*1.00	1.42	37.00
Beam 2	3 kN	Cycle 1	32.57	0.96	1.65	-8535.58	0.06	151684.17	-4251.51	N/A	75842.91	50.02	0.38	2.71	59.35	0.99	2.97	36.80
		Cycle 2	20.42	0.94	2.16	169.90	0.95	22.54	95.16	N/A	12.35	33.41	0.35	1.89	40.65	1.00	2.21	36.80
		Cycle 3	29.68	0.96	1.88	161.26	0.94	21.76	95.47	N/A	11.82	41.88	0.50	2.66	47.84	1.00	2.28	36.80
		Cycle 4	27.82	0.95	1.25	154.94	0.95	19.17	91.38	N/A	10.21	38.04	0.50	1.47	46.10	1.00	1.92	36.80
		Cycle 5	26.44	0.96	1.02	100.31	0.96	6.53	63.37	N/A	3.77	35.28	0.56	1.04	40.92	1.00	1.15	36.80
		Cycle 6	25.08	0.93	0.94	75.04	0.97	3.36	50.06	N/A	2.15	33.73	0.57	0.82	38.29	1.00	0.93	36.80
		Cycle 7	27.65	0.95	0.69	45.35	0.99	0.26	36.50	N/A	0.48	31.77	0.81	0.55	34.73	1.00	0.56	36.80

Table 4.19. Continued.

Beam #	Load	Cycle #	DIC_cmprs			ESG_all			Method 1			Method 2			Method 3			Theoretical
			Mean	R2	STDV	Mean	R2	STDV	Mean	R2	STDV	Mean	R2	STDV	Mean	R2	STDV	
Beam 2	4 kN	Cycle 1	34.65	0.98	1.78	164.08	0.85	12.22	99.36	N/A	7.00	48.35	0.53	2.58	55.07	1.00	2.13	36.80
		Cycle 2	22.84	0.96	1.83	97.52	0.99	2.59	60.18	N/A	2.21	34.28	0.43	1.82	40.38	*1.00	1.66	36.80
		Cycle 3	30.54	0.97	1.80	94.94	0.98	2.91	62.74	N/A	2.36	40.63	0.59	2.01	45.64	1.00	1.64	36.80
		Cycle 4	29.44	0.97	1.57	91.06	0.98	7.56	60.25	N/A	4.57	37.92	0.62	1.56	43.88	1.00	1.25	36.80
		Cycle 5	27.59	0.97	0.89	74.24	0.98	1.62	50.92	N/A	1.25	35.39	0.63	0.85	40.39	1.00	0.87	36.80
		Cycle 6	26.27	0.95	1.62	62.53	0.98	1.28	44.40	N/A	1.45	34.00	0.63	1.38	38.13	1.00	1.19	36.80
		Cycle 7	27.89	0.96	0.59	44.00	0.99	**0.15	35.94	N/A	***0.37	31.76	0.83	0.45	34.69	1.00	0.48	36.80
	5 kN	Cycle 4	30.42	0.98	0.89	73.47	0.99	3.43	51.95	N/A	2.16	37.81	0.68	0.82	43.03	1.00	0.79	36.80
		Cycle 5	28.67	0.98	0.48	63.39	0.99	2.08	46.03	N/A	1.28	35.52	0.70	0.43	39.85	1.00	0.50	36.80
		Cycle 6	27.30	0.97	0.46	56.24	0.99	1.30	41.77	N/A	0.88	34.03	0.70	0.45	37.51	1.00	0.54	36.80
		Cycle 7	28.20	0.96	0.60	42.89	0.99	0.27	35.55	N/A	0.43	31.80	0.85	0.46	34.44	1.00	0.40	36.80
	6 kN	Cycle 4	30.72	0.98	0.79	65.38	0.99	1.18	48.05	N/A	0.98	37.35	0.70	0.68	42.48	1.00	0.65	36.80
		Cycle 5	29.64	0.98	0.54	58.21	0.99	0.60	43.92	N/A	0.57	35.82	0.74	0.46	39.80	1.00	0.50	36.80
		Cycle 6	27.91	0.97	0.67	53.05	0.99	0.51	40.48	N/A	0.59	34.17	0.72	0.50	37.63	1.00	0.51	36.80
		Cycle 7	28.71	0.97	0.69	42.04	0.99	0.21	35.37	N/A	0.45	32.02	0.86	0.52	34.56	1.00	0.40	36.80
Beam 3	3 kN	Cycle 1	78.66	0.78	11.36	105.76	0.90	17.69	92.21	N/A	14.53	159.53	0.07	43.76	85.43	0.99	9.33	37.70
		Cycle 2	86.04	0.70	15.40	84.46	0.97	5.23	85.25	N/A	10.31	129.87	0.16	31.36	84.79	0.99	9.65	37.70
		Cycle 3	67.02	0.83	7.28	77.45	0.98	3.75	72.24	N/A	5.51	103.83	0.15	13.57	70.12	1.00	5.66	37.70
		Cycle 4	73.17	0.82	10.35	74.69	0.98	3.30	73.93	N/A	6.83	112.28	0.25	65.14	73.35	1.00	6.88	37.70
		Cycle 5	45.36	0.76	6.59	58.68	1.00	1.52	52.02	N/A	4.06	48.29	0.79	4.65	51.19	1.00	4.19	37.70
		Cycle 6	47.80	0.77	4.64	56.82	1.00	1.45	52.31	N/A	3.04	54.14	0.78	4.24	51.31	1.00	3.15	37.70

Table 4.19. Continued.

Beam #	Load	Cycle #	DIC_cmprs			ESG_all			Method 1			Method			Method 3			Theoretical
			Mean	R2	STDV	Mean	R2	STDV	Mean	R2	STDV	Mean	R2	STDV	Mean	R2	STDV	
Beam 3	4 kN	Cycle 1	60.14	0.89	5.87	68.86	0.99	2.07	64.50	N/A	3.97	77.92	0.42	8.02	63.15	1.00	3.87	37.70
		Cycle 2	63.99	0.84	5.14	64.86	0.99	1.06	64.43	N/A	3.10	73.87	0.56	4.70	64.22	1.00	3.05	37.70
		Cycle 3	56.63	0.90	4.08	62.17	1.00	0.78	59.40	N/A	2.43	70.73	0.44	4.30	58.58	1.00	2.66	37.70
		Cycle 4	59.25	0.91	4.54	60.76	1.00	1.04	60.01	N/A	2.79	70.09	0.63	4.88	59.79	1.00	2.89	37.70
		Cycle 5	39.19	0.89	2.69	51.50	1.00	0.55	45.34	N/A	1.62	42.24	0.86	1.69	44.81	1.00	1.72	37.70
		Cycle 6	41.55	0.87	2.90	49.96	1.00	0.50	45.76	N/A	1.70	45.24	0.90	2.64	45.08	*1.00	1.85	37.70
	5 kN	Cycle 4	49.44	0.95	2.32	53.89	1.00	1.60	51.67	N/A	1.96	56.82	0.79	2.55	51.20	1.00	1.69	37.70
		Cycle 5	36.86	0.94	1.35	47.54	1.00	0.96	42.20	N/A	1.16	39.89	0.90	1.04	41.72	1.00	0.97	37.70
		Cycle 6	38.64	0.91	2.21	46.48	1.00	0.78	42.56	N/A	1.50	41.80	0.93	2.07	41.98	1.00	1.40	37.70
	6 kN	Cycle 4	44.70	0.97	1.84	47.80	1.00	0.88	46.25	N/A	1.36	48.37	0.93	1.79	46.03	1.00	1.17	37.70
		Cycle 5	37.02	0.96	1.50	44.85	1.00	**0.28	40.93	N/A	0.89	39.06	0.92	1.04	40.78	1.00	***0.83	37.70
		Cycle 6	38.06	0.94	1.79	44.02	1.00	0.30	41.04	N/A	1.04	40.21	0.95	1.56	40.75	1.00	1.02	37.70

Note: * Estimate with the highest coefficient of determination for each beam is highlighted in yellow.

** Estimate with the lowest standard deviation for each beam is highlighted in green.

*** Estimate with the lowest standard deviation among the two-face combined data analyses is highlighted in blue.

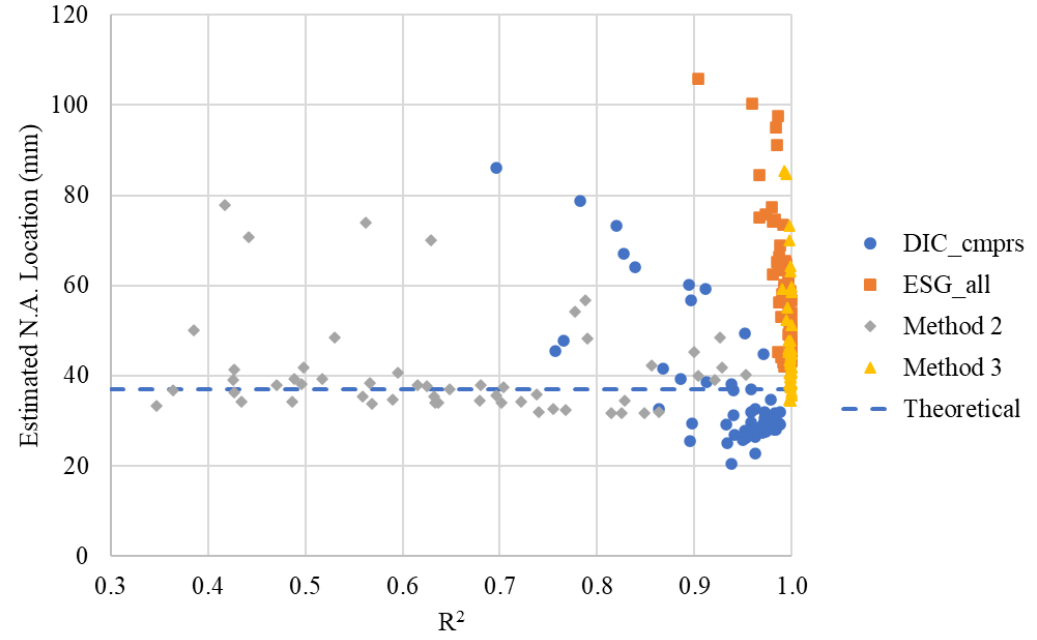

(a)

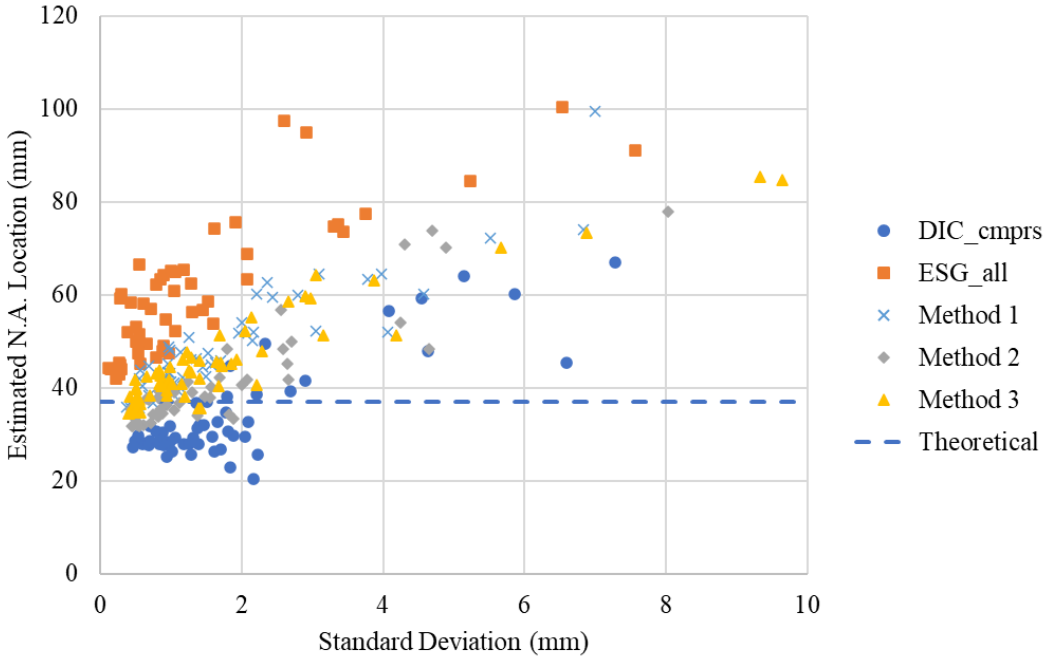

(b)

Figure 4.10. Batch 3 post-corrosion load test N.A. locations, plotted against (a) the corresponding coefficients of determination, and (b) the corresponding standard deviations.

4.4.8. Summary

Overall, the analysis presented in Sections 4.4.1. to 4.4.7 shows that both the standard deviation and coefficients of determination associated with best fit strain distribution can be used as indicators of the quality of the strain data in terms of its usefulness to calculate the N.A. location. It was found that the lower the standard deviation or the higher the coefficients of determination, the closer the estimates were to the theoretical values. The results selected by the highest coefficients of determination, lowest standard deviation and lowest standard deviation considering two-face combined data are summarized in Table 4.20. It was found that screening by standard deviation showed more advantages than screening by coefficients of determination. First, coefficients of determination are sensitive to the quantity of the data. If only two data points are used to identify the best fit function, the coefficients of determination would consistently be one, and thus be meaningless. The standard deviation does not have this limitation. The best results selected by the lowest standard deviation are generally closer to the theoretical values than the results selected by the highest coefficients of determination. The average of the absolute percent difference between the optimal coefficient of determination results and the theoretical value was 41%, whereas the average difference between the optimal standard deviation results and the theoretical value was 27%.

Considering ESG data alone generally provided the estimates with the lowest standard deviations. However, the results obtained using two-face combined data were generally better than those using the data from a single face. The average difference was only 24%. Thus, it is recommended to select the optimum data among the two face combined analyses ("Methods 1 to 3") based on the lowest standard deviation. Therefore, the blue cells (with triple asterisks) from Tables 4.11 to 4.19 were used to represent the best estimates that can be achieved by the surface based SHM techniques. The accuracy and feasibility of the proposed SHM technique are discussed in the following section.

Note the average percent difference for the optimal coefficient of determination and standard deviation results were calculated excluding the values for Batch 1 pre-corrosion, because in that set of experiments, only one side surface was monitored and there were no results for two-face combined analysis. For a fair comparison, other data for Batch 1 pre-corrosion were also excluded when calculating the average percentage errors.

Table 4.20. Summary of estimated N.A. locations selected based on the optimal coefficient of determination and standard deviation, in mm.

Beam Identification	Theoretical	R^2	|% diff|	STDV	|% diff|	STDV (two-face)	|% diff|
Batch 1 Beam 1 Pre	42.3	44.6	5%	42.5	0%	N/A	N/A
Batch 1 Beam 2 Pre	41.7	44.1	6%	43.2	4%	N/A	N/A
Batch 1 Beam 3 Pre	41.7	N/A	N/A	43.3	4%	N/A	N/A
Batch 1 Beam 1 Post	41.4	49.9	20%	38.9	6%	44.4	7%
Batch 1 Beam 2 Post	38.8	49.2	27%	31.6	19%	40.5	4%
Batch 1 Beam 3 Post	40.0	48.5	21%	48.8	22%	50.4	26%
Batch 2 Beam 1 Pre	37.8	58.7	55%	58.9	56%	56.3	49%
Batch 2 Beam 2 Pre	38.0	6.0	84%	41.4	9%	27.5	28%
Batch 2 Beam 3 Pre	37.6	37.2	1%	45.4	21%	34.8	8%
Batch 2 Beam 1 First Post	34.5	34.7	1%	28.6	17%	30.6	11%
Batch 2 Beam 2 First Post	34.8	37.4	7%	53.7	54%	37.4	7%
Batch 2 Beam 3 First Post	34.4	121.1	252%	62.7	82%	62.7	82%
Batch 2 Beam 1 Second Post	35.9	62.0	73%	48.3	34%	48.3	34%
Batch 2 Beam 2 Second Post	36.2	50.8	40%	42.7	18%	46.9	30%
Batch 2 Beam 3 Second Post	35.6	52.3	47%	47.7	34%	63.1	77%
Batch 3 Beam 1 Pre	38.5	29.6	23%	26.4	31%	26.4	31%
Batch 3 Beam 2 Pre	39.2	51.2	31%	43.4	11%	36.3	7%
Batch 3 Beam 3 Pre	39.0	46.0	18%	36.3	7%	45.3	16%
Batch 3 Beam 1 Post	37.0	35.6	4%	44.3	20%	38.2	3%
Batch 3 Beam 2 Post	36.8	40.4	10%	44.0	20%	35.9	2%
Batch 3 Beam 3 Post	37.7	45.1	20%	44.9	19%	40.8	8%
		Average	**41%**		**27%**		**24%**

4.5. Accuracy of the Estimated N.A. Location, Steel Bar Area, and Beam Capacity

The best estimates of the N.A. locations considering data from the two-faces, selected based on the lowest standard deviation of the estimated N.A. location while the load was held constant, were used to calculate the steel bar area and beam bending moment capacity. The estimates of the pre- and post corrosion loading tests are compared to the theoretical and actual values in Tables 4.21 and 4.22, respectively.

Table 4.21. Comparison of the estimated N.A. locations, steel bar areas, and bending moment capacities in the pre-corrosion load tests to the theoretical and actual values.

Beam #	Strain Data		Method	Applied Load (kN)	N.A. Location (mm)			As (mm^2)			Ultimate Capacity (kN)		
	Side 1	Side 2			Estimated	Theoretical	% Error	Estimated	Actual	% Error	Estimated	Theoretical	% Error
Batch 1 pre-corrosion													
Beam 1	ESG_G2&G3	none	N/A	8	42.5	42.3	0%	203	200	2%	30.9	30.5	1%
Beam 2	ESG_cmprs	none	N/A	8	43.2	41.7	4%	220	200	10%	32.2	29.8	8%
Beam 3	ESG_G2&G3	none	N/A	8	43.3	41.7	4%	221	200	11%	32.4	29.8	9%
Batch 2 pre-corrosion													
Beam 1	ESG_G2&G3	DIC_cmprs	Method 3	6	56.3	37.8	49%	309	100	209%	23.0	9.7	137%
Beam 2	ESG_G2&G3	DIC_cmprs	Method 3	6	27.5	38.0	-28%	45	100	-55%	4.6	9.7	-52%
Beam 3	ESG_G2&G3	DIC_cmprs	Method 3	6	34.8	37.6	-8%	82	100	-18%	8.1	9.7	-17%
Batch 3 pre-corrosion													
Beam 1	ESG_all	DIC_cmprs	Method 3	3	26.4	38.5	-31%	39	100	-61%	3.9	9.4	-59%
Beam 2	ESG_all	DIC_cmprs	Method 3	4	36.3	39.2	-7%	82	100	-18%	7.8	9.3	-16%
Beam 3	ESG_all	DIC_cmprs	Method 3	4	45.3	39.0	16%	150	100	50%	13.3	9.4	42%

Table 4.22. Comparison of the estimated N.A. locations, steel bar areas, and bending moment capacities in the post-corrosion load tests to the theoretical and actual values.

Beam #	Strain Data		Method	Applied Load	N.A. Location (mm)			As (mm^2)			Ultimate Capacity (kN)		
	Side 1	Side 2		(kN)	Estimated	Theoretical	% Error	Estimated	Actual	% Error	Estimated	Actual	% Error
Batch 1 post-corrosion													
Beam 1	ESG_all	DIC_cmprs	Method 3	5	44.4	41.4	7%	230	190	21%	32.8	14.8	122%
Beam 2	ESG_all	DIC_cmprs	Method 3	5	40.5	38.8	4%	185	165	12%	27.0	12.0	125%
Beam 3	ESG_all	DIC_cmprs	Method 3	5	50.4	40.0	26%	345	179	93%	42.1	17.5	141%
Batch 2 first post-corrosion													
Beam 1	ESG_all	DIC_cmprs	Method 3	4	30.6	34.5	-11%	58	78	-25%	5.9	12.2	-51%
Beam 2	ESG_all	DIC_cmprs	Method 3	4	37.4	34.8	7%	96	80	20%	9.4	9.9	-6%
Beam 3	ESG_all	DIC_cmprs	Method 3	4	62.7	34.4	82%	454	80	468%	26.3	9.8	168%
Batch 2 second post-corrosion													
Beam 1	ESG_notop	ESG_notop	Method 2	6	48.3	35.9	34%	173	78	122%	15.8	12.2	29%
Beam 2	ESG_notop	ESG_notop	Method 2	6	46.9	36.2	30%	160	80	100%	14.6	9.9	47%
Beam 3	ESG_notop	ESG_notop	Method 2	5	63.1	35.6	77%	437	80	446%	27.0	9.8	175%
Batch 3 post-corrosion													
Beam 1	ESG_all	DIC_cmprs	Method 3	6	38.2	37.0	3%	96	89	8%	9.2	11.3	-19%
Beam 2	ESG_all	DIC_cmprs	Method 3	4	35.9	36.8	-2%	81	86	-6%	7.7	12.4	-38%
Beam 3	ESG_all	DIC_cmprs	Method 3	6	40.8	37.7	8%	111	90	23%	10.3	12.7	-19%

For the pre-corrosion load tests, the estimated steel bar area is compared to the actual value, which is the original cross-sectional area of the uncorroded bars. The actual steel bar area was combined with measured beam dimensions and material properties to compute the theoretical N.A. location and bending moment capacity. Thus, the estimated N.A. locations and bending moment capacities can be compared to the theoretical values.

Despite the fact that the conditions of the Batch 1 beams were not ideal, the estimates were quite accurate for the pre-corrosion load test, as seen in Table 4.21. The estimated N.A. locations were within 4% (less than 1.5 mm) of the theoretical values. However, the 4% error was amplified to approximately 10% for the steel bar area comparison. This demonstrates that the N.A. location is not particularly sensitive to a change in the effective steel bar area. Lastly, the errors associated with the bending moment capacity slightly decreased to around 8%. There is not much room to further improve the accuracy of the estimated N.A. locations, since the errors were already within 1.5 mm, and the beam's dimensions and strain gauge locations were measured with a precision of 1 mm. Therefore, the best estimate using the surface strain-based SHM technique in predicting bending moment capacity for a small-scale beam like this would be approximately 8%.

If a full-size beam was being monitored and the error in estimated N.A. location could be kept at 1 mm, then the error in predicting the effective steel bar area would be lower. For example, consider a beam with cross-sectional dimensions of 400 mm in width and 700 mm in height with the same material properties. Using Equations 3.5 and 3.6, the estimated steel bar area decreases from 1005 mm^2 to 988 mm^2 when the estimated N.A location decreases from 131 mm to 130 mm below the top surface. Thus, a 1 mm change in N.A. location only corresponds to 1.7% difference in steel bar area. For the small-size beam used in the experiments, a 1 mm error in N.A. estimation corresponded to a 8% error in the estimated steel bar area. Therefore, the proposed SHM technique has the potential to reach higher accuracy on full-size beams.

In the pre-corrosion load tests for the beams in Batches 2 and 3, the errors associated with the estimates were much higher. The differences between the estimated and theoretical N.A. locations ranged from -31% to 49%. These errors were magnified to -61% to 209% for the steel bar area estimates and -59% to 137% for the bending moment capacity estimates. One possible explanation for the larger errors is that, compared to Batch 1, beams in these two batches had different dimensions and were much more slender. The slenderness effect can cause lateral

deflections and twisting in RC beams similar to what is experienced by slender steel beams (Revathi and Menon 2008). This could cause surface strains to be less uniform and leads to the high errors in the estimates. Also, a smaller amount of reinforcement was used for beams in these two batches, which could have further aggravated the slenderness effect (Revathi and Menon 2008). In addition, for the same percentage loss reinforcement due to corrosion, a smaller amount of reinforcement would cause less change to the N.A. location. Therefore, slenderer dimensions and a smaller reinforcement ratio could be the reason that the estimates for Batches 2 and 3 were less accurate.

For the post-corrosion load tests, the estimated steel bar areas were compared to the actual values determined using the gravimetric method after the steel bars had been extracted and cleaned. The actual steel bar areas were combined with measured beam dimensions and material properties to compute the theoretical N.A. locations. Thus, the estimated N.A. locations were compared to the theoretical values. The estimated bending moment capacity was compared to the actual failure load.

The estimates for beams in Batch 2 had very high errors. The estimated failure loads differed from the actual failure loads by -51% to 175%. Batches 1 and 3 were relatively more accurate. However, Batch 1 beams failed in shear instead of in flexure, so the actual failure loads were much lower than the estimated values. The calculated theoretical shear capacity for Batch 1 beams was 22.1 kN, and it does not depend on the amount of reinforcement, but is rather linearly proportional to the cross-sectional area of the beam. The bottom of the beams was cracked due to corrosion. This damage would not affect the beam's bending moment capacity much but would likely significantly affect its shear capacity. Therefore, the actual failure loads were much smaller than the theoretical shear capacity as well.

Even though the estimated N.A. locations for Batch 3 beams were quite close to the theoretical values, the estimated failure load differed significantly from the actual failure load. For example, for Beam 2 in Batch 3, the error in the estimated N.A. location was only -2%, but the error in the failure load was -38%. Since concrete is a non-homogeneous material, it is difficult to predict its bending moment capacity accurately. Table 4.23 compares both the estimated and the theoretical bending moment capacities to the actual failure loads. For Batch 3, the theoretically calculated values also differed from the actual values by 25% to 34%.

Table 4.23. Comparison of the estimated and theoretical bending moment capacities to the actual failure loads.

Beam #	Actual	Estimated	% Error	Theoretical	% Error
Batch 1 post-corrosion					
Beam 1	14.8	32.8	122%	28.2	91%
Beam 2	12.0	27.0	125%	24.5	104%
Beam 3	17.5	42.1	141%	26.3	50%
Batch 2 first post-corrosion					
Beam 1	12.2	5.9	-51%	7.8	-36%
Beam 2	9.9	9.4	-6%	7.9	-20%
Beam 3	9.8	26.3	168%	7.9	-19%
Batch 2 second post-corrosion					
Beam 1	12.2	15.8	29%	7.9	-36%
Beam 2	9.9	14.6	47%	7.9	-20%
Beam 3	9.8	27.0	175%	7.8	-20%
Batch 3 post-corrosion					
Beam 1	11.3	9.2	-19%	8.5	-25%
Beam 2	12.4	7.7	-38%	8.2	-34%
Beam 3	12.7	10.3	-19%	8.6	-33%

4.5. Summary

In the preliminary analysis presented in Appendix F, the estimated N.A. locations considering strain data from each face individually were compared to the theoretically calculated values. It was demonstrated that the effectiveness of the proposed SHM method was related to the surface smoothness of concrete, applied loads, number and locations of the gauges, and beam slenderness. It was found that the estimates were closer to the theoretical value when the applied loads were higher. This is because the beams might not be fully cracked when the applied loads were low. But Equation 3.4 is only valid when the beam has been fully cracked while under the elastic deformation zone. The preliminary analysis results also suggested that combining the strain data from the two side surfaces could improve the accuracy of the estimated N.A locations. Therefore, in this chapter, estimates were obtained using the two-face combined data and are presented with the corresponding coefficients of determination for the best-fit strain distributions and standard deviations of the estimated N.A. locations. It was found that both coefficient of determination and standard deviation can indicate the accuracy of the estimates. But using standard deviation as the screening criteria for the best result is more robust and reliable.

Therefore, among all the N.A. location estimates calculated for each beam at different applied load and using different data processing methods, the "best" estimate that was used to represent the effectiveness of the surface strain-based SHM technique was selected based on the lowest standard deviation associated with the combined two-face strain data.

The selected estimates of N.A. location were used to estimate the effective steel bar area and remaining bending moment capacity, and the estimates were compared to the theoretical or actual values to determine the accuracy of the estimates. Batch 1 pre-corrosion load tests obtained the most accurate N.A. location estimates. The estimated and theoretical N.A. locations were within 2% of each other or less than 1 mm. However, the differences were magnified to approximately 6% for the bending moment capacities. The N.A. locations would be more sensitive to the change in the loss of reinforcement are if larger beams were used.

In the post-corrosion load tests for Batch 1, the differences between the estimated and theoretical N.A. locations were between 3% and 24%, while the differences between the estimated bending moment capacities and the actual failure loads were between 121% and 142%. The large differences were because the beams all failed in shear instead of flexure. It was difficult to fit shear reinforcement in such a small cross-section. Therefore, for beams in Batches 2 and 3, slenderer beam dimensions and smaller reinforcement ratios were used.

Beams in Batches 2 and 3 all failed in flexure, but the errors in the estimates were quite high. In the pre-corrosion load tests for Batch 2, the surface had wrinkles and a thicker type of adhesive was used to attach the electrical strain gauges. The estimated N.A. locations differed from the theoretical values by between -28% and 49%. Even after the surfaces were smoothed using a grinder and appropriate adhesive was used for the post-corrosion load tests, the errors in the estimated N.A. locations during the post-corrosion load tests were still as high as -11% to 82 %, and the estimated bending moment capacities differed from the actual failure load by -51% to 175%. For Batch 3, the differences between the estimated and theoretical N.A. locations were between -31% to 16% for the pre-corrosion load tests and -2% to 8% for the post corrosion load tests. The estimated beam capacities differed from the actual failure loads by -19% to 38%. The high errors experienced by Batches 2 and 3 might be due to the slenderness effect.

Overall, this set of lab experiments did not demonstrate that the proposed SHM method had adequate effectiveness for practical implementation. The large errors in the results are believed

to be related to the choice of using small-scale beams. First, it was difficult to fit shear reinforcement into such a small cross-section. Without shear reinforcement, the beams were prone to fail in shear instead of in flexure. As a result, the length of the beams had to be increased to ensure that the flexural capacity was lower than the shear capacity. However, the increased length increased the slenderness effect, which further affected the accuracy of the estimates. The cross-sectional area for Batches 2 and 3 beams did not differ much from Batch 1 beams, however, the results obtained for Batches 2 and 3 were much worse than the results obtained for Batch 1. Therefore, the main reason for the increased errors was attributed to the increased slenderness of the beams. The small reinforcement ratios and small dimensions would also cause the N.A. location to be less sensitive to the loss of reinforcement due to corrosion. It is thought that the proposed SHM method may have the potential for better accuracy if used to monitor full-scale beams, which are larger in size, less slender, and laterally stable.

Another big challenge relates to the non-homogeneous properties of the concrete, which makes it difficult to accurately predict a reinforced concrete beam's flexural capacity even if all the required variables are known. As shown in Table 4.23, the theoretical flexural capacity calculated using the actual amount of reinforcement obtained after the bar had been extracted, cleaned, and weighed still differed from the actual failure load by -36% to -19%. Moreover, in real life applications, naturally corroded beam would be less uniform and subjected to other issues that affect the beam capacity, such as loss of bond. To fully understand the potential of the proposed SHM technique, it is recommended that additional experiments be conducted on larger beams.

CHAPTER 5 RELIABILITY AND ECONOMIC ANALYSIS

5.1. Introduction

Uncertainties are inevitable in structural design, because all the factors considered in design, including material properties, structural member dimensions, and the design loads are not known with complete certainty. For instance, the National Building Code of Canada (2015) specifies snow loads based on a 50-year return period, which means there is a 2% chance of these loads being exceeded in any one year. Thus, it is unrealistic to design a structure that is absolutely safe; rather, the structures are designed with an adequate level of safety, or in other words, with an acceptable risk of failure.

One way to quantify a structure's level of safety is through the reliability index, which is defined as follows (Frangopol and Messervey 2011):

$$\beta = \frac{\mu_R - \mu_L}{\sqrt{\sigma_R^2 + \sigma_L^2}} \tag{5.1}$$

where μ_R and μ_L are the mean values of resistance and load effect, respectively, and σ_R and σ_L are their corresponding standard deviations. This equation assumes that the two variables are normally distributed. To build a structure with an extremely high reliability index is not cost-effective; therefore, reliability indexes between 2 and 4 are typically adopted in structural assessments, which correspond to probabilities of failure between 0.02275 and 0.0000316 (Frangopol and Messervey, 2011).

For an existing structure, assuming that the load effect and its corresponding uncertainty are fixed, the reliability index can be increased in two ways: increasing the structural resistance through repairing or replacing the deteriorated structural members or decreasing the standard deviation in the estimated resistance by reducing the uncertainties of the variables on which it depends.

Implementing SHM systems can improve the reliability of a structure by means of the second approach mentioned above, even though an SHM system does not have any effect on the current condition of the structure. Furthermore, when multiple SHM systems are available to implement on a structure, assuming all of them can provide close estimates to the actual structural condition, the one with the highest level of precision should yield the highest reliability index. If a certain reliability index is used to determine whether to take a structural member out of service, an SHM system with a lower level of precision will result in lower β values that may suggest replacement providing that the estimated resistance doesn't change. However, the same structural member monitored by an advanced and more precise SHM system may be evaluated as having an adequate level of safety and be approved for a longer service time. Thus, even though a more advanced SHM system is usually associated with a higher cost, it can generate economic benefits through an extended lifespan. To determine if the implementation of an advanced SHM system, or even the implementation of any SHM system, is worth the investment, many factors must be considered, including the value, life span, the deterioration rate of the target structure, as well as the SHM costs.

As described in Chapter 3, Christensen et al. (2011) demonstrated how the economic benefits of alternative SHM systems with different uncertainties can be compared using the annual worth life-cycle cost (AWLCC) of a hypothetical beam. However, this approach has never been verified experimentally. The second objective of this research study was to demonstrate the value of a more precise SHM system through reliability and economic analyses using the experimental data. Two SHM systems with different levels of uncertainty were simulated by combining the data collected from different sets of monitoring equipment; a standard SHM system consisted of the strain monitoring equipment only, and an enhanced SHM system consisted of a cover meter in addition to the strain monitoring equipment. The use of strain monitoring equipment could identify the remaining effective reinforcing bar area due to corrosion, while the use of a cover meter reduced the uncertainty of the reinforcing bar location. Both of these SHM systems led to increased confidence in the estimated flexural resistances of the beams.

The methodologies used for the reliability and economic analyses were described in Chapter 3. The results of these analyses considering the two SHM systems are discussed in Sections 5.2 and 5.3, respectively. Lastly, a summary is provided in Section 5.4.

5.2. Results of Reliability Analysis

The reliability index was calculated separately for each beam and each load test based on the measurements from the standard and enhanced SHM systems, and the results are summarized in Table 5.1. Sample calculations can be found in Appendix I. As a reminder, the load effect was assumed to be known with certainty for these calculations. It would be difficult to calculate a reliability index for the case with no monitoring, because the remaining beam capacity is unknown.

The load effect, μ_L, was determined using the factored design resistance for each batch of beams as a reference. The factored design load for Batch 3 Beam 3 calculated according to CSA A23.3-14 was 3.28 kN·m (See Appendix I). As mentioned in Section 3.4.1, the load effect, μ_L was taken as the largest integer smaller than a beam's design load. Thus, for Batch 3, μ_L was set to 3 kN·m. Batches 2 and 3 had the same design configurations, thus, the same design load was assumed for Batch 2 beams. The design load for Batch 1 beams was around 6.84 kN·m; thus, μ_L was set to 6 kN·m for Batch 1.

The analysis for both the standard and enhanced SHM systems used the same N.A. locations, as selected in Chapter 4, because a cover meter will not affect the estimate of the neutral axis locations since they are based on measured strains. Thus, the estimated flexural resistances of the beams provided by these two SHM systems were identical. However, the standard deviations differed for the two systems. For the standard SHM system, the tolerance for the concrete cover thickness, specified by CSA A23.1-14 as ± 12 mm, was used to calculate a standard deviation of $\frac{12\ mm}{1.645} = 7.3\ mm$. For the enhanced monitoring system, the ± 2 mm precision of the cover meter was used to calculate the standard deviation of the cover thickness as $\frac{2\ mm}{1.645} = 1.2\ mm$. Thus, the enhanced SHM system provided the same mean resistance estimates, but with less uncertainty (σ_R was smaller). Consequently, the enhanced SHM system consistently provided higher reliability indexes than the standard SHM system, as shown in Table 5.1.

There were three beams for which negative β values were calculated for both the standard and enhanced SHM systems. A negative β value means the estimated capacity of the beam (μ_R) is lower than the load effect (μ_L). If the estimates accurately represent the actual beam condition, then a negative β value is an alarming alert that the structure requires immediate rehabilitation or

replacement. However, the negative β values obtained from this analysis are mainly due to the errors associated with the new SHM technique being evaluated. Since this technique did not achieve the desired accuracy, especially for smaller and slender beams, some of the β values for Batches 2 and 3 were unrealistically high or negative.

Table 5.1. Reliability indexes of the standard and enhanced SHM systems.

Batch #	Loading Test	Load Effect (kN*m)	Estimated Flexural Resistance (kN*m)	Standard SHM		Enhanced SHM	
				STDV (kN*m)	β	STDV (kN*m)	β
Batch 1	Beam 1 Pre	6	8.5	1.2	2.1	0.5	5.5
	Beam 1 Post	6	9.0	1.4	2.2	0.7	4.6
	Beam 2 Pre	6	8.9	1.3	2.2	0.5	6.1
	Beam 2 Post	6	7.4	1.1	1.3	0.6	2.6
	Beam 3 Pre	6	8.9	1.3	2.2	0.5	6.0
	Beam 3 Post	6	11.6	1.9	3.0	1.1	5.3
Batch 2	Beam 1 Pre	3	9.8	1.5	4.6	0.7	9.5
	Beam 1 Post	3	2.5	0.3	-1.5	0.1	-3.6
	Beam 1 Second Post	3	6.7	0.9	3.9	0.3	12.3
	Beam 2 Pre	3	2.0	0.3	-3.8	0.1	-7.2
	Beam 2 Post	3	4.0	0.5	1.8	0.2	4.8
	Beam 2 Second Post	3	6.2	0.9	3.6	0.3	11.3
	Beam 3 Pre	3	3.5	0.5	0.9	0.3	1.8
	Beam 3 Post	3	11.2	1.5	5.3	0.4	21.8
	Beam 3 Second Post	3	11.5	1.6	5.3	0.4	21.1
Batch 3 pre	Beam 1 Pre	3	1.7	0.2	-5.4	0.1	-9.6
	Beam 1 Post	3	3.9	0.6	1.7	0.2	4.4
	Beam 2 Pre	3	3.3	0.5	0.6	0.3	0.9
	Beam 2 Post	3	3.3	0.5	0.6	0.2	1.5
	Beam 3 Pre	3	5.7	0.9	2.9	0.5	5.0
	Beam 3 Post	3	4.4	0.6	2.1	0.3	4.7

A reliability index of 2 to 4 is commonly used in structural assessment (Frangopol and Messervey 2011). For the purpose of this discussion, it was assumed that a beam would be replaced when β drops below 2.

For Batch 1 beams, the estimates of the beams' conditions were quite accurate in the pre-corrosion load tests. However, in the post-corrosion load tests, the beam resistances were overestimated for Beams 1 and 3. Therefore, the reliability indexes for these two beams increased after corrosion. For Beam 2, β given by the standard monitoring system dropped from 2.2 in the pre-corrosion load test to 1.3 in the post corrosion load test, which means it required replacement after corrosion. However, with the enhanced monitoring system, β dropped from 5.5 to 2.5, which means the beam still had an adequate level of safety to remain in service.

The estimates for Batch 2 beams had the highest error among all three batches. The beam capacities for Beams 2 and 3 were underestimated in the pre-corrosion load tests. Thus, the reliability indexes increased instead of decreasing after the corrosion. The estimates for Beam 3 in the post-corrosion load tests were significantly overestimated, thereby resulting in an unrealistically high reliability index. It was difficult to draw useful conclusions when the errors in the estimates were so high. However, it was obvious that the enhanced monitoring system was able to provide higher reliability indexes. And when the reliability index was negative, the enhanced monitoring system also magnified the magnitude of the negative reliability index.

For Batch 3 Beam 1, the bending moment capacity was significantly underestimated in the pre-corrosion load test. Thus, negative β values were provided by both the standard and enhanced SHM systems, but the β values increased to more reasonable values in the post-corrosion load test. For Beam 2 in the pre-corrosion load test, its bending moment capacity was slightly underestimated, and it coincidentally happened to be the same as the estimate in the post-corrosion load test. For the standard SHM system, the standard deviation of the estimated beam capacity did not change, so the β values provided by the standard system were the same in the pre-corrosion and post-corrosion load tests. For the enhanced SHM system, the standard deviation decreased slightly in the post-corrosion load test, so the β value increased accordingly. The bending moment capacities for Beam 3 were slightly overestimated in both pre-corrosion and post-corrosion load tests. The reliability index evaluated by the standard SHM system was 2.9 before the corrosion process, and the value dropped to 2.1 in the post-corrosion load test,

which was approaching the critical value of β. This means the beam would require replacement soon if the standard SHM system were employed. However, with the enhanced SHM system, β was 5.0 in the pre-corrosion load test, and this value dropped to 4.7 in the post-corrosion load test. Based on these results, the beam could remain in service for a much longer period. The probability distribution diagrams for these two cases are shown in Figure 5.1. The probability of failure in each case corresponds to the area below the probability curves to the left of the load effect. The figure shows that even after the corrosion process, the enhanced monitoring system resulted in a lower probability of failure than that of the standard monitoring system before the corrosion. Therefore, the replacement of this beam can be safely delayed due to the use of a more precise SHM system.

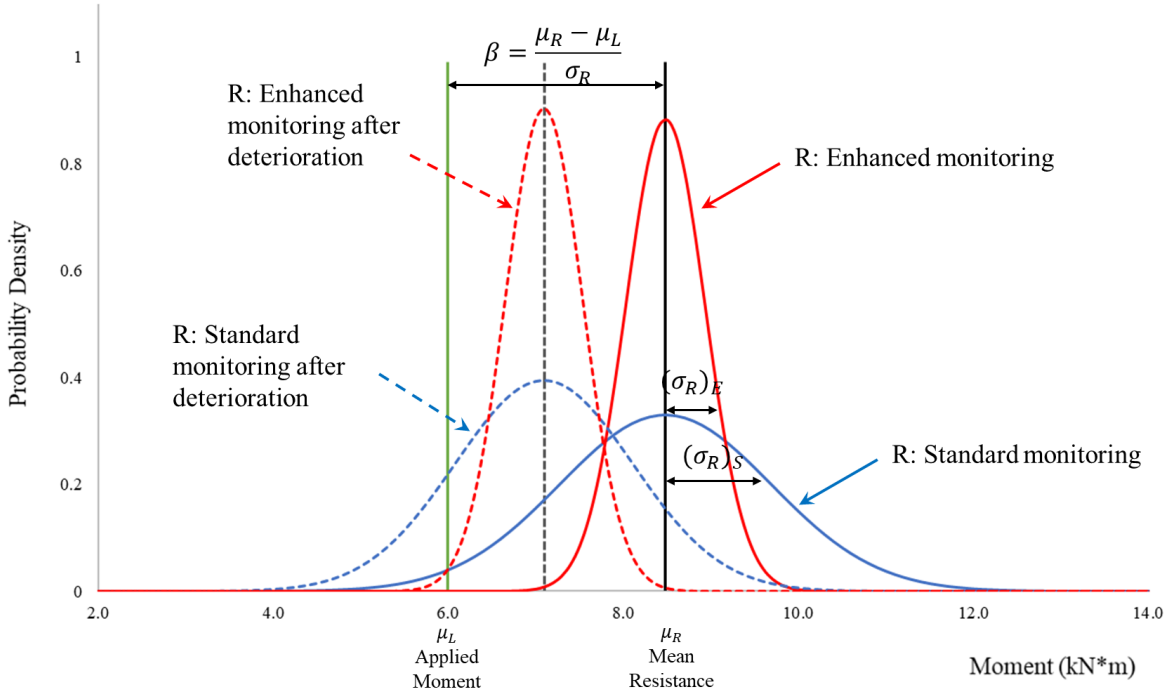

Figure 5.1. The probability distribution diagrams for bending moment resistance before and after corrosion for the standard and enhanced monitoring systems for Batch 3 Beam 3.

Theoretically, it was expected that β would decrease for all the beams after corrosion. Unfortunately, this was not the case due to the high errors in the estimated moment resistance. Nevertheless, the enhanced monitoring system consistently provided higher β values than the standard monitoring system (or higher absolute values in the negative cases), in some cases illustrating that the enhanced monitoring system is capable of extending the service life.

5.3. Results of Life-cycle Cost Analysis

The currency used for the economic study in this section is the U.S. dollar. In order to represent a more realistic case, it was assumed that the beams monitored in the lab experiment were the edge beams of the University Bridge in Saskatoon, SK. It was also assumed that the present time is 45 years into the service life of the bridge. Without the information provided by an SHM system, a bridge inspector may decide to replace all the edge beams due to the uncertainty of the deterioration condition of the beams. The total cost of replacement, as explained in Section 3.5, is $ 1,227,744 in 2021. If the reliability indexes provided by the SHM systems were used to aid this decision and a critical β value of 2 was applied, as shown in Table 5.2, six out of nine beams monitored by the standard SHM system showed adequate levels of safety, and this number went up to eight out of nine for the enhanced system.

Table 5.2. Decision regarding the replacement of the corroded beams based on reliability indexes.

Batch #	Load Test #	Standard SHM		Enhanced SHM	
		β	Decision	β	Decision
Batch 1	Beam 1 Post	2.2	Remain	4.6	Remain
	Beam 2 Post	1.3	Replace	2.6	Remain
	Beam 3 Post	3.0	Remain	5.3	Remain
Batch 2	Beam 1 Second Post	3.9	Remain	12.3	Remain
	Beam 2 Second Post	3.6	Remain	11.3	Remain
	Beam 3 Second Post	5.3	Remain	21.1	Remain
Batch 3	Beam 1 Post	1.7	Replace	4.4	Remain
	Beam 2 Post	0.6	Replace	1.5	Replace
	Beam 3 Post	2.1	Remain	4.7	Remain

The value of SHM systems mainly come from the extended life spans of the monitored structures. The beams that demonstrated adequate levels of safety would remain in service and be monitored continuously until their reliability indexes drop below the critical value. The length of the additional service life depends on the current beam capacity, the corrosion rate and the uncertainty associated with the SHM measurements. A very conservative estimate of the remaining service life can be obtained using Equations 3.13 to 3.15 assuming the highest rate of

corrosion (10 μA/cm^2) under natural environment. The results are summarized in Table 5.3, with sample calculations provided in Appendix J.

Table 5.3. Estimated remaining service life, in years, provided by the standard and enhanced SHM systems.

Beam ID	Standard SHM System	Enhanced SHM System
Batch 1 Beam 1	1.2	9.4
Batch 1 Beam 2	0	1.3
Batch 1 Beam 3	11.9	23.2
Batch 2 Beam 1	12.9	23.7
Batch 2 Beam 2	9.4	19.8
Batch 2 Beam 3	53.2	88.8
Batch 3 Beam 1	0	3.7
Batch 3 Beam 2	0	0
Batch 3 Beam 3	1.2	5.7

The economic benefits of the extended service life can be quantified by AWLCC, which breaks down the total life cycle cost of an asset into equal annualized costs considering the life span and discount rate. Without using any SHM system, the calculation of AWLCC only considers the replacement cost, which is $\$\,1{,}227{,}744$ in present value, over a 45-year life span. Assuming a discount rate of 5%, the AWLCC was calculated to be $69,075 per year using Equation 3.15. If a monitoring system is implemented, there can be two scenarios depending on whether the reliability index exceeds the critical threshold. If the reliability index is less than 2, the beam will be replaced immediately, at its originally schedule time, and the AWLCC will be even higher than if no SHM system had been used due to the additional cost of the monitoring system. On the other hand, if the reliability index is higher than 2, the additional service life might reduce the AWLCC of the beams and thus, the cost of the SHM system can be justified economically. For the standard SHM system, the total cost of monitoring was estimated assuming four electrical strain gauges were placed every two meters, and that the price of the gauge was the same as those used in the lab experiment, which was approximately $10 per gauge. The University Bridge is 378 metres long (City of Saskatoon 2020), which means the total length of the edge beams on both sides is $756\ \mathrm{m}$. Thus, the additional costs of the sensors are $\$10 \times 4 \times \frac{756\ \mathrm{m}}{2\ m} =$

$15,120. A 32-analog input DAQ module costs $1155 (OMB-DAQ-2416, Omega, Canada). Thus, the costs of the DAQ systems associated with the strain gauges are $\$1155 \times \frac{4 \times \frac{756\ \mathrm{m}}{2\ m}}{32} = \$54,574$. The total costs of the standard SHM system should be the sum of the costs for the gauges and the DAQ system, which is $69,694. A $6,000 cover meter is added to the enhanced monitoring system. Thus, the total costs for the implementation of the enhanced monitoring system are $75,694 up front. This does not include labour costs, which are omitted for this illustration.

A cashflow diagram is provided in Figure 5.2 using Batch 3 Beam 3 as an example. With the help of the standard or the enhanced monitoring system, the lifespan of these edge beams could be extended to 46.2 and 50.7 years, respectively. The additional service life was estimated using Faraday's Law, as described in Section 3.5, assuming a very aggressive corrosion rate. Since the replacement cost would occur in the future, the first step in calculating the AWLCC was to bring the future cost to its present value, given the 5% discount rate. Then, the present value of the replacement cost was combined with the SHM expense to calculate the AWLCC based on the estimated life span of 46.2 and 50.7 years. The AWLCC for Batch 3 Beam 3 monitored by the standard and enhanced monitoring system, was $68,526/year and $54,834/year, respectively. Without using any SHM systems, the AWLCC is $69,075/year. This means that the standard SHM system saved $549/year, while the enhanced SHM system saved $14,241/year. Sample calculations are provided in Appendix J.

The AWLCC for all the beams tested in the post-corrosion load tests are listed in Table 5.4. The predicted condition of the beams varied widely, ranging from requiring immediate replacement, which would result in a higher AWLCC with the implementation of SHM systems, to extending the life span up to 88.8 years, which would drastically reduce the AWLCC. In the end, the average savings provided by the standard monitoring system for all nine beams tested in lab was $14,803/year, while the savings associated with the enhanced monitoring system was $26,342/year.

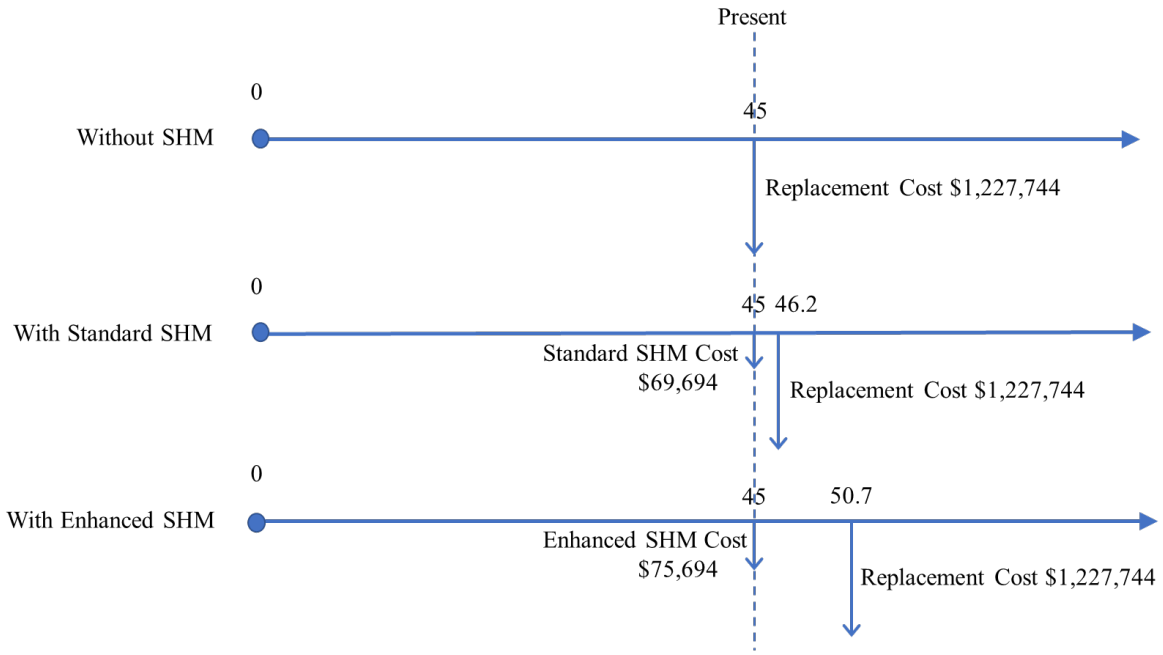

Figure 5.2. Cashflow for different monitoring scenarios for Batch 3 Beam 3.

The AWLCC analysis performed in this section was conducted for the purpose of demonstrating the savings provided by the implementation of SHM systems and comparing alternative monitoring systems. It is recognized, however, that the AWLCC values are not accurate, since the bending moment capacities estimated by the strain based SHM technique had high errors, especially for the slender and less reinforced beams in Batch 2 and Batch 3. The results of this economic analysis showed that the implementation of SHM systems resulted in reducing the AWLCC, and a more sophisticated system resulted in greater savings. However, the calculated savings would be different if any of the variables changed, including the total life cycle costs, the actual conditions of the beams, the deterioration rate, the discount rate, and the SHM costs. This research study, nevertheless, provided an example of how the economic value of alternative SHM systems can be evaluated.

Table 5.4. AWLCC for all beams tested in the post-corrosion load tests based on the information given by the standard and enhanced monitoring systems.

Beam ID	Standard SHM System		Enhanced SHM System	
	Additional Service Life (year)	AWLCC ($/year)	Additional Service Life (year)	AWLCC ($/year)
Batch 1 Beam 1	1.2	68440	9.4	45708
Batch 1 Beam 2	0	72996	1.3	68687
Batch 1 Beam 3	11.9	40322	23.2	24481
Batch 2 Beam 1	12.9	38572	23.7	23935
Batch 2 Beam 2	9.4	45464	19.8	28374
Batch 2 Beam 3	53.2	8136	88.8	4599
Batch 3 Beam 1	0	72996	3.7	60644
Batch 3 Beam 2	0	72996	0	73334
Batch 3 Beam 3	1.2	68526	5.7	54834
	Average	**54272**		**42733**
	Savings	**14803**		**26342**

5.4. Summary

This chapter described the reliability and economic analyses for the beams monitored in the lab experiment. The results showed that the reliability index of these beams can be significantly improved by the additional precision possessed by an enhanced monitoring system. A higher reliability index reflects greater confidence in the safety of the beam; thus, the beam would be approved for a longer service life. The extended service life can decrease the beam's AWLCC in two ways: delayed replacement cost (a present cost becomes a future cost), and an increased number of compounding periods. Assuming that the beams monitored in the lab experiment represented the edge beams of the University Bridge, the savings associated with the standard and enhanced monitoring systems were calculated to be $14,803/year and $26,342/year, respectively. Thus, the value of implementing a more sophisticated SHM system was demonstrated through improved reliability indexes and decreased AWLCCs for the beams.

CHAPTER 6 CONCLUSION AND RECOMMENDATIONS

6.1. Conclusions

The objectives of this research study were to experimentally evaluate the effectiveness of the surface strain based SHM method proposed by Christensen et al. (2011) and to demonstrate the value of implementing SHM systems with different levels of uncertainty through changes in the reliability index and the AWLCC of the monitored structure. The surface strain-based method, if proven to be effective, would be a Level 4 SHM technique, while most of the other SHM technologies for monitoring reinforced concrete beams are Level 2. It estimates the effective reinforcing bar area and remaining capacity of a corroded concrete beam through measuring the strain distribution on the side surfaces of the beam. The development of powerful techniques like this and the quantification of its economic benefits should encourage the field implementation of SHM systems.

The results of the experimental tests on nine small-scale corroded concrete beams showed that the accuracy of the proposed SHM technique was not ideal. The predicted flexural capacity differed from the actual failure load by -51% to 175%. The main reason for the large errors in the results is believed to be related to the use of small-scale beams. The surface strain distribution was greatly affected by the slenderness of the beams. Beams in the first batch were slightly wider and shorter than those in the second and third batches and used a higher amount of reinforcement; for these beams, the estimates of the N.A. locations were within 1 mm of the theoretical values. The small size of the beams also meant that a change in N.A. location was not particularly sensitive to a loss in the steel bar area due to corrosion. Although the errors of the estimated N.A. locations for Batch 1 beams in the pre-corrosion load tests were all within 1 mm, these errors were amplified to 6% for the estimated effective steel bar areas and 5% for the estimated flexural capacities.

If the error in estimated N.A. location could be kept at 1 mm for monitoring a full-size beam, then a 1 mm change in N.A. location only corresponds to about 1.7% difference in steel bar area. Therefore, the proposed SHM technique has the potential to reach higher levels of accuracy on full-size beams.

In addition to the issues associated with the use of the small beam sizes, there were other sources of error that could not be ignored. Because concrete is non-homogeneous in nature, it was difficult to make an accurate prediction of the capacity of a concrete beam. The theoretical flexural capacity calculated using the actual measured reinforcing bar area differed from the actual value by -36% to -19%. Moreover, in real life conditions, corrosion causes a decrease in a beam's capacity not only through reduced effective reinforcing bar area, but also through debonding between the steel bar and the concrete. In this set of lab experiments, the effect of loss of bond was eliminated by controlling the corrosion location and using a four-point loading set up. The use of the impressed current method for the accelerated corrosion also caused uniform corrosion around the targeted section of the steel bar, which is different from the conditions of beams that corrode under natural conditions. Therefore, even if the proposed SHM technique can estimate the effective steel bar area accurately, it would still be a challenge to estimate the beam capacity due to corrosion in real life.

Although the accuracy of the experimental results on these small-size beams was not satisfactory, many useful lessons were learned to improve the accuracy of the proposed SHM method:

1. The quality of the strain data is critical to the accuracy of estimated properties. To obtain reliable strain data, ideally the surface should be smooth, and the strain gauge should be placed in the compression zone, in the same plane and some distance away from the N.A. location.
2. The proposed SHM technique works better on beams that are less slender and have higher reinforcement ratios.
3. Within a beam's elastic deformation range, the higher the applied load, the higher the accuracy of the estimates.
4. Combining the data from two side surfaces improved the accuracy of the estimates.
5. It was found that both coefficient of determination of the best-fit strain distribution and standard deviation of the estimated N.A. locations can be used to estimate the reliability

of the estimated properties. The most accurate estimate is generally associated with a high coefficient of determination and low standard deviation values. However, using standard deviation as the screening criterion for the best estimate is more robust, as coefficient of determination can not be used as the screening criteria if only two strain gauges are used.

The experimental results were also used to demonstrate the value of SHM systems through reliability and economic analyses. Two SHM systems with different levels of uncertainty were formed and compared to each other. The standard SHM system considered only the strain data, while the enhanced SHM system considered both the strain data and data from a cover meter. It was demonstrated that the enhanced SHM system was able to increase the reliability index, and consequently, resulted in more savings in the annual worth of the life cycle costs (AWLCC) of the monitored structure. The economic analysis was conducted assuming the beams monitored in the lab were the edge beams of the University Bridge in Saskatoon, SK. Considering a total replacement cost of $1,227,744 and a discount rate of 5%, the standard SHM system provided an estimated saving of $14,803/year even when the additional costs of the SHM equipment were included. The enhanced SHM system resulted in a saving of $26,342/year including the additional cost of the cover meter.

The implementation of an SHM system does not always result in economic savings. If the condition of a structure is found to be lower than the required level of safety, the owner would incur the same replacement costs plus the cost of the SHM system. Nevertheless, the implementation of an SHM system can ensure the safety of the structure and aid the owner or engineer in the decision making regarding the maintenance and rehabilitation schedules.

6.2. Recommendations for Future Work

The following recommendations are made for further evaluating the effectiveness of the surface strain-based SHM technique:

1. Current experimental results demonstrated that the proposed SHM technique did not perform well on small-size beams; however, it has the potential to perform better on full-size beams. Therefore, it is recommended that laboratory experiments be conducted on full-size beams.

2. The corrosion that occurred in this set of lab experiments was well-controlled. The impact of loss of bond was eliminated and the corrosion occurred uniformly around the targeted section of the steel bars. Before field implementation, the proposed SHM technique should be tested on naturally corroded beams considering the debonding effect and localized pitting corrosion.
3. It is recommended that the SHM technique be tested using fibre optic sensors. The fibre optic sensors were not cost effective for the small beams used in this lab experiment; however, they would be more suitable for large scale structures. The multiplexing capability of the fibre optic sensors has the potential to convert the technique from a local SHM technique to a global one.

Lastly, more economic studies related to SHM systems using the framework demonstrated in this research study are recommended. To encourage the field implementation of SHM techniques, it is important to demonstrate the economic value associated with the implementation of SHM systems to structural owners.

REFERENCES

AbdAlla, A.N., Faraj, M.A., Samsuri, F., Rifai, D., Ali, K., and Al-Douri, Y. 2019. Challenges in improving the performance of eddy current testing: Review. Measurement and Control, **52**(1–2): 46–64. doi:10.1177/0020294018801382.

Abdo, M.A.-B. 2014. Structural Health Monitoring History , Applications and Future. *In* 1st edition. Open Science, New York.

Abdulkarem, M., Samsudin, K., Rokhani, F.Z., and A Rasid, M.F. 2020. Wireless sensor network for structural health monitoring: A contemporary review of technologies, challenges, and future direction. Structural Health Monitoring, **19**(3): 693–735. doi:10.1177/1475921719854528.

Agusta, A., Dalsgaard, J., Thöns, S., and Sørensen, J.D. 2019. Value of Information-based Inspection , Monitoring , and Damage Detection System Planning. *In* Proceedings of the 13th International Conference on Applications of Statistics and Probability in Civil Engineering, ICASP 2019 [352]. Seoul National University.

Ahmad, S. 2009. Techniques for Inducing Accelerated Corrosion of Steel in Concrete. The Arabian Journal for Science and Engineering, **34**(2): 95–104.

Albuquerque, B., Castro, D., Guimarães, F., and Ciampa, F. 2019. Comparative analysis of signal processing techniques for impedance-based SHM applications in noisy environments. Mechanical Systems and Signal Processing, **126**: 326–340. Elsevier Ltd. doi:10.1016/j.ymssp.2019.02.034.

Almusallam, A.A., and Al-gahtani, A.S. 1996. Effect of reinforcement strength corrosion on bond. Construction and Building Materials, **10**(2): 123–129.

Alonso, C., Andrade, C., Rodriguez, J., and Diez, J.M. 1998. Factors controlling cracking of concrete affected by reinforcement corrosion. Materials and Structures, **31**(7): 435–441. doi:10.1007/BF02480466.

Amafabia, D.A.M., Montalvão, D., David-West, O., and Haritos, G. 2017. A review of structural health monitoring techniques as applied to composite structures. SDHM Structural Durability and Health Monitoring, **11**(2): 91–147. doi:10.3970/sdhm.2017.011.091.

Amezquita-Sanchez, J.P., and Adeli, H. 2016. Signal Processing Techniques for Vibration-Based Health Monitoring of Smart Structures. Archives of Computational Methods in Engineering, **23**(1): 1–15. Springer Netherlands. doi:10.1007/s11831-014-9135-7.

Annamdas, V.G., and Radhika, M.A. 2013. Electromechanical impedance of piezoelectric transducers for monitoring metallic and non-metallic structures: A review of wired, wireless and energy-harvesting methods. Journal of Intelligent Material Systems and Structures, **24**(9): 1021–1042. doi:10.1177/1045389X13481254.

ASTM. 2015. A1034/A1034M-10a(2015) Standard Test Methods for Testing Mechanical Splices for Steel Reinforcing Bars. ASTM International, West Conshohocken, PA. doi:https://doi-org.cyber.usask.ca/10.1520/A1034_A1034M-10AR15.

ASTM. 2017. E917-17e1 Standard Practice for Measuring Life-Cycle Costs of Buildings and Building Systems. ASTM International, West Conshohocken, PA. doi:https://doi-org.cyber.usask.ca/10.1520/E0917-17E01.

Avci, O., Abdeljaber, O., Kiranyaz, S., Hussein, M., Gabbouj, M., and Inman, D.J. 2021. A review of vibration-based damage detection in civil structures : From traditional methods to Machine Learning and Deep Learning applications. Mechanical Systems and Signal Processing, **147**: 107077. The Authors. doi:10.1016/j.ymssp.2020.107077.

Bado, M.F., and Casas, J.R. 2021. A Review of Recent Distributed Optical Fiber Sensors Applications for Civil Engineering Structural Health Monitoring. Sensors, **21**(5): 1818. doi:10.3390/s21051818.

Bakht, B., Mufti, A.A., and Wegner, L.D. (*Editors*). 2011. Monitoring technologies for bridge management. Multi-science Publishing CO.LTD, Brentwood.

Balageas, D., Fritzen, C.-P., and Gemes, A. (*Editors*). 2006. Structural Health Monitoring. ISTE, London, UK. doi:10.1002/9780470612071.

Barthel, J., and Deiss, R. 2021. The limits of the Pourbaix diagram in the interpretation of the kinetics of corrosion and cathodic protection of underground pipelines. Materials and Corrosion, **72**(3): 434–445. doi:10.1002/maco.202011977.

Behnia, A., Kian, H., and Shiotani, T. 2014. Advanced structural health monitoring of concrete structures with the aid of acoustic emission. Construction and Building Materials, **65**: 282–302. Elsevier Ltd. doi:10.1016/j.conbuildmat.2014.04.103.

Benedetti, M. Di. 2012. Acoustic Emission in Structural Health Monitoring of Reinforced Concrete Structures. University of Miami.

Bhalla, S., and Soh, C.K. 2012. Smart Materials in Structural Health Monitoring, Control and Biomchanics. *In* Smart Materials in Structural Health Monitoring, Control and Biomechanics. Springer Berlin Heidelberg, Berlin, Heidelberg. pp. 17–51. doi:10.1007/978-3-642-24463-6_2.

Bisby, L.A., and Briglio, M.B. 2006. ISIS and SAMCO Educational Module 5: An Introduction to Structrual Health Monitoring. Winnipeg, Manitoba, Canada: ISIS Canada. Available from www.samco.org [accessed 25 April 2021].

Bolognani, D., Verzobio, A., Zonta, D., and Quigley, J. 2019. Quantifying the benefit of SHM: can the VoI be negative? *In* Sensors and Smart Structures Technologies for Civil, Mechanical, and Aerospace Systems 2019. *Edited by* K.-W. Wang, H. Sohn, H. Huang, and J.P. Lynch. SPIE. p. 52. doi:10.1117/12.2518878.

Brooks, J.J. 2015. Testing and Measurement. *In* Concrete and Masonry Movements. *Edited by* J.J. Brooks. Butterworth-Heinemann, Oxford. pp. 545–581. doi:10.1016/B978-0-12-801525-4.00016-9.

Brownjohn, J.M.W., De Stefano, A., Xu, Y.-L., Wenzel, H., and Aktan, A.E. 2011. Vibration-based monitoring of civil infrastructure: challenges and successes. Journal of Civil Structural Health Monitoring, **1**(3–4): 79–95. doi:10.1007/s13349-011-0009-5.

Calabrese, L., and Proverbio, E. 2020. A Review on the Applications of Acoustic Emission Technique in the Study of Stress Corrosion Cracking. Corrosion and Materials Degradation, **2**(1): 1–33. doi:10.3390/cmd2010001.

Cawley, P. 2018. Structural health monitoring: Closing the gap between research and industrial deployment. Structural Health Monitoring, **17**(5): 1225–1244. doi:10.1177/1475921717750047.

Chen, F., Chen, X., Xie, X., Feng, X., and Yang, L. 2013. Full-field 3D measurement using multi-camera digital image correlation system. Optics and Lasers in Engineering, **51**(9): 1044–1052. doi:10.1016/j.optlaseng.2013.03.001.

Christensen, P.N., Wegner, L.D., and Sparks, G.A. 2011. Life Cycle Savings of Structural Health Monitoring:A Value of Information Approach. *In* Monitoring Technologies for Bridge Management. *Edited by* B. Bakht, A.A. Mufti, and L.D. Wegner. Multi-science Publishing CO.LTD, Brentwood. pp. 3–31.

Cicek, V., and Al-Numan, B. 2011. Corrosion Chemistry. John Wiley & Sons, Inc., Hoboken, NJ, USA. doi:10.1002/9781118232163.

Cintrón, R., and Saouma, V. 2008. Strain Measurements with Digital Image Correlation System Vic-2D. The George E Brown, Jr. Network for Earthquake Engineering Simulation, CU-NEES-08-06,. Boulder.

City of Saskatoon. 2020. The History of our Bridges | Saskatoon.ca. Available from https://www.saskatoon.ca/moving-around/bridges/history-our-bridges [accessed 26 March 2020].

Correlated Solutions Inc. 2018. VIC-2D v6 Full-Field Deformation Measurement System. Available from https://www.correlatedsolutions.com/wp-content/uploads/2013/10/VIC-2D-Datasheet.pdf [accessed 25 February 2019].

CSA. 2014. A23.3-14 Design of Concrete Structures. CSA Group, Toronto, Ontario.

Dai, K.-Y., Liu, C., Lu, D.-G., and Yu, X.-H. 2020. Experimental investigation on seismic behavior of corroded RC columns under artificial climate environment and electrochemical chloride extraction: A comparative study. Construction and Building Materials, **242**: 118014. Elsevier Ltd. doi:10.1016/j.conbuildmat.2020.118014.

Das, S., and Patro, P.S.S.K. 2016. Vibration-based damage detection techniques used for health monitoring of structures : a review. Journal of Civil Structural Health Monitoring, **6**(3): 477–507. Springer Berlin Heidelberg. doi:10.1007/s13349-016-0168-5.

Das, S., and Saha, P. 2018. Structural health monitoring techniques implemented on IASC–ASCE benchmark problem: a review. Journal of Civil Structural Health Monitoring, **8**(4): 689–718. Springer Berlin Heidelberg. doi:10.1007/s13349-018-0292-5.

Diamantidis, D., Sykora, M., and Sousa, H. 2019. Quantifying the Value of Structural Health Information for Decision Support: Guide for Practising Engineers. COST Action TU 1402. Available from https://www.cost-tu1402.eu/-/media/Sites/cost-tu1402/Documents/deliverables/Guidelines/COST-Action-TU1402-Guidelines_pract_engineers.

Dyke, S.J., Bernal, D., Beck, J., and Ventura, C. 2002. Experimental Phase II of the Structural Health Monitoring Benchmark Problem. *In* 15th ASCE Engineering Mechanics Conference. New York.

Elwalwal, H.M., Mahzan, S.B.H., and Abdalla, A.N. 2017. Crack Inspection Using Guided Waves (GWs)/Structural Health Monitoring (SHM): Review. Journal of Applied Sciences, **17**(8): 415–428. doi:10.3923/jas.2017.415.428.

Farrar, C.R., and Worden, K. 2007. An introduction to structural health monitoring. Philosophical Transactions of the Royal Society A: Mathematical, Physical and Engineering Sciences, **365**(1851): 303–315. doi:10.1098/rsta.2006.1928.

Flynn, E.B., and Todd, M.D. 2010. A Bayesian approach to optimal sensor placement for structural health monitoring with application to active sensing. Mechanical Systems and Signal Processing, **24**(4): 891–903. Elsevier. doi:10.1016/j.ymssp.2009.09.003.

Frangopol, D.M., and Messervey, T.B. 2011. Effect of monitoring on the reliability of structures. *In* Monitoring Technologies for Bridge Management. *Edited by* B. Bakht, A.A. Mufti, and L.D. Wegner. Multi-science Publishing CO.LTD. pp. 515–560.

Fu, C., Jin, N., Ye, H., Liu, J., and Jin, X. 2018. Non-uniform corrosion of steel in mortar induced by impressed current method: An experimental and numerical investigation. Construction and Building Materials, **183**: 429–438. Elsevier Ltd. doi:10.1016/j.conbuildmat.2018.06.183.

Furtner, P., Stöger, M., and Schreyer, M. 2013. SHM data – management, treatment, analysis and interpretation – a solution for permanent monitoring systems. *In* Safety, Reliability, Risk and Life-Cycle Performance of Structures and Infrastructures. CRC Press, New York. pp. 2559–2564. doi:10.1201/b16387-369.

GB 50982. 2014. Technical code for monitoring of building and bridge structures. Ministry of Housing and Urban-Rural Development of China, and the General Administration of Quality Supervision, Inspection and Quarantine of China, Beijing.

Ghoni, R., Dollah, M., Sulaiman, A., and Ibrahim, F.M. 2014. Defect Characterization Based on Eddy Current Technique: Technical Review. Advances in Mechanical Engineering, **6**. doi:10.1155/2014/182496.

Girija, K., and Menon, D. 2011. Reduction in flexural strength in rectangular RC beams due to slenderness. Engineering Structures, **33**(8): 2398–2406. Elsevier Ltd. doi:10.1016/j.engstruct.2011.04.014.

Del Grosso, A.E. 2014. Structural Health Monitoring Standards. *In* IABSE Symposium, Madrid 2014: Engineering for Progress, Nature and People. International Association for Bridge and Structural Engineering (IABSE), Zurich, Switzerland. pp. 2991–2998. doi:10.2749/222137814814069804.

Guan, D., Chenxi, X., and Han, S. 2011. Testing study on concrete surface strain using electrical-resistance strain-measurement method. Research and Exploration in Laboratory, **30**(1): 30–32.

Güemes, A., Fernández-López, A., Díaz-Maroto, P., Lozano, A., and Sierra-Perez, J. 2018.

Structural Health Monitoring in Composite Structures by Fiber-Optic Sensors. Sensors, **18**(4): 1094. doi:10.3390/s18041094.

Güemes, A., Fernandez-Lopez, A., Pozo, A.R., and Sierra-Pérez, J. 2020. Structural Health Monitoring for Advanced Composite Structures: A Review. Journal of Composites Science, **4**(1): 13. doi:10.3390/jcs4010013.

Güemes, J.A., and Sierra-Pérez, J. 2013. Fiber Optics Sensors. *In* New Trends in Structural Health Monitoring. *Edited by* W. Ostachowicz and J.A. Güemes. Springer Vienna, Vienna. pp. 265–316. doi:10.1007/978-3-7091-1390-5_5.

Harms, T., Sedigh, S., and Bastianini, F. 2010. Structural Health Monitoring of Bridges Using Wireless Sensor Networks. IEEE Instrumentation and Measurement Magazine, **13**(6): 14–18. doi:10.1109/MIM.2010.5669608.

Hassan, M., Afzal, B., Kabir, S., and Sidek, O. 2012. An In-depth Review : Structural Health Monitoring using Fiber Optic Sensor. IETE Technical Review, **29**: 105–114. doi:10.4103/0256-4602.95383.

Hensley, S., Christensen, M., Small, S., Archer, D., Lakes, E., and Rogge, R. 2017. Digital image correlation techniques for strain measurement in a variety of biomechanical test models. Acta of Bioengineering and Biomechanics Original paper, **19**(3). doi:10.5277/ABB-00785-2016-04.

Hild, F., and Roux, S. 2006. Digital Image Correlation: from Displacement Measurement to Identification of Elastic Properties - a Review. Strain, **42**(2): 69–80. doi:10.1111/j.1475-1305.2006.00258.x.

Hong, S., Zheng, F., Shi, G., Li, J., Luo, X., Xing, F., Tang, L., and Dong, B. 2020. Determination of impressed current efficiency during accelerated corrosion of reinforcement. Cement and Concrete Composites, **108**: 103536. Elsevier Ltd. doi:10.1016/j.cemconcomp.2020.103536.

Housner, G.W., Bergman, L.A., Caughey, T.K., Chassiakos, A.G., Claus, R.O., Masri, S.F., Skelton, R.E., Soong, T.T., Spencer, B.F., and Yao, J.T.P. 1997. Structural control: Past, present, and future. Journal of Engineering Mechanics - ASCE, **123**(9): 897–971. American Society of Civil Engineers (ASCE). doi:10.1061/(ASCE)0733-9399(1997)123:9(897).

Huang, Y.H., Liu, L., Sham, F.C., Chan, Y.S., and Ng, S.P. 2010. Optical strain gauge vs. traditional strain gauges for concrete elasticity modulus determination. Optik, **121**(18): 1635–1641. Urban & Fischer. doi:10.1016/j.ijleo.2009.03.002.

Imam, A., Anifowose, F., and Azad, A.K. 2015. Residual Strength of Corroded Reinforced Concrete Beams Using an Adaptive Model Based on ANN. International Journal of Concrete Structures and Materials, **9**(2): 159–172. Korea Concrete Institute. doi:10.1007/s40069-015-0097-4.

Isah, B.W., Mohamad, H., Ahmad, N.R., Harahap, I.S.H., and Al-Bared, M.A.M. 2020. Uniaxial compression test of rocks: Review of strain measuring instruments. *In* IOP Conference Series: Earth and Environmental Science. IOP Publishing, Langkawi. doi:10.1088/1755-1315/476/1/012039.

Jeong, S., Hou, R., Lynch, J.P., Sohn, H., and Law, K.H. 2019. A scalable cloud-based cyberinfrastructure platform for bridge monitoring. Structure and Infrastructure Engineering, **15**(1): 82–102. Taylor & Francis. doi:10.1080/15732479.2018.1500617.

Jia, J., Zhang, X., Cai, L., Zhang, S., and Tu, Y. 2015. Sensors for high-temperature displacement, deformation, and strain measurement: A review : Jiuhong Jia. *In* Structural Health Monitoring and Integrity Management. *Edited by* K. Ding, S. Yuan, and Z. Wu. CRC Press, London. p. 25. Available from https://books.google.ca/books?id=k8bECQAAQBAJ&pg=PA25&lpg=PA25&dq=Sensors+for+high-temperature+displacement,+deformation,+and+strain+measurement:+A+review :+Jiuhong+Jia.+Structural+Health+Monitoring+and+Integrity+Management,+25.&source=bl&ots=Gurk77K5Sa&s.

Jiao, S., Cheng, L., Li, X., Li, P., and Ding, H. 2016. Monitoring fatigue cracks of a metal structure using an eddy current sensor. EURASIP Journal on Wireless Communications and Networking, **2016**(1): 188. EURASIP Journal on Wireless Communications and Networking. doi:10.1186/s13638-016-0689-y.

Johnson, E.A., Lam, H.F., Beck, J.L., and Katafygiotis, L.S. 2002. The Phase I IASC-ASCE Structural Health Monitoring Benchmark Problem using Simulated Data. ASCE Journal of Engineering Mechanics, **130**(1): 3–15. doi:10.1061/(ASCE)0733-9399(2004)130:1(3).

Jones, D.A. 1996. Principles and Prevention of Corrosion. Upper Saddle River, NJ : Prentice Hall. Available from https://books.google.ca/books?id=i8pRAAAAMAAJ.

Junior, P.O., Conte, S., D'Addona, D.M., Aguiar, P., and Bapstista, F. 2020. An improved impedance-based damage classification using Self-Organizing Maps. Procedia CIRP, **88**: 330–334. Elsevier B.V. doi:10.1016/j.procir.2020.05.057.

Khan, M.S., Caprani, C., Ghosh, S., and Ghosh, J. 2021. Value of strain-based structural health monitoring as decision support for heavy load access to bridges. Structure and Infrastructure Engineering, **0**(0): 1–16. Taylor & Francis. doi:10.1080/15732479.2021.1890140.

Khan, M.T.I. 2018. Structural Health Monitoring by Acoustic Emission Technique. *In* Structural Health Monitoring from Sensing to Processing. *Edited by* M.A. Wahab, Y.L. Zhou, and N.M.M. Maia. IntechOpen. doi:10.5772/intechopen.79483.

Khoo, S.-W., Karuppanan, S., and Tan, C.-S. 2016. A Review of Surface Deformation and Strain Measurement Using Two-Dimensional Digital Image Correlation. Metrology and Measurement Systems, **23**(3): 461–480. doi:10.1515/mms-2016-0028.

Klerk, W.J., Schweckendiek, T., den Heijer, F., and Kok, M. 2019. Value of Information of Structural Health Monitoring in Asset Management of Flood Defences. Infrastructures, **4**(3): 56. doi:10.3390/infrastructures4030056.

Koch, G., Varney, J., Thompson, N., Moghissi, O., Gould, M., and Payer, J. 2016. International Measures of Prevention , Application , and Economics of Corrosion Technologies Study. Houston.

Kralovec, C., and Schagerl, M. 2020. Review of Structural Health Monitoring Methods

Regarding a Multi-Sensor Approach for Damage Assessment of Metal and Composite Structures. Sensors, **20**(3): 826. doi:10.3390/s20030826.

Lan, C.M., and Liu, W.F. 2013. Structural Health Monitoring Cloud and its Applications for Large-Scale Infrastructures. Applied Mechanics and Materials, **330**: 418–425. Trans Tech Publications Ltd. doi:10.4028/www.scientific.net/AMM.330.418.

Larsson Ivanov, O., Björnsson, I., Honfi, D., and Leander, J. 2021. The practical value of structural health information for time dependence in bridge maintenance. Structure and Infrastructure Engineering, **0**(0): 1–16. Taylor & Francis. doi:10.1080/15732479.2021.1890141.

Li, H.-N., Yi, T.-H., Ren, L., Li, D.-S., and Huo, L.-S. 2014. Reviews on innovations and applications in structural health monitoring for infrastructures. Structural Monitoring and Maintenance, **1**(1): 1–45. doi:10.12989/smm.2014.1.1.001.

Li, J., Xie, X., Yang, G., Zhang, B., Siebert, T., and Yang, L. 2017. Whole-field thickness strain measurement using multiple camera digital image correlation system. Optics and Lasers in Engineering, **90**: 19–25. Elsevier Ltd. doi:10.1016/j.optlaseng.2016.09.012.

Long, L., Alcover, I.F., and Thöns, S. 2020. Utility analysis for SHM durations and service life extension of welds on steel bridge deck. Structure and Infrastructure Engineering, **0**(0): 1–13. Taylor & Francis. doi:10.1080/15732479.2020.1866026.

López-Higuera, J.M., Rodriguez, L., Quintela, A., Cobo, A., Madruga, F.J., Conde, O.M., Lomer, M., Quintela, M.A., and Mirapeix, J. 2010. Fiber optics in structural health monitoring. *In* Proceedings of SPIE 7853, Advanced Sensor Systems and Applications IV. *Edited by* B. Culshaw, Y. Liao, A. Wang, X. Bao, X. Fan, and L. Zhang. Beijing. p. 78530D. doi:10.1117/12.876192.

Loupos, K., and Amditis, A. 2017. Structural health monitoring fiber optic sensors. *In* Fiber Optic Sensors Current Status and Future Possibilities. *Edited by* I.R. Matias, S. Ikezawa, and J.C. Editors. Springer International Publishing, Switzerland. pp. 185–206. doi:10.1007/978-3-319-42625-9_9.

El Maaddawy, T.A., and Soudki, K.A. 2003. Effectiveness of Impressed Current Technique to Simulate Corrosion of Steel Reinforcement in Concrete. Journal of Materials in Civil Engineering, **15**(1): 41–47. doi:10.1061/(asce)0899-1561(2003)15:1(41).

Malumbela, G., Alexander, M., and Moyo, P. 2010. Cement and Concrete Research Interaction between corrosion crack width and steel loss in RC beams corroded under load. Cement and Concrete Research, **40**(9): 1419–1428. Elsevier Ltd. doi:10.1016/j.cemconres.2010.03.010.

Malumbela, G., Alexander, M., and Moyo, P. 2012. A step towards standardising accelerated corrosion tests on laboratory reinforced concrete specimens. Journal of the South African Institution of Civil Engineering, **54**(2): 78–85.

Manco, P., Caterino, M., Macchiaroli, R., Rinaldi, M., and Fera, M. 2021. Aircraft Maintenance: Structural Health Monitoring Influence on Costs and Practices. Macromolecular Symposia, **396**(1): 2000302. doi:10.1002/masy.202000302.

Mangat, P.S., and Elgarf, M.S. 1999. Flexural Strength of Concrete Beams with Corroding

Reinforcement. ACI Structural Journal, **96**(1): 149–158. doi:10.14359/606.

Mansour, A.E., Jan, H.Y., Member, L., Zigelman, C.I., Member, A., Chen, Y.N., Harding, S.J., and Member, A. 1984. Implementation of Reliability Methods to Marine Structures. Society of Naval Architects and Marine Engineers, **92**: 353–382.

Manthei, G., and Plenkers, K. 2018. Review on In Situ Acoustic Emission Monitoring in the Context of Structural Health Monitoring in Mines. Applied Sciences, **8**(9): 1595. doi:10.3390/app8091595.

Maraveas, C., and Bartzanas, T. 2021. Sensors for Structural Health Monitoring of Agricultural Structures. Sensors, **21**(1): 314. doi:10.3390/s21010314.

Mattsson, H.-Ä., Sundquist, H., and Silfwerbrand, J. 2007. The Real Service Life and Repair Costs for Bridge Edge Beams. Restoration of Buildings and Monuments, **13**(4): 215–228. De Gruyter. doi:10.1515/rbm-2007-6140.

Mba, D. 2006. Development of Acoustic Emission Technology for Condition Monitoring and Diagnosis of Rotating Machines: Bearings, Pumps, Gearboxes, Engines, and Rotating Structures. The Shock and Vibration Digest, **38**(1): 3–16. doi:10.1177/0583102405059054.

MeasureX. 2015. MSM31 DEMEC Mechanical Strain Gauge. Melbourne. Available from www.MeasureX.com.au [accessed 25 July 2020].

Michie, C. 2000. Optical Fiber Sensors for Advanced Composite Materials. *In* Comprehensive Composite Materials, 1st edition. *Edited by* A. Kelly and C.H. Zweben. Amsterdam, New York. pp. 475–491. doi:10.1016/B0-08-042993-9/00154-6.

Mitra, M., and Gopalakrishnan, S. 2016. Guided wave based structural health monitoring: A review. Smart Materials and Structures, **25**(5): 053001. IOP Publishing. doi:10.1088/0964-1726/25/5/053001.

Moreu, F., Li, X., Li, S., and Zhang, D. 2018. Technical Specifications of Structural Health Monitoring for Highway Bridges: New Chinese Structural Health Monitoring Code. Frontiers in Built Environment, **4**(March): 10. doi:10.3389/fbuil.2018.00010.

Motra, H.B., Hildebrand, J., and Dimmig-Osburg, A. 2014. Assessment of strain measurement techniques to characterise mechanical properties of structural steel. Engineering Science and Technology, an International Journal, **17**(4): 260–269. Elsevier Ltd. doi:10.1016/j.jestch.2014.07.006.

Mouret, M., Bascoul, A., and Escadeillas, G. 1997. Drops in concrete strength in summer related to the aggregate temperature. Cement and Concrete Research, **27**(3): 345–357. doi:10.1016/S0008-8846(97)00038-0.

Mufti, A.A. 2001. Guidelines for structural health monitoring. ISIS Canada, Winnipeg.

Na, W., and Baek, J. 2018. A Review of the Piezoelectric Electromechanical Impedance Based Structural Health Monitoring Technique for Engineering Structures. Sensors, **18**(5): 1307. doi:10.3390/s18051307.

Neubrex. 2020. NBX-8100 (Specs). Available from https://www.neubrex.com/htm/products/pro-

nbx8200.htm [accessed 21 September 2020].

NIST/SEMATECH. 2012. Engineering Statistics Handbook. doi:https://doi.org/10.18434/M32189.

Omega. 2016. Practical Strain Gage Measurements. *In* Omega Engineering. St-Eustache QC. Available from https://www.omega.co.uk/techref/pdf/StrainGage_Measurement.pdf.

Paliwal, N., and John, J. 2017. Lossy Mode Resonance Based Fiber Optic Sensors. *In* Fiber Optic Sensors Current Status and Future Possibilities. *Edited by* I.R. Matias, S. Ikezawa, and J. Corres. Springer International Publishing, Switzerland. pp. 31–50. doi:10.1007/978-3-319-42625-9_2.

Palumbo, N. 1991. Accelerated corrosion testing of steel reinforcement in concrete. McGill University.

Pan, B. 2018. Digital image correlation for surface deformation measurement: historical developments, recent advances and future goals. Measurement Science and Technology, **29**(8). IOP Publishing. doi:10.1088/1361-6501/aac55b.

Papadimitriou, C. 2004. Optimal sensor placement methodology for parametric identification of structural systems. Journal of Sound and Vibration, **278**(4–5): 923–947. doi:10.1016/j.jsv.2003.10.063.

Peeters, B., and De Roeck, G. 2001. One-year monitoring of the Z24-Bridge: environmental effects versus damage events. Earthquake Engineering & Structural Dynamics, **30**(2): 149–171. doi:10.1002/1096-9845(200102)30:2<149::AID-EQE1>3.0.CO;2-Z.

Pepe, V., De Angelis, A., and Pecce, M.R. 2019. Damage assessment of an existing RC infilled structure by numerical simulation of the dynamic response. Journal of Civil Structural Health Monitoring, **9**(3): 385–395. Springer Berlin Heidelberg. doi:10.1007/s13349-019-00340-z.

Pereira, A.A.C., and D'Almeida, J.R.M. 2019. Development of a Low-Cost Digital Image Correlation System to Evaluate the Behaviour of Thermoplastics at Large Deformation. *In* The 14th International Congress on Chemical and Process Engineering. *Edited by* S. Pierucci, J.J. Klemeš, and L. Piazza. AIDIC, Bologna. doi:10.3303/CET1974181.

Peters, W.H., and Ranson, W.F. 1982. Digital Imaging Techniques In Experimental Stress Analysis. Optical Engineering, **21**(3): 427–431. SPIE. doi:10.1117/12.7972925.

Proceq. 2007. RebaR detection system. Available from http://infrastruct.ie/wp-content/uploads/2013/04/Proceq-Profometer-5+.pdf [accessed 21 May 2018].

Qin, J., Thöns, S., and Faber, M.H. 2015. On the value of SHM in the context of service life integrity management. Proceedings of the 12th International Conference on Applications of Statistics and Probability in Civil Engineering,. Vancouver, Canada. doi:10.14288/1.0076291.

Racutanu, G. 1999. The Real Service Life of Road Bridges in Sweden - A Case Study. *In* Durability of Building Materials and Components 8. *Edited by* M.A. Lacasse and D.J. Vanier. Institure for Research in Construction, Ottawa ON. pp. 56–70. Available from

https://www.irbnet.de/daten/iconda/CIB2042.pdf [accessed 24 February 2019].

Rao, A.R.M., and Anandakumar, G. 2007. Optimal placement of sensors for structural system identification and health monitoring using a hybrid swarm intelligence technique. Smart Materials and Structures, **16**(6): 2658–2672. IOP Publishing. doi:10.1088/0964-1726/16/6/071.

Revathi, P., and Menon, D. 2008. Slenderness Effects in Reinforced Concrete Beams. (104).

Rueden, C.T., Schindelin, J., Hiner, M.C., DeZonia, B.E., Walter, A.E., Arena, E.T., and Eliceiri, K.W. 2017. ImageJ2: ImageJ for the next generation of scientific image data. BMC Bioinformatics, **18**(1): 529. doi:10.1186/s12859-017-1934-z.

Rytter, A. 1993. Vibrational Based Inspection of Civil Engineering Structures. Dept. of Buliding Technology and Structural Engineering, Aalborg University. Available from http://vbn.aau.dk/files/18588667/Vibrational_Based_Inspection_of_Civil_Engineering_Structures [accessed 20 May 2018].

SAE. 2013, September. Guidelines for Implementation of Structural Health Monitoring on Fixed Wing Aircraft (ARP6461). Aerospace Industry Steering Committee On Structural Health, Aerospace Industry Steering Committee On Structural Health. doi:https://doi.org/10.4271/ARP6461.

Samad, A.A., Ramadass, S., and Mathews, M.E. 2016. Study of Structural Behaviour of RC Slender Beams. **39**(2): 88–93.

Di Sante, R. 2015. Fibre Optic Sensors for Structural Health Monitoring of Aircraft Composite Structures: Recent Advances and Applications. Sensors, **15**(8): 18666–18713. doi:10.3390/s150818666.

Searls, O., Zhao, Z., Couch, A.L., and Sanayei, M. 2019. Real-Time Distributed Cloud Computing Architecture for Structural Health Monitoring. *In* Structures Congress 2019. American Society of Civil Engineers, Reston, VA. pp. 38–49. doi:10.1061/9780784482230.005.

Seo, J., Hu, J.W., and Lee, J. 2016. Summary Review of Structural Health Monitoring Applications for Highway Bridges. Journal of Performance of Constructed Facilities, **30**(4): 04015072. doi:10.1061/(ASCE)CF.1943-5509.0000824.

Shaladi, R., Alatshan, F., and Yang, C. 2015. An Overview on the Applications of Structural Health Monitoring Using Wireless Sensor Networks in Bridge Engineering. *In* International Conference on Advances in Science, Engineering, Technology and Natural Resources (ICASETNR-15) Aug. 27-28, 2015 Kota Kinabalu (Malaysia). International Institute of Chemical, Biological & Environmental Engineering. doi:10.15242/IICBE.C0815017.

Sharif Khodaei, Z., and Aliabadi, M.H. 2016. A Multi-Level Decision Fusion Strategy for Condition Based Maintenance of Composite Structures. Materials, **9**(9): 790. doi:10.3390/ma9090790.

Shipilov, S. 2016. What Corrosion Costs Canada : Or , Can We Afford to Ignore Corrosion ? *In* Annual Conference of Metallurgists of CIM. *Edited by* C. Barry and P. Wanjara. Sudbury.

Skokandić, D., and Mandić Ivanković, A. 2020. Value of additional traffic data in the context of bridge service-life management. Structure and Infrastructure Engineering,: 1–20. Taylor & Francis. doi:10.1080/15732479.2020.1857795.

Sophian, A., Tian, G., and Fan, M. 2017. Pulsed Eddy Current Non-destructive Testing and Evaluation: A Review. Chinese Journal of Mechanical Engineering, **30**(3): 500–514. Chinese Mechanical Engineering Society. doi:10.1007/s10033-017-0122-4.

Sousa, H., Wenzel, H., and Thöns, S. 2019. Quantifying the Value of Structural Health Information for Decision Support: Guide for Operators. COST Action TU 1402. Available from https://www.cost-tu1402.eu/-/media/Sites/cost-tu1402/Documents/deliverables/Guidelines/COST-Action-TU1402-Guidelines_pract_engineers.

Stansbury, E.E., and Buchanan, R.A. 2000. Fundamentals of Electrochemical Corrosion. ASM International, Ohio. Available from https://books.google.ca/books?id=baHwfLpWpP8C.

Strantza, M., Aggelis, D.G., de Baere, D., Guillaume, P., and van Hemelrijck, D. 2015. Evaluation of SHM system produced by additive manufacturing via acoustic emission and other NDT methods. Sensors (Switzerland), **15**(10): 26709–26725. doi:10.3390/s151026709.

Sun, H., and Büyüköztürk, O. 2015. Optimal sensor placement in structural health monitoring using discrete optimization. Smart Materials and Structures, **24**(12): 125034. doi:10.1088/0964-1726/24/12/125034.

Sutton, M., Wolters, W., Peters, W., Ranson, W., and McNeill, S. 1983. Determination of displacements using an improved digital correlation method. Image and Vision Computing, **1**(3): 133–139. doi:10.1016/0262-8856(83)90064-1.

Sykora, M., Diamantidis, D., Müller, D., and Sousa, H. 2020. A practical guide on the quantification of value of information gained by structural health monitoring and application to historic masonry structures. Structure and Infrastructure Engineering, **0**(0): 1–15. Taylor & Francis. doi:10.1080/15732479.2020.1857793.

Taheri, S. 2019. A review on five key sensors for monitoring of concrete structures. Construction and Building Materials, **204**: 492–509. Elsevier Ltd. doi:10.1016/j.conbuildmat.2019.01.172.

Thöns, S. 2013. SHM for Life Cycle Benefits. Bundesanstalt fuer Materialforschung und -pruefung (BAM), Berlin, Germany. Available from https://opus4.kobv.de/opus4-bam/frontdoor/index/index/docId/29181.

Thöns, S. 2019. Quantifying the Value of Structural Health Information for Decision Support : Guide for Scientists. COST Action TU 1402.

Thöns, S., and Faber, M.H. 2013. Assessing the value of structural health monitoring. *In* ICOSSAR'13 - 11th International conference on structural safety and reliability - Safety, reliability, risk and life-cycle performance of structures and infrastructures. *Edited by* G. Deodatis, B.R. Ellingwood, and D.M. Frangopol. CRC Press, Berlin. pp. 1–8. Available from https://opus4.kobv.de/opus4-bam/frontdoor/index/index/docId/28728.

Thöns, S., Faber, M.H., and Rücker, W. 2013. Life Cycle Cost Optimized Monitoring Systems

for Offshore Wind Turbine Structures. IRIS Industrial Safety and Life Cycle Engineering: Technologies / Standards / Applications,: 75–90.

Tokyo Measureing Instruments Lab. 2021. Concrete Material Use Strain Gauge: P Series Polyester Wire Strain Gauge. Available from https://tml.jp/e/product/strain_gauge/concrete.html#p_list.html [accessed 6 June 2021].

Tonelli, D., Luchetta, M., Rossi, F., Migliorino, P., and Zonta, D. 2020. Structural Health Monitoring Based on Acoustic Emissions: Validation on a Prestressed Concrete Bridge Tested to Failure. Sensors, **20**(24): 7272. doi:10.3390/s20247272.

Tsvetanov, F.A. 2021. Storing data from sensors networks. IOP Conference Series: Materials Science and Engineering, **1032**: 012012. IOP Publishing. doi:10.1088/1757-899X/1032/1/012012.

Wang, P., Yan, Y., Tian, G.Y., Bouzid, O., and Ding, Z. 2012. Investigation of Wireless Sensor Networks for Structural Health Monitoring. Journal of Sensors, **2012**: 1–7. doi:10.1155/2012/156329.

Warsi, Z.H., Irshad, S.M., Khan, F., Shahbaz, M.A., Junaid, M., and Amin, S.U. 2019. Sensors for Structural Health Monitoring: A Review. *In* 2019 Second International Conference on Latest trends in Electrical Engineering and Computing Technologies (INTELLECT). IEEE. pp. 1–6. doi:10.1109/INTELLECT47034.2019.8955453.

Wevers, M., and Lambrighs, K. 2009. Applications of Acoustic Emission for SHM: A Review. *In* Encyclopedia of Structural Health Monitoring. American Cancer Society. doi:https://doi.org/10.1002/9780470061626.shm011.

Worden, K., and Burrows, A.P. 2001. Optimal sensor placement for fault detection. Engineering Structures, **23**: 885–901.

Xiang, J., Yang, Z., and Aguilar, J.L. 2018. Structural health monitoring for mechanical structures using multi-sensor data. International Journal of Distributed Sensor Networks, **14**(9). doi:10.1177/1550147718802019.

Yamaguchi, I. 1981. A laser-speckle strain gauge. Journal of Physics E: Scientific Instruments, **14**(11): 1270–1273. IOP Publishing. doi:10.1088/0022-3735/14/11/012.

Yan, R., Chen, X., and Mukhopadhyay, S.C. 2017a. Advanced Signal Processing for Structural Health Monitoring. *In* Structural Health Monitoring. Smart Sensors, Measurement and Instrumentation. Springer, Cham. pp. 1–11. doi:10.1007/978-3-319-56126-4_1.

Yan, S., Ma, H., Li, P., Song, G., and Wu, J. 2017b. Development and Application of a Structural Health Monitoring System Based on Wireless Smart Aggregates. Sensors, **17**(7): 1641. Multidisciplinary Digital Publishing Institute (MDPI). doi:10.3390/s17071641.

Yang, Y., Li, Q., and Yan, B. 2017. Specifications and applications of the technical code for monitoring of building and bridge structures in China. Advances in Mechanical Engineering, **9**(1): 168781401668427. doi:10.1177/1687814016684272.

Yi, T.H., and Li, H.N. 2012. Methodology developments in sensor placement for health monitoring of civil infrastructures. International Journal of Distributed Sensor Networks,

2012. doi:10.1155/2012/612726.

Yin, J.-H., Zhu, H.-H., Yeung, A.T., Yin, J.H., Zhu, H.H., Jin, W., Yeung, A.T., and Mak, L.M. 2007. Performance Evaluation of Electrical Strain Gauges and Optical Fiber Sensors in Field Soil Nail Pullout Tests. *In* The HKIE Geotechnical Division Annual Seminar. Available from https://www.researchgate.net/publication/253081852 [accessed 19 October 2020].

Yuan, Y., Ji, Y., and Shah, S.P. 2007. Comparison of Two Accelerated Corrosion Techniques for Concrete Structures. ACI Structural Journal, **104**(3): 344–347. doi:10.14359/18624.

Zambon, I., Santamaria Ariza, M.P., Campos e Matos, J., and Strauss, A. 2020. Value of Information (VoI) for the Chloride Content in Reinforced Concrete Bridges. Applied Sciences, **10**(2): 567. doi:10.3390/app10020567.

Zhang, W., Lu, D., Qin, J., Thöns, S., and Faber, M.H. 2021. Value of information analysis in civil and infrastructure engineering: a review. Journal of Infrastructure Preservation and Resilience, **2**(1): 16. Journal of Infrastructure Preservation and Resilience. doi:10.1186/s43065-021-00027-0.

Zhang, W.Y., Zhang, R.Y., and Xi, L. 2012. Corrosion of Reinforced Concrete in Accelerated Tests. Advanced Materials Research, **610–613**: 485–489. doi:10.4028/www.scientific.net/AMR.610-613.485.

Zhao, X., Yu, Y., Li, M., and Ou, J. 2015. Cloud-structural health monitoring based on smartphone Cloud-Structural Health Monitoring based on smartphone. *In* International Conferences on Vibroengineering. pp. 241–246.

Zhou, L., Yan, G., Wang, L., and Ou, J. 2013. Review of Benchmark Studies and Guidelines for Structural Health Monitoring. Advances in Structural Engineering, **16**(7): 1187–1206. doi:10.1260/1369-4332.16.7.1187.

Zhou, Z. 2006. Vibration-based Damage Detection of Simple Bridge Superstructures. University of Saskatchewan. Available from https://ecommons.usask.ca/bitstream/handle/10388/etd-12192006-155541/zhou_z.pdf?sequence=1&isAllowed=y [accessed 20 May 2018].

Zonta, D., Glisic, B., and Adriaenssens, S. 2014. Value of information: impact of monitoring on decision-making. Structural Control and Health Monitoring, **21**(7): 1043–1056. doi:10.1002/stc.1631.

APPENDIX A Companion Specimen Test Results

As the steel bars used in the concrete beams were not from the same heat, their ultimate tensile strengths were determined through tensile tests conducted in the laboratory. Each steel bar was cut into three short sections (30 to 40 cm long) to be used as tensile test samples. The Instron 600DX UTM was used along with a pre-programmed test procedure in conformance with the ASTM A1034 (ASTM 2015).

The rest of the No.15 bar was cut into three pieces and used as reinforcement for Batch 1 beams. However, since Batch 2 and 3 beams were longer, each steel bar could only be used for two beams. The beam number that each steel bar was put into is listed in Table A.1, together with the mean and standard deviation of their tensile strengths.

The slump test results and the cast date of each batch of concrete are presented in Table A.2. The compressive testing results for the concrete cylinders are summarized in Table. A.3. The strengths for Batch 2 and Batch 3 were close to expected, however, for Batch 1 the concrete cylinders demonstrated high compressive strengths (with a mean of 55.9 MPa) in the pre-corrosion loading tests. The post-corrosion loading test was performed 110-day following the beam casting, and the compressive strength had dropped to 45.1 MPa. Generally concrete gains strength as it cures, and it is very rare that the concrete strength drops over time. It was found that the compressive strength of concrete may drop 15% to 17% for hot weather concreting (Mouret et al. 1997). However, the beams used in this experiment were cured in a humidity room at room temperature. Thus, it is unclear why the concrete compressive strength had dropped with time.

The outlier is defined as any individual specimen having more than 15% higher or lower than the average of the set. Note an outlier was identified during the pre-corrosion compressive cylinder testing for Batch 2.

Table A.1. Steel Bar Tensile Test Results.

Steel Bar #	Sample #	Yield Strength (Mpa)	Ultimate Tensile Strength (Mpa)	Beam #
No.15 bar	1	481.8	606.4	Batch 1, Beam 1 Batch 1, Beam 2 Batch 1, Beam 3
	2	481.4	607.7	
	3	483.5	608.1	
	Mean	482.3	607.4	
	Standard Deviation	1.1	0.9	
No.10 bar-1	1	445.6	668.3	Batch 2, Beam 1 Batch 2, Beam 2
	2	443.8	666.3	
	3	445.4	666.1	
	Mean	444.9	666.9	
	Standard Deviation	1.0	1.2	
No. 10 bar-2	1	448.5	667.4	Batch 2, Beam 3 Batch 3, Beam 1
	2	447.3	660.7	
	3	450.0	666.3	
	Mean	448.6	664.8	
	Standard Deviation	1.3	3.6	
No.10 bar-3	1	435.2	646.9	Batch 3, Beam 2 Batch 3, Beam 3
	2	439.0	650.3	
	3	437.7	650.6	
	Mean	437.3	649.3	
	Standard Deviation	1.9	2	

Table A.2. Concrete Slump Test Results on the Day of Casting.

Batch #	Cast Date	Slump (mm)
Batch 1	July 26, 2018	46
Batch 2	December 5, 2018	78
Batch 3	December 21, 2018	76

Table A.3. Concrete Compressive Testing Result.

Phase	Cylinder #	Test Date	Age (day)	Strength (MPa)	Modulus (GPa)
Batch 1 Pre-corrosion	1	August 23, 2018	28	58.2	31.6
	2	August 23, 2018	28	54.1	31.0
	3	August 23, 2018	28	56.4	33.0
	4	August 23, 2018	28	58.1	34.5
	5	August 23, 2018	28	53.7	32.9
	6	August 24, 2018	29	54.6	34.7
		Mean		55.9	32.9
		Standard Deviation		2.0	1.5
Batch 1 Post-corrosion	1	November 13, 2018	110	36.7	30.0
	2	November 13, 2018	110	39.4	34.3
	3	November 13, 2018	110	47.5	33.7
	4	November 13, 2018	110	57.0	33.0
	5	November 14, 2018	111	44.9	34.0
	6	November 14, 2018	111	45.0	-*
		Mean		45.1	33.0
		Standard Deviation		7.1	1.7
Batch 2 Pre-corrosion	1	January 2, 2019	28	26.2 (outlier)	24.8
	2	January 2, 2019	28	36.2	24.7
	3	January 3, 2019	29	38.3	25.9
	4	January 3, 2019	29	36.6	24.6
	5	January 3, 2019	29	36.5	24.7
	6	January 3, 2019	29	36.8	26.0
		Mean		36.9	25.1
		Standard Deviation		0.8	0.7

* Data missing due to dial gauge malfunctioning.

Table A.3. Continued.

Phase	Cylinder #	Test Date	Age (day)	Strength (MPa)	Modulus (GPa)
Batch 2 Second Post-corrosion	1	May 14, 2019	160	41.0	23.1
	2	May 14, 2019	160	41.4	21.9
	3	May 14, 2019	160	41.2	22.9
	4	May 14, 2019	160	40.5	21.7
	5	May 14, 2019	160	43.5	23.3
	6	May 14, 2019	160	40.4	22.9
		Mean		41.3	22.7
		Standard Deviation		1.1	0.7
Batch 3 Pre-corrosion	1	January 18, 2019	28	37.8	21.9
	2	January 18, 2019	28	38.9	24.7
	3	January 18, 2019	28	39.7	22.3
	4	January 18, 2019	28	37.9	23.4
	5	January 18, 2019	28	39.1	22.4
	6	January 18, 2019	28	36.6	22.1
		Mean		38.3	22.8
		Standard Deviation		1.1	1.1
Batch 3 Post-corrosion	1	January 26, 2019	36	37.2	21.9
	2	January 26, 2019	36	38.8	23.0
	3	January 26, 2019	36	39.1	23.4
	4	January 26, 2019	36	40.6	23.4
	5	January 26, 2019	36	39.7	22.9
	6	January 26, 2019	36	39.6	24.0
		Mean		39.2	23.1
		Standard Deviation		1.1	0.7

APPENDIX B Strain Gauge Locations

The detailed electrical strain gauge locations measured from the top surface of the beams are listed in the Table B.1. to Table B.5.

Table B.1. Batch 1 Pre-corrosion Strain-gauge Location (mm).

	Gauge 1	Gauge 2	Gauge 3	Gauge 4
Beam 1	61 (tension zone)	31	15	0
Beam 2	60 (tension zone)	30	15	0
Beam 3	131 (tension zone)	117 (tension zone)	25	12

Table B.2. Batch 1 Post-corrosion Strain-gauge Location (mm).

	Gauge 1	Gauge 2	Gauge 3	Gauge 4
Beam 1	31	23 (new)	15	0 (new)
Beam 2	22 (new)	0 （new）	15	0
Beam 3	131 (broken)	18 (new)	25 (broken)	0 (new)

Table B.3. Batch 2 Pre- and Post-corrosion Strain-gauge Location (mm).

	Gauge 1	Gauge 2	Gauge 3	Gauge 4
Beam 1	30	20	10 (broken)	0
Beam 2	30	20	10	0 (broken)
Beam 3	30	20	10 (broken)	0

Table B.4. Batch 2 Second Post-corrosion Strain-gauge Location (mm).

	Gauge 1	Gauge 2	Gauge 3	Gauge 4	Gauge 5	Gauge 6	Gauge 7	Gauge 8
Beam 1	30	20	10	0	30	20	10	0
Beam 2	30	20	10	0	30	20	10	0
Beam 3	30	20	10	0	30	20	10	0

Table B.5. Batch 3 Pre- and Post-corrosion Strain-gauge Location (mm).

	Gauge 1	Gauge 2	Gauge 3	Gauge 4
Beam 1	30	20	10	0
Beam 2	30	20	10	0
Beam 3	30	20	10	0

APPENDIX C Sample Calculation of Corrosion Rate Using Faraday's Law

Faraday's law was used to estimate the total amount of current required to for the corrosion process. The following is a sample calculation demonstrating this p1rocess, using the preliminary corrosion test as an example.

Sample Calculation for the Preliminary Corrosion Test

Basic Factors:

Faraday's Law: $M = \frac{W \cdot I \cdot T}{n \cdot F}$

Where,

$F := 96487\ A \cdot \frac{s}{mol}$ Faraday constant

$W := 56\ \frac{gm}{mol}$ Atomic weight

$n := 2$ Equivalents changed

Specimen Factors:

Steel bar length: $l := 389\ mm$

Steel bar Original Mass: $M_o := 583\ gm$

Mass of the target corroded section: $M_{tar} := M_o \cdot \frac{100\ mm}{389\ mm} = 149.871\ gm$

Target Weight Loss: $M_{loss} := M_{tar} \cdot 10\% = 14.987\ gm$

Required Total Amount of Current to Go Through

$$It := \frac{M_{loss} \cdot 2 \cdot F}{W} = 14.346\ A \cdot hr$$

Expected Duration of Corroison:

If, $I := 50\ mA$

$t := \frac{It}{I} = 286.918\ hr$

APPENDIX D Sample Calculation for the Theoretically Calculated Values

The following sample calculations took Batch 3 Beam 3 in the pre-corrosion load test as example, showing how the cracking load, theoretical neutral axis location, elastic limits, and beam capacity are calculated.

The cracking load and elastic limits were used to determine the suitable loading range during the load test. The cracking load was calculated based on CSA A23.3-14 (2014). Two elastic limits were calculated for each beam. The more conservative, or lower, estimate assumed that the elastic region ends when the most extreme concrete fiber at the top of the beam reaches 45% of its ultimate compressive strength. However, the beams in Batches 2 and 3 were designed for lower capacities, and consequently the gaps between the cracking load and this elastic limit were very narrow. Additionally, it was found that a higher applied load could mitigate the magnitude of error. Therefore, a more liberal (higher) elastic limit was estimated using steel yielding as the criterion.

The theoretical neutral axis location and beam capacity were compared to the estimates provided by the SHM systems, and thus the effectiveness of the proposed SHM technique can be evaluated.

Properties of Batch 3 Beam 3 in the Pre-corrosion Load Test:

Geometry: (Values presented at the beginning of Chapter 4)

$b := 72\ mm$ $h := 140\ mm$ $A_{bar} := 100\ mm^2$

$CC := 33\ mm$ $d_{bar} := 11.3\ mm$ $d := h - \left(CC + \frac{d_{bar}}{2}\right) = 101.35\ mm$

Concrete Properties: Material Properties see Appendix A

$f'_c := 38.3\ MPa = \left(5.55 \cdot 10^3\right)\ psi$ $\lambda := 1$ For normal density concrete

$\alpha_1 := 0.85 - 0.0015 \cdot \frac{f'_c}{MPa} = 0.793$ $\beta_1 := 0.97 - 0.0025 \cdot \frac{f'_c}{MPa} = 0.87$

$E_c := 22.8\ GPa$

Steel Properties:

$f_s := 649.3\ MPa$ $E_s := 200\ GPa$ $\varepsilon_y := 0.002$

$f_y := 437.3\ MPa$ $n := \frac{E_s}{E_c} = 8.77$

Find Cracking Load: Based on Section S8.6.4 in CSA A23.3-14

Locate Centroid before crack: $y_{bar} := \frac{b \cdot h \cdot \frac{h}{2} + (n-1) \cdot A_{bar} \cdot d}{b \cdot h + (n-1) \cdot A_{bar}} = 72.24\ mm$

Modulus of Rupture: $f_r := 0.6 \cdot \lambda \cdot \sqrt{f'_c} \cdot \sqrt{MPa} = 3.71\ MPa$

Moment of inertia of gross concrete section: $I_g := \frac{b \cdot h^3}{12}$

From centroidal axis to extreme fibre in tension: $Y_t := h - y_{bar} = 67.76\ mm$

Cracking Moment: $M_{cr} := \frac{f_r \cdot I_g}{Y_t} = 0.9\ kN \cdot m$

Cracking Load: $P_{cr} := \frac{M_{cr}}{0.85\ m} \cdot 2 = 2.12\ kN$

Theoretical Neutral Axis Location After Cracking:

Neutral axis is located at the centroid:

$$b \cdot c \cdot \frac{c}{2} = (d-c) \cdot n \cdot A_{bar} \xrightarrow{solve, c, explicit, simplify} \begin{bmatrix} \frac{\sqrt{A_{bar} \cdot n \cdot (A_{bar} \cdot n + 2 \cdot b \cdot d)} - A_{bar} \cdot n}{b} \\ \frac{-\sqrt{A_{bar} \cdot n \cdot (A_{bar} \cdot n + 2 \cdot b \cdot d)} - A_{bar} \cdot n}{b} \end{bmatrix}$$

$$c := \frac{\sqrt{A_{bar} \cdot n \cdot (A_{bar} \cdot n + 2 \cdot b \cdot d)} - A_{bar} \cdot n}{b} = 38.98\ mm$$

Theoretical Neutral Axis Location: $c = 38.98\ mm$

Cracked moment of inertia: $I_{ct} := \frac{b \cdot c^3}{3} + n \cdot A_{bar} \cdot (d-c)^2 = (4.83 \cdot 10^6)\ mm^4$

Curvature when the beam just cracked: $\phi_{cr} := \frac{M_{cr}}{E_c \cdot I_{ct}} = (8.19 \cdot 10^{-3})\ \frac{1}{m}$

Find Elastic Limit:

The more conservative limit is defined as $f_c = 0.45\ f'_c$
(The most extreme concrete fiber at the top of the beam reaches 45% of its ultimate compressive strength)

Strain at the top surface: $\varepsilon_c = \frac{f_c}{E_c} = \frac{0.45 \cdot f'_c}{E_c}$ $\varepsilon_c := \frac{0.45 \cdot f'_c}{E_c} = 7.56 \cdot 10^{-4}$

Curvature at this point: $\phi_{0.45f'c} := \frac{\varepsilon_c}{c} = (1.939 \cdot 10^{-2})\ \frac{1}{m}$

Since the beam is within its elastic region: $\frac{M_{0.45f'c}}{M_{cr}} = \frac{\phi_{0.45f'c}}{\phi_{cr}}$

Solve for moment at this point: $M_{0.45f'c} := \frac{M_{cr}}{\phi_{cr}} \cdot \phi_{0.45f'c} = 2.14\ kN \cdot m$

The more conservative elastic limit: $P_{els} := \frac{M_{0.45f'c}}{0.85\ m} \cdot 2 = 5.03\ kN$

Check steel: $\varepsilon_s := \frac{\varepsilon_c}{c} \cdot (d-c) = 1.21 \cdot 10^{-3} < \varepsilon_y = 2 \cdot 10^{-3}$
So steel is still elastic

The more liberal elastic limit is defined as $\varepsilon_s := 0.002$ (When steel yields)

Strain at top concrete fiber: $\varepsilon_c := \frac{\varepsilon_s}{(d-c)} \cdot c = 1.25 \cdot 10^{-3}$

Curvature at this point: $\phi := \frac{\varepsilon_c}{c} = 0.03 \ \frac{1}{m}$

Solve for moment at this point: $M_{els} := \frac{M_{cr}}{\phi_{cr}} \cdot \phi = 3.53 \ kN \cdot m$

The more liberal elastic limit: $P_{els} := \frac{M_{els}}{0.85 \ m} \cdot 2 = 8.32 \ kN$

Predict Beam Capacity

Due to flexural failure:

Tensile force in the steel bar: $T := f_y \cdot A_{bar} = 43.73 \ kN$

Compressive force in concrete: $Cc = \alpha_1 \cdot f'_c \cdot na \cdot \beta_1 \cdot b$

Force equilibrium: $T = Cc$

Solve for neutral axis location: $na := \frac{T}{\alpha_1 \cdot f'_c \cdot \beta_1 \cdot b} = 22.89 \ mm$

Moment capacity: $M_n := T \cdot \left(d - na \cdot \frac{\beta_1}{2}\right) = 3.99 \ m \cdot kN$

Load capacity due to flexural failure: $P := \frac{M_n}{0.85 \ m} \cdot 2 = 9.4 \ kN$

Due to shear failure:

$d_{v1} := 0.9 \cdot d = 91.22 \ mm$ $d_{v2} := 0.72 \cdot h = 100.8 \ mm$

$d_v := \max(d_{v1}, d_{v2}) = 100.8 \ mm$ $V_{max} := 0.25 \cdot f'_c \cdot b \cdot d_v = 69.49 \ kN$

If minimal transverse reinforcement is met $\beta = 0.18$

If not, $\beta = \frac{230}{1000 + \frac{s_{ze}}{mm}}$

$a_g := 13\ mm$ Specified nominal aggregate size

$$s_{ze} := \frac{35 \cdot d_v}{15 + \frac{a_g}{mm}} = 126\ mm$$

$$\beta := \frac{230}{1000 + \frac{s_{ze}}{mm}} = 0.20426$$

Shear capacity: $V_c := \lambda \cdot \beta \cdot \sqrt{f'_c} \cdot \sqrt{MPa} \cdot b \cdot d_v = 9.17\ kN$ $< V_{max}$

Considering the loading test set up: $\frac{P}{2} = V_c$

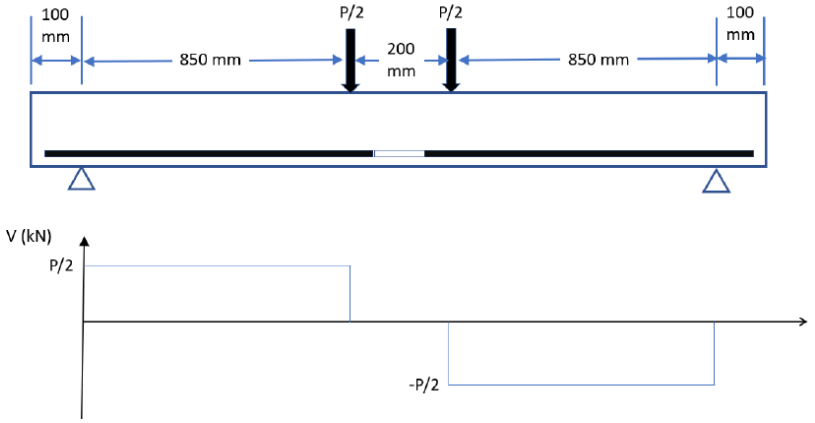

Load capacity due to shear failure: $P := V_c \cdot 2 = 18.3\ kN$

APPENDIX E Sample Calculation of Using Best Fit Function to Find Neutral Axis Locations

A sample calculation of using the least square method to find the best fit function of the gauges' location and readings is provided in this section. The x-intercept in the best fit function is the neutral axis location measured from the top surface of the beam.

The data used for this sample calculation is from the Batch 3 pre-corrosion loading test for Beam 3 Cycle 1 at 60s. The load being applied at this moment was 3kN. The results obtained at the end of this sample calculation are slightly different than those presented in Chapter 4, because the sample calculation found the neutral axis location at an instant, whereas tables in Chapter 4 list averaged neutral axis locations over the period of time while a certain load was maintained.

Raw Data: **Batch 3 Beam 3 Cycle 1 at 60s (3kN)**

DIC Locations:	DIC Readings:	ESG Locations:	ESG Readings:
$d_1 := 6\ mm$	$\varepsilon_1 := -0.000263573$	$d_a := 30\ mm$	$\varepsilon_a := -0.000064792$
$d_2 := 11\ mm$	$\varepsilon_2 := -0.000183131$	$d_b := 20\ mm$	$\varepsilon_b := -0.000117104$
$d_3 := 14\ mm$	$\varepsilon_3 := -0.000196333$	$d_c := 10\ mm$	$\varepsilon_c := -0.000174313$
$d_4 := 18\ mm$	$\varepsilon_4 := -0.000128553$	$d_d := 0\ mm$	$\varepsilon_d := -0.000229126$
$d_5 := 22\ mm$	$\varepsilon_5 := -0.00011853$		
$d_6 := 26\ mm$	$\varepsilon_6 := -9.98 \cdot 10^{-5}$		
$d_7 := 33\ mm$	$\varepsilon_7 := -0.000104707$		
$d_8 := 41\ mm$	$\varepsilon_8 := -4.13 \cdot 10^{-5}$		
$d_9 := 48\ mm$	$\varepsilon_9 := -5.91 \cdot 10^{-5}$		
$d_{10} := 55\ mm$	$\varepsilon_{10} := -4.39 \cdot 10^{-5}$		
$d_{11} := 62\ mm$	$\varepsilon_{11} := -2.66 \cdot 10^{-5}$		
$d_{12} := 70\ mm$	$\varepsilon_{12} := 5.93 \cdot 10^{-6}$		
$d_{13} := 78\ mm$	$\varepsilon_{13} := 6.53 \cdot 10^{-6}$		
$d_{14} := 85\ mm$	$\varepsilon_{14} := 1.55 \cdot 10^{-6}$		
$d_{15} := 92\ mm$	$\varepsilon_{15} := 3.32 \cdot 10^{-5}$		
$d_{16} := 100\ mm$	$\varepsilon_{16} := 4.16 \cdot 10^{-6}$		
$d_{17} := 107\ mm$	$\varepsilon_{17} := 2.09 \cdot 10^{-6}$		
$d_{18} := 115\ mm$	$\varepsilon_{18} := -5.14 \cdot 10^{-5}$		
$d_{19} := 122\ mm$	$\varepsilon_{19} := -8.68 \cdot 10^{-5}$		
$d_{20} := 130\ mm$	$\varepsilon_{20} := -9.39 \cdot 10^{-5}$		

DIC Gauges 1 to 7 are in the compression zone

Best fit function: (Least Square Method)

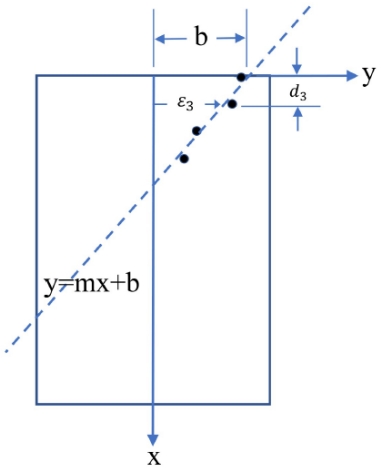

$$y = mx + b$$

where, $$m = \frac{\sum (x_i - x_{bar}) \cdot (y_i - y_{bar})}{\sum (x_i - x_{bar})^2}$$

m is the slope.

$$b = y_{bar} - x_{bar} \cdot m$$

b is the y-intercept

Function of the best fit line: $y = mx + b$

Strain gauge locations can be seen as the independent variables (x-coordinate); while the strain readings can be seen as the dependent variables (y-coordinates). Therefore, the x-intercept is equivalent to the N.A. location.

When y=0, $$x = \frac{y - b}{m} = N.A.$$

Method 1: (Using best fit function to find the N.A. location on each side separately, then take an average)

Find the N.A. location on the DIC side: (Using gauges in compressive zone only)

$$\varepsilon_{DIC} := \begin{bmatrix} -0.000263573 \\ -0.000183131 \\ -0.000196333 \\ -0.000128553 \\ -0.00011853 \\ -9.98 \cdot 10^{-5} \\ -0.000104707 \end{bmatrix} \qquad d_{DIC} := \begin{bmatrix} 6 \\ 11 \\ 14 \\ 18 \\ 22 \\ 26 \\ 33 \end{bmatrix} mm$$

$$y_{bar} := \frac{\sum_{i=1}^{7} \varepsilon_{DIC_i}}{7} = -1.564 \cdot 10^{-4} \qquad x_{bar} := \frac{\sum_{i=1}^{7} d_{DIC_i}}{7} = (1.857 \cdot 10)\ mm$$

$$m_{DIC} := \frac{\sum_{i=1}^{7} \left(\varepsilon_{DIC_i} - y_{bar}\right) \cdot \left(d_{DIC_i} - x_{bar}\right)}{\sum_{i=1}^{7} \left(d_{DIC_i} - x_{bar}\right)^2} = \left(5.887 \cdot 10^{-6}\right) \frac{1}{mm}$$

$$b_{DIC} := y_{bar} - x_{bar} \cdot m_{DIC} = -2.657 \cdot 10^{-4}$$

$$N.A._{DIC} := \frac{-b_{DIC}}{m_{DIC}} = 45.134\ mm$$

Find the N.A. location on the ESG side: (Using all four)

$$\varepsilon_{ESG} := \begin{bmatrix} -0.000064792 \\ -0.000117104 \\ -0.000174313 \\ -0.000229126 \end{bmatrix} \qquad d_{ESG} := \begin{bmatrix} 30 \\ 20 \\ 10 \\ 0 \end{bmatrix} mm$$

$$y_{bar} := \frac{\sum_{i=1}^{4} \varepsilon_{ESG_i}}{4} = -1.463 \cdot 10^{-4} \qquad x_{bar} := \frac{\sum_{i=1}^{4} d_{ESG_i}}{4} = (1.5 \cdot 10)\ mm$$

$$m_{ESG} := \frac{\sum_{i=1}^{4} \left(\varepsilon_{ESG_i} - y_{bar}\right) \cdot \left(d_{ESG_i} - x_{bar}\right)}{\sum_{i=1}^{4} \left(d_{ESG_i} - x_{bar}\right)^2} = \left(5.502 \cdot 10^{-6}\right) \frac{1}{mm}$$

$$b_{ESG} := y_{bar} - x_{bar} \cdot m_{ESG} = -2.289 \cdot 10^{-4}$$

$$N.A._{ESG} := \frac{-b_{ESG}}{m_{ESG}} = 41.596\ mm$$

Take an Average:

$$N.A._{avg} := \frac{N.A._{DIC} + N.A._{ESG}}{2} = 43.365\ mm$$

Method 2: Combine the data from both faces then apply the best fit funtion

DIC Locations:	DIC Readings:	ESG Locations:	ESG Readings:
$d_1 := 6\ mm$	$\varepsilon_1 := -0.000263573$	$d_a := 30\ mm$	$\varepsilon_a := -0.000064792$
$d_2 := 11\ mm$	$\varepsilon_2 := -0.000183131$	$d_b := 20\ mm$	$\varepsilon_b := -0.000117104$
$d_3 := 14\ mm$	$\varepsilon_3 := -0.000196333$	$d_c := 10\ mm$	$\varepsilon_c := -0.000174313$
$d_4 := 18\ mm$	$\varepsilon_4 := -0.000128553$	$d_d := 0\ mm$	$\varepsilon_d := -0.000229126$
$d_5 := 22\ mm$	$\varepsilon_5 := -0.00011853$		
$d_6 := 26\ mm$	$\varepsilon_6 := -9.98 \cdot 10^{-5}$		
$d_7 := 33\ mm$	$\varepsilon_7 := -0.000104707$		

Combine two faces data

$$d := \begin{bmatrix} 30 \\ 20 \\ 10 \\ 0 \\ 6 \\ 11 \\ 14 \\ 18 \\ 22 \\ 26 \\ 33 \end{bmatrix} mm \qquad \varepsilon := \begin{bmatrix} -0.000064792 \\ -0.000117104 \\ -0.000174313 \\ -0.000229126 \\ -0.000263573 \\ -0.000183131 \\ -0.000196333 \\ -0.000128553 \\ -0.00011853 \\ -9.98 \cdot 10^{-5} \\ -0.000104707 \end{bmatrix}$$

(First four entries are from ESG, then the rest are form DIC)

Apply Best Fit:

$$x_{bar} := \frac{\sum_{i=1}^{11} d_i}{11} = 17.273\ mm \qquad y_{bar} := \frac{\sum_{i=1}^{11} \varepsilon_i}{11} = -1.527 \cdot 10^{-4}$$

$$m_{esg\_dic} := \frac{\sum_{i=1}^{11} \left(\varepsilon_i - y_{bar}\right) \cdot \left(d_i - x_{bar}\right)}{\sum_{i=1}^{11} \left(d_i - x_{bar}\right)^2} = 0.005\ \frac{1}{m}$$

$$b_{esg\_dic} := y_{bar} - x_{bar} \cdot m_{esg\_dic} = -2.466 \cdot 10^{-4}$$

$$N.A._{esg\_dic} := \frac{-b_{esg\_dic}}{m_{esg\_dic}} = 45.387\ mm$$

Method 3: Calculate averaged strains between the two faces, and then apply the best fit function.

Find the projected DIC readings at the same depths as the ESG gauges (DIC gauges are not at the same locations as the ESG gauges, thus, best fit functions are used to find the projected DIC readings at desired locations.)

As calculated in Method 1, the DIC best fit function is:

$$m_{DIC} = (5.887 \cdot 10^{-6}) \frac{1}{mm} \qquad b_{DIC} = -2.657 \cdot 10^{-4}$$

$$y = x \cdot m_{DIC} + b_{DIC} \rightarrow y = \frac{0.000005887076493579006 4 \cdot x}{mm} - 0.00026570670630932439$$

ESG gauge locations: $x_{esg} := \begin{bmatrix} 30 \\ 20 \\ 10 \\ 0 \end{bmatrix} mm$

Projected DIC readings at the same depths: $y_{dicfit} := m_{DIC} \cdot x_{esg} + b_{DIC} = \begin{bmatrix} -8.909 \cdot 10^{-5} \\ -1.48 \cdot 10^{-4} \\ -2.068 \cdot 10^{-4} \\ -2.657 \cdot 10^{-4} \end{bmatrix}$

Averaged strains:

$$y_{esg} := \begin{bmatrix} -0.000064792 \\ -0.000117104 \\ -0.000174313 \\ -0.000229126 \end{bmatrix} \qquad y_{dicfit\_esg} := \frac{y_{esg} + y_{dicfit}}{2} = \begin{bmatrix} -7.694 \cdot 10^{-5} \\ -1.325 \cdot 10^{-4} \\ -1.906 \cdot 10^{-4} \\ -2.474 \cdot 10^{-4} \end{bmatrix}$$

Apply Best Fit:

$$x_{bar} := \frac{\sum_{i=1}^{4} x_{esg_i}}{4} = 15 \ mm \qquad y_{bar} := \frac{\sum_{i=1}^{4} y_{dicfit\_esg_i}}{4} = -1.619 \cdot 10^{-4}$$

$$m_{dicfit\_esg} := \frac{\sum_{i=1}^{4} \left(y_{dicfit\_esg_i} - y_{bar}\right) \cdot \left(x_{esg_i} - x_{bar}\right)}{\sum_{i=1}^{4} \left(x_{esg_i} - x_{bar}\right)^2} = 5.695 \frac{1}{m^2} \cdot mm$$

$$b_{dicfit\_esg} := y_{bar} - x_{bar} \cdot m_{dicfit\_esg} = -0.247 \frac{1}{m} \cdot mm$$

$$N.A._{dicfit\_esg} := \frac{-b_{dicfit\_esg}}{m_{dicfit\_esg}} = 43.425 \ mm$$

Summary:

Theoretical N.A. Location: $N.A._{thry} := 39.0\ mm$

Single face:

DIC side: $N.A._{DIC} = 45.134\ mm$ $diff := \frac{N.A._{DIC} - N.A._{thry}}{N.A._{thry}} = 15.728\%$

ESG side: $N.A._{ESG} = 41.596\ mm$ $diff := \frac{N.A._{ESG} - N.A._{thry}}{N.A._{thry}} = 6.656\%$

Two faces together:

Method 1: $N.A._{avg} = 43.365\ mm$ $diff := \frac{N.A._{avg} - N.A._{thry}}{N.A._{thry}} = 11.192\%$

Method 2: $N.A._{esg\_dic} = 45.387\ mm$ $diff := \frac{N.A._{esg\_dic} - N.A._{thry}}{N.A._{thry}} = 16.377\%$

Method 3: $N.A._{dicfit\_esg} = 43.425\ mm$ $diff := \frac{N.A._{dicfit\_esg} - N.A._{thry}}{N.A._{thry}} = 11.345\%$

APPENDIX F Procedure Optimization based on N.A. Locations Estimated using data from Each Individual Face

F.1. Introduction

This appendix presents and discusses the results of preliminary analyses which were conducted during the time gaps between the load tests. The preliminary analyses consisted of estimating the N.A. locations using the data from each face individually. The main purpose of conducting these analyses was to identify the optimum gauge locations and the level of the load that can provide the most reliable data and most accurate estimates.

Assume the strain distribution of the concrete is perfectly linear with the distance away from the N.A. and the strains can be measured accurately, the location of the gauge should not affect the accuracy of the estimates. However, some places can potentially be problematic to the reliability of the obtained strain data. For example, cracks might occur in the tension zone, and the extreme tensile strains at the cracks might damage the integrity of the gauges. If all the gauges were to be placed in the compression zone, due to the limitation of space, gauges might be placed on the top of the beams, which is not in the same plane with the other gauges, or close to the N.A. location, which might have very small readings. To verity these assumptions, N.A. locations were estimated using data with and without gauges in the problematic locations, and the differences of the results with the theoretical N.A. locations were calculated and compared.

Like the location of the gauges, the level of the applied load to the beams, in theory, should not have an effect at the accuracy of the estimates. After the beam has been cracked, the N.A. should remain at the same location throughout the elastic deformations state of the beams. To verify this, the estimated N.A. locations were computed using strain data obtained at different applied load, and the accuracy of the results were compared.

In Section F.3, the conditions of the beams at each load test and the composition of the data groups to be compared are explained before the estimated N.A. locations using different data groups are presented and compared to the theoretical values. Besides investigating the effect of the gauge locations and the level of the applied load, the consistency of the estimates from the two sides and any other abnormal phenomenon observed are also discussed. Lastly, the outcomes of the preliminary analysis for each load test were summarized in Section F.3., along with recommendations to data collection and processing procedures.

F.2. Neutral Axis Analysis by Each Load Test

F.2.1. Batch 1 Pre-corrosion Load Test

Prior to corrosion, Batch 1 beams had a cracking load of 4.9 kN, and a conservative elastic limit of 14.8 kN. During this load test, each beam was gradually loaded until 8 kN repeatedly. This batch of beams had honeycombing in the concrete, which may have affected the quality of the bond between the concrete and the electrical strain gauges. The surfaces of this batch of beams also had pieces of wooden form adhered to them due to the use of adhesive at the cold joints. Therefore, the suitable area for the attachment of gauges was reduced.

Only electrical strain gauges were used for monitoring, and there were four gauges attached to each beam. Both Beam 1 and Beam 2 had three gauges attached to the side surfaces, one in the tension zone (G1), two in the compression zone (G2 and G3), and the fourth on the top of the beams (G4). Beam 3 had all gauges attached on the side surface, two in the tension zone (G1 and G2) and two in the compression zone (G3 and G4). The gauges in the tension zone and gauges on top of the beams were suspected to have negative effects to the estimated results. To investigate the impact of locating the gauges in these two locations, N.A. locations were estimated using all strain data (ESG_all), data excluding the top gauges (ESG_notop), data excluding the ones in the tension zones (ESG_cmprs), and data excluding the top and tension gauges (ESG_G2&G3). The estimated N.A. locations using these data groups for Batch 1 pre-corrosion load test are summarized in Table F.1. The theoretical N.A. locations for Beams 1 to 3 were 42.9 mm, 42.3 mm, and 42.3 mm, respectively. The estimates are compared to the theoretical values and illustrated in Figures F.1 to F.3. Since Beam 3 did not have any gauge placed on top of it, the cells for “ESG_all” and “ESG_cmprs” are left empty as they are equivalent to “ESG_notop” and “ESG_G2&G3”, respectively. Also, for Beam 3, it was actually

G1 and G2 located in the less questionable locations (in the compression zone and on the side surface), but the name "ESG_G2&G3" generally represents gauges in these locations.

Table F.1. Batch 1 pre-corrosion load test N.A. locations, measured from top surface in mm.

Beam #	Load	Cycle #	ESG_all	ESG_notop	ESG_cmprs	ESG_G2&G3
Beam 1	5 kN	Cycle 1	55.6	57.1	44.8	45.4
		Cycle 2	51.2	52.6	39.5	41.8
	6 kN	Cycle 1	55.6	57.1	44.6	45.2
		Cycle 2	51.5	52.9	39.9	42.2
	7 kN	Cycle 1	55.1	56.8	43.7	44.5
		Cycle 2	51.7	53.1	40.0	42.4
	8 kN	Cycle 1	54.8	56.4	43.0	44.0
		Cycle 2	51.8	53.4	42.5	39.8
Beam 2	5 kN	Cycle 1	54.6	57.6	41.7	49.3
		Cycle 2	57.3	60.8	43.9	51.2
		Cycle 3	56.1	59.0	44.3	51.6
	6 kN	Cycle 1	55.3	58.6	41.9	49.4
		Cycle 2	57.0	60.4	43.9	50.8
		Cycle 3	55.9	58.7	44.1	50.9
	7 kN	Cycle 1	56.1	59.5	42.9	49.9
		Cycle 2	56.7	59.9	43.9	50.3
		Cycle 3	55.8	58.5	44.1	50.3
	8 kN	Cycle 1	56.3	59.6	43.2	49.9
		Cycle 2	56.9	60.0	44.0	50.2
		Cycle 3	55.8	58.5	44.1	50.1
Beam 3	5 kN	Cycle 1	N/A	87.3	N/A	47.9
		Cycle 2	N/A	58.8	N/A	48.1
		Cycle 3	N/A	53.7	N/A	46.2
	6 kN	Cycle 1	N/A	88.9	N/A	46.3
		Cycle 2	N/A	58.4	N/A	47.1
		Cycle 3	N/A	53.6	N/A	45.3
	7 kN	Cycle 1	N/A	86.8	N/A	45.3
		Cycle 2	N/A	57.2	N/A	46.0
		Cycle 3	N/A	53.1	N/A	44.4
	8 kN	Cycle 1	N/A	62.0	N/A	42.9
		Cycle 2	N/A	53.0	N/A	44.4
		Cycle 3	N/A	51.0	N/A	43.3

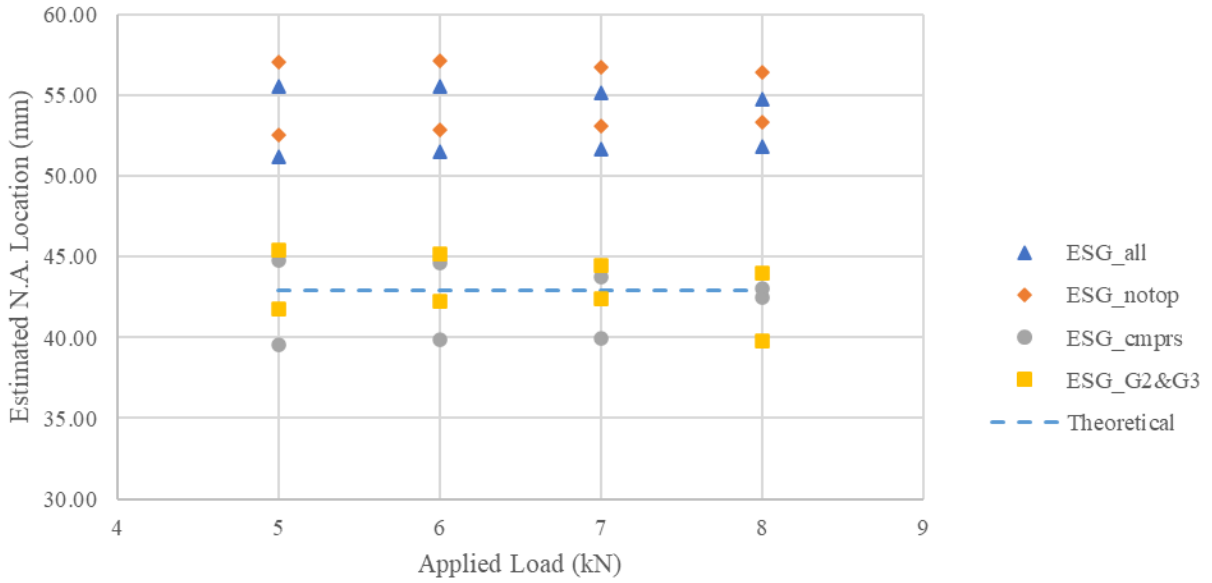

Figure F.1. Comparison of estimated N.A. locations to the theoretical value for Batch 1 Beam 1 pre-corrosion load test.

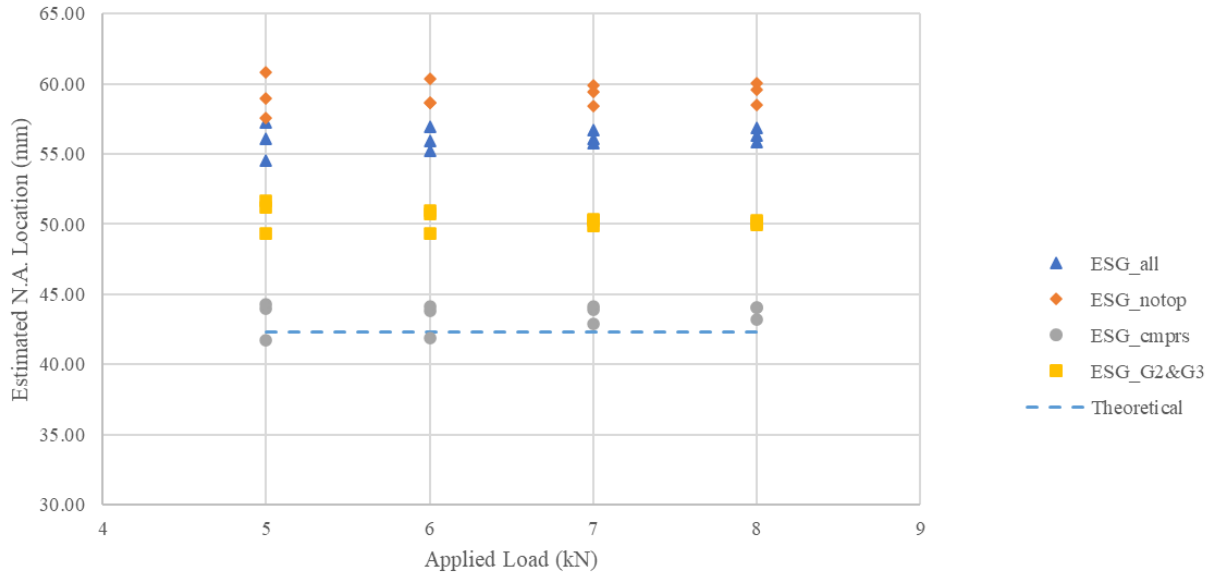

Figure F.2. Comparison of estimated N.A. locations to the theoretical value for Batch 1 Beam 2 pre-corrosion load test.

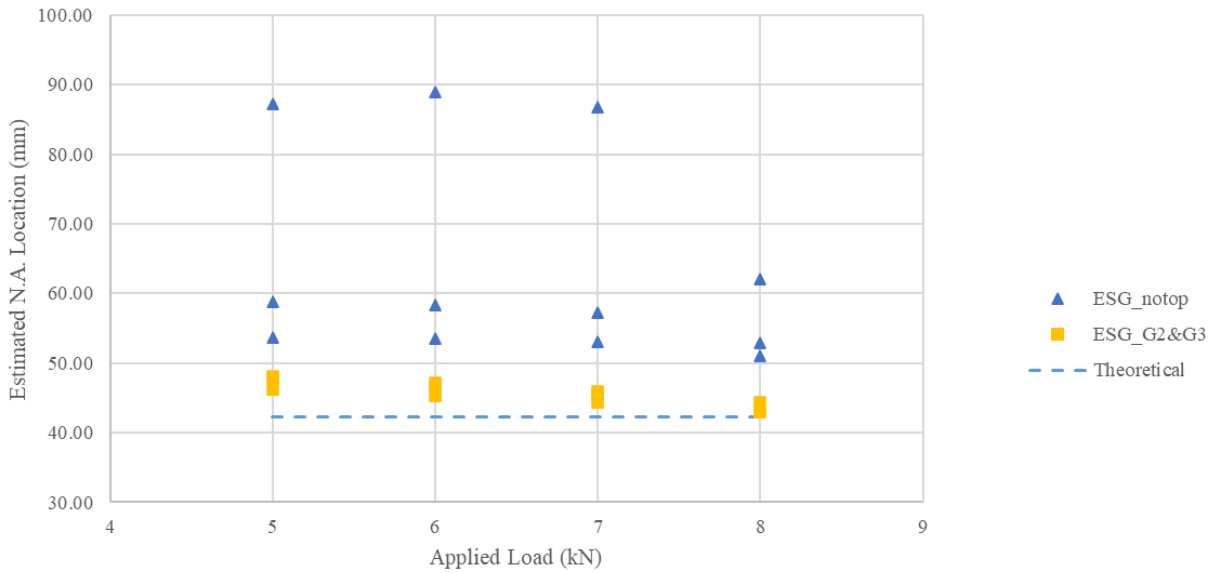

Figure F.3. Comparison of estimated N.A. locations to the theoretical value for Batch 1 Beam 3 pre-corrosion load test.

The results of Batch 1 pre-corrosion load test can be used to analyze the quality of the data from the tension zone and from the top of the beam, as well as the effect of the level of the applied load.

Effect of the Location of the Gauges

As shown in Figures F.1. to F.3, estimates obtained using the data groups "ESG_all" and "ESG_notop" were consistently the furthest away from the theoretical N.A. locations. These two data groups both contained gauges in the tension zone. Therefore, it proved that strain data from the tension zone had a negative impact to the accuracy of the results, and strain gauges should not be placed in the tension zone in the future. Excluding the gauges on top of the beams, however, did not show a clear advantage. Estimates using "ESG_comprs" and "ESG_G2&G3" were equally close to the theoretical value for Beam 1. For Beam 2, excluding the gauges on top of the beams led to bigger errors. This might be an indication that Batch 1 beams did not have severe asymmetrical conditions, thus having a top gauge which was not in the same plane as the other gauges did not harm the results. This also suggested that having more strain data would increase the accuracy in estimation if the data were reliable.

Effect of the Level of the Applied Load

Increasing the applied load had little impact on the results for this batch of beams, as predicted by theory. However, in a few cases such as "ESG_cmprs" for Beam 1 and "ESG_notop" for

Beam 3, the accuracy of the estimates increased with higher loads. Also, it was observed that for Beam 1 “ESG_all” and Beam 2 “ESG_all” and “ESG_notop”, even though the accuracy of the estimates did not increase, the variances among different cycles were reduced. Based on this batch of data, higher loads had the potential to increase the accuracy and reduce the variance of the results, but the evidence were not obvious.

F.2.2. Batch 1 Post-corrosion Load Test

After corrosion, the cracking load and the elastic limit of batch 1 beams changed to around 4.3 kN and 11 kN, respectively. Due to concerns about the corroded beams’ conditions, these beams were only loaded to a maximum of 6 kN repeatedly. In addition to the electrical strain gauges, the DIC 3D system was implemented for monitoring the strain changes on the opposite side of the beams.

Most of the electrical strain gauges attached for the pre-corrosion load tests were broken and completely disconnected from the reader unit due to corroded wires. A few gauges in the compression zone were still functioning, however, their integrity was questioned. Two new gauges were attached to the compressive zone of each beam to ensure the minimum required number of gauges was met. Beam 2 had one new gauge placed on the top of the beam and beside an old one. However, these two gauges provided different readings under the same load. One possible reason is due to the asymmetrical conditions, so the strains were indeed different; the other possible reason is that the old gauge was not functioning well. Therefore, comparisons were made between estimated N.A. locations using all ESG data (ESG_all), the data from new ESGs (ESG_new), as well as all DIC data (DIC_all), and the DIC data in the compression zone only (DIC_cmprs). The results are summarized in Table F.2. Again, the estimates are compared to the theoretical values and illustrated in Figures F.4 to F.6.

Table F.2. Batch 1 post-corrosion load test N.A. locations, measured from top surface in mm.

Beam #	Load	Cycle #	DIC_all	DIC_cmprs	ESG_all	ESG_new
Beam 1	5 kN	Cycle 1	68.4	61.9	41.0	41.0
		Cycle 2	78.4	49.9	38.7	37.8
		Cycle 3	69.7	48.0	38.7	37.9
		Cycle 4	52.4	40.6	39.1	38.2
		Cycle 5	76.6	51.1	39.9	39.0
		Cycle 6	64.3	46.4	39.4	38.3
	6 kN	Cycle 1	69.5	61.3	41.0	40.7
		Cycle 2	79.0	49.7	38.8	37.9
		Cycle 3	69.2	48.6	38.9	38.0
		Cycle 4	52.9	41.4	39.3	38.3
		Cycle 5	73.9	50.7	39.9	39.1
		Cycle 6	65.5	-26.0	39.6	38.4
Beam 2	5 kN	Cycle 1	78.6	-296.9	31.5	34.4
		Cycle 2	70.9	49.2	30.1	32.8
		Cycle 3	73.3	49.0	31.5	33.9
		Cycle 4	68.6	46.4	29.6	34.1
		Cycle 5	69.4	49.1	30.1	34.4
	6 kN	Cycle 1	78.6	223.9	31.7	34.5
		Cycle 2	70.8	49.3	30.8	33.4
		Cycle 3	72.6	49.2	31.9	34.3
		Cycle 4	71.1	46.8	30.0	34.4
		Cycle 5	68.0	53.3	30.5	34.7
Beam 3	5 kN	Cycle 1	58.2	57.7	N/A	48.9
		Cycle 2	63.3	48.4	N/A	53.1
		Cycle 3	58.7	58.9	N/A	53.2
	6 kN	Cycle 1	58.3	55.1	N/A	48.8
		Cycle 2	64.5	48.5	N/A	53.2
		Cycle 3	58.4	55.9	N/A	53.5

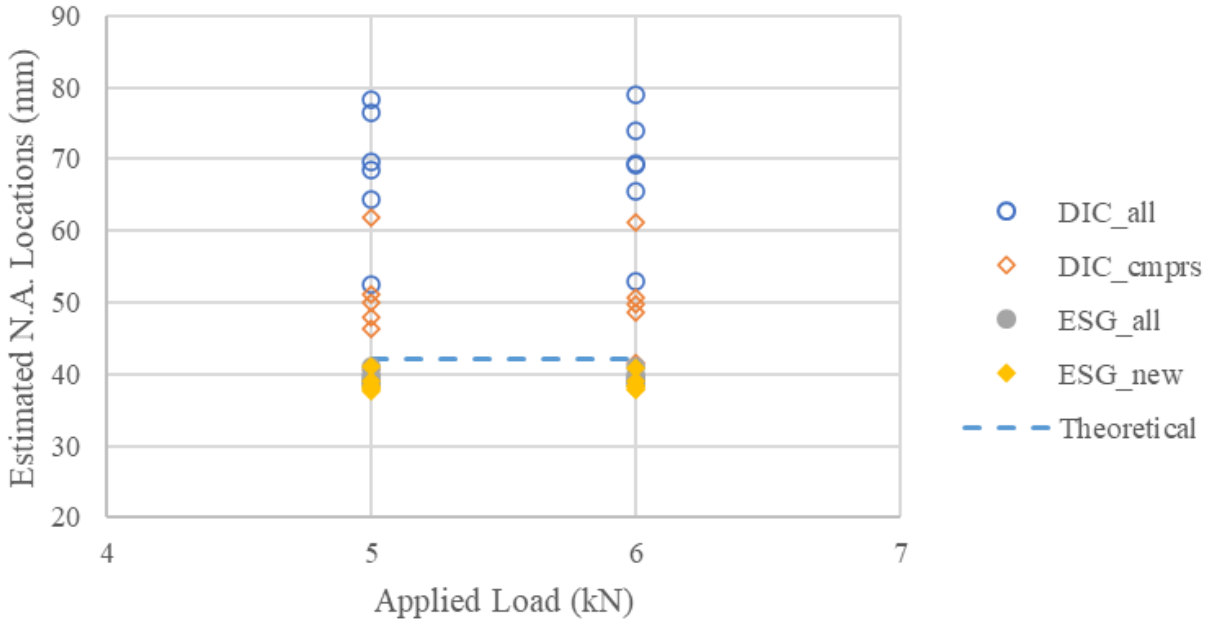

Figure F.4. Comparison of estimated N.A. locations to the theoretical value for Batch 1 Beam 1 post-corrosion load test.

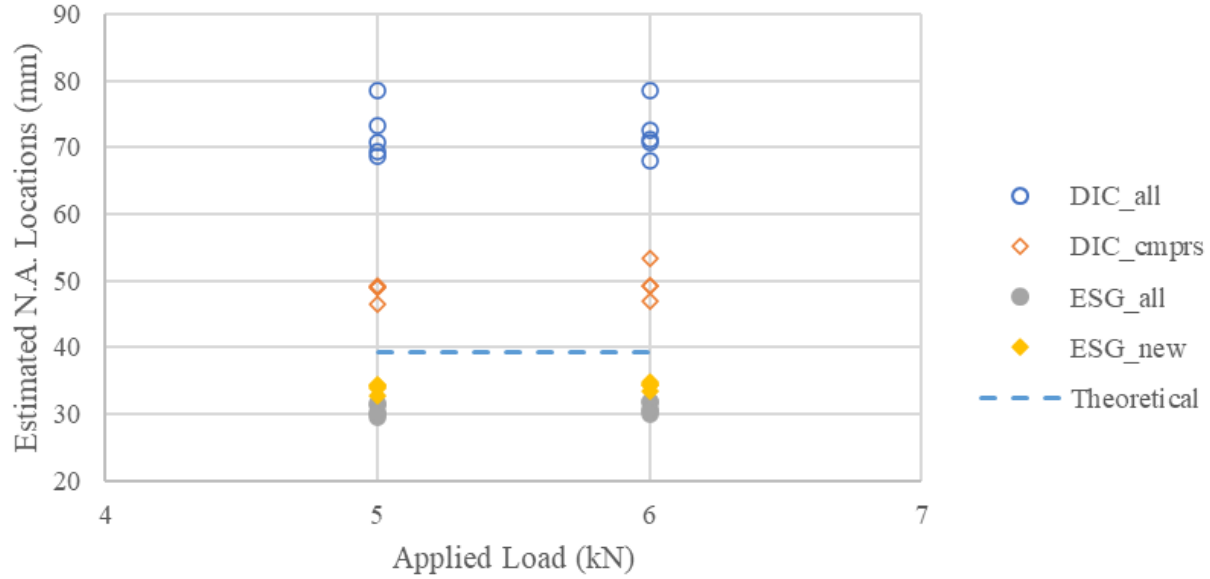

Figure F.5. Comparison of estimated N.A. locations to the theoretical value for Batch 1 Beam 2 post-corrosion load test.

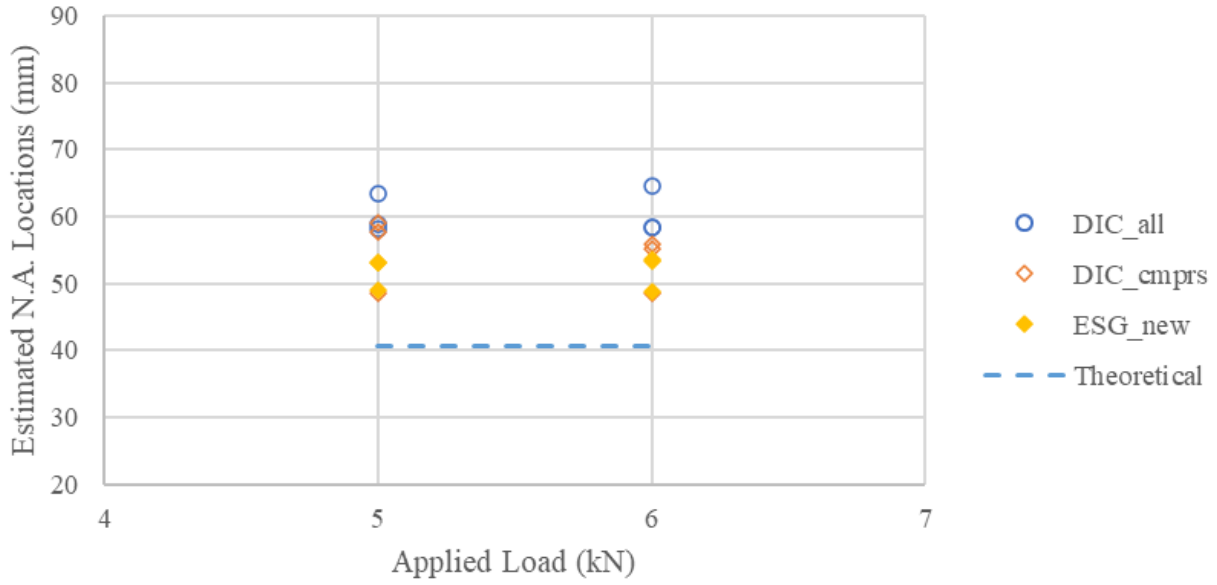

Figure F.6. Comparison of estimated N.A. locations to the theoretical value for Batch 1 Beam 3 post-corrosion load test.

For the Batch 1 post-corrosion load tests, all the electrical strains gauges attached before corrosion in the tension zone were lost, and there were not enough gauges to compare the effect of the top gauges. So, the ESG results were mainly used to investigate the reliability of the old gauges by comparing the accuracy of the estimates of "ESG_all" and "ESG_new". The effect of the tension strains was continued to be investigated by the DIC data. The results estimated based on the DIC data were compared to those based on the ESG data in general. Lastly, since these beams were only loaded to 6 kN, the influence of the applied load on the accuracy of the estimates was not evident.

Integrity of the Old Gauges

The reliability of the gauges attached prior to corrosion was determined by comparing the accuracy of the estimates using "ESG_all" and "ESG_new". For Beam 1, the benefits of using only data from the new electrical strain gauges are not distinct. For Beam 2, "ESG_new" provided slightly more accurate results than "ESG_all". For Beam 3, the comparison was not available, since all the old gauges attached on this beam before corrosion were lost. In general, the integrity of the old gauges seemed reliable as long as they stayed connected.

Reliability of the DIC Data

On the DIC side, using data in the compression zone only substantially improved the results compared to those obtained using all the DIC data, which indicated that for the DIC monitoring, strain data in the tension zone were also not reliable. Note "DIC_cmprs" results had a couple of the outliers in the first cycle of the load tests for Beam 2. These outliers were automatically omitted in Figure F.5 due to the restricted boundaries of the y-axis. When compared to the ESG data, the gaps between the estimates and the theoretical values were quite high for the DIC data, which might be due to the poor quality of the collected data. The DIC readings are very sensitive to the surface conditions, so the honeycombing on the surfaces of these beams may have negatively affected the accuracy of the DIC data. A screen capture of an image from the DIC analysis software (VIC-3D, Correlated Solutions Inc., US) provided in Figure 4.5 shows that extreme or empty strain values are presented at the dents on the concrete surfaces.

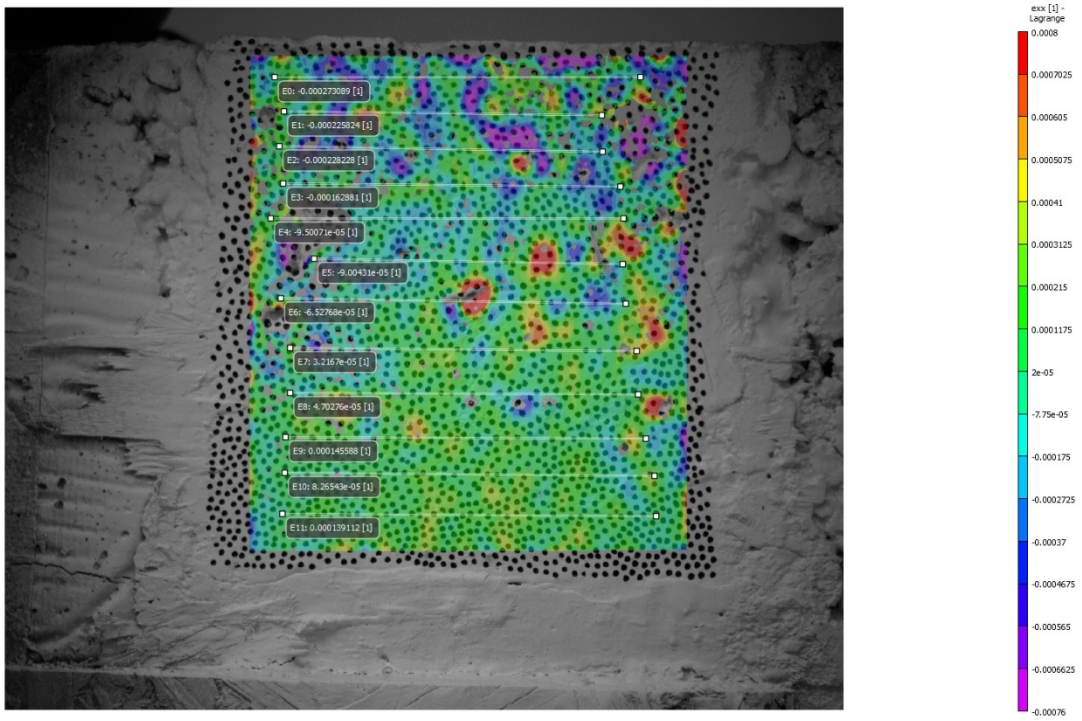

Figure F.7. DIC image for Batch 1 Beam 3 post-corrosion load test.

Consistency of the Data from the Two Faces

It was also observed from the figures that for Beams 1 and 2, the estimates obtained by the DIC data and ESG data lied on the opposite side of the theoretical N.A. locations. Thus, eccentric

loading was suspected to had happened to these load tests, causing one side less loaded and the other side heavier loaded. Better estimates may be obtained by combining the data from the two faces. However, for Beam 3, the two sides were consistent with each other, and both overestimated the distance of the N.A. location from the top of the beam.

F.2.3. Batch 2 Pre-corrosion Load Test

Observation of the results obtained for the beams in Batch 1 motivated changes to be made for the subsequent batches of beams. To ensure the beams failed in flexure instead of in shear, the length of the beams was increased, and a smaller size of reinforcing steel bar was used for Batches 2 and 3. The decrease in the amount of reinforcement led to the neutral axes moving upwards. Since it was discovered that the strain data provided by the gauges in the compression zone performed better, the beams' width was decreased to ensure the neutral axes were located around 40 mm below the top surface, so there was enough space to put all gauges in the compression zone. The concrete mix proportions were also adjusted to avoid honeycombing. As for the beams' surface smoothness, even though the use of wax paper prevented the form from adhering to the beams, it caused wrinkling on the concrete surfaces, which may have affected the reliability of the measured strain data. Figure F.8 shows an example of the DIC analysis for Beam 3. Higher compressive strain readings were measured along the ditches on the surface. On the ESG side, a new type of adhesive with a thicker texture was used for this batch of beams. It was expected that this new type of glue could fill in the unevenness of the surfaces.

As a result of less reinforcement and lower moment capacity for this batch of beams, the gap between the cracking load (around 2.2 kN) and the conservative elastic limit (around 4.9 kN) was also narrow. Therefore, the beams were gradually loaded to 6 kN repeatedly, which was within the liberal elastic limit (around 8.5 kN).

Four ESGs, labelled G1 to G4 were placed at 30, 20, 10 and 0 mm below the top surface of each beam. Refer to Appendix B. Like the analysis done for the Batch 1 post-corrosion load test, comparisons were made among "DIC_all", "DIC_cmprs", "ESG_all", and "ESG_notop". It was suspected that G1 may have been too close to the N.A., so it might not be able to provide reliable measurements under such a small deformation. Thus, an additional alternative using data from G2 and G3 only was compared with the other four alternatives. The results are summarized in

Table F.3. The results were also compared to the theoretical values and illustrated in Figures F.9 to F.11.

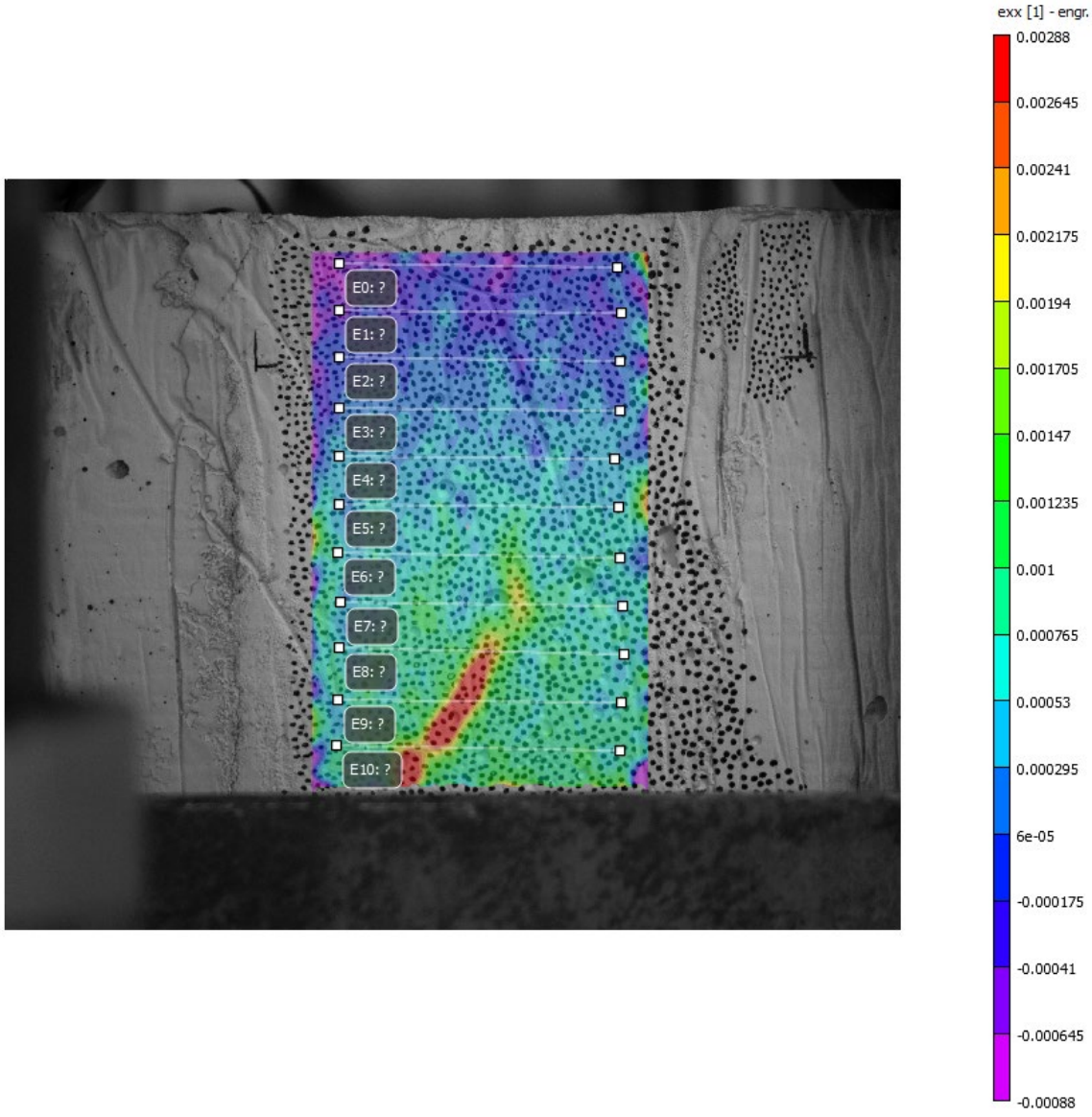

Figure F.8. DIC analysis from the pre-corrosion load test for Batch 2 Beam 3 Cycle 3 at 6 kN, showing how surface wrinkling affected calculated strains.

Table F.3. Batch 2 pre-corrosion load test N.A. locations, measured from top surface in mm.

Beam #	Load	Cycle #	DIC_all	DIC_cmprs	ESG_all	ESG_notop	ESG_23
Beam 1	3 kN	Cycle 1	63.8	72.8	-580.9	138.9	101.6
		Cycle 2	85.2	92.4	-1038.7	120.1	98.6
		Cycle 3	65.3	69.0	4.6	-21.6	102.7
	4 kN	Cycle 1	64.9	67.0	364.5	102.1	65.9
		Cycle 2	85.8	90.2	232.6	95.0	66.3
		Cycle 3	66.0	61.3	197.8	90.7	69.1
	5 kN	Cycle 1	64.6	59.0	98.2	71.2	59.7
		Cycle 2	81.5	77.6	96.4	69.9	60.4
		Cycle 3	63.2	54.7	95.9	69.7	62.5
	6 kN	Cycle 1	63.7	58.7	81.1	64.6	58.0
		Cycle 2	80.7	73.0	79.1	63.4	58.9
		Cycle 3	62.8	53.2	78.9	63.6	60.9
Beam 2	3 kN	Cycle 1	-8.1	-1.2	227.9	38.8	29.2
		Cycle 2	-14.9	-25.2	-1351.5	46.8	36.5
		Cycle 3	0.7	-5.7	682.1	48.4	37.7
		Cycle 4	-13.8	-31.8	284.2	48.5	38.3
	4 kN	Cycle 1	-4.8	2.7	151.1	39.8	31.9
		Cycle 2	-10.6	-13.4	126.6	46.6	38.6
		Cycle 3	2.6	2.7	127.0	47.8	39.5
		Cycle 4	-8.2	-23.2	118.4	47.5	40.0
	5 kN	Cycle 1	0.3	8.1	93.3	41.6	35.8
		Cycle 2	-4.2	-2.8	88.5	46.1	39.9
		Cycle 3	5.9	7.6	87.8	47.0	40.5
		Cycle 4	-0.2	-4.1	84.6	46.7	40.9
	6 kN	Cycle 1	0.7	8.4	87.8	42.2	36.3
		Cycle 2	-2.4	1.0	77.1	46.0	40.7
		Cycle 3	7.7	9.6	76.5	46.7	41.1
		Cycle 4	3.7	6.0	74.0	46.4	41.4
Beam 3	3 kN	Cycle 1	29.9	31.0	-746.6	138.7	79.8
		Cycle 2	26.7	27.4	178.9	100.1	56.4
		Cycle 3	18.4	19.1	132.9	79.4	74.6
	4 kN	Cycle 1	34.7	35.3	94.6	74.0	53.2
		Cycle 2	28.2	28.5	79.1	64.8	49.9
		Cycle 3	22.1	23.1	74.5	59.8	57.8
	5 kN	Cycle 1	36.6	36.4	66.3	57.5	47.1
		Cycle 2	29.5	29.5	63.6	55.7	46.9
		Cycle 3	23.9	25.0	61.8	53.3	52.1
	6 kN	Cycle 1	37.7	37.2	58.1	52.0	44.9
		Cycle 2	30.1	30.1	57.8	51.9	45.4
		Cycle 3	23.9	24.7	57.0	50.5	49.6

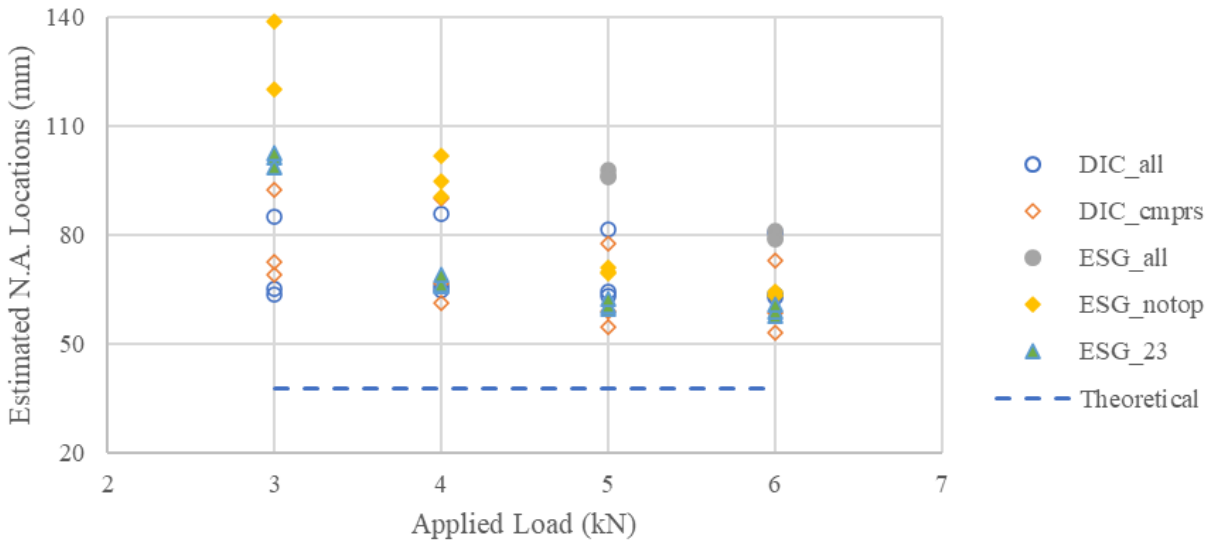

Figure F.9. Comparison of estimated N.A. locations to the theoretical value for Batch 2 Beam 1 pre-corrosion load test.

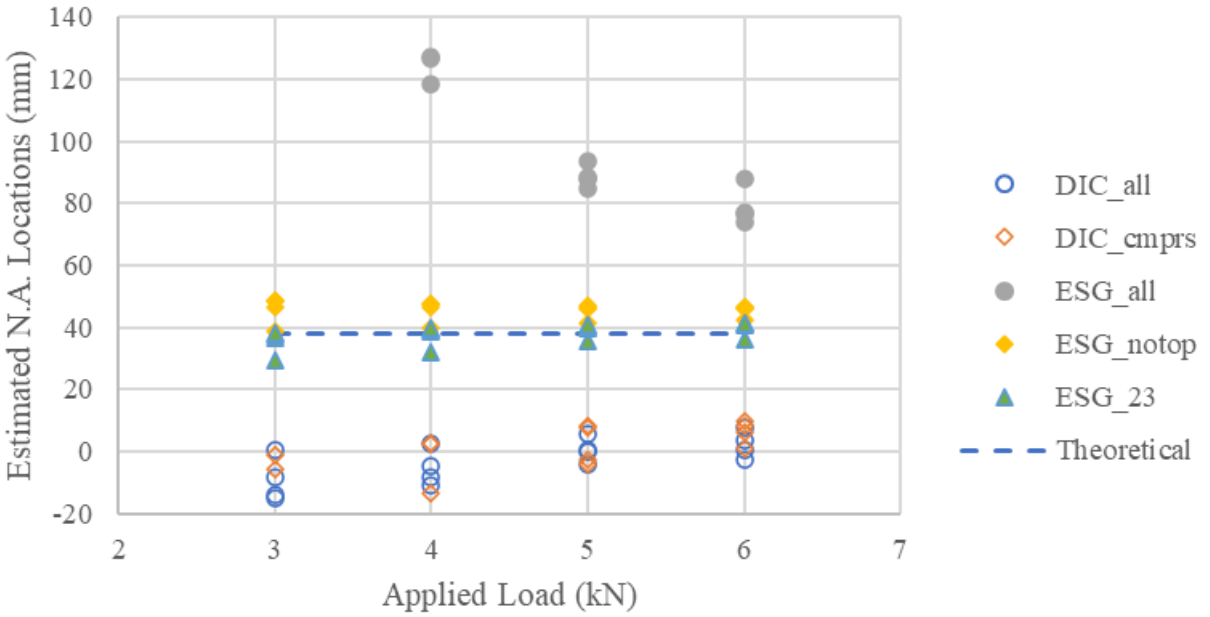

Figure F.10. Comparison of estimated N.A. locations to the theoretical value for Batch 2 Beam 2 pre-corrosion load test.

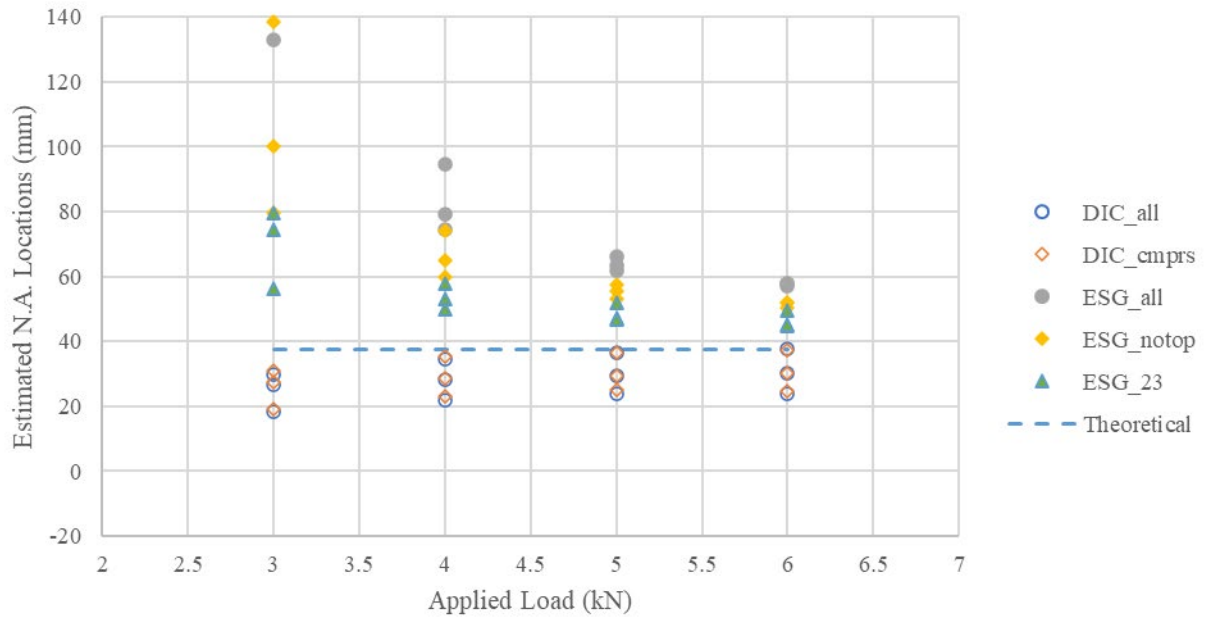

Figure F.11. Comparison of estimated N.A. locations to the theoretical value for Batch 2 Beam 3 pre-corrosion load test.

This set of ESG data were used to investigate the reliabilities of the top gauges and gauges located close to the N.A. locations. And for the DIC data, Comparisons were made between "DIC_all" and "DIC_cmprs" again. Also, the consistency of the results from the two faces and the effect of the level of loading are discussed. In general, the estimates made by both sides were quire poor, the reasons are also discussed.

Effect of the Location of the Electrical Strain Gauges

For all three beams, "ESG_all" provided the worst estimates, while "ESG_notop" provided better estimates, and the "ESG_G2& G3" gave the most accurate estimates. "ESG_all" was the worst meaning the strain gauges placed close to the N.A. locations had a negative effect to the accuracy of the estimates. And estimates using data excluding the top gauges ("ESG_G2& G3") had better results than "ESG_notop" indicated that the top gauges also had a negative impact. This was not observed for the Batch 1 beams. The reason might be because Batch 2 beams were slenderer, and the slenderness effect had caused the lateral deflection and twisting of the beams.

Effect of the Level of the Applied Load

There was an obvious improvement of accuracy under higher applied load, in general. This might because higher load can promote more linearly distributed strains.

Consistency of the Data from the Two Faces

Estimates from two sides were consistent for Beam 1 but were opposite for Beams 2 and 3.

Effect of the Location of the DIC gauges

For this set of the load tests, estimates obtained using all DIC data and DIC data in the compression zone only were very consistent with each other. The data from the tension zone did not affect the accuracy of the estimates. It was suspected the beams did not crack or they had extremely tight bonding.

Slenderness Effect

In general, both DIC and ESG estimates for this set of beams were poor, which may have been due to the wrinkling of surfaces and the new type of adhesive used for the ESGs. Since this batch of beams were slenderer and the estimates were off, slenderness effect was suspected. Slenderness effect can cause lateral deflections and twisting of RC beams similar to what is experienced by slender steel beams (Revathi and Menon 2008). Thus, the surface strains could be affected and be uneven on the two sides. The beams in Batch 2 were much slenderer than those in Batch 1, because the length was increased, and the width was decreased. Aside from a beam's dimension, the slenderness of concrete beams is also affected by the reinforcement ratio and concrete strength (Revathi and Menon 2008), both of which were smaller for Batch 2 beams as well. Existing concrete codes do not account for slenderness effects when calculating a beam's bending moment capacity (Revathi and Menon 2008). CSA A23.3 -14 only specifies that the minimum required thickness of simply supported beams be $1/16^{th}$ of the clear span length, and that the maximum distance between lateral supports be 50b or $200b^2/d$, whichever is smaller (CSA 2014). The beams used in this lab experiment met all the requirements in the CSA concrete code. However, many researchers have reported that the current provisions in concrete codes are not adequate to account for slenderness effects, and many studies have shown the

existence of lateral buckling on even less slender RC beams (Revathi and Menon 2008, Girija and Menon 2011, Samad et al. 2016).

F.2.4. Batch 2 First Post-corrosion Load Test

After corrosion, the beams' cracking load changed to around 2.1 kN and the conservative elastic limit dropped to around 4.5 kN, so each beam was gradually loaded until 4 kN repeatedly. The built-up corrosion product had cracked the beams longitudinally then spilled out and strained the DIC pattern drawn previously. Therefore, a grinder was used to remove the stains as well as the wrinkled surfaces on the DIC sides; then, new patterns were drawn on the smooth surfaces. For the purpose of protecting the ESGs during the corrosion process, the exposed copper wires at the connections were covered by a layer of glue to isolate any moisture and oxygen. Only three out of twelve gauges were damaged this time (G3 for Beam 1, G4 for Beam 2, and G3 for Beam 3). Comparisons were made among estimated N.A. locations using all the DIC data, the compressive DIC data, and the ESG data from all the working gauges. The results are presented in Table F.4. Comparisons to the theoretical values are illustrated in Figures F.12 to F.14.

Table F.4. Batch 2 first post-corrosion load test N.A. locations, measured from top surface in mm.

Beam #	Load	Cycle #	DIC_all	DIC_cmprs	ESG_all
Beam 1	3 kN	Cycle 1	72.5	130.9	18.4
		Cycle 2	-137.6	-903.6	-739.3
		Cycle 3	104.6	44.7	28.6
		Cycle 4	32.1	33.5	-489.3
	4 kN	Cycle 1	92.5	-76.7	21.7
		Cycle 2	-791.9	162.5	124.1
		Cycle 3	94.8	48.6	29.3
		Cycle 4	36.6	34.7	158.4
Beam 2	3 kN	Cycle 1	55.6	72.4	57.6
		Cycle 2	17.1	20.3	71.3
		Cycle 3	20.9	26.9	73.1
	4 kN	Cycle 1	49.2	56.5	53.7
		Cycle 2	15.3	18.9	59.4
		Cycle 3	18.0	21.4	60.2
Beam 3	3 kN	Cycle 1	65.8	-2028.7	-19.2
		Cycle 2	27.2	46.7	-19.1
		Cycle 3	26.4	46.5	-20.6
		Cycle 4	16.8	22.1	-21.9
	4 kN	Cycle 1	64.6	-237.1	-29.7
		Cycle 2	31.9	-85.8	-45.1
		Cycle 3	28.3	12.8	-52.4
		Cycle 4	21.4	44.4	-56.8

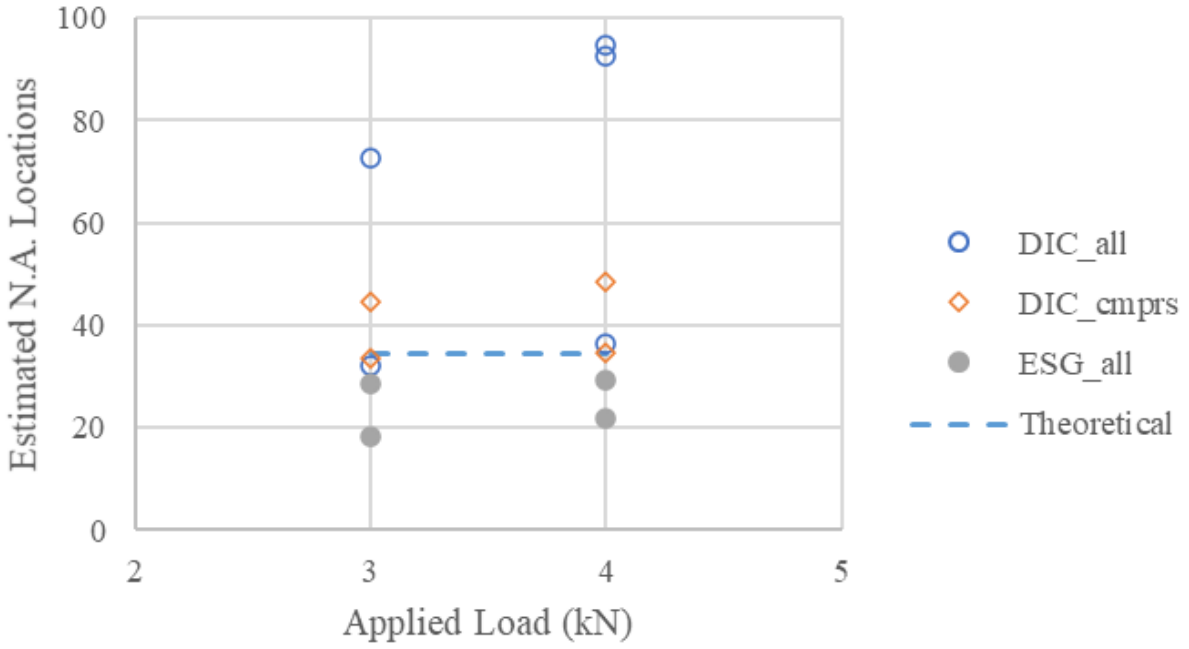

Figure F.12. Comparison of estimated N.A. locations to the theoretical value for Batch 2 Beam 1 first post-corrosion load test.

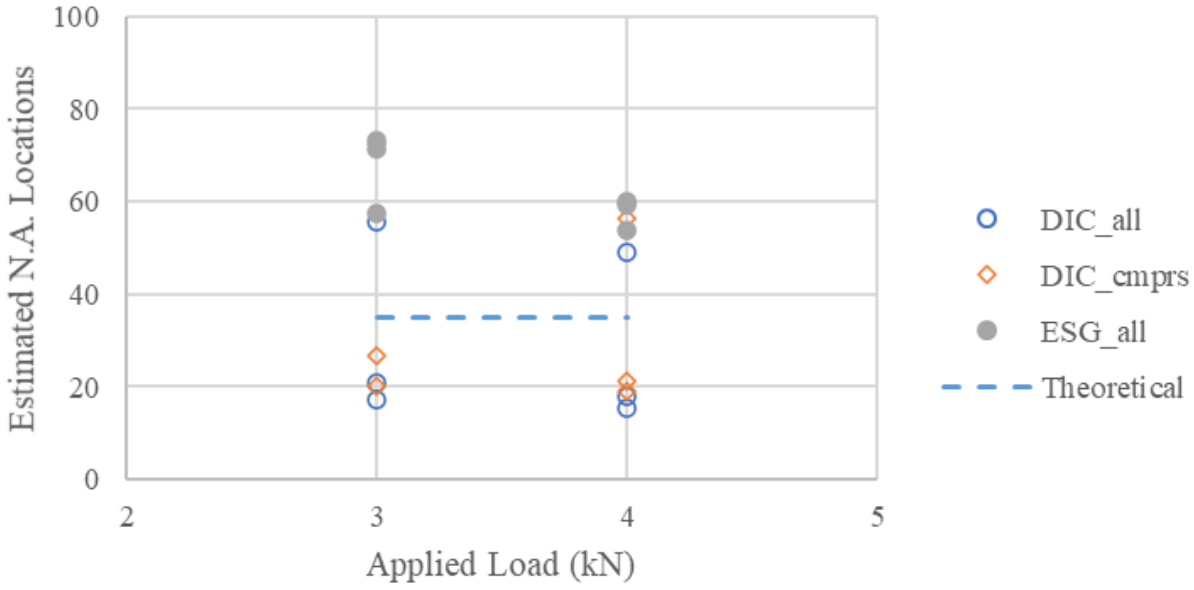

Figure F.13. Comparison of estimated N.A. locations to the theoretical value for Batch 2 Beam 2 first post-corrosion load test.

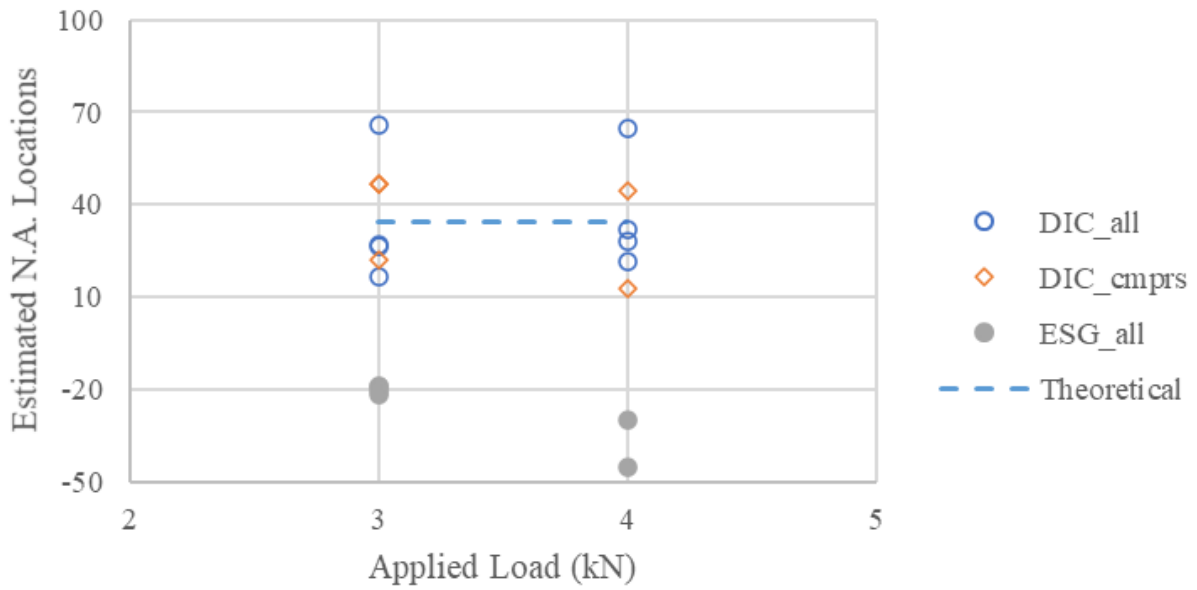

Figure F.14. Comparison of estimated N.A. locations to the theoretical value for Batch 2 Beam 3 first post-corrosion load test.

As shown in the table and the figures, the advantage of using higher loads was not apparent. This might be because the applied loads were not high enough. The ESG results had very high errors, which might be due to the type of glue used and any inconspicuous damage that may have been experienced during the corrosion process. Using the DIC data in the compression zone only increased the accuracy of the estimates for Beam 1; however, its advantage was not evident for Beams 2 and 3. Lastly, for all three beams, the estimated N.A. locations from two sides lay on the opposite side of the theoretical N.A. location.

Since not many useful conclusions could be drawn from the Batch 2 post-corrosion load test, the beams were saved from failure at the end of the post-corrosion load test, and a second post-corrosion load test was conducted.

F.2.5. Batch 2 Second Post-corrosion Load Test

The previously attached ESGs and the painted DIC surface, as well as the wrinkling on both side surfaces, were removed using a grinder. Four new ESGs were attach on each of the side surfaces using the original adhesive that came with the ESGs from the same manufacturer. The results of the N.A. analysis for each individual face are presented in Table F.5. Face 2 was originally the DIC side. Comparisons to the theoretical values were presented in Figures F.15 to F.17.

Table F.5. Batch 2 second post-corrosion load test N.A. locations, measured from top surface in mm.

Beam #	Load	Cycle #	Face 1			Face 2		
			ESG_all	ESG_notop	ESG_G2&G3	ESG_all	ESG_notop	ESG_G2&G3
Beam 1	3 kN	Cycle 1	93.6	74.3	73.9	93.3	65.1	50.0
		Cycle 2	59.3	57.9	53.5	120.4	78.7	64.1
		Cycle 3	71.1	65.6	60.4	95.0	69.8	59.3
		Cycle 4	70.1	62.0	62.4	90.5	68.0	58.6
		Cycle 5	61.2	55.4	59.0	99.5	71.1	60.7
		Cycle 6	70.1	63.4	53.5	97.3	70.7	60.9
		Cycle 7	72.3	65.9	62.4	96.4	70.3	61.1
		Cycle 8	76.6	69.4	63.5	99.4	72.4	62.3
		Cycle 9	81.7	70.7	68.5	90.1	68.8	60.0
		Cycle 10	78.8	69.8	68.1	100.6	73.0	64.0
		Cycle 11	92.9	78.5	73.3	96.7	71.8	63.1
	4 kN	Cycle 4	58.2	52.7	53.9	70.8	58.3	51.9
		Cycle 5	52.0	48.2	50.5	74.8	60.2	53.3
		Cycle 6	56.3	52.5	46.7	72.3	59.0	52.6
		Cycle 7	56.0	52.7	51.0	70.2	57.7	52.2
		Cycle 8	58.2	54.5	51.5	71.0	58.6	52.7
		Cycle 9	60.5	55.3	53.9	66.9	56.5	51.1
		Cycle 10	59.1	54.8	53.6	71.8	58.8	53.6
		Cycle 11	64.8	58.8	56.3	69.2	57.7	52.6
	5 kN	Cycle 7	51.7	48.8	47.7	63.7	53.7	49.1
		Cycle 8	52.2	49.5	47.3	62.8	53.6	49.0
		Cycle 9	53.0	49.6	48.5	58.8	51.3	47.3
		Cycle 10	51.6	48.6	47.6	61.7	52.8	48.8
		Cycle 11	55.1	51.3	49.5	59.8	52.0	48.0
	6 kN	Cycle 9	50.2	47.2	46.2	56.0	49.3	45.7
		Cycle 10	48.3	45.9	44.9	57.5	50.1	46.5
		Cycle 11	50.3	47.6	45.9	55.3	48.9	45.4

Table F.5. Continued.

Beam #	Load	Cycle #	Face 1			Face 2		
			ESG_all	ESG_notop	ESG_G2&G3	ESG_all	ESG_notop	ESG_G2&G3
Beam 2	3 kN	Cycle 1	67.3	56.3	48.6	-24.8	-37.8	-12.1
		Cycle 2	60.2	53.2	47.8	-970.3	235.0	-387.7
		Cycle 3	55.5	50.2	44.8	334.7	185.0	-1723.7
		Cycle 4	58.5	52.9	47.5	-174.3	326.5	-974.2
		Cycle 5	59.2	52.8	48.3	-2031.6	220.4	-55.1
		Cycle 6	61.1	52.5	49.7	34.6	383.5	-1084.7
		Cycle 7	62.9	53.0	49.6	16.6	412.8	1172.5
		Cycle 8	63.8	53.2	51.5	-3353.2	227.6	108.1
		Cycle 9	61.4	52.4	50.0	-44.0	209.5	10689.2
	4 kN	Cycle 3	50.2	46.6	42.4	148.7	90.4	130.1
		Cycle 4	50.3	47.2	43.4	204.0	105.1	164.5
		Cycle 5	50.1	46.6	43.5	115.5	81.5	108.8
		Cycle 6	51.1	46.5	44.5	128.9	85.7	126.5
		Cycle 7	51.4	46.5	44.1	119.3	83.2	111.8
		Cycle 8	52.5	47.1	45.5	102.8	78.5	109.0
		Cycle 9	51.3	46.5	44.6	105.2	78.0	107.6
	5 kN	Cycle 5	47.1	44.4	41.6	83.8	66.6	74.6
		Cycle 6	47.0	43.9	42.1	81.7	66.0	74.9
		Cycle 7	46.7	43.6	41.5	76.3	63.4	69.9
		Cycle 8	47.8	44.2	42.7	70.4	60.8	68.0
		Cycle 9	46.9	43.7	41.8	70.5	60.3	67.9
	6 kN	Cycle 7	44.2	41.8	39.7	63.6	55.4	57.4
		Cycle 8	45.4	42.7	41.0	59.8	53.8	56.3
		Cycle 9	44.4	42.0	40.1	58.5	52.7	55.3

Table F.5. Continued.

Beam #	Load	Cycle #	Face 1			Face 2		
			ESG_all	ESG_notop	ESG_G2&G3	ESG_all	ESG_notop	ESG_G2&G3
Beam 3	3 kN	Cycle 1	-208.5	230.0	47.5	-55.4	-72.7	-110.8
		Cycle 2	146.6	54.1	51.4	-131.0	-519.2	-326.1
		Cycle 3	129.4	53.2	50.3	-473.5	-928.7	-1213.9
		Cycle 4	151.8	53.6	51.6	-181.2	-8131.1	-753.0
		Cycle 5	154.5	53.4	51.7	-170.6	-585.4	-311.4
		Cycle 6	-8097.3	56.9	55.5	-82.9	-161.1	-94.7
		Cycle 7	254.2	58.2	49.9	-134.4	619.2	-266.3
		Cycle 8	115.0	51.4	50.0	-285.2	-119.0	493.0
	4 kN	Cycle 3	87.4	50.5	48.6	1966.0	231.4	494.0
		Cycle 4	86.0	50.2	48.8	-3972.6	248.9	605.6
		Cycle 5	81.7	49.6	48.5	47.2	214.1	1164.0
		Cycle 6	103.8	52.0	51.2	1095.5	434.1	-223.3
		Cycle 7	88.9	52.3	46.8	200.8	266.1	287.4
		Cycle 8	71.5	47.6	46.5	1941.3	158.6	332.7
	5 kN	Cycle 5	68.0	47.7	47.0	184.0	118.0	158.3
		Cycle 6	75.7	49.1	48.6	289.5	154.8	230.7
		Cycle 7	66.1	48.5	44.4	156.6	106.8	126.2
		Cycle 8	58.4	45.1	44.1	121.6	90.6	109.2
	6 kN	Cycle 7	57.0	46.3	42.5	93.6	77.0	85.0
		Cycle 8	52.3	43.6	42.1	83.1	70.6	78.0

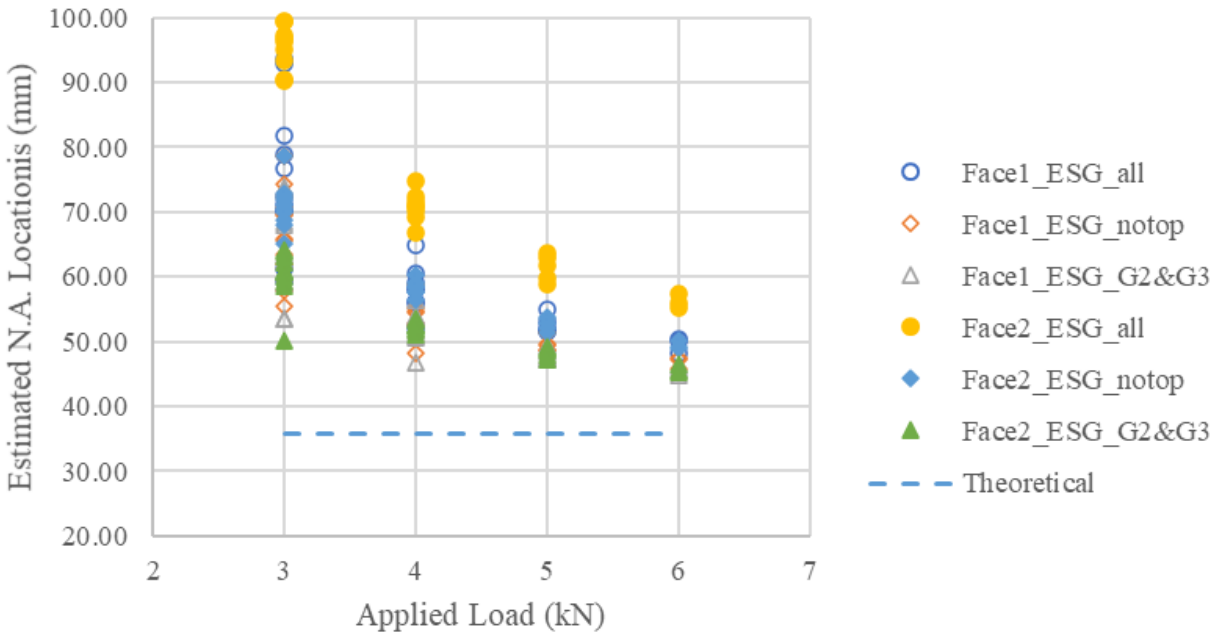

Figure F.15. Comparison of estimated N.A. locations to the theoretical value for Batch 2 Beam 1 second post-corrosion load test.

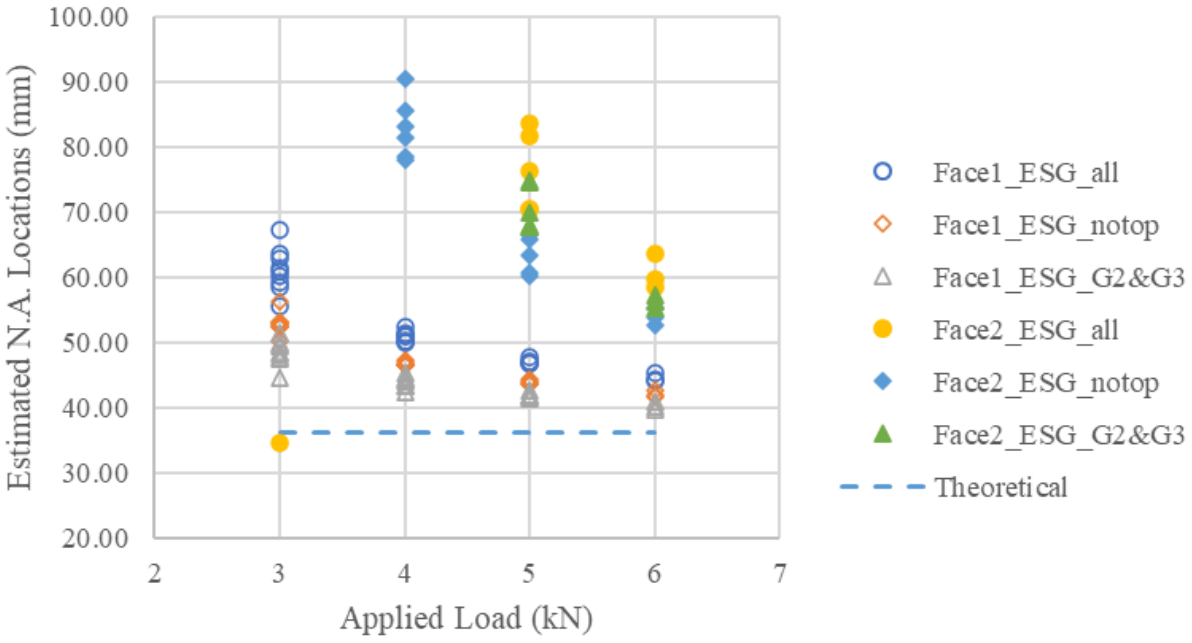

Figure F.16. Comparison of estimated N.A. locations to the theoretical value for Batch 2 Beam 2 second post-corrosion load test.

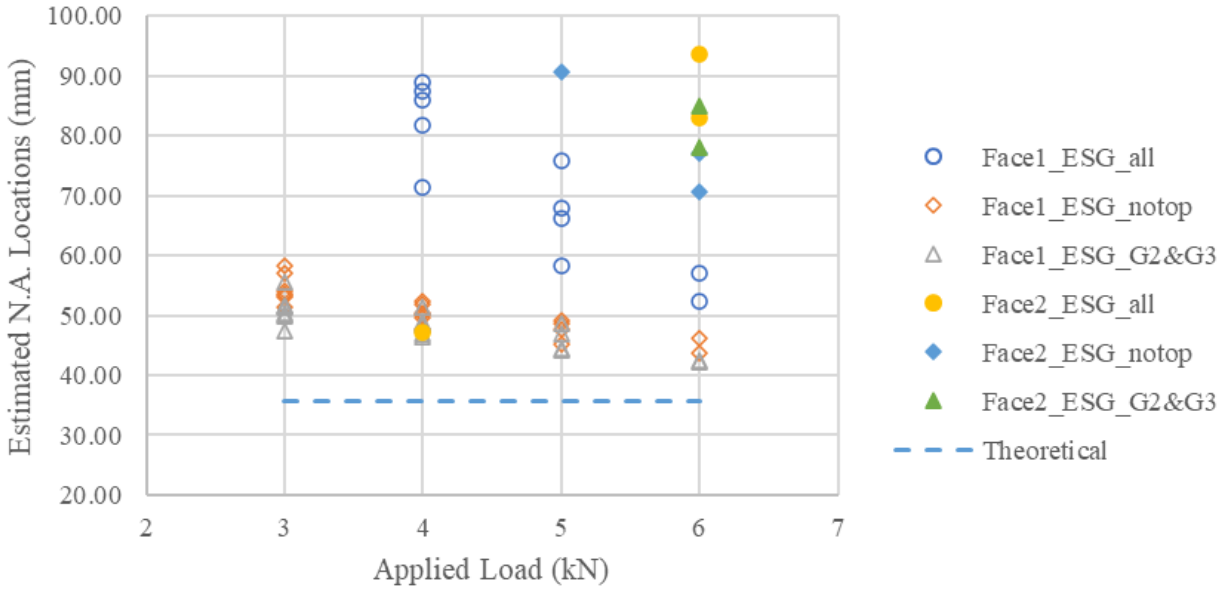

Figure F.17. Comparison of estimated N.A. locations to the theoretical value for Batch 2 Beam 3 second post-corrosion load test.

The Existence of Eccentric Loading

The main purpose of this set of data was to verify the existence of eccentric loading. Both sides were monitored by ESGs, and the factors associated with the unevenness of the surface and the type of the glue were removed. Although the estimates from the DIC and ESG data frequently lay on the opposite sides of the theoretical N.A. location for the other load tests, the phenomenon was not observed for this set of the load tests. Both sides overestimated the distance of the N.A. locations measured from the top of the beams.

Effect of the Location of the Electrical Strain Gauges

For Beam 1, Face 1 data aligned with Face 2 data well. For both faces, “ESG_all” provided the worst estimates, and “ESG_notop” and “ESG_G2&G3” were comparable. For Beams 2 and 3, Face 2 data were significantly worse than the Face 1 data. And for each face, again “ESG_all” provided the worst estimates, and “ESG_notop” and “ESG_G2&G3” were comparable. Thus, the top gauges had a negative effect to the accuracy of the results.

Effect of the Level of the Applied Load

For all beams, better results were achieved under higher applied loads.

F.2.6. Batch 3 Pre-corrosion Load Test

Batch 3 beams had the same design configuration and concrete mix ratios as Batch 2 beams. The cracking load was about 2.1 kN and the conservative elastic limit was about 4.9 kN. Since Batch 2 did not achieve accurate estimates under lower applied load, Beam 1 and Beam 2 were loaded to 6 kN in this load test, which was still within the liberal elastic limit (8.2 kN). Beam 3 exhibited a proportional relationship between strain and load even at lower loads, so it was not loaded past the conservative elastic limit. Moreover, to increase the reliability of the measured strain data, the concrete surfaces were smoothed using a grinder, and the original type of adhesive was used for attaching the ESGs. The results of the individual face analysis are provided in Table F.6. Comparisons to the theoretical values were presented in Figures F.18 to F.20.

Table F.6. Batch 3 pre-corrosion load test N.A. locations, measured from top surface in mm.

Beam #	Load	Cycle #	DIC_all	DIC_cmprs	ESG_all	ESG_notop	ESG_23
Beam 1	3 kN	Cycle 1	7.5	13.5	124.5	107.4	119.1
		Cycle 2	21.4	22.7	115.2	95.0	115.1
		Cycle 3	23.7	23.9	115.9	95.9	116.5
	4 kN	Cycle 1	8.6	14.9	55.3	48.7	90.7
		Cycle 2	21.1	22.8	84.2	74.5	88.3
		Cycle 3	23.9	23.9	82.9	73.8	87.3
Beam 2	3 kN	Cycle 1	32.9	29.1	57.0	55.4	69.7
		Cycle 2	102.8	69.0	44.3	44.8	57.5
		Cycle 3	98.1	64.5	44.1	44.7	57.1
	4 kN	Cycle 1	41.5	32.2	57.0	57.2	66.2
		Cycle 2	93.5	61.5	43.5	44.1	56.4
		Cycle 3	91.5	59.7	43.4	44.1	56.1
Beam 3	3 kN	Cycle 1	133.3	52.6	40.4	40.6	49.5
		Cycle 2	153.5	65.4	36.9	37.8	46.2
		Cycle 3	602.6	75.9	36.3	37.1	45.6
	4 kN	Cycle 1	158.0	52.3	39.2	39.6	48.2
		Cycle 2	151.3	64.2	36.8	37.7	45.9
		Cycle 3	411.8	70.8	36.3	37.1	45.4

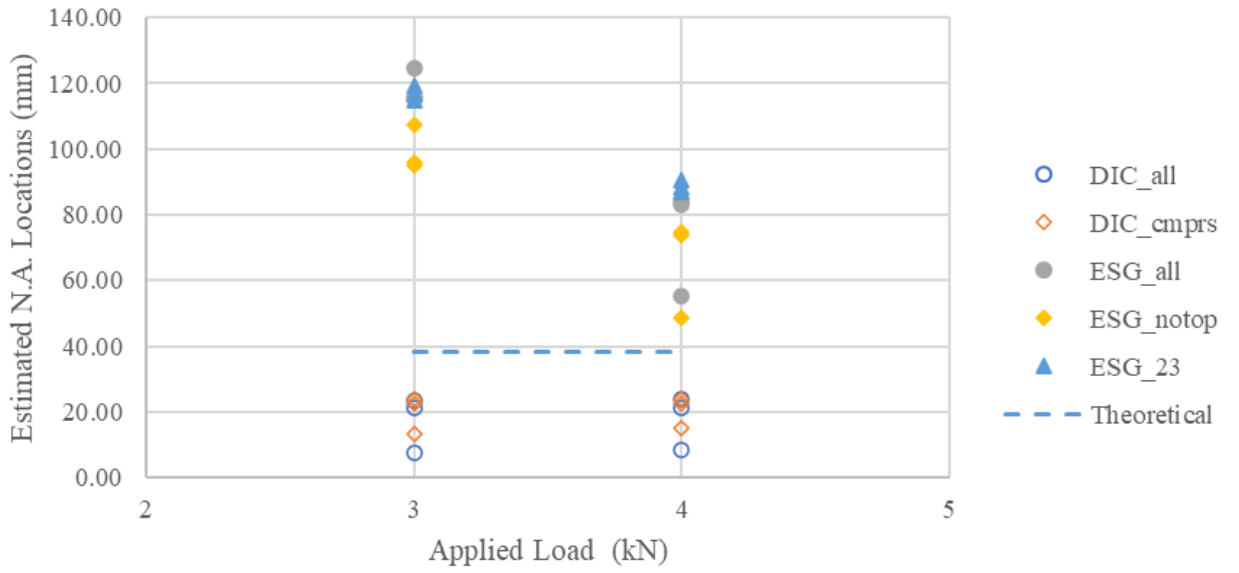

Figure F.18. Comparison of estimated N.A. locations to the theoretical value for Batch 3 Beam 1 pre-corrosion load test.

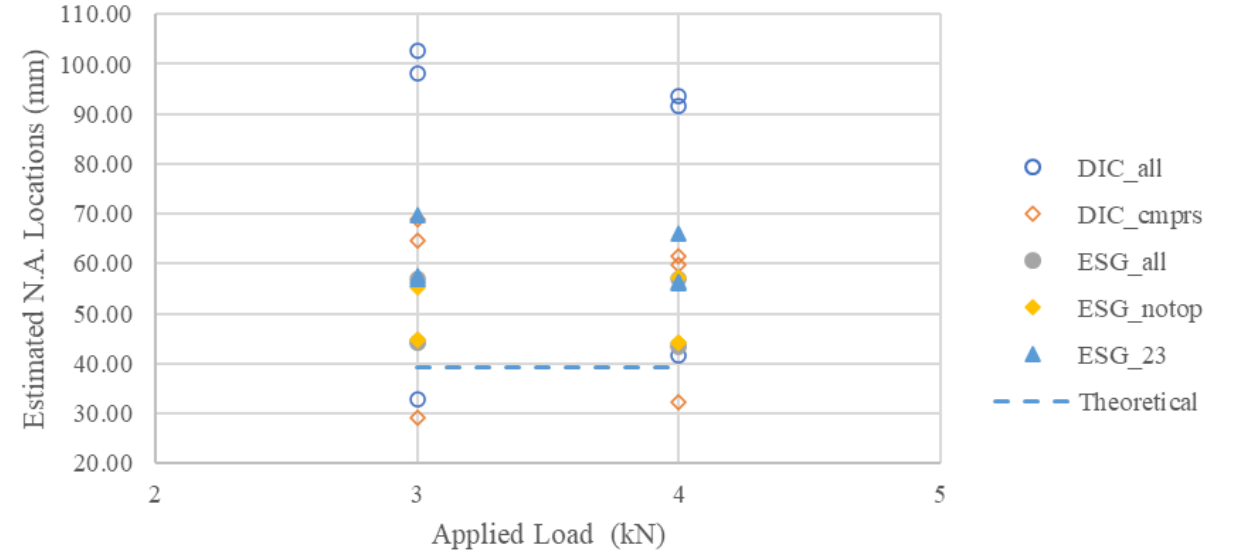

Figure F.19. Comparison of estimated N.A. locations to the theoretical value for Batch 3 Beam 2 pre-corrosion load test.

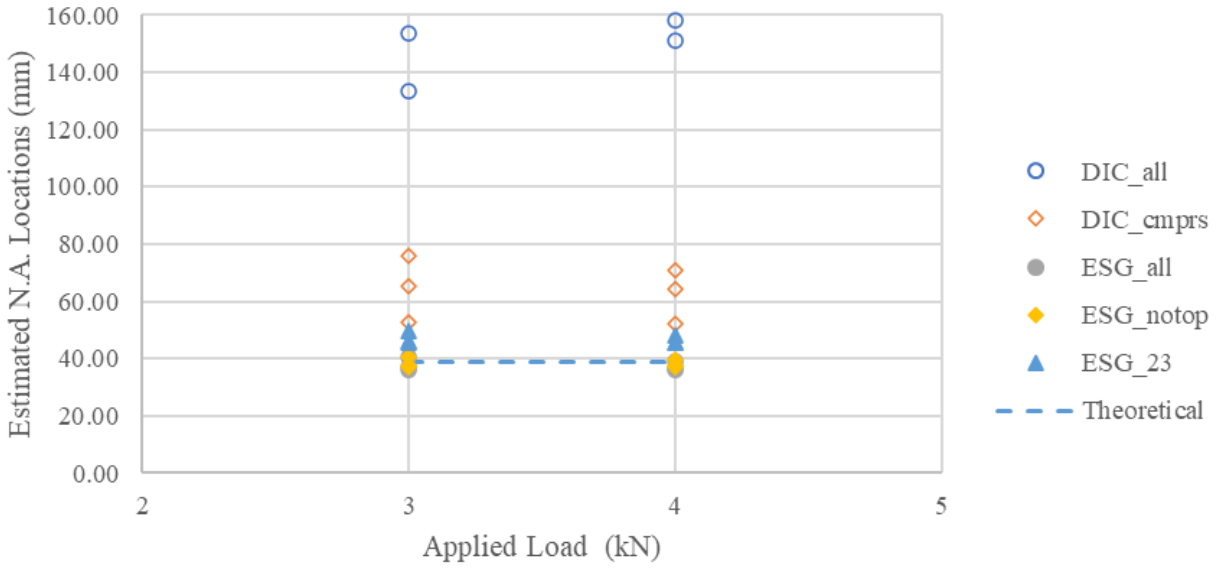

Figure F.20. Comparison of estimated N.A. locations to the theoretical value for Batch 3 Beam 3 pre-corrosion load test.

Effect of the Location of the Gauges

For the ESG side, the location of the strain gauges did not affect the accuracy of the estimates much. The DIC results using the compressive strains only performed much better than using all the data for Beams 2 and 3. But the difference was not obvious for Beam 1.

Effect of the Level of the Applied Load

For Beam 1 and 2, better results were achieved under higher applied loads. Beam 3 did not demonstrate this trend. However, the ESG estimates for Beam 3 were already very close to the theoretical value even at lower loads.

Complementarity of the Data from the Two Faces

Complementarity of the data from the two faces were observed for Beam 1, but not for Beams 2 and 3.

F.2.7. Batch 3 Post-corrosion Load Test

After corrosion, the cracking load, as well as the conservative and liberal elastic limits changed to around 2.1 kN, 4.8 kN and 7.3 kN, respectively. All the beams were loaded to 6 kN repeatedly. The same protection method was applied to the ESGs during corrosion, but all the electrical strain gauges attached for the pre-corrosion load test survived the corrosion process, perhaps

because Batch 3 beams were corroded less than Batch 2. However, the DIC faces were still stained by the corrosion product, so the DIC patterns were ground off and repainted. The results of the individual face analysis are summarized in Table F.7. Comparisons to the theoretical values were presented in Figures F.21 to F.23.

Table F.7. Batch 3 post-corrosion load test N.A. locations, measured from top surface in mm.

Beam #	Load	Cycle #	DIC_all	DIC_cmprs	ESG_all	ESG_notop	ESG_G2&G3
Beam 1	3 kN	Cycle 1	31.8	32.6	75.7	66.9	66.4
		Cycle 2	29.5	29.5	65.2	59.8	58.5
		Cycle 3	25.3	25.6	64.3	59.2	57.6
		Cycle 4	32.5	32.0	63.4	58.6	57.2
		Cycle 5	24.2	25.6	57.0	53.6	52.2
		Cycle 6	26.8	29.3	49.0	47.5	46.1
	4 kN	Cycle 1	31.7	31.3	66.5	61.1	60.6
		Cycle 2	29.8	29.3	60.1	56.6	55.3
		Cycle 3	26.9	26.9	59.3	56.0	54.5
		Cycle 4	33.1	32.0	58.5	55.3	54.0
		Cycle 5	26.2	27.9	52.3	50.2	48.9
		Cycle 6	25.1	28.3	45.2	44.4	43.3
	5 kN	Cycle 4	33.2	31.8	54.8	52.6	51.5
		Cycle 5	26.8	28.0	49.4	48.0	46.8
		Cycle 6	24.4	28.3	44.3	43.7	42.5
	6 kN	Cycle 4	33.5	31.8	52.0	50.5	49.3
		Cycle 5	28.4	29.2	47.4	46.4	45.2
		Cycle 6	23.3	28.0	43.2	42.8	41.6
Beam 2	3 kN	Cycle 1	35.7	32.6	-8535.6	4080.5	-87.0
		Cycle 2	16.9	20.4	169.9	139.4	164.0
		Cycle 3	30.1	29.7	161.3	131.3	162.4
		Cycle 4	27.4	27.8	154.9	127.2	156.5
		Cycle 5	25.5	26.4	100.3	85.1	92.7
		Cycle 6	21.8	25.1	75.0	65.5	66.9
		Cycle 7	29.4	27.6	45.4	42.8	39.6
	4 kN	Cycle 1	41.1	34.6	164.1	158.9	-4205.1
		Cycle 2	19.6	22.8	97.5	88.1	90.8
		Cycle 3	32.1	30.5	94.9	85.4	90.3
		Cycle 4	30.4	29.4	91.1	82.2	87.0
		Cycle 5	27.6	27.6	74.2	66.8	67.9
		Cycle 6	24.2	26.3	62.5	56.8	56.2
		Cycle 7	30.6	27.9	44.0	41.9	38.7
	5 kN	Cycle 4	32.7	30.4	73.5	68.2	69.6
		Cycle 5	30.1	28.7	63.4	58.6	58.1
		Cycle 6	26.9	27.3	56.2	52.2	50.8
		Cycle 7	31.9	28.2	42.9	41.1	38.0
	6 kN	Cycle 4	33.8	30.7	65.4	61.4	61.2
		Cycle 5	32.2	29.6	58.2	54.5	53.2
		Cycle 6	28.6	27.9	53.1	49.8	48.0
		Cycle 7	33.6	28.7	42.0	40.5	37.4

Table F.7. Continued.

Beam #	Load	Cycle #	DIC_all	DIC_cmprs	ESG_all	ESG_notop	ESG_G2&G3
Beam 3	3 kN	Cycle 1	69.4	78.7	105.8	88.8	181.4
		Cycle 2	73.5	86.0	84.5	73.6	80.8
		Cycle 3	77.3	67.0	77.5	69.7	75.1
		Cycle 4	83.3	73.2	74.7	67.7	72.3
		Cycle 5	50.4	45.4	58.7	57.5	59.3
		Cycle 6	63.4	47.8	56.8	56.0	57.2
	4 kN	Cycle 1	66.7	60.1	68.9	66.2	83.5
		Cycle 2	69.4	64.0	64.9	61.4	63.3
		Cycle 3	74.3	56.6	62.2	59.6	60.9
		Cycle 4	80.1	59.3	60.8	58.4	59.4
		Cycle 5	49.9	39.2	51.5	51.4	51.3
		Cycle 6	61.7	41.5	50.0	50.0	49.9
	5 kN	Cycle 4	78.7	49.4	53.9	53.1	52.8
		Cycle 5	53.7	36.9	47.5	47.8	47.1
		Cycle 6	62.4	38.6	46.5	46.8	46.1
	6 kN	Cycle 4	79.0	44.7	47.8	48.1	46.6
		Cycle 5	58.6	37.0	44.9	45.3	44.2
		Cycle 6	64.4	38.1	44.0	44.5	43.6

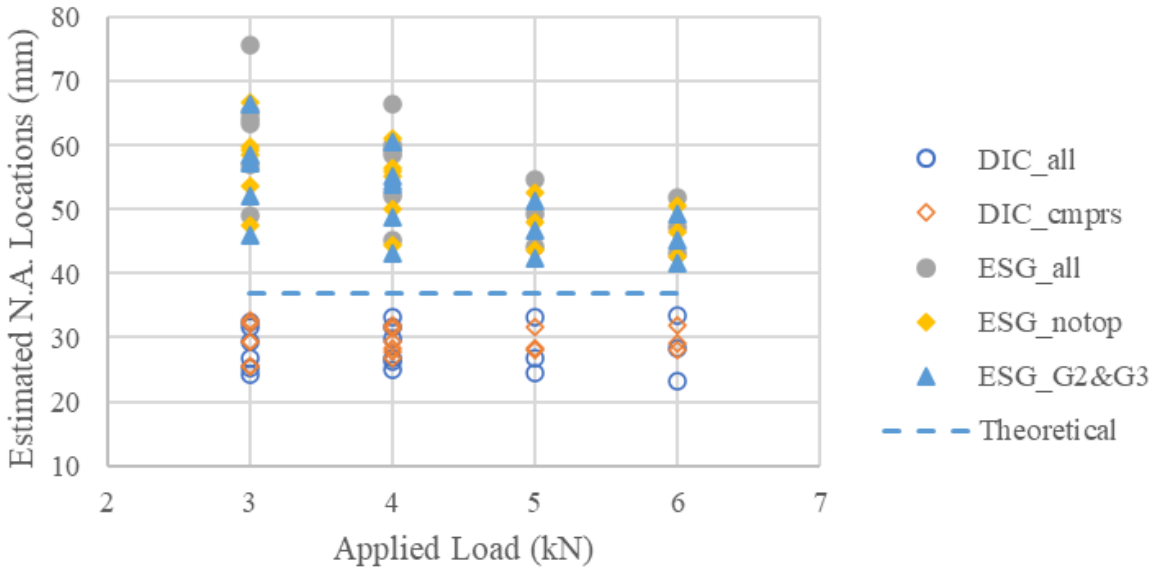

Figure F.21. Comparison of estimated N.A. locations to the theoretical value for Batch 3 Beam 1 post-corrosion load test.

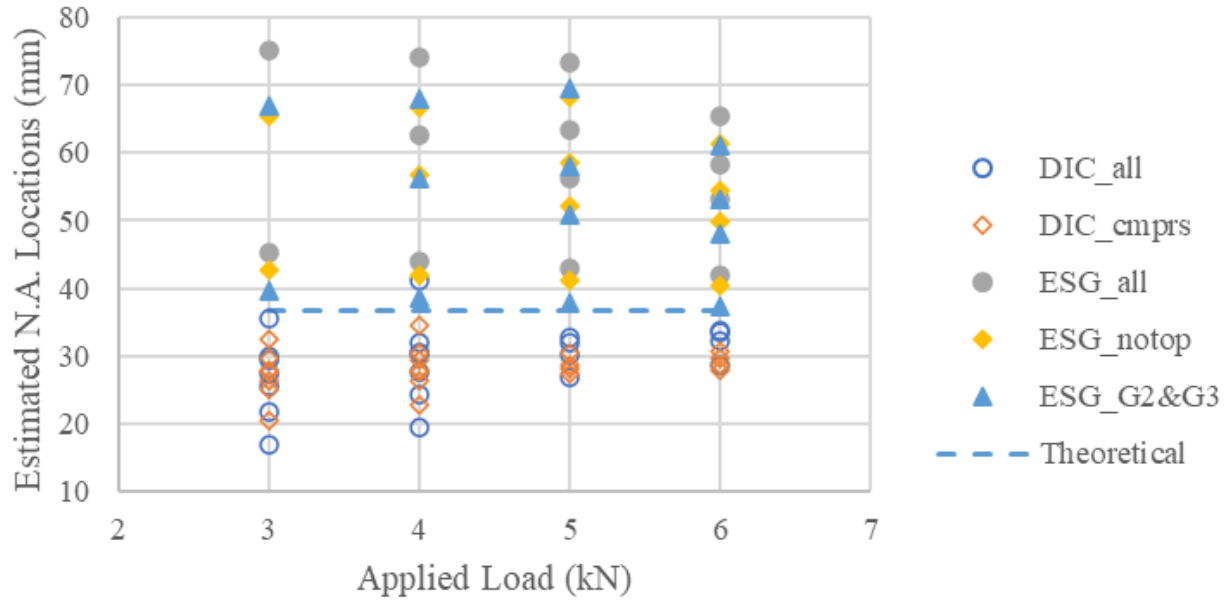

Figure F.22. Comparison of estimated N.A. locations to the theoretical value for Batch 3 Beam 2 post-corrosion load test.

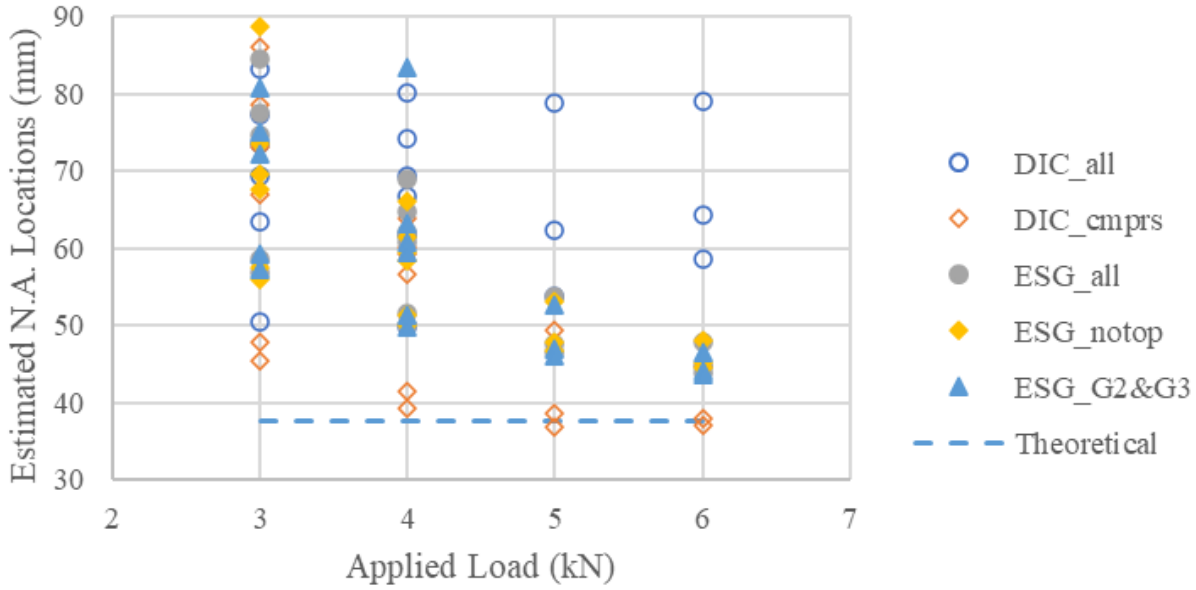

Figure F.23. Comparison of estimated N.A. locations to the theoretical value for Batch 3 Beam 3 post-corrosion load test.

Effect of the Location of the Gauges

The ESG results using Gauges 2 and 3 were slightly better than the other two ESG results, but the difference was not significant. The DIC results using the compressive strains only performed

much better than using all the data for Beams 3. But the differences were not obvious for Beams 1 and 2.

Effect of the Level of the Applied Load

For all beams, better results were achieved under higher applied loads.

Consistency of the Data from the Two Faces

Consistency of the data from the two faces were observed for Beam 3, but not for Beams 1 and 2.

F.4. The Optimal Procedures

The preliminary analyses done in this appendix aimed to find the optimum strain collection and analysis procedures. The results of the preliminary analysis are summarized in Table F.8.

Modifications in the data collection procedures were made throughout the seven load tests to identify the optimal procedures for implementing the proposed SHM technique. Although the final accuracy of the results achieved by Batch 3 was still below expectations, many lessons were learned from these analyses.

Regarding the location of the gauges, it was suspected that gauges located in the tension zone, on the top of the beam, and close to N.A. locations might have adverse effect on the accuracy of the estimates. Among the 18 load tests that compared the effect of using tensile strains, 11 of them showed it resulted in negative effects, and seven of them showed there was no significant impact. The top gauges caused negative effect for six out of 14 cases. No significant impact was found for the rest of the cases, except for Batch 1 Beam 2 pre-corrosion load test, including the top gauge increased the accuracy of the estimates. Having gauges located close to the N.A. location did not seem to be very problematic, as long as they are in the compression side; only two out of the 12 cases showed negative effect, and the rests showed no significant impact. In summary, for obtaining more reliable strain data, strain gauges should be placed in the compression zone and ideally in the same plane (i.e., not on the top of the beams). Especially for the electrical strain gauges, the gauges placed in the tension zone were less reliable and more prone to damage due to the extreme strains at the tensile cracks. Gauges close to the neutral axes were less problematic, but it is not recommended if the space is enough.

Table F.8. Summary of the results of the preliminary analyses.

Load Test	Tension Gauge	Top Gauge	Gauge Close to N.A.	Higher Load	Two Face Opposite
Batch 1 Beam 1 Pre	negative	no difference	N/A	no difference	N/A
Batch 1 Beam 2 Pre	negative	positive	N/A	no difference	N/A
Batch 1 Beam 3 Pre	negative	N/A	N/A	no difference	N/A
Batch 1 Beam 1 Post	negative	N/A	N/A	no difference	Yes
Batch 1 Beam 2 Post	negative	N/A	N/A	no difference	Yes
Batch 1 Beam 3 Post	negative	N/A	N/A	no difference	No
Batch 2 Beam 1 Pre	negative	negative	negative	positive	No
Batch 2 Beam 2 Pre	no difference	negative	no difference	positive	Yes
Batch 2 Beam 3 Pre	no difference	negative	negative	positive	Yes
Batch 2 Beam 1 First Post	negative	N/A	N/A	no difference	Yes
Batch 2 Beam 2 First Post	no difference	N/A	N/A	no difference	Yes
Batch 2 Beam 3 First Post	no difference	N/A	N/A	no difference	Yes
Batch 2 Beam 1 Second Post	N/A	negative	no difference	positive	No
Batch 2 Beam 2 Second Post	N/A	negative	no difference	positive	No
Batch 2 Beam 3 Second Post	N/A	negative	no difference	positive	No
Batch 3 Beam 1 Pre	no difference	no difference	no difference	positive	Yes
Batch 3 Beam 2 Pre	negative	no difference	no difference	positive	No
Batch 3 Beam 3 Pre	negative	no difference	no difference	no difference	No
Batch 3 Beam 1 Post	no difference	no difference	no difference	positive	Yes
Batch 3 Beam 2 Post	no difference	no difference	no difference	positive	Yes
Batch 3 Beam 3 Post	negative	no difference	no difference	positive	No

For the optimum level of the applied load, it appears that the accuracy of the estimates can be improved and the variance between different cycles of the loading can be reduced by applying higher loads in most of the cases. For the cases that did not show significant impact, it was mostly because they were not loaded to a much higher load or accurate estimates were already obtained at lower loads. So, in short, higher loads are better than lower ones. This might because the concrete is a non-homogeneous material and higher loads can cause the strain to be more evenly distributed. Larger strain readings under higher loads may also mitigate some errors and increase the accuracy in the strain gauge readings.

Regarding the data analysis procedures, the N.A. locations estimated considering the strain data from each face separately were not as accurate as expected. However, it was found that for many cases, the estimates from each face lay on opposite side of the theoretical N.A. locations. Therefore, eccentric loading was suspected causing the one side to be less loaded and the other side to be higher loaded. Therefore, the average of the estimates using data from both sides should be closer to the theoretical N.A. location than any estimates from each individual face. Although the second post-corrosion load tests for Batch 2 beams proved that eccentric loading did not happen to all cases, and for some cases, the estimates from the two faces aligned with each other quite well, it would still be beneficial to obtain the estimates using combined data from two faces, as more data should increase the reliability of the results. Therefore, it is recommended that the N.A. locations should be estimated considering strains obtained from the two side surfaces. Three different methods for combining the data were tested and discussed in Chapter 4.

APPENDIX G Sample Raw Strain Data Provided by ESG and DIC

Table G.1. ESG Raw Data from the Pre-corrosion Load Test for Batch 3 Beam 3 Cycle 1.

Load (kN)	Strain 1	Strain 2	Strain 3	Strain 4	Time (s)
0.29	2.58E-06	-8.12E-07	6.90E-08	1.69E-06	1
0.28	2.27E-06	-7.64E-07	3.53E-07	1.11E-06	2
0.30	2.05E-06	-1.35E-06	1.47E-06	1.52E-06	3
0.27	2.18E-06	-6.05E-07	6.90E-07	8.92E-07	4
0.28	2.39E-06	-1.04E-06	7.16E-07	7.02E-07	5
0.29	2.25E-06	-5.28E-07	1.15E-06	1.65E-06	6
0.29	1.69E-06	-2.64E-07	2.81E-07	1.29E-06	7
0.28	1.60E-06	-4.48E-07	5.09E-07	1.14E-06	8
0.28	1.51E-06	4.01E-07	2.81E-07	7.87E-07	9
0.28	8.50E-07	-1.43E-06	-1.54E-06	-1.18E-06	10
0.37	-2.78E-06	-7.37E-06	-8.40E-06	-7.91E-06	11
0.51	-7.64E-06	-1.53E-05	-1.79E-05	-1.84E-05	12
0.60	-1.15E-05	-2.12E-05	-2.52E-05	-2.65E-05	13
0.68	-1.43E-05	-2.42E-05	-2.98E-05	-3.08E-05	14
0.69	-1.48E-05	-2.60E-05	-3.23E-05	-3.26E-05	15
0.69	-1.61E-05	-2.72E-05	-3.47E-05	-3.45E-05	16
0.78	-1.71E-05	-2.88E-05	-3.53E-05	-3.76E-05	17
0.77	-1.81E-05	-3.08E-05	-3.87E-05	-4.06E-05	18
0.86	-1.94E-05	-3.46E-05	-4.31E-05	-4.51E-05	19
0.85	-2.17E-05	-3.71E-05	-4.70E-05	-4.99E-05	20
0.95	-2.32E-05	-4.02E-05	-5.00E-05	-5.50E-05	21
1.01	-2.54E-05	-4.27E-05	-5.46E-05	-5.91E-05	22
1.02	-2.75E-05	-4.46E-05	-5.84E-05	-6.50E-05	23
1.11	-2.84E-05	-4.77E-05	-6.22E-05	-6.87E-05	24
1.18	-2.92E-05	-4.99E-05	-6.50E-05	-7.23E-05	25
1.20	-3.07E-05	-5.27E-05	-6.90E-05	-7.78E-05	26
1.27	-3.21E-05	-5.42E-05	-7.12E-05	-8.03E-05	27
1.31	-3.34E-05	-5.62E-05	-7.55E-05	-8.51E-05	28
1.35	-3.52E-05	-5.89E-05	-7.79E-05	-8.84E-05	29

Table G.1. Continued.

Load (kN)	Strain 1	Strain 2	Strain 3	Strain 4	Time (s)
1.42	-3.51E-05	-6.08E-05	-8.09E-05	-9.34E-05	30
1.42	-3.70E-05	-6.28E-05	-8.40E-05	-9.74E-05	31
1.51	-3.88E-05	-6.44E-05	-8.66E-05	-1.02E-04	32
1.60	-3.88E-05	-6.70E-05	-9.02E-05	-1.07E-04	33
1.59	-3.95E-05	-6.95E-05	-9.39E-05	-1.11E-04	34
1.68	-4.18E-05	-7.15E-05	-9.68E-05	-1.16E-04	35
1.70	-4.25E-05	-7.26E-05	-1.00E-04	-1.20E-04	36
1.76	-4.32E-05	-7.46E-05	-1.04E-04	-1.24E-04	37
1.77	-4.41E-05	-7.55E-05	-1.04E-04	-1.26E-04	38
1.84	-4.49E-05	-7.78E-05	-1.08E-04	-1.32E-04	39
1.92	-4.63E-05	-8.11E-05	-1.12E-04	-1.38E-04	40
1.99	-4.71E-05	-8.30E-05	-1.16E-04	-1.43E-04	41
2.09	-4.84E-05	-8.46E-05	-1.19E-04	-1.47E-04	42
2.11	-4.80E-05	-8.59E-05	-1.20E-04	-1.51E-04	43
2.17	-4.94E-05	-8.75E-05	-1.24E-04	-1.56E-04	44
2.17	-5.04E-05	-8.92E-05	-1.26E-04	-1.59E-04	45
2.25	-5.16E-05	-9.08E-05	-1.30E-04	-1.63E-04	46
2.27	-5.09E-05	-9.19E-05	-1.31E-04	-1.66E-04	47
2.35	-5.22E-05	-9.49E-05	-1.34E-04	-1.72E-04	48
2.43	-5.38E-05	-9.60E-05	-1.39E-04	-1.78E-04	49
2.49	-5.39E-05	-9.88E-05	-1.43E-04	-1.83E-04	50
2.52	-5.59E-05	-1.01E-04	-1.46E-04	-1.87E-04	51
2.57	-5.69E-05	-1.02E-04	-1.48E-04	-1.92E-04	52
2.60	-5.73E-05	-1.04E-04	-1.52E-04	-1.97E-04	53
2.57	-5.81E-05	-1.04E-04	-1.51E-04	-1.94E-04	54
2.65	-5.85E-05	-1.06E-04	-1.55E-04	-2.01E-04	55
2.75	-6.06E-05	-1.09E-04	-1.60E-04	-2.09E-04	56
2.82	-6.17E-05	-1.13E-04	-1.65E-04	-2.15E-04	57
2.91	-6.23E-05	-1.15E-04	-1.69E-04	-2.20E-04	58
2.90	-6.35E-05	-1.16E-04	-1.72E-04	-2.25E-04	59
3.00	**-6.48E-05**	**-1.17E-04**	**-1.74E-04**	**-2.29E-04**	**60**
3.00	-6.54E-05	-1.20E-04	-1.78E-04	-2.33E-04	61
3.08	-6.62E-05	-1.22E-04	-1.82E-04	-2.38E-04	62
3.17	-6.75E-05	-1.24E-04	-1.84E-04	-2.44E-04	63
3.19	-6.79E-05	-1.26E-04	-1.89E-04	-2.48E-04	64
3.25	-6.85E-05	-1.28E-04	-1.91E-04	-2.54E-04	65
3.23	-6.98E-05	-1.30E-04	-1.94E-04	-2.59E-04	66
3.25	-6.97E-05	-1.29E-04	-1.94E-04	-2.57E-04	67
3.25	-6.89E-05	-1.29E-04	-1.94E-04	-2.57E-04	68
3.24	-6.90E-05	-1.28E-04	-1.94E-04	-2.57E-04	69
3.24	-6.94E-05	-1.28E-04	-1.93E-04	-2.56E-04	70

Table G.1. Continued.

Load (kN)	Strain 1	Strain 2	Strain 3	Strain 4	Time (s)
3.25	-6.78E-05	-1.29E-04	-1.92E-04	-2.56E-04	71
3.24	-6.84E-05	-1.28E-04	-1.94E-04	-2.57E-04	72
3.24	-6.75E-05	-1.28E-04	-1.93E-04	-2.56E-04	73
3.25	-6.85E-05	-1.28E-04	-1.93E-04	-2.56E-04	74
3.22	-6.83E-05	-1.28E-04	-1.93E-04	-2.58E-04	75
3.16	-6.79E-05	-1.27E-04	-1.93E-04	-2.57E-04	76
3.21	-6.79E-05	-1.28E-04	-1.93E-04	-2.57E-04	77
3.15	-6.83E-05	-1.27E-04	-1.93E-04	-2.57E-04	78
3.16	-6.77E-05	-1.28E-04	-1.93E-04	-2.57E-04	79
3.17	-6.87E-05	-1.28E-04	-1.92E-04	-2.57E-04	80
3.15	-6.90E-05	-1.28E-04	-1.94E-04	-2.58E-04	81
3.15	-6.89E-05	-1.28E-04	-1.93E-04	-2.57E-04	82
3.17	-6.84E-05	-1.28E-04	-1.94E-04	-2.57E-04	83
3.15	-6.88E-05	-1.29E-04	-1.93E-04	-2.56E-04	84
3.16	-6.78E-05	-1.29E-04	-1.93E-04	-2.58E-04	85
3.17	-6.80E-05	-1.29E-04	-1.94E-04	-2.58E-04	86
3.16	-6.85E-05	-1.28E-04	-1.94E-04	-2.57E-04	87
3.17	-6.77E-05	-1.29E-04	-1.95E-04	-2.58E-04	88
3.17	-6.79E-05	-1.29E-04	-1.94E-04	-2.58E-04	89
3.17	-6.92E-05	-1.28E-04	-1.94E-04	-2.58E-04	90
3.16	-6.76E-05	-1.29E-04	-1.94E-04	-2.59E-04	91
3.16	-6.81E-05	-1.28E-04	-1.94E-04	-2.59E-04	92
3.15	-6.81E-05	-1.28E-04	-1.94E-04	-2.58E-04	93
3.17	-6.75E-05	-1.28E-04	-1.94E-04	-2.58E-04	94
3.16	-6.87E-05	-1.28E-04	-1.95E-04	-2.59E-04	95
3.15	-6.81E-05	-1.29E-04	-1.95E-04	-2.59E-04	96
3.15	-6.83E-05	-1.29E-04	-1.95E-04	-2.58E-04	97
3.17	-6.86E-05	-1.29E-04	-1.95E-04	-2.58E-04	98
3.18	-6.88E-05	-1.29E-04	-1.94E-04	-2.58E-04	99
3.18	-6.83E-05	-1.29E-04	-1.94E-04	-2.58E-04	100
3.18	-6.83E-05	-1.29E-04	-1.94E-04	-2.58E-04	101
3.19	-6.90E-05	-1.29E-04	-1.95E-04	-2.59E-04	102
3.17	-6.89E-05	-1.29E-04	-1.95E-04	-2.59E-04	103
3.18	-6.85E-05	-1.28E-04	-1.95E-04	-2.59E-04	104
3.14	-6.89E-05	-1.28E-04	-1.95E-04	-2.59E-04	105
3.17	-6.79E-05	-1.29E-04	-1.96E-04	-2.60E-04	106
3.17	-6.91E-05	-1.29E-04	-1.95E-04	-2.59E-04	107
3.18	-6.90E-05	-1.28E-04	-1.95E-04	-2.59E-04	108
3.17	-6.88E-05	-1.29E-04	-1.95E-04	-2.59E-04	109
3.18	-6.82E-05	-1.29E-04	-1.95E-04	-2.59E-04	110
3.15	-6.86E-05	-1.29E-04	-1.95E-04	-2.60E-04	111

Table G.1. Continued.

Load (kN)	Strain 1	Strain 2	Strain 3	Strain 4	Time (s)
3.18	-6.79E-05	-1.29E-04	-1.95E-04	-2.60E-04	112
3.17	-6.77E-05	-1.29E-04	-1.95E-04	-2.60E-04	113
3.17	-6.88E-05	-1.29E-04	-1.95E-04	-2.60E-04	114
3.14	-6.84E-05	-1.29E-04	-1.95E-04	-2.61E-04	115
3.17	-6.86E-05	-1.29E-04	-1.95E-04	-2.60E-04	116
3.15	-6.84E-05	-1.29E-04	-1.95E-04	-2.60E-04	117
3.18	-6.89E-05	-1.29E-04	-1.96E-04	-2.60E-04	118
3.16	-6.84E-05	-1.29E-04	-1.95E-04	-2.61E-04	119
3.15	-6.88E-05	-1.30E-04	-1.96E-04	-2.60E-04	120
3.14	-6.79E-05	-1.30E-04	-1.95E-04	-2.61E-04	121
3.15	-6.83E-05	-1.29E-04	-1.96E-04	-2.62E-04	122
3.17	-6.92E-05	-1.29E-04	-1.96E-04	-2.61E-04	123
3.16	-6.84E-05	-1.29E-04	-1.95E-04	-2.61E-04	124
3.16	-6.86E-05	-1.29E-04	-1.96E-04	-2.61E-04	125
3.15	-6.85E-05	-1.30E-04	-1.96E-04	-2.61E-04	126
3.16	-6.82E-05	-1.29E-04	-1.97E-04	-2.61E-04	127
3.15	-6.82E-05	-1.29E-04	-1.96E-04	-2.61E-04	128
3.17	-6.86E-05	-1.30E-04	-1.96E-04	-2.61E-04	129
3.18	-6.86E-05	-1.30E-04	-1.95E-04	-2.61E-04	130
3.16	-6.92E-05	-1.30E-04	-1.96E-04	-2.62E-04	131
3.15	-6.91E-05	-1.29E-04	-1.97E-04	-2.61E-04	132
3.16	-6.94E-05	-1.30E-04	-1.97E-04	-2.63E-04	133
3.15	-6.93E-05	-1.30E-04	-1.97E-04	-2.64E-04	134
3.24	-7.02E-05	-1.33E-04	-2.00E-04	-2.67E-04	135
3.33	-7.10E-05	-1.35E-04	-2.04E-04	-2.73E-04	136
3.35	-7.23E-05	-1.37E-04	-2.08E-04	-2.79E-04	137
3.42	-7.30E-05	-1.39E-04	-2.12E-04	-2.85E-04	138
3.49	-7.44E-05	-1.42E-04	-2.16E-04	-2.90E-04	139
3.48	-7.52E-05	-1.44E-04	-2.19E-04	-2.94E-04	140
3.58	-7.63E-05	-1.46E-04	-2.23E-04	-2.98E-04	141
3.62	-7.74E-05	-1.49E-04	-2.26E-04	-3.03E-04	142
3.64	-7.74E-05	-1.49E-04	-2.29E-04	-3.08E-04	143
3.65	-7.84E-05	-1.51E-04	-2.31E-04	-3.11E-04	144
3.75	-7.86E-05	-1.53E-04	-2.36E-04	-3.19E-04	145
3.82	-8.07E-05	-1.57E-04	-2.40E-04	-3.26E-04	146
3.90	-8.23E-05	-1.59E-04	-2.45E-04	-3.32E-04	147
3.96	-8.34E-05	-1.62E-04	-2.49E-04	-3.38E-04	148
3.97	-8.35E-05	-1.64E-04	-2.52E-04	-3.42E-04	149
4.08	-8.56E-05	-1.67E-04	-2.56E-04	-3.48E-04	150
4.06	-8.70E-05	-1.68E-04	-2.60E-04	-3.52E-04	151
4.13	-8.85E-05	-1.70E-04	-2.63E-04	-3.57E-04	152

Table G.1. Continued.

Load (kN)	Strain 1	Strain 2	Strain 3	Strain 4	Time (s)
4.15	-8.88E-05	-1.74E-04	-2.68E-04	-3.64E-04	153
4.22	-8.94E-05	-1.76E-04	-2.72E-04	-3.70E-04	154
4.28	-9.08E-05	-1.78E-04	-2.76E-04	-3.74E-04	155
4.21	-9.12E-05	-1.77E-04	-2.76E-04	-3.73E-04	156
4.21	-9.02E-05	-1.77E-04	-2.75E-04	-3.74E-04	157
4.25	-9.04E-05	-1.77E-04	-2.75E-04	-3.74E-04	158
4.23	-9.05E-05	-1.77E-04	-2.74E-04	-3.74E-04	159
4.22	-9.11E-05	-1.77E-04	-2.76E-04	-3.73E-04	160
4.22	-9.10E-05	-1.76E-04	-2.75E-04	-3.73E-04	161
4.21	-9.10E-05	-1.77E-04	-2.75E-04	-3.74E-04	162
4.20	-9.02E-05	-1.77E-04	-2.75E-04	-3.74E-04	163
4.24	-9.15E-05	-1.77E-04	-2.75E-04	-3.74E-04	164
4.22	-9.04E-05	-1.77E-04	-2.75E-04	-3.74E-04	165
4.22	-9.09E-05	-1.77E-04	-2.75E-04	-3.74E-04	166
4.23	-9.08E-05	-1.78E-04	-2.74E-04	-3.74E-04	167
4.23	-9.04E-05	-1.77E-04	-2.75E-04	-3.74E-04	168
4.20	-9.10E-05	-1.77E-04	-2.76E-04	-3.75E-04	169
4.15	-9.08E-05	-1.77E-04	-2.75E-04	-3.74E-04	170
4.12	-9.13E-05	-1.78E-04	-2.76E-04	-3.74E-04	171
4.14	-9.12E-05	-1.78E-04	-2.75E-04	-3.75E-04	172
4.14	-9.06E-05	-1.78E-04	-2.76E-04	-3.75E-04	173
4.13	-9.09E-05	-1.78E-04	-2.76E-04	-3.76E-04	174
4.13	-9.16E-05	-1.79E-04	-2.76E-04	-3.75E-04	175
4.14	-9.16E-05	-1.78E-04	-2.76E-04	-3.75E-04	176
4.13	-9.03E-05	-1.78E-04	-2.76E-04	-3.75E-04	177
4.15	-9.04E-05	-1.78E-04	-2.76E-04	-3.76E-04	178
4.14	-9.11E-05	-1.78E-04	-2.77E-04	-3.76E-04	179
4.15	-9.14E-05	-1.79E-04	-2.77E-04	-3.76E-04	180
4.13	-9.11E-05	-1.78E-04	-2.78E-04	-3.76E-04	181
4.15	-9.11E-05	-1.78E-04	-2.76E-04	-3.76E-04	182
4.14	-9.02E-05	-1.78E-04	-2.77E-04	-3.76E-04	183
4.15	-9.10E-05	-1.78E-04	-2.78E-04	-3.76E-04	184
4.15	-9.16E-05	-1.79E-04	-2.78E-04	-3.75E-04	185
4.16	-9.11E-05	-1.78E-04	-2.77E-04	-3.76E-04	186
4.16	-9.14E-05	-1.78E-04	-2.77E-04	-3.76E-04	187

Table G.2. DIC Raw Data from the Pre-corrosion Load Test for Batch 3 Beam 3 Cycle 1.

Load (kN)	Time (s)	E0	E1	E2	E3	E4	E5	E6	E7	E8	E9	E10	E11	E12	E13	E14	E15	E16	E17	E18	E19
0.29	1	6.5E-05	2.7E-05	3.6E-07	6.9E-05	5.3E-05	5.4E-05	3.2E-05	5.7E-05	4.8E-05	3.0E-05	3.1E-05	5.4E-05	1.2E-04	1.0E-04	1.5E-04	1.1E-04	1.5E-04	9.7E-05	3.5E-05	8.6E-05
0.28	2	2.8E-05	4.3E-05	1.5E-05	9.4E-05	3.9E-05	4.1E-05	5.7E-05	7.2E-05	4.6E-05	1.9E-05	8.0E-05	9.5E-05	1.2E-04	8.6E-05	1.4E-04	9.3E-05	1.3E-04	6.9E-05	2.0E-05	7.3E-05
0.30	3	4.5E-05	6.5E-05	6.9E-06	1.0E-04	5.9E-05	7.6E-05	5.4E-05	5.7E-05	7.5E-05	8.2E-05	6.5E-05	1.2E-04	1.3E-04	1.4E-04	1.1E-04	1.3E-04	1.8E-04	1.1E-04	8.7E-05	9.1E-05
0.27	4	1.7E-05	1.7E-05	4.2E-05	7.3E-05	2.8E-05	5.6E-05	4.6E-05	7.7E-05	5.5E-05	6.4E-05	1.5E-05	5.9E-05	1.2E-04	9.9E-05	1.0E-04	1.2E-04	1.3E-04	1.2E-04	4.9E-05	6.4E-05
0.28	5	9.5E-06	8.2E-05	3.5E-05	5.7E-05	6.9E-05	5.2E-05	8.6E-05	4.0E-05	3.4E-05	4.6E-05	8.0E-05	8.2E-05	1.3E-04	1.2E-04	1.2E-04	1.2E-04	1.3E-04	9.5E-05	4.1E-05	6.6E-05
0.29	6	3.7E-05	2.3E-05	3.2E-05	4.4E-05	3.2E-05	3.8E-05	4.9E-05	4.0E-05	5.7E-05	4.0E-05	4.8E-05	8.5E-05	1.1E-04	1.1E-04	1.3E-04	1.1E-04	1.1E-04	9.6E-05	4.7E-05	4.5E-05
0.29	7	3.4E-05	3.5E-05	1.8E-05	9.4E-05	5.8E-05	7.7E-05	3.6E-05	6.0E-05	3.5E-05	7.2E-05	5.4E-05	8.0E-05	1.2E-04	1.1E-04	1.1E-04	9.4E-05	8.9E-05	1.1E-04	8.1E-05	6.6E-05
0.28	8	-1.0E-05	2.4E-05	-8.3E-06	6.0E-05	4.3E-05	2.5E-05	-3.3E-07	4.3E-05	2.6E-05	-1.1E-05	1.8E-05	1.0E-04	1.1E-04	7.8E-05	1.2E-04	8.8E-05	7.6E-05	8.5E-05	2.0E-05	6.7E-05
0.28	9	4.8E-05	4.0E-05	1.6E-05	6.9E-05	4.1E-05	5.6E-05	4.4E-05	6.3E-05	1.9E-05	4.4E-05	3.6E-05	6.9E-05	1.0E-04	9.1E-05	1.2E-04	8.7E-05	1.0E-04	9.3E-05	3.6E-05	4.9E-05
0.28	10	9.5E-07	5.4E-05	1.4E-06	3.8E-05	3.3E-05	4.2E-05	1.4E-05	1.3E-05	6.3E-06	5.1E-05	3.2E-05	7.9E-05	8.7E-05	6.9E-05	1.0E-04	8.0E-05	7.9E-05	8.5E-05	5.0E-05	9.7E-06
0.37	11	-7.9E-06	1.8E-05	-3.3E-05	2.5E-05	2.6E-05	4.2E-05	-5.1E-07	1.9E-05	3.0E-05	5.2E-05	2.7E-05	7.5E-05	7.7E-05	1.1E-04	7.6E-05	6.9E-05	8.7E-05	6.5E-05	3.3E-05	4.5E-05
0.51	12	3.2E-05	2.6E-05	2.6E-05	6.3E-05	6.3E-05	4.2E-05	2.3E-05	4.2E-05	3.6E-05	7.9E-05	6.8E-05	7.9E-05	1.2E-04	8.6E-05	1.2E-04	1.0E-04	1.4E-04	9.4E-05	8.1E-05	7.6E-05
0.60	13	-1.6E-05	1.2E-05	-1.7E-05	6.1E-05	-1.4E-05	3.6E-06	1.7E-05	6.3E-05	2.8E-05	4.6E-05	4.2E-05	7.6E-05	1.1E-04	1.1E-04	9.3E-05	7.4E-05	1.1E-04	1.1E-04	1.3E-05	5.5E-05
0.68	14	-5.3E-05	-2.3E-05	-1.7E-05	2.1E-06	1.8E-05	-1.4E-05	-1.7E-05	1.4E-05	5.8E-06	-9.9E-07	-1.7E-05	5.0E-05	7.2E-05	5.6E-05	8.1E-05	9.0E-05	9.5E-05	4.6E-05	8.4E-06	4.0E-05
0.69	15	-2.0E-05	-4.8E-06	2.2E-05	4.3E-05	3.4E-05	1.1E-05	3.0E-05	5.2E-05	9.8E-06	3.9E-05	2.5E-05	8.4E-05	1.2E-04	9.3E-05	9.1E-05	8.9E-05	1.1E-04	7.1E-05	3.2E-05	3.0E-05
0.69	16	-5.2E-05	-4.1E-05	-6.9E-05	-1.5E-05	-2.1E-05	-9.1E-06	-2.1E-05	2.7E-05	1.1E-05	1.2E-05	2.9E-05	5.9E-05	9.0E-05	9.2E-05	1.0E-04	1.0E-04	1.3E-04	9.9E-05	5.3E-05	6.6E-05
0.78	17	2.9E-05	5.5E-07	-2.9E-05	4.0E-05	1.4E-06	1.8E-05	7.7E-06	5.2E-05	4.5E-05	4.5E-05	3.5E-05	6.8E-05	6.5E-05	1.1E-04	1.1E-04	5.5E-05	1.1E-04	5.8E-05	1.7E-05	2.4E-05
0.77	18	-2.2E-05	-3.6E-05	-3.7E-05	4.5E-07	-1.2E-05	5.6E-06	-1.7E-05	7.0E-07	2.1E-06	3.2E-05	3.0E-05	6.4E-05	8.6E-05	7.6E-05	1.3E-04	7.5E-05	7.9E-05	4.4E-05	2.6E-06	1.2E-05
0.86	19	-3.7E-05	1.4E-05	-5.1E-05	3.6E-05	-1.3E-05	3.5E-06	-5.2E-06	7.1E-06	-2.2E-06	5.2E-05	1.1E-05	1.2E-04	1.0E-04	1.1E-04	8.0E-05	6.6E-05	1.0E-04	5.8E-05	8.0E-06	-1.4E-05
0.85	20	-7.3E-05	-2.8E-05	-2.6E-05	-2.4E-05	-4.1E-05	-2.6E-05	-2.3E-05	4.0E-06	-1.9E-05	4.4E-05	-1.1E-05	3.7E-05	7.8E-05	6.2E-05	6.3E-05	7.1E-05	7.5E-05	6.0E-05	1.7E-06	-8.6E-06
0.95	21	-4.7E-05	-5.4E-05	-7.2E-05	-1.4E-07	-2.6E-05	-1.3E-08	3.9E-07	3.5E-05	-1.4E-05	2.5E-06	2.0E-06	6.6E-05	8.9E-05	8.4E-05	6.1E-05	7.6E-05	5.6E-05	6.1E-05	4.2E-05	3.7E-05
1.01	22	-4.7E-05	-6.0E-05	-6.1E-05	-4.4E-06	3.1E-06	-2.8E-06	-4.6E-05	-1.8E-05	-2.3E-06	3.3E-05	2.1E-05	5.5E-05	9.6E-05	6.6E-05	1.1E-04	6.2E-05	8.7E-05	7.2E-05	-1.5E-05	-5.1E-07
1.02	23	-7.3E-05	-6.2E-05	-4.9E-05	-7.7E-06	-2.2E-05	-1.3E-05	-5.4E-05	1.2E-05	1.8E-05	7.8E-06	3.7E-06	4.2E-05	9.3E-05	7.5E-05	9.8E-05	7.0E-05	9.7E-05	5.4E-05	4.6E-06	8.4E-05
1.11	24	-1.4E-04	-7.4E-05	-1.1E-04	-8.3E-06	-3.0E-05	-3.0E-05	-1.1E-05	-2.3E-05	-3.5E-05	-1.8E-05	-8.7E-06	4.3E-05	2.9E-05	5.1E-05	8.0E-05	6.0E-05	6.0E-05	4.2E-05	1.7E-05	-1.2E-05
1.18	25	-1.2E-04	-6.0E-05	-8.7E-05	-9.6E-05	-8.2E-05	-4.8E-05	-4.0E-05	-2.1E-05	-2.9E-05	-3.2E-05	-3.2E-05	-2.4E-05	2.5E-05	2.0E-05	1.2E-05	3.3E-05	1.1E-05	-3.2E-06	-7.1E-05	-8.5E-05
1.20	26	-2.8E-05	-6.2E-05	-4.8E-05	2.2E-05	-3.9E-05	2.6E-05	-8.0E-06	3.1E-05	-8.9E-06	4.1E-05	2.9E-05	9.4E-05	8.3E-05	9.2E-05	9.1E-05	5.7E-05	8.7E-05	5.4E-05	7.0E-05	-1.2E-05
1.27	27	-6.3E-05	-6.3E-05	-4.1E-05	2.8E-05	3.1E-05	3.1E-05	2.1E-05	5.5E-05	2.7E-05	4.2E-05	3.4E-05	8.9E-05	7.1E-05	4.3E-05	7.9E-05	3.8E-05	3.5E-05	2.8E-05	-2.6E-05	-7.6E-06
1.31	28	-6.9E-05	-6.6E-05	-5.2E-05	-2.1E-05	-2.0E-05	5.2E-07	-2.3E-05	1.2E-05	-4.0E-05	5.3E-06	1.1E-05	6.0E-05	8.8E-05	6.5E-05	9.2E-05	6.7E-05	8.4E-05	2.6E-05	-4.6E-05	2.4E-05
1.35	29	-1.1E-04	-8.3E-05	-8.4E-05	-1.8E-05	-6.0E-05	-4.6E-05	-1.3E-05	2.0E-05	-2.3E-05	3.0E-05	1.3E-05	8.8E-05	9.0E-05	6.8E-05	8.5E-05	4.9E-05	9.0E-05	5.5E-05	-4.2E-05	-1.4E-05
1.42	30	-1.1E-04	-1.1E-04	-9.9E-05	-2.5E-05	-4.0E-05	-2.7E-05	-5.4E-05	-7.4E-06	-3.0E-05	7.5E-06	3.1E-05	7.1E-05	1.0E-04	9.1E-05	8.3E-05	7.6E-05	8.0E-05	7.7E-05	-2.5E-05	2.1E-05
1.42	31	-1.2E-04	-7.1E-05	-5.9E-05	-2.6E-05	-3.0E-05	-9.8E-06	-7.3E-06	1.7E-05	2.4E-05	2.0E-05	1.7E-05	8.1E-05	8.0E-05	8.0E-05	1.0E-04	6.4E-05	4.4E-05	6.4E-05	1.4E-05	5.8E-05

Table G.2. Continued.

Load (kN)	Time (s)	E0	E1	E2	E3	E4	E5	E6	E7	E8	E9	E10	E11	E12	E13	E14	E15	E16	E17	E18	E19
1.51	32	-1.6E-04	-1.2E-04	-1.1E-04	-6.9E-05	-1.1E-04	-4.0E-05	-7.5E-05	-5.0E-05	-8.4E-06	1.3E-06	1.3E-05	4.1E-05	5.2E-05	2.6E-05	6.5E-05	7.0E-05	6.8E-05	3.9E-05	-2.2E-05	-2.9E-05
1.60	33	-1.0E-04	-8.3E-05	-8.1E-05	-4.7E-05	-7.5E-05	-1.9E-05	-6.2E-06	-1.1E-05	-2.4E-05	2.2E-05	-4.4E-06	3.9E-05	9.1E-05	6.2E-05	9.6E-05	6.2E-05	8.3E-05	5.9E-06	-6.5E-06	-3.8E-05
1.59	34	-1.0E-04	-8.2E-05	-1.1E-04	-4.2E-05	-5.9E-05	-5.3E-05	-4.7E-05	2.1E-05	-9.9E-06	-1.7E-05	5.1E-06	3.5E-05	9.7E-05	6.7E-05	8.9E-05	6.5E-05	7.2E-05	3.0E-05	-3.6E-05	2.0E-05
1.68	35	-1.6E-04	-1.1E-04	-1.3E-04	-2.7E-05	-6.4E-05	-3.4E-05	-3.7E-05	1.9E-05	-3.9E-05	9.7E-06	1.9E-05	4.9E-05	7.7E-05	3.0E-05	7.7E-05	4.8E-05	7.7E-05	1.7E-06	-1.2E-05	-2.6E-05
1.70	36	-1.6E-04	-1.3E-04	-1.1E-04	-3.4E-05	-5.5E-05	-4.2E-05	-5.7E-05	-3.2E-05	-8.4E-06	-6.9E-07	1.3E-06	6.9E-05	6.1E-05	5.3E-05	4.9E-05	5.0E-05	5.2E-05	4.9E-05	-3.8E-05	2.9E-06
1.76	37	-1.4E-04	-1.1E-04	-1.2E-04	-5.1E-05	-7.4E-05	-5.5E-05	-3.9E-05	-2.3E-06	-5.3E-05	7.4E-06	2.5E-05	4.2E-05	9.5E-05	4.6E-05	4.7E-05	6.7E-05	5.0E-05	2.4E-05	-2.5E-06	-3.9E-05
1.77	38	-1.4E-04	-1.3E-04	-7.8E-05	-5.0E-05	-5.1E-05	-3.6E-05	-3.2E-05	-3.2E-05	-1.7E-05	4.0E-05	-6.4E-06	7.5E-05	7.6E-05	5.1E-05	7.7E-05	3.8E-05	8.6E-05	3.5E-05	-3.1E-05	6.6E-06
1.84	39	-1.5E-04	-8.9E-05	-1.4E-04	-8.5E-05	-9.0E-05	-6.9E-05	-3.8E-05	-3.0E-05	-2.1E-05	7.4E-06	1.8E-06	3.9E-05	5.4E-05	2.5E-05	5.9E-05	4.4E-05	6.3E-05	2.7E-05	-3.7E-05	-7.3E-06
1.92	40	-1.3E-04	-1.2E-04	-1.6E-04	-7.3E-05	-1.0E-04	-5.7E-05	-5.5E-05	-6.5E-06	-2.7E-05	8.0E-07	3.5E-05	4.0E-05	8.2E-05	4.6E-05	6.0E-05	6.5E-05	5.4E-05	2.7E-05	-1.5E-05	-7.4E-05
1.99	41	-2.1E-04	-1.2E-04	-1.7E-04	-8.5E-05	-1.1E-04	-9.5E-05	-8.1E-05	-1.9E-05	-4.7E-05	-3.3E-05	-2.6E-05	2.7E-05	2.7E-05	2.3E-05	3.9E-05	5.0E-05	4.3E-05	-5.1E-06	-4.8E-05	-7.5E-05
2.09	42	-1.3E-04	-1.3E-04	-1.6E-04	-5.3E-05	-1.0E-04	-6.4E-05	-3.3E-05	-3.2E-05	-1.8E-05	-2.2E-05	-1.3E-06	4.7E-05	1.0E-04	5.8E-05	8.0E-05	3.8E-05	5.3E-05	-2.1E-06	-2.3E-05	-4.4E-05
2.11	43	-1.8E-04	-2.0E-04	-1.6E-04	-1.5E-04	-1.5E-04	-9.5E-05	-7.5E-05	-3.7E-05	-5.2E-05	-1.5E-05	-7.2E-06	6.6E-05	5.0E-05	3.7E-05	3.9E-05	3.3E-05	2.0E-05	1.6E-06	-4.3E-05	-2.2E-05
2.17	44	-1.9E-04	-1.5E-04	-1.5E-04	-5.5E-05	-9.6E-05	-8.5E-05	-7.0E-05	-8.2E-07	-2.3E-05	-5.2E-06	1.9E-06	2.1E-05	3.2E-05	2.8E-05	1.2E-05	2.1E-05	3.6E-05	-9.8E-06	-1.1E-04	-2.0E-05
2.17	45	-2.1E-04	-1.9E-04	-1.4E-04	-8.9E-05	-1.2E-04	-1.1E-04	-8.1E-05	-3.0E-05	-7.1E-05	-7.1E-06	-6.4E-06	4.7E-05	5.7E-05	1.8E-05	2.7E-05	8.8E-07	5.5E-05	2.6E-05	-4.5E-05	-6.8E-05
2.25	46	-8.7E-05	-9.3E-05	-8.2E-05	-2.5E-05	-4.7E-05	1.8E-05	-3.4E-06	5.5E-05	4.5E-05	8.1E-05	2.9E-05	9.3E-05	9.6E-05	1.8E-05	3.9E-05	5.7E-05	4.0E-05	2.1E-05	-5.2E-05	-1.6E-06
2.27	47	-1.7E-04	-1.8E-04	-1.8E-04	-1.1E-04	-1.2E-04	-1.6E-04	-9.9E-05	-1.1E-04	-1.0E-04	-9.0E-05	-6.0E-05	-5.2E-05	-6.9E-05	-9.2E-05	-7.3E-05	-1.2E-04	-8.0E-05	-1.4E-04	-2.1E-04	-1.6E-04
2.35	48	-2.6E-04	-2.3E-04	-2.4E-04	-1.7E-04	-1.6E-04	-1.6E-04	-1.5E-04	-1.1E-04	-1.5E-04	-8.8E-05	-1.2E-04	-4.3E-05	-5.1E-05	-5.4E-05	-4.9E-05	-9.8E-05	-9.8E-05	-1.5E-04	-1.8E-04	-1.7E-04
2.43	49	-3.1E-04	-2.4E-04	-2.5E-04	-1.8E-04	-2.0E-04	-1.6E-04	-1.6E-04	-8.6E-05	-1.2E-04	-4.8E-05	-9.3E-05	-3.9E-05	3.2E-06	-2.1E-05	1.4E-05	1.1E-05	4.3E-05	1.1E-05	-5.7E-05	-7.2E-05
2.49	50	-2.2E-04	-1.5E-04	-1.7E-04	-1.4E-04	-1.6E-04	-1.4E-04	-1.4E-04	-9.2E-05	-8.6E-05	-7.8E-05	-4.7E-05	-2.7E-05	-1.6E-05	-2.1E-05	4.3E-06	-1.4E-06	2.7E-05	-2.4E-05	-5.2E-05	-7.4E-05
2.52	51	-2.4E-04	-2.5E-04	-1.9E-04	-9.9E-05	-1.5E-04	-1.1E-04	-9.6E-05	-1.1E-05	-4.8E-05	-3.3E-05	-6.0E-06	3.9E-05	4.3E-05	1.6E-05	3.7E-05	2.0E-05	4.7E-05	-3.0E-05	-7.6E-05	-6.5E-05
2.57	52	-2.2E-04	-1.9E-04	-1.8E-04	-1.2E-04	-1.3E-04	-1.0E-04	-9.1E-05	-5.0E-05	-8.1E-05	-2.3E-05	-4.3E-05	7.5E-06	5.1E-05	-1.4E-05	4.3E-05	1.7E-05	1.4E-05	-1.7E-05	-1.0E-04	-5.3E-05
2.60	53	-2.1E-04	-1.9E-04	-2.1E-04	-9.5E-05	-1.3E-04	-1.1E-04	-6.4E-05	-3.8E-05	-7.2E-05	-5.5E-06	-1.4E-05	2.6E-05	6.0E-05	3.0E-05	3.9E-05	4.6E-06	1.1E-05	-4.3E-06	-7.1E-05	-8.7E-05
2.57	54	-2.0E-04	-2.2E-04	-1.6E-04	-1.1E-04	-1.3E-04	-1.1E-04	-1.1E-04	-4.2E-05	-7.9E-05	-5.3E-05	6.3E-06	3.8E-05	5.0E-05	-9.4E-07	3.2E-05	1.1E-05	2.6E-05	-8.9E-06	-8.4E-05	-4.7E-05
2.65	55	-2.3E-04	-1.8E-04	-1.9E-04	-9.6E-05	-1.2E-04	-1.0E-04	-1.2E-04	-3.0E-05	-4.6E-05	-3.9E-05	-4.0E-05	-1.6E-05	1.8E-05	1.2E-05	2.8E-05	-2.4E-05	1.3E-05	-1.7E-05	-1.1E-04	-7.9E-05
2.75	56	-2.6E-04	-1.9E-04	-2.2E-04	-1.0E-04	-1.4E-04	-9.4E-05	-1.3E-04	-2.4E-05	-8.9E-05	-5.1E-05	-3.1E-06	1.1E-05	4.0E-05	2.5E-05	2.4E-05	8.7E-06	2.1E-05	-5.3E-05	-9.2E-05	-9.2E-05
2.82	57	-2.4E-04	-2.2E-04	-2.0E-04	-1.2E-04	-1.5E-04	-8.8E-05	-8.8E-05	-5.9E-05	-6.8E-05	-1.8E-05	-3.3E-05	4.2E-05	4.1E-05	9.1E-06	2.6E-05	1.7E-05	2.3E-05	-1.8E-05	-8.9E-05	-1.1E-04
2.91	58	-2.3E-04	-2.0E-04	-2.1E-04	-1.2E-04	-1.5E-04	-1.4E-04	-9.2E-05	-7.9E-05	-8.6E-05	-5.0E-05	-7.4E-05	-1.3E-05	2.7E-05	-2.4E-05	3.2E-05	-5.1E-05	-3.1E-05	-4.8E-05	-1.5E-04	-1.1E-04
2.90	59	-2.3E-04	-2.0E-04	-2.0E-04	-1.1E-04	-1.3E-04	-1.3E-04	-1.3E-04	-1.5E-05	-4.5E-05	1.6E-05	-8.2E-06	-1.0E-06	2.0E-05	-5.2E-05	9.1E-06	-1.9E-05	-2.3E-05	-7.6E-05	-8.5E-05	-5.2E-05
3.00	**60**	**-2.6E-04**	**-1.8E-04**	**-2.0E-04**	**-1.3E-04**	**-1.2E-04**	**-1.0E-04**	**-1.0E-04**	**-4.1E-05**	**-5.9E-05**	**-4.4E-05**	**-2.7E-05**	**5.9E-06**	**6.5E-06**	**1.5E-06**	**3.3E-05**	**4.2E-06**	**2.1E-06**	**-5.1E-05**	**-8.7E-05**	**-9.4E-05**
3.00	61	-3.0E-04	-2.9E-04	-3.1E-04	-2.4E-04	-2.3E-04	-2.2E-04	-1.9E-04	-1.3E-04	-1.1E-04	-1.3E-04	-1.2E-04	-4.2E-05	-5.4E-05	-1.0E-04	-4.0E-05	-7.2E-05	-9.8E-05	-1.4E-04	-1.8E-04	-2.2E-04
3.08	62	-1.6E-04	-1.8E-04	-2.5E-04	-1.3E-04	-1.3E-04	-1.1E-04	-1.0E-04	-4.6E-05	-3.8E-05	-2.1E-05	-3.2E-05	-4.4E-05	1.6E-05	-1.2E-05	7.3E-06	-1.7E-05	-3.3E-06	-5.7E-05	-1.6E-04	-1.3E-04

Table G.2. Continued.

Load (kN)	Time (s)	E0	E1	E2	E3	E4	E5	E6	E7	E8	E9	E10	E11	E12	E13	E14	E15	E16	E17	E18	E19
3.17	63	-2.4E-04	-2.0E-04	-2.6E-04	-1.2E-04	-1.2E-04	-1.5E-04	-1.4E-04	-3.4E-05	-5.8E-05	2.9E-05	-4.7E-05	-5.6E-07	1.7E-05	1.2E-05	2.0E-05	2.1E-05	1.1E-05	-3.6E-05	-7.4E-05	-3.1E-05
3.19	64	-2.1E-04	-2.0E-04	-2.6E-04	-1.5E-04	-1.7E-04	-1.0E-04	-1.2E-04	-1.0E-04	-4.8E-05	-4.3E-05	-7.6E-05	-1.3E-05	9.4E-06	-3.1E-05	-6.3E-06	-5.4E-06	-7.1E-06	-5.7E-05	-1.2E-04	-7.7E-05
3.25	65	-2.2E-04	-2.1E-04	-2.0E-04	-1.4E-04	-1.6E-04	-1.3E-04	-1.2E-04	-9.4E-05	-8.2E-05	-1.1E-05	-3.4E-05	-3.0E-05	1.8E-05	-3.6E-05	1.6E-05	6.6E-06	-3.0E-05	-7.7E-05	-1.2E-04	-8.7E-05
3.23	66	-2.7E-04	-2.1E-04	-2.5E-04	-1.6E-04	-1.7E-04	-1.2E-04	-1.2E-04	-8.4E-05	-5.9E-05	-2.8E-05	-4.5E-05	-1.2E-05	4.0E-05	-1.7E-05	6.9E-06	-1.1E-07	-1.9E-06	-6.2E-05	-1.5E-04	-1.2E-04
3.25	67	-2.4E-04	-2.1E-04	-2.4E-04	-1.3E-04	-1.5E-04	-1.1E-04	-1.2E-04	-2.5E-05	-5.1E-05	-4.0E-05	-5.6E-05	-2.7E-05	2.3E-05	4.0E-06	1.4E-05	3.0E-05	-2.3E-05	-5.6E-05	-1.2E-04	-1.2E-04
3.25	68	-2.3E-04	-2.3E-04	-2.5E-04	-1.5E-04	-1.6E-04	-1.0E-04	-8.4E-05	-4.9E-05	-8.8E-05	-6.7E-05	-3.0E-05	-8.4E-06	3.8E-05	-1.3E-05	6.3E-06	-2.9E-05	-1.1E-05	-4.6E-05	-8.0E-05	-4.6E-05
3.24	69	-3.1E-04	-2.0E-04	-2.3E-04	-1.6E-04	-1.5E-04	-1.5E-04	-1.6E-04	-6.8E-05	-9.9E-05	-5.5E-05	-4.2E-05	-3.1E-06	2.5E-05	-8.3E-06	-2.4E-05	-1.4E-05	-2.6E-05	-3.3E-05	-1.3E-04	-7.4E-05
3.24	70	-2.4E-04	-2.1E-04	-2.6E-04	-1.3E-04	-2.0E-04	-1.3E-04	-1.1E-04	-7.1E-05	-6.3E-05	-3.7E-05	-4.0E-05	3.2E-06	-5.0E-06	-4.6E-06	2.7E-05	-8.4E-06	1.4E-05	-4.1E-05	-9.8E-05	-1.5E-04
3.25	71	-3.1E-04	-2.6E-04	-2.3E-04	-1.9E-04	-1.9E-04	-1.6E-04	-1.7E-04	-1.3E-04	-1.0E-04	-9.5E-05	-7.0E-05	-3.0E-05	-2.2E-05	-6.4E-05	-4.1E-05	-6.8E-05	-7.0E-05	-8.9E-05	-1.9E-04	-1.5E-04
3.24	72	-2.5E-04	-2.5E-04	-2.0E-04	-1.7E-04	-1.8E-04	-1.2E-04	-1.1E-04	-7.1E-05	-6.4E-05	-3.2E-05	-3.5E-05	-6.3E-06	3.9E-05	-1.2E-05	4.1E-05	2.1E-05	1.9E-05	-2.0E-05	-9.1E-05	-1.6E-04
3.24	73	-2.7E-04	-2.3E-04	-2.2E-04	-9.2E-05	-1.7E-04	-1.3E-04	-1.1E-04	-5.4E-05	-3.7E-05	-6.0E-05	-4.9E-05	3.4E-05	1.7E-05	-9.5E-06	-2.4E-06	-3.0E-05	1.1E-05	-6.3E-05	-1.2E-04	-1.2E-04
3.25	74	-2.6E-04	-2.2E-04	-2.5E-04	-1.5E-04	-1.8E-04	-1.2E-04	-1.7E-04	-6.9E-05	-8.3E-05	-4.9E-05	-6.5E-05	1.3E-05	2.7E-05	3.2E-05	1.7E-05	-1.5E-05	1.7E-05	-5.0E-05	-1.1E-04	-9.7E-05
3.22	75	-2.7E-04	-2.1E-04	-2.1E-04	-1.1E-04	-1.5E-04	-1.2E-04	-1.0E-04	-6.2E-05	-3.5E-05	-1.6E-05	-1.1E-05	1.3E-05	-2.8E-05	7.9E-06	-3.7E-06	1.0E-05	-1.2E-05	-3.8E-05	-1.5E-04	-1.2E-04
3.16	76	-3.0E-04	-2.4E-04	-2.2E-04	-1.5E-04	-1.6E-04	-1.2E-04	-1.1E-04	-8.6E-05	-5.4E-05	-5.7E-05	-6.0E-05	-5.2E-06	4.2E-07	-2.7E-05	1.9E-05	-7.4E-06	-1.1E-05	-4.4E-05	-1.4E-04	-7.2E-05
3.21	77	-2.7E-04	-2.5E-04	-2.4E-04	-1.4E-04	-1.4E-04	-1.4E-04	-1.4E-04	-8.9E-05	-8.2E-05	-7.7E-05	-4.8E-05	3.0E-06	-1.1E-05	-1.2E-05	6.4E-07	-4.2E-05	-1.6E-05	-7.0E-05	-1.3E-04	-9.8E-05
3.15	78	-2.7E-04	-2.7E-04	-2.8E-04	-2.0E-04	-2.3E-04	-2.0E-04	-1.5E-04	-1.1E-04	-6.7E-05	-1.1E-04	-7.3E-05	-2.1E-05	-5.6E-06	-5.6E-05	-1.6E-05	-1.4E-05	-3.0E-05	-1.2E-04	-2.0E-04	-1.4E-04
3.16	79	-2.4E-04	-2.1E-04	-2.1E-04	-1.2E-04	-1.5E-04	-1.3E-04	-1.1E-04	-6.4E-05	-5.4E-05	-3.3E-05	-2.0E-05	2.2E-05	2.2E-05	2.5E-05	-2.0E-06	1.0E-06	1.3E-05	-5.6E-05	-1.4E-04	-6.7E-05
3.17	80	-3.3E-04	-2.9E-04	-2.5E-04	-1.2E-04	-1.8E-04	-1.5E-04	-1.2E-04	-8.5E-05	-1.1E-04	-5.7E-05	-5.2E-05	-1.6E-05	-1.8E-05	-4.4E-05	-5.0E-06	-4.3E-05	-3.5E-05	-8.5E-05	-1.6E-04	-1.4E-04
3.15	81	-3.5E-04	-3.1E-04	-2.6E-04	-2.6E-04	-2.1E-04	-1.9E-04	-1.8E-04	-1.1E-04	-1.4E-04	-8.4E-05	-6.6E-05	-3.3E-05	-3.3E-05	-5.2E-05	-2.9E-05	-4.1E-05	-4.8E-05	-6.1E-05	-1.4E-04	-1.3E-04
3.15	82	-2.7E-04	-2.3E-04	-2.1E-04	-1.5E-04	-1.5E-04	-1.1E-04	-1.2E-04	-7.5E-05	-5.2E-05	1.4E-05	-4.4E-05	1.4E-05	-2.1E-06	1.2E-05	2.7E-05	-3.9E-06	-7.6E-06	-4.2E-05	-1.4E-04	-5.8E-05
3.17	83	-2.6E-04	-2.3E-04	-2.3E-04	-1.5E-04	-1.5E-04	-1.2E-04	-1.0E-04	-4.1E-05	-8.4E-05	-5.4E-05	-5.5E-05	-1.8E-05	-2.6E-05	-3.1E-05	-8.4E-06	-4.2E-05	-1.8E-05	-1.1E-04	-1.3E-04	-1.5E-04
3.15	84	-3.0E-04	-2.8E-04	-2.6E-04	-1.6E-04	-2.1E-04	-1.7E-04	-1.8E-04	-9.2E-05	-9.9E-05	-6.1E-05	-3.5E-05	1.1E-06	1.8E-06	1.7E-06	-1.4E-05	-1.2E-05	7.4E-06	-2.0E-05	-7.1E-05	-7.9E-05
3.16	85	-1.8E-04	-1.7E-04	-1.3E-04	-9.0E-05	-1.1E-04	-6.8E-05	-6.8E-05	-1.1E-05	1.3E-05	1.1E-05	1.4E-05	4.8E-05	3.1E-05	1.5E-05	2.2E-05	-2.5E-06	-1.6E-05	-2.9E-05	-1.1E-04	-1.0E-04
3.17	86	-2.7E-04	-1.8E-04	-1.9E-04	-1.4E-04	-1.4E-04	-1.0E-04	-1.3E-04	-4.0E-05	-7.1E-05	-2.8E-05	-3.9E-05	2.7E-05	2.1E-05	-4.4E-05	-5.3E-06	-1.3E-07	-1.4E-06	-6.6E-05	-1.6E-04	-1.4E-04
3.16	87	-2.9E-04	-2.3E-04	-2.3E-04	-2.1E-04	-1.8E-04	-1.7E-04	-1.1E-04	-8.2E-05	-8.6E-05	-4.8E-05	-3.9E-05	-1.8E-05	3.8E-07	-2.7E-05	3.7E-06	1.6E-05	-4.5E-05	-3.8E-05	-8.5E-05	-1.4E-04
3.17	88	-2.6E-04	-2.6E-04	-2.4E-04	-1.9E-04	-1.9E-04	-1.5E-04	-1.6E-04	-7.6E-05	-7.6E-05	-3.1E-05	-5.6E-05	5.0E-06	3.0E-05	-7.8E-06	-2.7E-06	-1.6E-05	1.2E-05	-3.2E-05	-1.2E-04	-1.3E-04
3.17	89	-3.0E-04	-2.5E-04	-2.2E-04	-1.4E-04	-1.7E-04	-1.0E-04	-1.3E-04	-4.1E-05	-5.0E-05	1.4E-05	9.7E-08	5.9E-05	7.5E-05	2.2E-05	4.5E-05	4.8E-05	4.9E-05	-3.0E-06	-1.1E-04	-6.7E-05
3.17	90	-4.2E-04	-4.0E-04	-4.3E-04	-3.3E-04	-3.4E-04	-3.0E-04	-2.7E-04	-1.8E-04	-2.0E-04	-1.6E-04	-2.0E-04	-1.5E-04	-1.6E-04	-1.7E-04	-1.7E-04	-1.9E-04	-1.8E-04	-1.9E-04	-2.7E-04	-2.4E-04
3.16	91	-2.7E-04	-2.0E-04	-2.1E-04	-1.4E-04	-1.2E-04	-1.1E-04	-1.0E-04	-2.3E-05	-5.7E-05	-4.2E-05	-7.1E-05	-1.2E-05	-4.5E-07	-6.9E-06	5.2E-06	-1.7E-05	5.5E-06	-5.5E-05	-9.5E-05	-9.9E-05
3.16	92	-2.3E-04	-2.3E-04	-2.0E-04	-1.5E-04	-1.7E-04	-1.1E-04	-1.2E-04	-6.2E-05	-5.3E-05	-2.0E-05	-5.3E-05	-2.4E-05	7.8E-06	-8.4E-06	1.1E-05	-2.9E-05	-6.2E-06	-3.3E-05	-1.1E-04	-1.0E-04
3.15	93	-2.5E-04	-2.3E-04	-2.6E-04	-1.6E-04	-1.3E-04	-1.3E-04	-1.2E-04	-7.0E-05	-6.9E-05	-4.3E-05	-5.5E-05	-8.8E-06	1.0E-05	-2.2E-05	2.4E-05	1.2E-05	-2.7E-05	-6.1E-05	-1.0E-04	-1.2E-04

Table G.2. Continued.

Load (kN)	Time (s)	E0	E1	E2	E3	E4	E5	E6	E7	E8	E9	E10	E11	E12	E13	E14	E15	E16	E17	E18	E19
3.17	94	-2.7E-04	-1.8E-04	-1.9E-04	-1.4E-04	-1.3E-04	-1.2E-04	-1.3E-04	-4.5E-05	-5.8E-05	-3.6E-05	-4.9E-05	3.8E-05	6.4E-06	-4.0E-06	3.3E-05	-7.9E-06	-5.2E-06	-6.2E-05	-1.5E-04	-9.5E-05
3.16	95	-3.0E-04	-2.3E-04	-2.3E-04	-1.5E-04	-1.5E-04	-1.2E-04	-7.6E-05	-5.4E-05	-6.0E-05	-5.1E-05	-1.9E-05	1.8E-05	1.2E-05	-9.9E-07	2.8E-05	-1.8E-05	-2.1E-05	-5.2E-05	-1.3E-04	-1.2E-04
3.15	96	-2.2E-04	-2.0E-04	-2.2E-04	-1.4E-04	-1.6E-04	-1.3E-04	-1.4E-04	-6.0E-05	-6.6E-05	-2.7E-06	-1.9E-05	-7.9E-06	-1.8E-05	-3.5E-05	-1.4E-05	-4.1E-05	1.3E-05	-6.1E-05	-7.6E-05	-8.6E-05
3.15	97	-2.5E-04	-2.1E-04	-2.3E-04	-1.0E-04	-1.4E-04	-8.7E-05	-1.1E-04	-7.7E-05	-4.6E-05	-8.8E-05	-5.6E-05	-6.5E-06	9.6E-06	4.7E-06	1.0E-05	-3.3E-05	1.1E-05	-4.8E-05	-1.0E-04	-1.4E-04
3.17	98	-2.6E-04	-2.5E-04	-2.3E-04	-1.7E-04	-1.6E-04	-1.1E-04	-6.8E-05	-5.0E-05	-4.9E-05	-9.1E-06	-2.5E-05	-6.8E-06	5.5E-06	-6.6E-06	-2.3E-06	-3.8E-05	4.4E-06	-7.5E-05	-1.2E-04	-9.1E-05
3.18	99	-2.9E-04	-2.3E-04	-2.0E-04	-1.9E-04	-1.2E-04	-1.2E-04	-1.3E-04	-6.9E-05	-9.8E-05	-3.1E-05	-5.5E-05	-5.0E-05	1.3E-05	-3.8E-05	-1.2E-05	-4.0E-05	-5.3E-06	-8.3E-05	-1.1E-04	-1.2E-04
3.18	100	-2.2E-04	-2.1E-04	-2.7E-04	-1.5E-04	-1.6E-04	-9.8E-05	-1.2E-04	-7.6E-05	-3.1E-05	-3.7E-05	-2.6E-05	2.0E-05	4.0E-05	4.7E-06	1.6E-05	4.5E-06	-9.0E-06	-1.8E-05	-1.3E-04	-1.2E-04
3.18	101	-2.1E-04	-1.6E-04	-2.4E-04	-1.1E-04	-1.3E-04	-1.2E-04	-1.3E-04	-3.9E-05	-2.5E-05	-3.6E-05	-2.9E-05	3.2E-06	4.6E-05	8.7E-06	5.1E-06	5.1E-08	-5.2E-06	-6.6E-05	-1.1E-04	-9.0E-05
3.19	102	-2.2E-04	-2.0E-04	-2.0E-04	-1.3E-04	-1.6E-04	-1.2E-04	-1.1E-04	-5.3E-05	-5.5E-05	-6.8E-06	-2.5E-05	-1.4E-05	1.7E-05	-1.1E-05	-6.0E-06	-9.1E-06	3.1E-05	-4.0E-05	-9.9E-05	-1.3E-04
3.17	103	-2.4E-04	-2.5E-04	-2.4E-04	-1.3E-04	-1.8E-04	-1.4E-04	-8.6E-05	-6.5E-05	-2.2E-05	9.0E-06	-1.3E-06	-4.7E-06	1.9E-05	-2.3E-05	3.1E-05	-2.7E-05	1.2E-06	-4.6E-05	-1.1E-04	-1.2E-04
3.18	104	-3.0E-04	-2.3E-04	-2.6E-04	-1.3E-04	-1.8E-04	-1.4E-04	-1.5E-04	-7.6E-05	-1.2E-04	-4.7E-05	-3.8E-05	-4.5E-05	-1.9E-05	-4.0E-05	-1.4E-05	-3.9E-05	-2.4E-05	-4.0E-05	-1.1E-04	-1.4E-04
3.14	105	-2.8E-04	-2.4E-04	-1.9E-04	-1.9E-04	-2.0E-04	-1.4E-04	-1.4E-04	-6.9E-05	-8.9E-05	-4.7E-05	-2.6E-05	8.1E-06	-9.0E-06	6.8E-06	8.5E-06	2.2E-07	-4.0E-06	-5.3E-05	-1.4E-04	-1.1E-04
3.17	106	-2.6E-04	-2.3E-04	-2.3E-04	-1.3E-04	-1.6E-04	-1.3E-04	-1.3E-04	-6.5E-05	-8.8E-05	-3.3E-05	-5.3E-05	-4.0E-06	6.4E-06	-4.4E-07	-6.3E-06	-2.9E-05	1.1E-06	-6.6E-05	-1.2E-04	-1.2E-04
3.17	107	-2.9E-04	-2.7E-04	-2.5E-04	-1.6E-04	-1.8E-04	-1.7E-04	-1.1E-04	-9.6E-05	-7.9E-05	-6.3E-05	-5.3E-05	-1.6E-05	7.1E-06	-3.0E-05	-1.0E-06	-1.7E-05	-5.4E-06	-5.4E-05	-1.3E-04	-1.6E-04
3.18	108	-2.6E-04	-2.4E-04	-2.3E-04	-1.5E-04	-1.9E-04	-1.4E-04	-1.1E-04	-6.2E-05	-7.4E-05	-4.4E-05	-3.0E-05	-1.8E-05	3.5E-05	-3.3E-05	-1.5E-05	-1.5E-05	-2.4E-05	-6.3E-05	-1.0E-04	-1.3E-04
3.17	109	-2.7E-04	-2.8E-04	-2.3E-04	-2.0E-04	-2.1E-04	-1.4E-04	-1.1E-04	-7.0E-05	-1.2E-04	-5.9E-05	-4.9E-05	-1.7E-05	7.8E-06	-1.7E-05	-1.2E-06	-1.9E-05	-1.7E-05	-6.0E-05	-1.5E-04	-1.3E-04
3.18	110	-2.6E-04	-2.4E-04	-2.1E-04	-1.3E-04	-1.6E-04	-1.4E-04	-1.1E-04	-5.4E-05	-6.7E-05	-7.7E-05	-4.4E-05	-5.4E-06	-1.3E-05	-4.3E-05	2.0E-05	-1.4E-05	-1.2E-06	-7.7E-05	-1.1E-04	-9.4E-05
3.15	111	-2.6E-04	-2.4E-04	-2.3E-04	-1.2E-04	-1.6E-04	-1.2E-04	-1.1E-04	-5.5E-05	-7.0E-05	1.5E-05	-4.9E-05	3.0E-06	9.9E-06	-7.2E-07	-1.7E-05	-1.9E-05	-2.8E-06	-4.7E-05	-9.0E-05	-1.1E-04
3.18	112	-2.3E-04	-2.4E-04	-2.8E-04	-1.6E-04	-1.9E-04	-1.4E-04	-1.2E-04	-6.2E-05	-9.6E-05	-3.5E-05	-4.7E-05	2.7E-05	4.6E-06	3.6E-05	2.6E-05	1.1E-05	-7.8E-06	1.3E-05	-1.1E-04	-1.7E-04
3.17	113	-2.3E-04	-1.9E-04	-1.9E-04	-1.5E-04	-1.2E-04	-1.0E-04	-5.7E-05	-2.5E-05	-7.2E-05	-1.8E-05	-7.4E-06	1.8E-05	3.1E-05	3.2E-05	1.7E-06	-1.2E-05	7.2E-06	-4.3E-05	-1.1E-04	-5.5E-05
3.17	114	-2.4E-04	-2.3E-04	-2.1E-04	-1.5E-04	-1.4E-04	-1.0E-04	-1.2E-04	-8.0E-05	-3.6E-05	-4.4E-05	-2.1E-05	3.2E-05	4.7E-05	-6.1E-06	-2.5E-06	2.4E-06	1.6E-05	-1.9E-05	-1.1E-04	-9.3E-05
3.14	115	-2.5E-04	-1.8E-04	-2.4E-04	-1.3E-04	-1.4E-04	-1.1E-04	-8.9E-05	-7.3E-05	-7.7E-05	-5.5E-05	-2.3E-05	-4.7E-06	2.4E-05	-9.7E-07	7.2E-06	-4.3E-05	-2.9E-05	-4.1E-05	-9.9E-05	-8.3E-05
3.17	116	-2.6E-04	-2.1E-04	-2.0E-04	-1.2E-04	-1.6E-04	-1.2E-04	-9.3E-05	-2.5E-05	-4.5E-05	-1.9E-05	-2.9E-05	1.3E-05	1.1E-05	2.4E-05	1.8E-05	1.5E-05	-2.6E-05	-3.7E-05	-9.4E-05	-8.8E-05
3.15	117	-2.0E-04	-1.8E-04	-1.8E-04	-1.2E-04	-1.0E-04	-8.8E-05	-6.4E-05	-4.4E-05	3.5E-06	-1.1E-06	-1.4E-06	3.9E-05	7.1E-05	3.3E-05	5.1E-05	1.9E-05	1.3E-06	-2.6E-05	-6.8E-05	-9.2E-05
3.18	118	-2.8E-04	-2.5E-04	-2.4E-04	-1.9E-04	-1.8E-04	-1.6E-04	-1.3E-04	-9.4E-05	-1.2E-04	-5.9E-05	-5.7E-05	-6.1E-06	-4.7E-05	-2.1E-05	2.6E-05	-2.7E-05	-4.8E-05	-5.4E-05	-1.2E-04	-7.1E-05
3.16	119	-2.7E-04	-2.2E-04	-1.9E-04	-1.4E-04	-1.5E-04	-1.0E-04	-1.4E-04	-4.7E-05	-3.7E-05	-2.8E-05	-1.8E-05	2.9E-05	2.0E-05	3.5E-05	1.9E-05	1.2E-05	-1.1E-05	-4.8E-05	-7.5E-05	-8.1E-05
3.15	120	-2.7E-04	-2.6E-04	-2.8E-04	-1.9E-04	-2.0E-04	-1.4E-04	-1.6E-04	-9.3E-05	-1.2E-04	-7.8E-05	-5.3E-05	-2.1E-05	-1.1E-06	-5.6E-05	-1.2E-05	-3.8E-05	-2.5E-05	-3.4E-05	-1.1E-04	-1.2E-04
3.14	121	-3.7E-04	-3.5E-04	-3.2E-04	-2.4E-04	-2.0E-04	-2.3E-04	-2.1E-04	-1.4E-04	-1.1E-04	-1.2E-04	-1.3E-04	-9.9E-05	-7.6E-05	-7.9E-05	-9.5E-05	-1.1E-04	-8.9E-05	-9.1E-05	-1.5E-04	-1.8E-04
3.15	122	-2.9E-04	-2.9E-04	-3.0E-04	-2.0E-04	-1.9E-04	-1.8E-04	-2.2E-04	-1.8E-04	-1.7E-04	-1.2E-04	-1.5E-04	-1.1E-04	-8.7E-05	-1.1E-04	-9.5E-05	-1.1E-04	-1.2E-04	-1.7E-04	-2.2E-04	-2.2E-04
3.17	123	-2.5E-04	-2.5E-04	-2.4E-04	-1.5E-04	-1.6E-04	-1.3E-04	-1.3E-04	-4.1E-05	-7.9E-05	-5.8E-05	-1.8E-05	4.0E-06	1.5E-06	3.1E-07	2.4E-05	-2.5E-05	-2.1E-05	-3.5E-05	-8.7E-05	-9.2E-05
3.16	124	-2.5E-04	-2.6E-04	-2.1E-04	-1.5E-04	-1.7E-04	-1.4E-04	-1.4E-04	-5.1E-05	-6.8E-05	-4.1E-05	-6.3E-05	-1.1E-05	-1.7E-05	-3.9E-05	-2.0E-05	-3.1E-05	-2.4E-05	-5.9E-05	-1.5E-04	-1.2E-04

Table G.2. Continued.

Load (kN)	Time (s)	E0	E1	E2	E3	E4	E5	E6	E7	E8	E9	E10	E11	E12	E13	E14	E15	E16	E17	E18	E19
3.16	125	-2.6E-04	-2.1E-04	-2.5E-04	-2.0E-04	-1.4E-04	-1.2E-04	-1.1E-04	-7.4E-05	-8.1E-05	-5.4E-05	-1.2E-05	-2.7E-05	6.5E-07	-1.1E-05	6.7E-06	-8.5E-06	-2.4E-07	-3.9E-05	-1.3E-04	-9.1E-05
3.15	126	-2.7E-04	-2.2E-04	-2.3E-04	-1.6E-04	-1.8E-04	-1.6E-04	-1.4E-04	-7.8E-05	-7.9E-05	-5.2E-05	-3.3E-05	-1.3E-05	-3.9E-05	-3.1E-06	2.1E-05	-3.2E-05	2.1E-06	-7.3E-05	-1.4E-04	-1.1E-04
3.16	127	-3.1E-04	-2.5E-04	-2.3E-04	-1.5E-04	-1.9E-04	-1.2E-04	-1.2E-04	-5.6E-05	-6.2E-05	-3.1E-05	-3.4E-05	-3.1E-06	3.0E-05	-1.8E-06	-3.9E-06	5.4E-07	-2.9E-05	-9.6E-05	-1.2E-04	-9.9E-05
3.15	128	-2.3E-04	-2.1E-04	-2.3E-04	-1.5E-04	-1.5E-04	-1.4E-04	-1.2E-04	-6.5E-05	-5.9E-05	-1.5E-05	-2.1E-05	-2.3E-05	-2.7E-06	-3.3E-05	-1.6E-05	-3.1E-05	-1.1E-05	-5.6E-05	-1.5E-04	-9.8E-05
3.17	129	-2.4E-04	-2.5E-04	-2.6E-04	-1.4E-04	-1.6E-04	-1.4E-04	-1.1E-04	-6.2E-05	-4.6E-05	-4.2E-05	-5.0E-05	-6.3E-06	4.6E-05	2.4E-06	4.8E-05	-3.3E-05	-2.1E-05	-5.9E-05	-1.4E-04	-1.8E-04
3.18	130	-2.7E-04	-2.0E-04	-2.3E-04	-1.7E-04	-1.5E-04	-1.4E-04	-1.5E-04	-6.5E-05	-8.9E-05	2.7E-06	-4.3E-05	-1.1E-05	1.1E-05	-1.2E-05	-9.9E-06	8.4E-06	-9.3E-06	-5.0E-05	-8.9E-05	-1.3E-04
3.16	131	-2.8E-04	-2.6E-04	-2.3E-04	-1.7E-04	-1.6E-04	-1.4E-04	-1.2E-04	-1.1E-04	-7.4E-05	-6.7E-05	-3.0E-05	-2.6E-05	-2.4E-06	-4.1E-05	-2.1E-05	-4.9E-05	-8.6E-05	-8.4E-05	-1.6E-04	-1.0E-04
3.15	132	-2.7E-04	-2.7E-04	-2.5E-04	-1.6E-04	-2.0E-04	-1.5E-04	-1.2E-04	-9.4E-05	-9.9E-05	-4.1E-05	-5.3E-05	-3.8E-05	-5.2E-05	-2.9E-05	-3.6E-05	-3.4E-05	-1.2E-05	-6.1E-05	-7.6E-05	-1.0E-04
3.16	133	-2.6E-04	-2.3E-04	-2.3E-04	-1.7E-04	-1.5E-04	-1.5E-04	-1.3E-04	-6.3E-05	-9.3E-05	-7.7E-05	-6.8E-05	-2.8E-05	4.4E-06	-2.9E-05	-1.3E-05	-2.7E-05	-1.9E-05	-9.1E-05	-1.3E-04	-1.7E-04
3.15	134	-2.8E-04	-2.1E-04	-2.7E-04	-1.8E-04	-1.7E-04	-1.5E-04	-1.3E-04	-4.0E-05	-9.6E-05	-3.2E-05	-4.2E-05	1.0E-05	3.3E-05	-2.7E-05	-7.3E-06	-3.0E-05	-7.2E-05	-7.4E-05	-1.1E-04	-1.0E-04
3.24	135	-3.2E-04	-2.9E-04	-2.9E-04	-1.9E-04	-2.4E-04	-1.9E-04	-1.8E-04	-8.2E-05	-5.9E-05	-7.3E-05	-4.7E-05	-1.4E-05	2.3E-05	-4.8E-06	-3.0E-05	-3.5E-05	-2.2E-05	-6.2E-05	-1.5E-04	-9.9E-05
3.33	136	-3.2E-04	-2.9E-04	-2.6E-04	-2.3E-04	-2.0E-04	-1.4E-04	-1.3E-04	-8.9E-05	-1.1E-04	-3.6E-05	-5.6E-05	-6.7E-06	9.3E-06	-1.8E-05	3.3E-06	-1.8E-05	-5.3E-06	-9.5E-05	-9.5E-05	-1.1E-04
3.35	137	-3.2E-04	-2.6E-04	-2.3E-04	-2.1E-04	-2.1E-04	-1.4E-04	-1.2E-04	-8.3E-05	-7.3E-05	-4.1E-05	-1.9E-05	-1.7E-05	-2.3E-05	-4.0E-05	-4.1E-07	-3.0E-05	-2.5E-05	-6.5E-05	-1.4E-04	-1.2E-04
3.42	138	-2.8E-04	-2.6E-04	-2.5E-04	-1.9E-04	-2.0E-04	-1.6E-04	-1.4E-04	-1.2E-04	-7.5E-05	-4.7E-05	-5.5E-05	-5.1E-06	7.3E-06	-2.6E-05	-1.5E-05	-2.1E-05	-4.0E-05	-6.3E-05	-1.0E-04	-1.3E-04
3.49	139	-2.8E-04	-2.4E-04	-2.6E-04	-1.8E-04	-1.5E-04	-1.5E-04	-1.3E-04	-4.2E-05	-8.9E-05	-7.8E-05	-3.8E-05	-1.4E-05	1.0E-05	-2.4E-05	-1.5E-06	-5.1E-05	-4.4E-05	-8.7E-05	-1.5E-04	-1.5E-04
3.48	140	-3.2E-04	-2.8E-04	-2.8E-04	-1.7E-04	-2.0E-04	-1.5E-04	-1.3E-04	-8.0E-05	-8.6E-05	-4.3E-05	-3.7E-05	-5.6E-05	4.8E-06	-1.1E-05	-6.1E-06	-3.5E-05	-2.7E-05	-8.3E-05	-1.8E-04	-1.7E-04
3.58	141	-3.8E-04	-2.6E-04	-3.3E-04	-1.8E-04	-2.2E-04	-1.9E-04	-1.2E-04	-1.1E-04	-1.1E-04	-6.0E-05	-7.3E-05	-3.8E-05	-3.4E-06	-8.0E-06	-5.2E-05	-5.5E-05	-4.9E-05	-9.9E-05	-1.9E-04	-1.7E-04
3.62	142	-3.3E-04	-3.1E-04	-2.9E-04	-2.2E-04	-2.3E-04	-1.9E-04	-1.4E-04	-9.3E-05	-8.4E-05	-1.7E-05	-6.8E-05	-6.0E-05	-3.5E-05	-4.8E-05	-2.8E-05	-1.7E-05	-2.5E-05	-7.9E-05	-1.6E-04	-1.5E-04
3.64	143	-3.5E-04	-3.1E-04	-3.2E-04	-2.5E-04	-2.3E-04	-1.7E-04	-1.4E-04	-9.6E-05	-8.9E-05	-6.7E-05	-6.1E-05	-2.8E-05	-4.7E-06	-8.9E-06	-8.4E-06	-3.6E-05	-3.7E-05	-1.0E-04	-2.0E-04	-1.9E-04
3.65	144	-4.1E-04	-2.8E-04	-2.7E-04	-2.3E-04	-2.5E-04	-1.5E-04	-1.6E-04	-9.8E-05	-8.9E-05	-5.9E-05	-8.1E-05	-1.5E-05	-2.6E-05	-6.8E-05	-4.5E-05	-5.6E-05	-3.5E-05	-9.5E-05	-1.8E-04	-1.7E-04
3.75	145	-3.7E-04	-3.3E-04	-3.3E-04	-2.1E-04	-2.1E-04	-1.9E-04	-1.6E-04	-1.3E-04	-1.3E-04	-6.3E-05	-7.6E-05	-1.5E-05	-5.4E-05	-6.7E-05	4.1E-06	-7.7E-05	-5.4E-05	-1.1E-04	-1.7E-04	-2.0E-04
3.82	146	-4.0E-04	-3.5E-04	-3.4E-04	-2.5E-04	-2.6E-04	-1.9E-04	-1.7E-04	-1.3E-04	-9.5E-05	-5.1E-05	-6.3E-05	-2.8E-05	-2.0E-05	-6.4E-05	-4.7E-05	-9.0E-05	-6.5E-05	-1.1E-04	-1.8E-04	-1.6E-04
3.90	147	-3.4E-04	-3.3E-04	-3.3E-04	-2.3E-04	-2.7E-04	-2.0E-04	-1.9E-04	-1.4E-04	-1.3E-04	-7.8E-05	-9.3E-05	-2.7E-05	-4.0E-05	-4.9E-05	-2.9E-05	-6.7E-05	-4.9E-05	-1.1E-04	-2.0E-04	-1.8E-04
3.96	148	-4.1E-04	-3.1E-04	-3.3E-04	-2.5E-04	-2.7E-04	-2.1E-04	-1.9E-04	-1.1E-04	-1.2E-04	-9.9E-05	-8.7E-05	-4.8E-05	-2.8E-05	-6.0E-05	-2.8E-05	-6.6E-05	-4.7E-05	-1.1E-04	-1.8E-04	-1.8E-04
3.97	149	-4.0E-04	-3.6E-04	-3.1E-04	-2.4E-04	-2.3E-04	-1.9E-04	-2.0E-04	-1.2E-04	-9.6E-05	-5.3E-05	-6.4E-05	-2.4E-05	-9.4E-06	-4.6E-05	-3.8E-05	-6.3E-05	-1.6E-05	-1.0E-04	-1.7E-04	-1.9E-04
4.08	150	-3.5E-04	-2.7E-04	-3.0E-04	-2.1E-04	-2.0E-04	-2.0E-04	-1.4E-04	-3.3E-05	-7.9E-05	-3.9E-05	-5.7E-05	-3.2E-05	2.4E-05	-3.8E-05	1.7E-06	-2.5E-05	-2.4E-05	-1.1E-04	-1.8E-04	-1.7E-04
4.06	151	-3.6E-04	-3.5E-04	-3.4E-04	-2.5E-04	-2.5E-04	-2.3E-04	-2.0E-04	-1.3E-04	-1.2E-04	-9.2E-05	-6.8E-05	-4.2E-05	-6.8E-05	-4.0E-05	-5.3E-05	-7.4E-05	-7.2E-05	-1.1E-04	-1.7E-04	-1.6E-04
4.13	152	-4.1E-04	-3.4E-04	-3.6E-04	-2.8E-04	-2.4E-04	-2.2E-04	-1.8E-04	-1.3E-04	-1.3E-04	-8.3E-05	-6.5E-05	-5.3E-05	-4.3E-05	-4.0E-05	-5.2E-05	-5.3E-05	-4.7E-05	-1.3E-04	-2.0E-04	-1.8E-04
4.15	153	-4.0E-04	-3.5E-04	-2.9E-04	-2.6E-04	-2.6E-04	-2.1E-04	-2.1E-04	-9.0E-05	-7.2E-05	-4.8E-05	-7.0E-05	-3.0E-05	-1.1E-05	-5.2E-05	-4.6E-05	-6.8E-05	-7.3E-05	-1.0E-04	-1.7E-04	-1.7E-04
4.22	154	-3.9E-04	-3.7E-04	-3.0E-04	-2.5E-04	-2.6E-04	-2.1E-04	-1.3E-04	-1.2E-04	-1.1E-04	-6.1E-05	-8.5E-05	-2.8E-05	-3.9E-05	-7.3E-05	-3.3E-05	-6.8E-05	-7.1E-05	-1.3E-04	-1.8E-04	-1.6E-04
4.28	155	-4.0E-04	-3.2E-04	-3.1E-04	-2.4E-04	-2.3E-04	-2.0E-04	-1.8E-04	-1.1E-04	-1.2E-04	-8.3E-05	-7.6E-05	-5.4E-05	-5.3E-05	-9.1E-05	-6.5E-05	-6.3E-05	-7.4E-05	-1.5E-04	-2.1E-04	-2.7E-04

Table G.2. Continued.

Load (kN)	Time (s)	E0	E1	E2	E3	E4	E5	E6	E7	E8	E9	E10	E11	E12	E13	E14	E15	E16	E17	E18	E19
4.21	156	-3.7E-04	-3.1E-04	-3.5E-04	-2.7E-04	-1.9E-04	-1.8E-04	-1.6E-04	-9.9E-05	-9.9E-05	-8.0E-05	-6.5E-05	-4.1E-05	-2.9E-05	-2.2E-05	-1.9E-05	-3.9E-05	-5.0E-05	-1.4E-04	-1.6E-04	-1.8E-04
4.21	157	-3.9E-04	-3.2E-04	-3.3E-04	-2.5E-04	-2.8E-04	-1.9E-04	-1.7E-04	-9.1E-05	-1.2E-04	-3.7E-05	-5.3E-05	-1.4E-05	-3.3E-05	-4.1E-05	-1.8E-05	-4.3E-05	-5.7E-05	-1.1E-04	-1.9E-04	-2.0E-04
4.25	158	-3.9E-04	-3.6E-04	-3.7E-04	-2.6E-04	-2.5E-04	-2.5E-04	-1.9E-04	-1.1E-04	-1.1E-04	-1.2E-04	-1.1E-04	-5.3E-05	-5.6E-05	-7.7E-05	-6.2E-05	-5.3E-05	-9.1E-05	-1.4E-04	-2.1E-04	-2.1E-04
4.23	159	-4.2E-04	-3.2E-04	-2.9E-04	-2.1E-04	-2.5E-04	-1.9E-04	-1.8E-04	-1.3E-04	-1.1E-04	-5.6E-05	-8.9E-05	-4.7E-05	-3.5E-05	-4.9E-05	-7.7E-05	-7.6E-05	-8.9E-05	-1.4E-04	-1.7E-04	-2.5E-04
4.22	160	-4.4E-04	-3.5E-04	-3.5E-04	-2.6E-04	-2.9E-04	-2.4E-04	-2.0E-04	-1.3E-04	-1.7E-04	-1.1E-04	-8.8E-05	-7.0E-05	-4.6E-05	-1.3E-04	-7.6E-05	-1.0E-04	-1.2E-04	-1.4E-04	-2.3E-04	-2.7E-04
4.22	161	-3.8E-04	-3.4E-04	-3.2E-04	-2.5E-04	-2.7E-04	-2.3E-04	-2.1E-04	-1.4E-04	-1.2E-04	-8.9E-05	-9.9E-05	-3.5E-05	-4.0E-05	-5.2E-05	-6.1E-05	-7.7E-05	-6.1E-05	-1.6E-04	-2.2E-04	-2.4E-04
4.21	162	-3.5E-04	-3.8E-04	-3.0E-04	-2.3E-04	-2.4E-04	-1.9E-04	-1.7E-04	-1.2E-04	-1.1E-04	-8.0E-05	-7.5E-05	-4.3E-05	-6.9E-05	-5.5E-05	-5.9E-05	-8.3E-05	-8.1E-05	-1.2E-04	-1.6E-04	-2.5E-04
4.20	163	-4.2E-04	-3.6E-04	-3.3E-04	-2.6E-04	-2.5E-04	-2.1E-04	-1.9E-04	-1.3E-04	-1.2E-04	-6.5E-05	-8.8E-05	-7.2E-05	-5.0E-05	-6.3E-05	-4.5E-05	-5.1E-05	-3.8E-05	-1.4E-04	-2.3E-04	-1.8E-04
4.24	164	-3.9E-04	-3.5E-04	-3.2E-04	-1.9E-04	-2.3E-04	-1.8E-04	-1.7E-04	-1.2E-04	-1.0E-04	-5.9E-05	-8.6E-05	-2.3E-05	-4.3E-05	-7.1E-05	-2.1E-05	-4.3E-05	-5.5E-05	-9.4E-05	-1.7E-04	-1.5E-04
4.22	165	-3.9E-04	-3.4E-04	-3.3E-04	-2.9E-04	-2.8E-04	-2.1E-04	-1.6E-04	-1.5E-04	-1.2E-04	-6.9E-05	-8.3E-05	-5.5E-05	-4.9E-05	-7.3E-05	-1.9E-05	-6.9E-05	-4.2E-05	-1.1E-04	-1.8E-04	-2.0E-04
4.22	166	-3.6E-04	-3.2E-04	-3.2E-04	-2.4E-04	-2.4E-04	-1.9E-04	-1.9E-04	-1.1E-04	-8.5E-05	-1.1E-04	-9.2E-05	-4.8E-05	-3.0E-05	-5.8E-05	-5.3E-05	-6.9E-05	-7.1E-05	-1.2E-04	-1.7E-04	-2.5E-04
4.23	167	-3.8E-04	-3.3E-04	-3.4E-04	-2.6E-04	-2.5E-04	-2.0E-04	-1.7E-04	-1.2E-04	-8.8E-05	-9.8E-05	-1.2E-04	-4.5E-05	-3.0E-05	-5.9E-05	-5.2E-05	-6.4E-05	-7.7E-05	-1.2E-04	-1.9E-04	-2.2E-04
4.23	168	-3.5E-04	-3.3E-04	-3.7E-04	-2.4E-04	-2.7E-04	-2.0E-04	-1.8E-04	-1.2E-04	-1.5E-04	-1.2E-04	-8.3E-05	-6.0E-05	-3.4E-05	-7.3E-05	-5.4E-05	-6.1E-05	-6.7E-05	-1.3E-04	-1.7E-04	-2.2E-04
4.20	169	-3.7E-04	-3.3E-04	-3.3E-04	-2.1E-04	-2.1E-04	-1.9E-04	-1.5E-04	-7.7E-05	-6.8E-05	-6.8E-05	-5.9E-05	-2.6E-05	-2.1E-05	-6.2E-05	-4.4E-05	-3.8E-05	-4.7E-05	-1.3E-04	-1.6E-04	-2.2E-04
4.15	170	-3.6E-04	-3.4E-04	-3.4E-04	-2.9E-04	-2.2E-04	-2.2E-04	-1.9E-04	-1.3E-04	-1.2E-04	-1.1E-04	-1.1E-04	-8.8E-05	-7.6E-05	-1.1E-04	-6.7E-05	-8.3E-05	-4.0E-05	-1.5E-04	-2.4E-04	-2.1E-04
4.12	171	-4.1E-04	-3.7E-04	-3.4E-04	-2.4E-04	-3.0E-04	-2.2E-04	-1.7E-04	-4.8E-05	-8.4E-05	-9.8E-06	-6.2E-05	2.4E-06	-7.7E-06	-1.2E-05	-2.3E-05	-2.3E-06	-1.1E-05	-1.0E-04	-1.5E-04	-2.1E-04
4.14	172	-4.7E-04	-4.1E-04	-3.9E-04	-3.0E-04	-3.0E-04	-2.7E-04	-2.0E-04	-1.3E-04	-1.7E-04	-1.2E-04	-1.3E-04	-8.2E-05	-8.3E-05	-1.5E-04	-9.9E-05	-9.7E-05	-9.0E-05	-1.4E-04	-2.1E-04	-2.1E-04
4.14	173	-4.0E-04	-3.6E-04	-3.4E-04	-2.7E-04	-2.6E-04	-2.1E-04	-1.8E-04	-1.1E-04	-1.2E-04	-8.9E-05	-9.2E-05	-6.9E-05	-4.0E-05	-9.4E-05	-4.0E-05	-5.1E-05	-2.9E-05	-1.1E-04	-1.9E-04	-2.1E-04
4.13	174	-4.1E-04	-3.6E-04	-3.8E-04	-2.5E-04	-2.7E-04	-2.4E-04	-1.7E-04	-1.1E-04	-1.3E-04	-1.4E-04	-1.2E-04	-6.1E-05	-9.4E-05	-8.2E-05	-6.8E-05	-7.4E-05	-8.1E-05	-1.1E-04	-2.4E-04	-2.3E-04
4.13	175	-3.5E-04	-3.5E-04	-3.3E-04	-2.3E-04	-2.6E-04	-1.9E-04	-1.3E-04	-4.9E-05	-1.1E-04	-5.5E-05	-5.5E-05	-3.3E-05	-2.7E-05	-6.0E-05	-2.1E-05	-3.9E-05	-2.9E-05	-1.0E-04	-1.9E-04	-2.0E-04
4.14	176	-4.2E-04	-3.5E-04	-3.6E-04	-2.4E-04	-2.6E-04	-2.2E-04	-1.7E-04	-1.3E-04	-1.4E-04	-1.1E-04	-8.4E-05	-5.3E-05	-3.8E-05	-9.1E-05	-5.2E-05	-7.8E-05	-8.6E-05	-1.4E-04	-2.1E-04	-2.1E-04
4.13	177	-3.9E-04	-3.2E-04	-3.7E-04	-2.5E-04	-2.1E-04	-1.8E-04	-1.4E-04	-1.1E-04	-1.1E-04	-7.9E-05	-2.7E-05	-5.1E-06	-8.0E-06	-4.7E-05	-4.2E-05	-5.2E-05	-2.1E-05	-1.1E-04	-2.0E-04	-2.4E-04
4.15	178	-3.7E-04	-3.6E-04	-3.1E-04	-2.0E-04	-2.4E-04	-1.8E-04	-1.2E-04	-9.0E-05	-8.7E-05	-1.0E-04	-7.8E-05	-2.7E-05	-1.6E-05	-3.1E-05	-5.8E-05	-6.3E-05	-5.0E-05	-1.9E-04	-1.6E-04	-2.0E-04
4.14	179	-4.0E-04	-3.7E-04	-3.8E-04	-2.8E-04	-2.7E-04	-2.1E-04	-1.8E-04	-1.3E-04	-1.1E-04	-9.0E-05	-9.1E-05	-4.1E-05	-2.5E-05	-7.3E-05	-6.2E-05	-7.3E-05	-8.8E-05	-1.5E-04	-2.1E-04	-2.0E-04
4.15	180	-3.5E-04	-3.5E-04	-3.2E-04	-2.7E-04	-2.2E-04	-2.1E-04	-1.5E-04	-1.0E-04	-9.3E-05	-7.7E-05	-7.3E-05	-4.5E-05	-4.5E-05	-6.2E-05	-4.7E-05	-3.6E-05	-4.9E-05	-1.2E-04	-2.0E-04	-1.9E-04
4.13	181	-3.7E-04	-3.9E-04	-3.4E-04	-2.7E-04	-2.2E-04	-2.4E-04	-1.7E-04	-1.2E-04	-1.1E-04	-9.6E-05	-8.9E-05	-4.5E-05	-5.2E-05	-8.7E-05	-7.2E-05	-8.9E-05	-7.1E-05	-1.4E-04	-1.9E-04	-2.3E-04
4.15	182	-3.8E-04	-3.7E-04	-3.1E-04	-2.5E-04	-2.8E-04	-2.0E-04	-1.7E-04	-1.2E-04	-1.3E-04	-1.2E-04	-1.3E-04	-5.4E-05	-7.9E-05	-1.0E-04	-5.3E-05	-7.8E-05	-8.5E-05	-1.5E-04	-1.9E-04	-2.9E-04
4.14	183	-3.6E-04	-3.5E-04	-3.5E-04	-2.4E-04	-2.4E-04	-2.2E-04	-1.9E-04	-9.2E-05	-1.4E-04	-7.8E-05	-7.8E-05	-5.8E-05	-1.4E-05	-7.1E-05	-3.6E-05	-7.2E-05	-6.7E-05	-1.2E-04	-1.8E-04	-2.0E-04
4.15	184	-3.8E-04	-3.4E-04	-3.5E-04	-2.5E-04	-2.7E-04	-2.0E-04	-1.8E-04	-1.1E-04	-1.2E-04	-9.4E-05	-7.3E-05	-4.7E-05	-4.0E-05	-9.0E-05	-5.7E-05	-6.5E-05	-9.5E-05	-1.5E-04	-2.3E-04	-1.6E-04
4.15	185	-4.1E-04	-3.4E-04	-3.1E-04	-2.3E-04	-2.4E-04	-1.8E-04	-1.8E-04	-7.2E-05	-8.1E-05	-6.3E-05	-6.2E-05	-5.9E-06	-3.1E-05	-4.1E-05	-4.3E-05	-8.6E-05	-6.9E-05	-1.1E-04	-2.1E-04	-2.2E-04
4.16	186	-4.5E-04	-3.6E-04	-3.8E-04	-2.6E-04	-2.8E-04	-2.2E-04	-1.7E-04	-1.4E-04	-1.6E-04	-1.1E-04	-1.2E-04	-1.0E-04	-7.2E-05	-7.8E-05	-9.8E-05	-8.3E-05	-8.2E-05	-1.9E-04	-2.3E-04	-2.7E-04

APPENDIX H Python Codes

The following are the sample Python Codes for calculating the estimated N.A. locations using Batch 3 pre-corrosion load tests as an example.

```python
#%%
import numpy as np
import matplotlib.pyplot as plt
import pandas as pd
plt.style.use('default')
import os
import fnmatch
from pathlib2 import Path

# Define a Function for All Calculation Needed for a Beam
def analyze_one_cycle(batch_num, pre_post, beam_num, cycle,show_figure=True, verbose=0):

    ##############  Prepare files  #################
    home_dir=Path(r'C:\Users\xim41\Google Drive\Master\8.0 load test data\Raw Data for Python')
    batch_num=batch_num
    pre_post=pre_post
    beam_num=beam_num
    cycle=cycle
    save_dir = Path('C:/Users/xim41/Google Drive/Zoe+Peng/ZoeConcrete/Results')
    save_name='Batch'+str(batch_num)+'_'+pre_post+'corrosion_Beam'+str(beam_num)+'_'+str(cycle)

    current_folder=home_dir
    folder_list_lv1 = os.listdir(current_folder)

    ##################### 1. DIC Analysis ##############################
    # 1.1 find readings for DIC and ESG
    for folder in folder_list_lv1:
        if (str(batch_num) in folder)&('readings' in folder.lower()):
            current_folder = current_folder/folder

    folder_list_lv2 = os.listdir(current_folder)
    for folder in folder_list_lv2:
        if pre_post in folder.lower():
            current_folder = current_folder/folder

    folder_list_lv3 = os.listdir(current_folder)
    for folder in folder_list_lv3:
        if 'dic' in folder.lower():
            dic_folder = current_folder/folder
        elif 'esg' in folder.lower():
            esg_folder = current_folder/folder
        else:
            print('Something is wrong in the current folder '+ str(current_folder))

    dic_file = dic_folder/(str(beam_num)+'-'+str(int(cycle))+'.csv')
    esg_file = esg_folder/(str(beam_num)+'-'+str(int(cycle))+'.txt')
```

```
# 1.2 find locations file for DIC
current_folder=home_dir
folder_list_lv1 = os.listdir(current_folder)
for folder in folder_list_lv1:
    if (str(batch_num) in folder)&('positions' in folder.lower()):
        current_folder = current_folder/folder

folder_list_lv2 = os.listdir(current_folder)
for folder in folder_list_lv2:
    if pre_post in folder.lower():
        current_folder = current_folder/folder
loc_folder=current_folder
loc_list = fnmatch.filter(os.listdir(loc_folder),str(beam_num)+'*.csv') # find a list of files with the current beam_num

for file_name in loc_list:
    if str(int(cycle)) in file_name[1:]:
        loc_file = loc_folder/file_name # find the file for current cycle
        break # once the file is found, exit the for loop.

# 1.3 get the theoretical N.A. location for the current beam
theory_file = Path(r'C:\Users\xim41\Google Drive\Master\8.0 load test data\Raw Data for Python\Theoretical Values.xlsx')
theory_content=pd.read_excel(theory_file,header=0)
theory_value=theory_content[theory_content['BATCH']==batch_num][theory_content['PREPOST']==pre_post][theory_content['BEAM']==beam_num]['VALUE'].values[0]

###############  2. Difine Least Square Fit Function  ############################
def least_square_fit(positions, readings):
    # length = min(len)
    positions = positions[:readings.shape[1]]
    position_mean = positions.mean()
    reading_mean = readings.mean(axis=1)
    reading_mean = reading_mean.reshape(len(reading_mean), 1)
    # print(reading_mean[:10])
    m = ((readings - reading_mean) * (positions - position_mean)).sum(axis=1) / (
        np.square(positions - position_mean)).sum(axis=0)
    # print(m[:10])
    b = reading_mean.flatten() - m * position_mean.flatten()
    neutral_axis = -b / m
    m_len = m.shape[0]
    fi = m.reshape(m_len, 1) * (positions) + b.reshape(len(b), 1)
    ss_res = (np.square(readings - fi)).sum(axis=1)
    ss_tot = (np.square(readings - reading_mean)).sum(axis=1)
    r2 = 1 - ss_res / ss_tot
    print(r2.shape)
    return (neutral_axis, m, r2)

############### DIC neutral axis location (All sensors) ################
def fix_nan(data):
    return(data.fillna(method='ffill')) #  ffill: propagate last valid observation forward to next valid backfill (DIC has some empty cells)
dic_loc = pd.read_csv(loc_file,header=0, usecols=[6]).values.flatten()
dic_read_data  = pd.read_csv(dic_file,header=None,skiprows=[0,1,2])
dic_read_data = fix_nan(dic_read_data).iloc[:,1:]
dic_read=dic_read_data.values
dic_b,_,dic_b_r2= least_square_fit(dic_loc,dic_read)

############### DIC neutral axis location (compressive sensors only) ####
dic_loc_cmprs=dic_loc[dic_loc<theory_value]
n_cmprs=len(dic_loc_cmprs)
dic_read_cmprs=dic_read_data.iloc[:,:n_cmprs].values
dic_b_cmprs,dic_m_cmprs,dic_b_cmprs_r2= least_square_fit(dic_loc_cmprs,dic_read_cmprs)

##########################3.ESG Analysis ##################
#3.1 Prepare ESG Data
esg_data_all = pd.read_csv(esg_file,sep='\t',header=None)
# get rid of initial useless data
col1 = esg_data_all.iloc[:,0]
starting_row = [i for i, e in enumerate(col1) if e == '600DX Disp'][-1]
esg_data = esg_data_all.iloc[starting_row:,:].reset_index()#.iloc[::2,:]
#name the columns
esg_data.columns=esg_data.iloc[0]
esg_data=(esg_data.drop(esg_data.index[0]).reset_index()).iloc[:,2:].dropna(axis=1,how='all')
#change string to float
for col in esg_data.columns:
    esg_data[col] = esg_data[col].astype('float')

#3.2 find out starting time for esg, and extracting half of the data
load_3000_ind = abs(esg_data['600DX Load'].astype('float')-3).idxmin()+1
time_dif = esg_data.iloc[load_3000_ind,-1]-60
esg_data.iloc[:,-1] = esg_data.iloc[:,-1]-time_dif
start_time_ind = esg_data.iloc[:,-1].abs().idxmin()
esg_data = esg_data.iloc[start_time_ind:,:].iloc[::2,:].reset_index().iloc[:,1:]
time = esg_data.iloc[:,-1].to_numpy().astype('float')
load = esg_data.iloc[:,1].to_numpy().astype('float')
```

```
################## neutral axis location (All Sensors)#############
esg_read = esg_data.iloc[:,[2,3,4,5]].values.astype('float')
esg_loc = np.array([30,20,10,0])
esg_b,_,esg_b_r2= least_square_fit(esg_loc,esg_read)

################## ESG Neutral Axis Location (No Top Gauges)#############
esg_loc_notop=np.array([30,20,10])
esg_read_notop=esg_data.iloc[:,2:5].values.astype('float')
esg_b_notop,_,esg_b_notop_r2 = least_square_fit(esg_loc_notop,esg_read_notop)

################## ESG Neutral Axis Location (No Top Gauges)#############
esg_loc_23=np.array([20,10])
esg_read_notop=esg_data.iloc[:,3:5].values.astype('float')
esg_b_23,_,esg_b_23_r2 = least_square_fit(esg_loc_notop,esg_read_notop)


################## Two Face Best Fit Together#############
#used DIC compressive only and ESG new gauges
esg_dic_loc=np.concatenate((esg_loc,dic_loc_cmprs),axis=0) # ESG repeated twice to balance the weight to DIC, cause DIC had more gauges
dic_read_cmprs=dic_read_cmprs[10:10+min(len(esg_b),len(dic_b)-10)]
esg_read=esg_read[:min(len(esg_b),len(dic_b)-10)]
esg_dic_read=np.concatenate((esg_read,dic_read_cmprs),axis=1)
esg_dic_b,_,esg_dic_b_r2= least_square_fit(esg_dic_loc,esg_dic_read)

# print(esg_read_23.shape)
# print(dic_read_cmprs.shape)

################# DIC best fit first then combined with ESG best fit#############
def dic_function(x):
    y = x*dic_m_cmprs-dic_b_cmprs*dic_m_cmprs
    return y
dic_fit_read_cmprs = np.array([dic_function(loc) for loc in esg_loc]).T

length = min(len(esg_read),len(dic_fit_read_cmprs)-10)
# print(length)
dic_fit_read_cmprs = dic_fit_read_cmprs[10:10+length]
esg_read = esg_read[:length]
# print(len(dic_fit_read_cmprs),len(esg_read))
dic_esg = (dic_fit_read_cmprs+esg_read)/2
dicfit_esg_b,_,dicfit_esg_b_r2 = least_square_fit(esg_loc,dic_esg)

################### 4. Combine DIC ESG Data Along with Loading ###############
dic_b_start=dic_b[10:10+min(len(esg_b),len(dic_b)-10)] # remove first 10 entries of DIC_b (DIC started 10 s earlier)
dic_b_cmprs_start=dic_b_cmprs[10:10+min(len(esg_b),len(dic_b)-10)]
dic_b_start_r2 = dic_b_r2[10:10 + min(len(esg_b), len(dic_b) - 10)]
dic_b_cmprs_start_r2 = dic_b_cmprs_r2[10:10 + min(len(esg_b), len(dic_b) - 10)]
dic_esg_dict={'dic_b':dic_b_start,'dic_b_cmprs':dic_b_cmprs_start,
              'esg_b':esg_b[:min(len(esg_b),len(dic_b)-10)],
              'esg_b_notop':esg_b_notop[:min(len(esg_b),len(dic_b)-10)],
              'esg_b_23': esg_b_23[:min(len(esg_b), len(dic_b) - 10)],
              'esg_dic_b':esg_dic_b,
              'dicfit_esg_b':dicfit_esg_b,
              'load':esg_data['600DX Load'][:min(len(esg_b),len(dic_b)-10)]}
dic_esg_r2_dict = {'dic_b_r2': dic_b_start_r2,
                   'dic_b_cmprs_r2': dic_b_cmprs_start_r2,
                   'esg_b_r2': esg_b_r2[:min(len(esg_b), len(dic_b) - 10)],
                   'esg_b_notop_r2': esg_b_notop_r2[:min(len(esg_b), len(dic_b) - 10)],
                   'esg_b_23_r2': esg_b_23_r2[:min(len(esg_b), len(dic_b) - 10)],
                   'esg_dic_b_r2': esg_dic_b_r2,
                   'dicfit_esg_r2': dicfit_esg_b_r2,
                   'load': esg_data['600DX Load'][:min(len(esg_b), len(dic_b) - 10)]}
dic_esg_df = pd.DataFrame.from_dict(dic_esg_dict)
dic_esg_r2_df = pd.DataFrame.from_dict(dic_esg_r2_dict)
dic_esg_df.to_csv(r'C:/Users/xim41/Google Drive/Zoe+Peng/ZoeConcrete/detailed_results/'+save_name+'.csv')
```

```
##################### Averaged N.A.Location for Loadings over 4kN at 1kN intervals ######################
ave_elas_dict = {}
std_elas_dict = {}
for i in range(3, 10):
    if i < 9:
        load_interval = dic_esg_df[(dic_esg_df['load'] > i) & (dic_esg_df['load'] < (i + 1))].iloc[:, :-1]
        ave_elas_dict[str(i) + '~' + str(i + 1)] = load_interval.mean(axis=0)
        std_elas_dict[str(i) + '~' + str(i + 1)] = np.std(load_interval, axis=0)
    else:
        pass
        # ave_elas_dict[str(i)+'~max']=dic_esg_df[(dic_esg_df['load']>i)].iloc[:,:-1].mean(axis=0)

ave_elas_r2_dict = {}
for i in range(3, 10):
    if i < 9:
        load_interval = dic_esg_r2_df[(dic_esg_r2_df['load'] > i) & (dic_esg_r2_df['load'] < (i + 1))].iloc[:, :-1]
        ave_elas_r2_dict[str(i) + '~' + str(i + 1)] = load_interval.mean(axis=0)
    else:
        pass

ave_elas = pd.DataFrame.from_dict(ave_elas_dict)
ave_elas['Order'] = np.arange(len(ave_elas))
std_elas = pd.DataFrame.from_dict(std_elas_dict)
std_elas['Order'] = np.arange(len(std_elas))
ave_elas_r2 = pd.DataFrame.from_dict(ave_elas_r2_dict)
ave_elas_r2['Order'] = np.arange(len(ave_elas_r2))
ave_std = pd.concat([ave_elas, ave_elas_r2, std_elas], keys=['NeutralAxis', 'R2', 'STD']).reset_index()
ave_std = ave_std.sort_values(by=['Order', 'level_0'])
# print(ave_std)
ave_std = ave_std.drop('Order', axis=1)
ave_std.to_csv(save_dir / Path(save_name + '.csv'))
return
```

```
batch_nums=[3]
pre_posts=['pre']
beam_nums=[1,2,3]
cycles = np.arange(1,20)
for batch_num in batch_nums:
    for pre_post in pre_posts:
        for beam_num in beam_nums:
            for cycle in cycles:
                try:
                    analyze_one_cycle(batch_num,pre_post,beam_num,cycle,show_figure=False)
                except:
                    continue
```

APPENDIX I Sample Calculation for the Reliability Index

The following are the sample calculations for the reliability analysis using Batch 3 Beam 3 in pre-corrosion load test as an example.

Estimated N.A. Locations

$c := 45.3\ mm$ $\sigma_c := 1.50\ mm$ (Experimental) Table 4.19

Material Properties

Concrete Strength $f'_c := 38.3\ MPa$ $\sigma_{f'c} := 1.1\ MPa$ (Experimental) Table 4.2

Concrete Modulus $E_c := 22.8\ GPa$ $\sigma_{Ec} := 1.1\ GPa$

Whitney Stress Block Factors

$$\alpha_1 := 0.85 - 0.0015 \cdot \frac{f'_c}{MPa} = 0.793$$

$$\sigma_{\alpha 1} := \sqrt{(-0.0015)^2 \cdot \left(\frac{\sigma_{f'c}}{MPa}\right)^2} = 0.002$$

$$\beta_1 := 0.97 - 0.0025 \cdot \frac{f'_c}{MPa} = 0.874$$

$$\sigma_{\beta 1} := \sqrt{(-0.0025)^2 \cdot \left(\frac{\sigma_{f'c}}{MPa}\right)^2} = 0.003$$

Steel Yield Strength $f_y := 437.3\ MPa$ $\sigma_{fy} := 1.9\ MPa$ (Experimental) Table 4.1

Steel Modulus $E_s := 200\ GPa$ $\sigma_{Es} := 6.2\ GPa$

Theoretical value from Literature (Mansour et. al, 1984)

Modulus Ratio $n := \frac{E_s}{E_c} = 8.772$ $\sigma_n := \sqrt{\left(\frac{1}{E_c}\right)^2 \cdot {\sigma_{Es}}^2 + \left(\frac{-E_s}{{E_c}^2}\right)^2 \cdot {\sigma_{Ec}}^2} = 0.5$

Beam Configurations

Rebar Diameter $d_b := 11.3\ mm$ $\sigma_{db} := 0\ mm$ (Variance Assumed to be very small)

Width $b := 72\ mm$ $\sigma_b := \frac{1\ mm}{1.645} = 0.608\ mm$ (Measured using ruler with 1 mm accuracy)

Height $h := 140\ mm$ $\sigma_h := \frac{1\ mm}{1.645} = 0.608\ mm$

Concrete Cover $cc := 33\ mm$

Standard SHM: (Without Cover Meter) $\sigma_{cc1} := \frac{12\ mm}{1.645} = 0.007\ m$ (CSA A23.1-14)

Enhanced SHM: (With Cover Meter) $\sigma_{cc2} := \frac{2\ mm}{1.645} = 0.001\ m$ (Measured by cover meter with 2 mm tolerance)

Rebar Depth $d := h - cc - \frac{d_b}{2} = 101.35\ mm$

Standard SHM: $\sigma_{d1} := \sqrt{1^2 \cdot \sigma_h^{\,2} + (-1)^2 \cdot \sigma_{cc1}^{\,2}} = 7.32\ mm$

Enhanced SHM: $\sigma_{d2} := \sqrt{1^2 \cdot \sigma_h^{\,2} + (-1)^2 \cdot \sigma_{cc2}^{\,2}} = 1.36\ mm$

Transformed Steel Bar Area

$$A_t(b,c,d) := \frac{b \cdot c^2}{2 \cdot (d-c)}$$

$$\frac{\mathrm{d}}{\mathrm{d}b} A_t(b,c,d) = \frac{c^2}{2 \cdot (d-c)}$$

$$\frac{\mathrm{d}}{\mathrm{d}c} A_t(b,c,d) = \frac{4 \cdot b \cdot c \cdot d - 2 \cdot b \cdot c^2}{4 \cdot (d-c)^2} = \frac{2 \cdot b \cdot c \cdot d - b \cdot c^2}{2 \cdot (d-c)^2}$$

$$\frac{\mathrm{d}}{\mathrm{d}d} A_t(b,c,d) = \frac{-2 \cdot b \cdot c^2}{4 \cdot (d-c)^2} = \frac{-b \cdot c^2}{2 \cdot (d-c)^2}$$

$$A_t := \frac{b \cdot c^2}{2 \cdot (d-c)} = 1318.024\ mm^2$$

Standard SHM System:

$$\sigma_{At1} := \sqrt{\left(\frac{c^2}{2 \cdot (d-c)}\right)^2 \cdot \sigma_b^{\,2} + \left(\frac{2 \cdot b \cdot c \cdot d - b \cdot c^2}{2 \cdot (d-c)^2}\right)^2 \cdot \sigma_c^{\,2} + \left(\frac{-b \cdot c^2}{2 \cdot (d-c)^2}\right)^2 \cdot \sigma_{d1}^{\,2}}$$

$$\sigma_{At1} = 211.6\ mm^2$$

Enhanced SHM System:

$$\sigma_{At2} := \sqrt{\left(\frac{c^2}{2 \cdot (d-c)}\right)^2 \cdot \sigma_b^{\,2} + \left(\frac{4 \cdot b \cdot c \cdot d - 2 \cdot b \cdot c^2}{4 \cdot (d-c)^2}\right)^2 \cdot \sigma_c^{\,2} + \left(\frac{-2 \cdot b \cdot c^2}{4 \cdot (d-c)^2}\right)^2 \cdot \sigma_{d2}^{\,2}}$$

$$\sigma_{At2} = 127.147\ mm^2$$

Estimated Steel Bar Area

$$A_s(A_t, n) := \frac{A_t}{n}$$

$$\frac{d}{dA_t} A_s(A_t, n) = \frac{1}{n}$$

$$\frac{d}{dn} A_s(A_t, n) = \frac{-A_t}{n^2}$$

$$A_s := \frac{A_t}{n} = 150.255\ mm^2$$

Standard SHM System:

$$\sigma_{As1} := \sqrt{\left(\frac{1}{n}\right)^2 \cdot {\sigma_{At1}}^2 + \left(\frac{-A_t}{n^2}\right)^2 \cdot {\sigma_n}^2} = 25.615\ mm^2$$

Enhanced SHM System:

$$\sigma_{As2} := \sqrt{\left(\frac{1}{n}\right)^2 \cdot {\sigma_{At2}}^2 + \left(\frac{-A_t}{n^2}\right)^2 \cdot {\sigma_n}^2} = 16.862\ mm^2$$

Flexual Capacity

$$M_u(A_s, f_y, d, b, \alpha_1, f'_c) := A_s \cdot f_y \cdot d - \frac{{A_s}^2 \cdot {f_y}^2}{2 \cdot b \cdot \alpha_1 \cdot f'_c}$$

$$\frac{d}{dA_s} M_u(A_s, f_y, d, b, \alpha_1, f'_c) = f_y \cdot d - \frac{2 \cdot A_s \cdot {f_y}^2}{2 \cdot b \cdot \alpha_1 \cdot f'_c}$$

$$\frac{d}{df_y} M_u(A_s, f_y, d, b, \alpha_1, f'_c) = A_s \cdot d - \frac{2 \cdot {A_s}^2 \cdot f_y}{2 \cdot b \cdot \alpha_1 \cdot f'_c}$$

$$\frac{d}{dd} M_u(A_s, f_y, d, b, \alpha_1, f'_c) = A_s \cdot f_y$$

$$\frac{d}{df'_c} M_u(A_s, f_y, d, b, \alpha_1, f'_c) = \frac{{A_s}^2 \cdot {f_y}^2 \cdot (2 \cdot b \cdot \alpha_1)}{4 \cdot b^2 \cdot {\alpha_1}^2 \cdot {f'_c}^2}$$

$$\frac{d}{db} M_u(A_s, f_y, d, b, \alpha_1, f'_c) = \frac{{A_s}^2 \cdot {f_y}^2 \cdot (2 \cdot \alpha_1 \cdot f'_c)}{4 \cdot b^2 \cdot {\alpha_1}^2 \cdot {f'_c}^2}$$

$$\frac{d}{d\alpha_1} M_u(A_s, f_y, d, b, \alpha_1, f'_c) = \frac{{A_s}^2 \cdot {f_y}^2 \cdot (2 \cdot b \cdot f'_c)}{4 \cdot b^2 \cdot {\alpha_1}^2 \cdot {f'_c}^2}$$

$$M_u := A_s \cdot f_y \cdot d - \frac{{A_s}^2 \cdot {f_y}^2}{2 \cdot b \cdot \alpha_1 \cdot f'_c} = 5.672\ kN \cdot m$$

Standard SHM System:

$$\sigma_{Mu1} := \sqrt{\left(f_y \cdot d - \frac{2 \cdot A_s \cdot f_y^{\,2}}{2 \cdot b \cdot \alpha_1 \cdot f'_c}\right)^2 \cdot \sigma_{As1}^{\,2} + \left(A_s \cdot d - \frac{2 \cdot A_s^{\,2} \cdot f_y}{2 \cdot b \cdot \alpha_1 \cdot f'_c}\right)^2 \cdot \sigma_{fy}^{\,2} + \left(A_s \cdot f_y\right)^2 \cdot \sigma_{d1}^{\,2} + \left(\frac{A_s^{\,2} \cdot f_y^{\,2} \cdot (2 \cdot b \cdot \alpha_1)}{4 \cdot b^2 \cdot \alpha_1^{\,2} \cdot f_c^{\,2}}\right)^2 \cdot \sigma_{fc}^{\,2} + \left(\frac{A_s^{\,2} \cdot f_y^{\,2} \cdot (2 \cdot \alpha_1 \cdot f'_c)}{4 \cdot b^2 \cdot \alpha_1^{\,2} \cdot f_c^{\,2}}\right)^2 \cdot \sigma_b^{\,2} + \left(\frac{A_s^{\,2} \cdot f_y^{\,2} \cdot (2 \cdot b \cdot f'_c)}{4 \cdot b^2 \cdot \alpha_1^{\,2} \cdot f_c^{\,2}}\right)^2 \cdot \sigma_{\alpha 1}^{\,2}}$$

$$\sigma_{Mu1} = 0.933 \ m \cdot kN$$

Enhanced SHM System:

$$\sigma_{Mu2} := \sqrt{\left(f_y \cdot d - \frac{2 \cdot A_s \cdot f_y^{\,2}}{2 \cdot b \cdot \alpha_1 \cdot f'_c}\right)^2 \cdot \sigma_{As2}^{\,2} + \left(A_s \cdot d - \frac{2 \cdot A_s^{\,2} \cdot f_y}{2 \cdot b \cdot \alpha_1 \cdot f'_c}\right)^2 \cdot \sigma_{fy}^{\,2} + \left(A_s \cdot f_y\right)^2 \cdot \sigma_{d2}^{\,2} + \left(\frac{A_s^{\,2} \cdot f_y^{\,2} \cdot (2 \cdot b \cdot \alpha_1)}{4 \cdot b^2 \cdot \alpha_1^{\,2} \cdot f_c^{\,2}}\right)^2 \cdot \sigma_{fc}^{\,2} + \left(\frac{A_s^{\,2} \cdot f_y^{\,2} \cdot (2 \cdot \alpha_1 \cdot f'_c)}{4 \cdot b^2 \cdot \alpha_1^{\,2} \cdot f_c^{\,2}}\right)^2 \cdot \sigma_b^{\,2} + \left(\frac{A_s^{\,2} \cdot f_y^{\,2} \cdot (2 \cdot b \cdot f'_c)}{4 \cdot b^2 \cdot \alpha_1^{\,2} \cdot f_c^{\,2}}\right)^2 \cdot \sigma_{\alpha 1}^{\,2}}$$

$$\sigma_{Mu2} = 0.534 \ m \cdot kN$$

Plot the Probability Distribution Figure

$x := 0, 0.1 .. 30$

Without Cover Meter

$$f(x) := \frac{1}{\frac{\sigma_{Mu1}}{kN \cdot m} \cdot \sqrt{2 \cdot \pi}} \cdot e^{\frac{-\left(x - \frac{M_u}{kN \cdot m}\right)^2}{2 \cdot \left(\frac{\sigma_{Mu1}}{kN \cdot m}\right)^2}}$$

With Cover Meter

$$g(x) := \frac{1}{\frac{\sigma_{Mu2}}{kN \cdot m} \cdot \sqrt{2 \cdot \pi}} \cdot e^{\frac{-\left(x - \frac{M_u}{kN \cdot m}\right)^2}{2 \cdot \left(\frac{\sigma_{Mu2}}{kN \cdot m}\right)^2}}$$

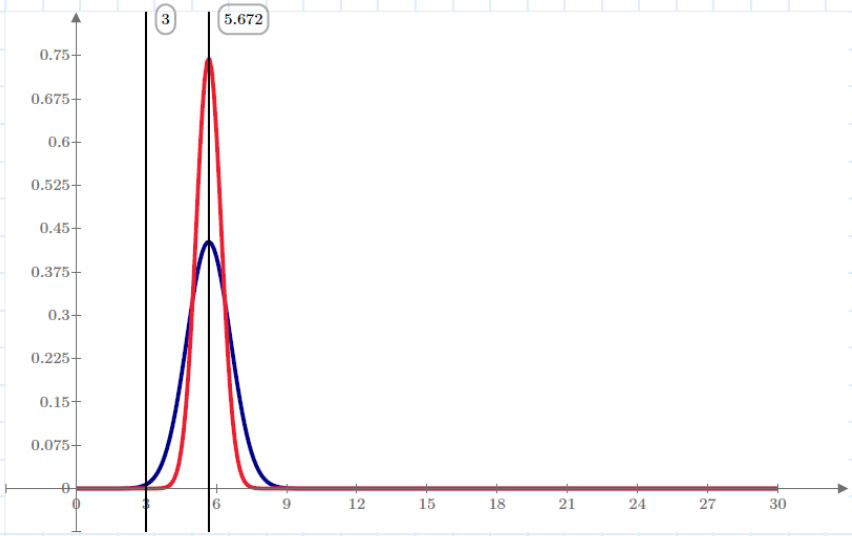

Find the Design Capacity for this beam

Factored Steel Tension and Concrete Compression:

$A_s := 100\ mm^2$

$\phi_c := 0.65$ $\quad C_c = \phi_c \cdot \alpha_1 \cdot f'_c \cdot na \cdot \beta_1 \cdot b$ (Section 8.4.2, CSA A23.3-14)

$\phi_s := 0.85$ $\quad T := \phi_s \cdot f_y \cdot A_s$ (Section 8.4.3, CSA A23.3-14)

$T = C_c$

$0.85 \cdot f_y \cdot A_s = 0.65 \cdot \alpha_1 \cdot f'_c \cdot na \cdot \beta_1 \cdot b$

$$na := \frac{0.85 \cdot f_y \cdot A_s}{0.65 \cdot \alpha_1 \cdot f'_c \cdot \beta_1 \cdot b} = 29.929\ mm$$

$$M_n := T \cdot \left(d - \frac{\beta_1 \cdot na}{2} \right) = 3.281\ m \cdot kN$$

Reliability Index

Standard SHM System: $\beta_1 := \frac{M_u - M_n}{\sigma_{Mu1}} = 2.563$

Enhanced SHM System: $\beta_2 := \frac{M_u - M_n}{\sigma_{Mu2}} = 4.474$

APPENDIX J Sample Calculation for Economic Analysis

The following are the sample calculations for the economic analysis using Batch 3 Beam 3 as an example.

Define Variables

Economic:

Discount Rate: $i := 5\%$

Replacement Cost: $C_{replace} := 1227744 \quad dollars$

Standard SHM Cost: $C_{SHMs} := 69693.75 \quad dollars$

Enhanced SHM Cost: $C_{SHMe} := C_{SHMs} + 6000 = 75694 \quad dollars$

Reliability:

Load Effect: $\mu_L := 3 \ \boldsymbol{kN \cdot m}$

Critical Reliability Index: $\beta := 2$

Faraday Corrosion:

Atomic Weight: $W := 56 \ \frac{\boldsymbol{gm}}{\boldsymbol{mol}}$

Current Density: $I := 10 \cdot 10^{-6} \ \frac{\boldsymbol{A}}{\boldsymbol{cm^2}}$

Number of Equivalents Exchanged: $n := 2$

Faraday Constant: $F := 96485.34 \ \boldsymbol{A} \cdot \frac{\boldsymbol{s}}{\boldsymbol{mol}}$

Configuration:

Beam Width: $b := 72 \ \boldsymbol{mm}$

Beam Height: $h := 140 \ \boldsymbol{mm}$

Concrete Cover: $cc := 33 \ \boldsymbol{mm}$

Rebar Depth: $d := h - cc - \frac{11.3 \ \boldsymbol{mm}}{2} = 101 \ \boldsymbol{mm}$

Material Properties:

Steel Yield Strength: $f_y := 437.3 \ \boldsymbol{MPa}$

Concrete Strength: $f'_c := 39.2 \ \boldsymbol{MPa}$

$$\alpha_1 := 0.85 - 0.0015 \cdot \frac{f'_c}{\boldsymbol{MPa}} = 0.791$$

$$\beta_1 := 0.97 - 0.0025 \cdot \frac{f'_c}{\boldsymbol{MPa}} = 0.872$$

Steel Density: $\rho_s := 8.05\ \frac{gm}{cm^3}$

Circumstance 1: Without Any Monitoring System

Life Span: $y := 45\ yr$

Annual Worth Life Cycle Cost:

$$AWLCC_1 := C_{replace} \cdot \left(\frac{i \cdot (1+i)^{\frac{y}{yr}}}{(1+i)^{\frac{y}{yr}} - 1} \right) = 69075 \quad dollars$$

Circumstance 2: Using Standard SHM System

Reliability Index: $\beta := 2.1$

STDV of Mean Resistance: $\sigma_R := 0.6\ kN \cdot m$

Estimated Rebar Area: $A_e := 111\ mm^2$

Find the Minimum Allowable Rebar Area
(assume end of service life when β drops to 2):

Corresponding Resistance when β drops to 2:

$$\frac{\mu_{Rallow} - \mu_L}{\sigma_R} = \beta = 2$$

$$\mu_{Rallow} := 2 \cdot \sigma_R + \mu_L = 4.2\ kN \cdot m$$

Corresponding Rebar area when β drops to 2:

$$\mu_{Rallow} = T \cdot \left(d - \frac{\beta_1 \cdot c}{2} \right) \qquad c = \frac{\left(d - \frac{\mu_{Rallow}}{T} \right) \cdot 2}{\beta_1}$$

$$T = f_y \cdot A_s \qquad c = \frac{\left(d - \frac{\mu_{Rallow}}{f_y \cdot A_s} \right) \cdot 2}{\beta_1}$$

$$C_c = \alpha_1 \cdot f'_c \cdot c \cdot \beta_1 \cdot b = T \qquad c = \frac{T}{\alpha_1 \cdot f'_c \cdot \beta_1 \cdot b} = \frac{f_y \cdot A_s}{\alpha_1 \cdot f'_c \cdot \beta_1 \cdot b}$$

$$\frac{\left(d - \frac{\mu_{Rallow}}{f_y \cdot A_s} \right) \cdot 2}{\beta_1} = \frac{f_y \cdot A_s}{\alpha_1 \cdot f'_c \cdot \beta_1 \cdot b} \xrightarrow{solve,\ A_s,\ explicit} \left[\begin{array}{l} \frac{-\sqrt{f'_c{}^2 \cdot f_y^2 \cdot \alpha_1^2 \cdot b^2 \cdot d^2 - 2 \cdot f'_c \cdot f_y^2 \cdot \alpha_1 \cdot \mu_{Rallow} \cdot b} + f'_c \cdot f_y \cdot \alpha_1 \cdot b \cdot d}{f_y^2} \\ \frac{\sqrt{f'_c{}^2 \cdot f_y^2 \cdot \alpha_1^2 \cdot b^2 \cdot d^2 - 2 \cdot f'_c \cdot f_y^2 \cdot \alpha_1 \cdot \mu_{Rallow} \cdot b} + f'_c \cdot f_y \cdot \alpha_1 \cdot b \cdot d}{f_y^2} \end{array} \right]$$

$$A_{allow} := \frac{\sqrt{b^2 \cdot d^2 \cdot \alpha_1^{\,2} \cdot f'_c{}^2 - 2 \cdot b \cdot \alpha_1 \cdot f'_c \cdot \mu_{Rallow}} + b \cdot d \cdot \alpha_1 \cdot f'_c}{f_y} = 930 \ mm^2$$

$$A_{allow} := -\frac{\sqrt{b^2 \cdot d^2 \cdot \alpha_1^{\,2} \cdot f'_c{}^2 - 2 \cdot b \cdot \alpha_1 \cdot f'_c \cdot \mu_{Rallow}} - b \cdot d \cdot \alpha_1 \cdot f'_c}{f_y} = 106 \ mm^2$$

Real Root

$$d_{allow} := \sqrt{\frac{A_{allow} \cdot 4}{\pi}} = 11.591 \ mm$$

Find the Extended Life Span:

Allowable mass loss per unit surface area:

$$M := \frac{(A_e - A_{allow}) \cdot 10 \ cm \cdot \rho_s}{\pi \cdot d_{allow} \cdot 10 \ cm} = 1.211 \ \frac{kg}{m^2}$$

Faraday's Law:

$$M = \frac{W \cdot I \cdot T}{n \cdot F}$$

Additional Service Life:

$$T := \frac{M \cdot n \cdot F}{W \cdot I} = 1.3 \ yr$$

Total Life Span:

$$y_2 := 45 \ yr + T = 46.3 \ yr$$

Annual Worth Life Cycle Cost:

Present Cost of the Replacement:

$$P_2 := \frac{C_{replace}}{(1+i)^{\frac{T}{yr}}} = 1151033$$

Annual Worth Life Cycle Cost:

$$AWLCC_2 := (P_2 + C_{SHMs}) \cdot \left(\frac{i \cdot (1+i)^{\frac{y_2}{yr}}}{(1+i)^{\frac{y_2}{yr}} - 1} \right) = 68147 \quad dollars$$

Circumstance 3: With Enhanced SHM System

Reliability Index:

$$\beta := 4.7$$

STDV of Mean Resistance:

$$\sigma_R := 0.3 \ kN \cdot m$$

Estimated Rebar Area:

$$A_e = 111 \ mm^2$$

Find the Minimum Allowable Rebar Area
(assume end of service life when β drops to 2):

Corresponding Resistance when β drops to 2:

$$\frac{\mu_{Rallow}-\mu_L}{\sigma_R}=\beta=2$$

$$\mu_{Rallow}:=2\cdot\sigma_R+\mu_L=3.6\ \ kN\cdot m$$

Corresponding Rebar area when β drops to 2:

$$\mu_{Rallow}=T\cdot\left(d-\frac{\beta_1\cdot c}{2}\right)\qquad c=\frac{\left(d-\frac{\mu_{Rallow}}{T}\right)\cdot 2}{\beta_1}$$

$$T=f_y\cdot A_s\qquad c=\frac{\left(d-\frac{\mu_{Rallow}}{f_y\cdot A_s}\right)\cdot 2}{\beta_1}$$

$$C_c=\alpha_1\cdot f'_c\cdot c\cdot\beta_1\cdot b=T\qquad c=\frac{T}{\alpha_1\cdot f'_c\cdot\beta_1\cdot b}=\frac{f_y\cdot A_s}{\alpha_1\cdot f'_c\cdot\beta_1\cdot b}$$

$$\frac{\left(d-\frac{\mu_{Rallow}}{f_y\cdot A_s}\right)\cdot 2}{\beta_1}=\frac{f_y\cdot A_s}{\alpha_1\cdot f'_c\cdot\beta_1\cdot b}\xrightarrow{solve,\,A_s,\,explicit}\left[\begin{array}{c}\frac{-\sqrt{f'_c{}^2\cdot f_y^2\cdot\alpha_1^2\cdot b^2\cdot d^2-2\cdot f'_c\cdot f_y^2\cdot\alpha_1\cdot\mu_{Rallow}\cdot b}+f'_c\cdot f_y\cdot\alpha_1\cdot b\cdot d}{f_y^2}\\ \frac{\sqrt{f'_c{}^2\cdot f_y^2\cdot\alpha_1^2\cdot b^2\cdot d^2-2\cdot f'_c\cdot f_y^2\cdot\alpha_1\cdot\mu_{Rallow}\cdot b}+f'_c\cdot f_y\cdot\alpha_1\cdot b\cdot d}{f_y^2}\end{array}\right]$$

$$A_{allow}:=\frac{\sqrt{b^2\cdot d^2\cdot\alpha_1{}^2\cdot f'_c{}^2-2\cdot b\cdot\alpha_1\cdot f'_c\cdot\mu_{Rallow}}+b\cdot d\cdot\alpha_1\cdot f'_c}{f_y}=946\ \ mm^2$$

$$A_{allow}:=-\frac{\sqrt{b^2\cdot d^2\cdot\alpha_1{}^2\cdot f'_c{}^2-2\cdot b\cdot\alpha_1\cdot f'_c\cdot\mu_{Rallow}}-b\cdot d\cdot\alpha_1\cdot f'_c}{f_y}=89\ \ mm^2$$

Real Root

$$d_{allow}:=\sqrt{\frac{A_{allow}\cdot 4}{\pi}}=10.636\ \ mm$$

Find the Extended Life Span:

Allowable mass loss per unit surface area:

$$M:=\frac{\left(A_e-A_{allow}\right)\cdot 10\ cm\cdot\rho_s}{\pi\cdot d_{allow}\cdot 10\ cm}=5.335\ \frac{kg}{m^2}$$

Faraday's Law:

$$M=\frac{W\cdot I\cdot T}{n\cdot F}$$

Additional Service Life:

$$T:=\frac{M\cdot n\cdot F}{W\cdot I}=5.8\ \ yr$$

Total Life Span: $y_3 := 45\ yr + T = 50.8\ yr$

Annual Worth Life Cycle Cost:

Present Cost of the Replacement: $P_3 := \frac{C_{replace}}{(1+i)^{\frac{T}{yr}}} = 9.24 \cdot 10^5$

Annual Worth Life Cycle Cost:

$$AWLCC_3 := (P_3 + C_{SHMe}) \cdot \left(\frac{i \cdot (1+i)^{\frac{y_3}{yr}}}{(1+i)^{\frac{y_3}{yr}} - 1} \right) = 54553 \quad dollars$$

Summary:

	Life Span	Annual Worth of LCC
Without SHM:	$y = 45\ yr$	$AWLCC_1 = 69075$ *dollars*
With Standard SHM:	$y_2 = 46.3\ yr$	$AWLCC_2 = 68147$ *dollars*
With Enhanced SHM:	$y_3 = 50.8\ yr$	$AWLCC_3 = 54553$ *dollars*

APPENDIX K Copyright Permission for Figure 2.2

ELSEVIER LICENSE
TERMS AND CONDITIONS

Aug 01, 2020

This Agreement between University of Saskatchewan -- Zoe Mao ("You") and Elsevier ("Elsevier") consists of your license details and the terms and conditions provided by Elsevier and Copyright Clearance Center.

License Number	4880450491665
License date	Aug 01, 2020
Licensed Content Publisher	Elsevier
Licensed Content Publication	Elsevier Books
Licensed Content Title	Concrete and Masonry Movements
Licensed Content Author	J.J. Brooks
Licensed Content Date	Jan 1, 2015
Licensed Content Pages	37
Start Page	545
End Page	581
Type of Use	reuse in a thesis/dissertation
Portion	figures/tables/illustrations
Number of figures/tables/illustrations	1

Format	electronic
Are you the author of this Elsevier chapter?	No
Will you be translating?	No
Title	Master Student
Institution name	University of Saskatchewan
Expected presentation date	Dec 2020
Portions	Figure 16.17. Demountable mechanical Demec strain gauges.
Requestor Location	University of Saskatchewan 543 Kloppenburg Cres Saskatoon, SK S7W 0P1 Canada Attn: University of Saskatchewan
Publisher Tax ID	GB 494 6272 12
Total	0.00 CAD

Terms and Conditions

INTRODUCTION

1. The publisher for this copyrighted material is Elsevier. By clicking "accept" in connection with completing this licensing transaction, you agree that the following terms and conditions apply to this transaction (along with the Billing and Payment terms and conditions established by Copyright Clearance Center, Inc. ("CCC"), at the time that you opened your Rightslink account and that are available at any time at http://myaccount.copyright.com).

GENERAL TERMS

2. Elsevier hereby grants you permission to reproduce the aforementioned material subject to the terms and conditions indicated.

3. Acknowledgement: If any part of the material to be used (for example, figures) has appeared in our publication with credit or acknowledgement to another source, permission must also be sought from that source. If such permission is not obtained then that material may not be included in your publication/copies. Suitable acknowledgement to the source must be made, either as a footnote or in a reference list at the end of your publication, as follows:

"Reprinted from Publication title, Vol /edition number, Author(s), Title of article / title of chapter, Pages No., Copyright (Year), with permission from Elsevier [OR APPLICABLE SOCIETY COPYRIGHT OWNER]." Also Lancet special credit - "Reprinted from The Lancet, Vol. number, Author(s), Title of article, Pages No., Copyright (Year), with permission from Elsevier."

4. Reproduction of this material is confined to the purpose and/or media for which permission is hereby given.

5. Altering/Modifying Material: Not Permitted. However figures and illustrations may be altered/adapted minimally to serve your work. Any other abbreviations, additions, deletions and/or any other alterations shall be made only with prior written authorization of Elsevier Ltd. (Please contact Elsevier at permissions@elsevier.com). No modifications can be made to any Lancet figures/tables and they must be reproduced in full.

6. If the permission fee for the requested use of our material is waived in this instance, please be advised that your future requests for Elsevier materials may attract a fee.

7. Reservation of Rights: Publisher reserves all rights not specifically granted in the combination of (i) the license details provided by you and accepted in the course of this licensing transaction, (ii) these terms and conditions and (iii) CCC's Billing and Payment terms and conditions.

8. License Contingent Upon Payment: While you may exercise the rights licensed immediately upon issuance of the license at the end of the licensing process for the transaction, provided that you have disclosed complete and accurate details of your proposed use, no license is finally effective unless and until full payment is received from you (either by publisher or by CCC) as provided in CCC's Billing and Payment terms and conditions. If full payment is not received on a timely basis, then any license preliminarily granted shall be deemed automatically revoked and shall be void as if never granted. Further, in the event that you breach any of these terms and conditions or any of CCC's Billing and Payment terms and conditions, the license is automatically revoked and shall be void as if never granted. Use of materials as described in a revoked license, as well as any use of the materials beyond the scope of an unrevoked license, may constitute copyright infringement and publisher reserves the right to take any and all action to protect its copyright in the materials.

9. Warranties: Publisher makes no representations or warranties with respect to the licensed material.

10. Indemnity: You hereby indemnify and agree to hold harmless publisher and CCC, and their respective officers, directors, employees and agents, from and against any and all claims arising out of your use of the licensed material other than as specifically authorized pursuant to this license.

11. No Transfer of License: This license is personal to you and may not be sublicensed, assigned, or transferred by you to any other person without publisher's written permission.

12. No Amendment Except in Writing: This license may not be amended except in a writing signed by both parties (or, in the case of publisher, by CCC on publisher's behalf).

13. Objection to Contrary Terms: Publisher hereby objects to any terms contained in any purchase order, acknowledgment, check endorsement or other writing prepared by you, which terms are inconsistent with these terms and conditions or CCC's Billing and Payment terms and conditions. These terms and conditions, together with CCC's Billing and Payment terms and conditions (which are incorporated herein), comprise the entire agreement between you and publisher (and CCC) concerning this licensing transaction. In the event of any conflict between your obligations established by these terms and conditions and those established by CCC's Billing and Payment terms and conditions, these terms and conditions shall control.

14. Revocation: Elsevier or Copyright Clearance Center may deny the permissions described in this License at their sole discretion, for any reason or no reason, with a full refund payable to you. Notice of such denial will be made using the contact information provided by you. Failure to receive such notice will not alter or invalidate the denial. In no event will Elsevier or Copyright Clearance Center be responsible or liable for any costs, expenses or damage incurred by you as a result of a denial of your permission request, other than a refund of the amount(s) paid by you to Elsevier and/or Copyright Clearance Center for denied permissions.

LIMITED LICENSE

The following terms and conditions apply only to specific license types:

15. **Translation**: This permission is granted for non-exclusive world **English** rights only unless your license was granted for translation rights. If you licensed translation rights you may only translate this content into the languages you requested. A professional translator must perform all translations and reproduce the content word for word preserving the integrity of the article.

16. **Posting licensed content on any Website**: The following terms and conditions apply as follows: Licensing material from an Elsevier journal: All content posted to the web site must maintain the copyright information line on the bottom of each image; A hyper-text must be included to the Homepage of the journal from which you are licensing at http://www.sciencedirect.com/science/journal/xxxxx or the Elsevier homepage for books at http://www.elsevier.com; Central Storage: This license does not include permission for a scanned version of the material to be stored in a central repository such as that provided by Heron/XanEdu.

Licensing material from an Elsevier book: A hyper-text link must be included to the Elsevier homepage at http://www.elsevier.com . All content posted to the web site must maintain the copyright information line on the bottom of each image.

Posting licensed content on Electronic reserve: In addition to the above the following clauses are applicable: The web site must be password-protected and made available only to bona fide students registered on a relevant course. This permission is granted for 1 year only. You may obtain a new license for future website posting.

17. **For journal authors:** the following clauses are applicable in addition to the above:

Preprints:

A preprint is an author's own write-up of research results and analysis, it has not been peer-reviewed, nor has it had any other value added to it by a publisher (such as formatting, copyright, technical enhancement etc.).

Authors can share their preprints anywhere at any time. Preprints should not be added to or enhanced in any way in order to appear more like, or to substitute for, the final versions of articles however authors can update their preprints on arXiv or RePEc with their Accepted Author Manuscript (see below).

If accepted for publication, we encourage authors to link from the preprint to their formal publication via its DOI. Millions of researchers have access to the formal publications on ScienceDirect, and so links will help users to find, access, cite and use the best available version. Please note that Cell Press, The Lancet and some society-owned have different preprint policies. Information on these policies is available on the journal homepage.

Accepted Author Manuscripts: An accepted author manuscript is the manuscript of an article that has been accepted for publication and which typically includes author-incorporated changes suggested during submission, peer review and editor-author communications.

Authors can share their accepted author manuscript:

- immediately
  - via their non-commercial person homepage or blog
  - by updating a preprint in arXiv or RePEc with the accepted manuscript
  - via their research institute or institutional repository for internal institutional uses or as part of an invitation-only research collaboration work-group
  - directly by providing copies to their students or to research collaborators for their personal use
  - for private scholarly sharing as part of an invitation-only work group on commercial sites with which Elsevier has an agreement
- After the embargo period
  - via non-commercial hosting platforms such as their institutional repository
  - via commercial sites with which Elsevier has an agreement

In all cases accepted manuscripts should:

- link to the formal publication via its DOI
- bear a CC-BY-NC-ND license - this is easy to do
- if aggregated with other manuscripts, for example in a repository or other site, be shared in alignment with our hosting policy not be added to or enhanced in any way to appear more like, or to substitute for, the published journal article.

Published journal article (JPA): A published journal article (PJA) is the definitive final record of published research that appears or will appear in the journal and embodies all value-adding publishing activities including peer review co-ordination, copy-editing, formatting, (if relevant) pagination and online enrichment.

Policies for sharing publishing journal articles differ for subscription and gold open access articles:

Subscription Articles: If you are an author, please share a link to your article rather than the full-text. Millions of researchers have access to the formal publications on ScienceDirect, and so links will help your users to find, access, cite, and use the best available version.

Theses and dissertations which contain embedded PJAs as part of the formal submission can be posted publicly by the awarding institution with DOI links back to the formal publications on ScienceDirect.

If you are affiliated with a library that subscribes to ScienceDirect you have additional private sharing rights for others' research accessed under that agreement. This includes use for classroom teaching and internal training at the institution (including use in course packs and courseware programs), and inclusion of the article for grant funding purposes.

Gold Open Access Articles: May be shared according to the author-selected end-user license and should contain a CrossMark logo, the end user license, and a DOI link to the formal publication on ScienceDirect.

Please refer to Elsevier's posting policy for further information.

18. **For book authors** the following clauses are applicable in addition to the above: Authors are permitted to place a brief summary of their work online only. You are not allowed to download and post the published electronic version of your chapter, nor may you scan the printed edition to create an electronic version. **Posting to a repository:** Authors are permitted to post a summary of their chapter only in their institution's repository.

19. **Thesis/Dissertation**: If your license is for use in a thesis/dissertation your thesis may be submitted to your institution in either print or electronic form. Should your thesis be published commercially, please reapply for permission. These requirements include permission for the Library and Archives of Canada to supply single copies, on demand, of the complete thesis and include permission for Proquest/UMI to supply single copies, on demand, of the complete thesis. Should your thesis be published commercially, please reapply for permission. Theses and dissertations which contain embedded PJAs as part of the formal submission can be posted publicly by the awarding institution with DOI links back to the formal publications on ScienceDirect.

Elsevier Open Access Terms and Conditions

You can publish open access with Elsevier in hundreds of open access journals or in nearly 2000 established subscription journals that support open access publishing. Permitted third party re-use of these open access articles is defined by the author's choice of Creative Commons user license. See our open access license policy for more information.

Terms & Conditions applicable to all Open Access articles published with Elsevier:

Any reuse of the article must not represent the author as endorsing the adaptation of the article nor should the article be modified in such a way as to damage the author's honour or reputation. If any changes have been made, such changes must be clearly indicated.

The author(s) must be appropriately credited and we ask that you include the end user license and a DOI link to the formal publication on ScienceDirect.

If any part of the material to be used (for example, figures) has appeared in our publication with credit or acknowledgement to another source it is the responsibility of the user to ensure their reuse complies with the terms and conditions determined by the rights holder.

Additional Terms & Conditions applicable to each Creative Commons user license:

CC BY: The CC-BY license allows users to copy, to create extracts, abstracts and new works from the Article, to alter and revise the Article and to make commercial use of the Article (including reuse and/or resale of the Article by commercial entities), provided the user gives appropriate credit (with a link to the formal publication through the relevant DOI), provides a link to the license, indicates if changes were made and the licensor is not represented as endorsing the use made of the work. The full details of the license are available at http://creativecommons.org/licenses/by/4.0.

CC BY NC SA: The CC BY-NC-SA license allows users to copy, to create extracts, abstracts and new works from the Article, to alter and revise the Article, provided this is not done for commercial purposes, and that the user gives appropriate credit (with a link to the formal publication through the relevant DOI), provides a link to the license, indicates if changes were made and the licensor is not represented as endorsing the use made of the work. Further, any new works must be made available on the same conditions. The full details of the license are available at http://creativecommons.org/licenses/by-nc-sa/4.0.

CC BY NC ND: The CC BY-NC-ND license allows users to copy and distribute the Article, provided this is not done for commercial purposes and further does not permit distribution of the Article if it is changed or edited in any way, and provided the user gives appropriate credit (with a link to the formal publication through the relevant DOI), provides a link to the license, and that the licensor is not represented as endorsing the use made of the work. The full details of the license are available at http://creativecommons.org/licenses/by-nc-nd/4.0. Any commercial reuse of Open Access articles published with a CC BY NC SA or CC BY NC ND license requires permission from Elsevier and will be subject to a fee.

Commercial reuse includes:

- Associating advertising with the full text of the Article
- Charging fees for document delivery or access
- Article aggregation
- Systematic distribution via e-mail lists or share buttons

Posting or linking by commercial companies for use by customers of those companies.

20. **Other Conditions**:

v1.9

Questions? customercare@copyright.com or +1-855-239-3415 (toll free in the US) or +1-978-646-2777.